Crystal-Structure Studies and Techniques at High Pressure

Thesis submitted by

David Robert Allan

For the Degree of

Doctor of Philosophy

Department of Physics

The University of Edinburgh

January 1993

Declaration

Except where otherwise stated, the research undertaken in this thesis was the unaided work of the author. Where the work was done in collaboration with others, a significant contribution was made by the author.

signed

David R. Allan

Acknowledgements

I take great pleasure in recording my appreciation of those who have helped and supported me throughout the course of this work. I am especially grateful to the following:

My supervisor, Professor R.J. Nelmes for his guidance, patience and encoragement, and for introducing me to the field of high-pressure diffraction.

Dr. P.D. Hatton for his encouragement, optimism (particularly when the work wasn't going to plan) and many useful discussions.

Dr. J.S. Loveday with whom the neutron powder-diffraction experiments were done, Dr. R.O. Piltz for his help, cheerfulness, sense of humour and freely expressed opinions, and Dr. M.I. McMahon for his help and companionship over the last year at the SRS Daresbury Laboratory.

Dr. H. Ahsbahs for providing access to his pressure cell, and to Dr. W.F. Kuhs and R. Dorwarth with whom the single-crystal neutron-diffraction experiments were done.

Dr. P.A. Thomas for her encouragement of the experiment on KTP, for her provision of a suitable sample and for her help with the interpretation of the results.

To the S.E.R.C. for financial support.

I would also like to take the opportunity to express my thanks to all those friends and colleagues in the Physics Department at Edinburgh and at the SRS Daresbury Laboratory who have made the last three years extremely enjoyable.

Finally and above all, I am grateful to my parents for their unfailing encouragement, understanding and support throughout.

This thesis is dedicated to my late brother Maurice G. Allan (1965-1989).

Abstract

This thesis is concerned with the application of high-pressure diffraction techniques — involving both x-rays and neutrons, single crystal and powder samples — to the study of crystal-structures at high pressure and to the development of such techniques for the determination of crystal-structures with greater accuracy and more reliabilty. The current state-of-the-art high-pressure diffraction techniques are reviewed and applied to the study of a number of interesting materials.

The crystal structure of $KTiOPO_4$ (KTP) has been determined as a function of pressure as its phase transition at 5.5 GPa is approached, using single-crystal x-ray diffraction techniques. The principal changes with pressure are in the coordination environments of the potassium atoms and in the linking angles of the TiO_6-PO_4 structural framework. In general the distortions of the TiO_6 octahedra, which have been linked to the second harmonic generating properties of KTP, are retained although there are some small changes in the Ti-O bond lengths. The structure of the high-pressure phase of KTP has also been determined, using single-crystal x-ray diffraction, and it appears that, although the phase transition is strongly first-order and involves a 4.2% reduction of the unit-cell volume, the $Pna2_1$ space-group symmetry of the low-pressure phase is retained. The main structural changes at the phase transition involve tilting of the PO_4 tetrahedra relative to the TiO_6 octahedra, while both units remain relatively unchanged in size and shape. In particular, the TiO_6 octahedra remain highly distorted and retain their anomalously short Ti-OT bonds. The potassium atoms are also observed to undergo relatively large movements of about 0.5Å along the polar c-axis at the transition.

The crystal structure of KH_2PO_4 (KDP) has been determined at 2.9 GPa, a pressure just below that of its high-pressure ambient-temperature phase transition, using single-crystal neutron diffraction. It appears that the oxygen-oxygen distance, 2R, undergoes a uniform compression to 2.9 GPa which is moderated by the rotation of the essentially rigid PO_4 tetrahedra around their $\bar{4}$-axes. The compression of 2R is also accompanied by a re-orientation of the hydrogen bond which is observed to increase its inclination with respect to the ab-plane. The hydrogen atom site separation, δ, is not found to vanish as the phase transition

Contents

is approached, as has previously been proposed, but, instead exhibits a linear decrease with pressure to a value which is only about 25% smaller than that at ambient pressure.

The crystal structures of α-rhombohedral boron (α-boron) and boron carbide (B_4C) have been determined as a function of pressure, using single-crystal x-ray diffraction techniques and both x-ray and neutron powder-diffraction techniques. It appears, within the precision of the refined structural parameters, that the $B_{11}C$ icosahedra of B_4C and the B_{12} icosahedra of α-boron are not significantly different. This result casts some doubt on the structural interpretation of the pronounced decrease in the bulk modulus of boron carbide that has been observed, from indirect measurements, below the 13% carbon concentration.

Chapter 1

Introduction

1.1 Pressure as an Experimental Parameter

Nonambient studies of crystalline materials are crucial to an understanding of the solid state. By varying the thermodynamic variables of temperature and pressure, experiments can be performed to establish the nature of many physical phenomena exhibited by these materials. The parameter of temperature can be used to alter the thermal energy of the atoms within the crystal structure and is routinely applied in many physical investigations over the range of several orders of magnitude both above and below ambient temperature. Hydrostatic pressure, on the other hand, tends to be underutilised as a thermodynamic parameter although it enables the variation of interatomic distances and atomic potentials at constant thermal energy and, in this sense, is an extremely powerful variable. It is also significant that variable-temperature experiments only investigate a very narrow line along the temperature axis of pressure-temperature diagrams although, when coupled with variable-pressure, these phase diagrams can assume great complexity. (For example, the simple molecule of H_2O has been shown to exhibit ten crystal structures under the combination of nonambient temperature and pressure (Liu and Bassett (1986).) The high-pressure regions of such phase diagrams contain much that is of both applied and scientific value.

High-pressure can lead to a range of dramatic changes in the physical properties of

many materials. The semiconductor InSb, for example, assumes a metallic phase at a pressure of 2.1 GPa through a first-order structural phase transition (Nelmes *et al* (1992a). Metallisation has also been observed for the simple molecular crystal I_2 through a more gradual phase transition which is completed at approximately 17 GPa (Shimomura *et al* (1978)). Other elements such as boron and hydrogen have been predicted to transform to metals at very much higher pressures (Mailhiot *et al* (1990), LeSar *et al* (1989)). Indeed, the experimental confirmation of the latter has generated great interest in the scientific community and has done much to extend the obtainable pressure range into the megabar region.

Hydrostatic pressure has also been shown to influence the electrical transport properties of materials in a more subtle manner than metallisation. For example, the refractory semi-conductor boron carbide (B_4C) has been demonstrated to have a conductivity which decreases with increasing pressure. This result was found to be in semi-quantitative agreement with the theoretical predictions of a model which attributes the electronic transport to bipolaronic hopping (Samara *et al* (1985)). Pressure has also been found to influence the transition temperature in the high-temperature oxide superconductors. One of the largest effects was observed in the 1-2-4 compound $YBa_2Cu_4O_8$ which has a dT_c/dP of 5.5K/GPa (Bucher *et al* (1989)). This result has aided the theoretical interpretation of the 'oxygen pressure' effect in raising the transition temperature of the 1-2-3 compound $YBa_2Cu_3O_x$ as x is increased from 6.5 to 7 (Cava *et al* (1988)).

The study of the electronic structure and bonding of atoms can also be aided by high-pressure. Cesium, for example, is believed to undergo a 6s-5d electronic transition under pressure, which progresses continuously from ambient pressure and discontinuously near 4.2 GPa (Jayaraman *et al* (1967)). The study of the susceptibilty of covalent and ionic crystals under pressure has also aided the interpretation of the dependence of the nonlinear optical susceptibility on bond length (Levine (1974), Van Vechten (1969)). A final example of the use of high-pressure is in the study of the hydrogen ordering transition in materials such as KH_2PO_4 (KDP). At ambient pressure the transition temperature (T_c) is 122K, which can be reduced to 0K under a pressure of 1.7 GPa (Samara (1971)). Interpretation of the sensitivity of T_c with pressure has led to a revision of the theory for the transition (McMahon *et al* (1990)).

Although there is clearly a wealth of interesting physical phenomena and a variety of different phase diagrams at high pressure, it is rather surprising that relatively few crystal-structure studies have been performed above ambient-pressure. Indeed, the identification of high-pressure structural phase transitions has often been inferred indirectly through optical measurements, such as Raman spectroscopy (Sharma (1989)) and reflectivity (Bassett *et al* (1967)), or the measurement of physical properties, such as compressibility (Bridgman (1971)), resistance (Mao and Bell (1981)) or capacitance (Bao *et al* (1991)). Although Raman spectroscopy measurements may give valuable symmetry information about the atomic environments within a crystal structure, these methods do not allow the determination of the lattice type or spacegroup, let alone the positions of atoms within the unit cell. As a consequence, the structures of many high-pressure phases are completely unknown.

In order to determine the full structure of these high-pressure phases the techniques of x-ray and neutron diffraction must be applied. However, it is rather surprising that diffraction techniques have achieved only limited success at high pressure. For example, although x-ray powder diffraction techniques have been applied at pressures in excess of 3Mbar, and have successfully determined the lattice type and spacegroup of many materials, it has not generally been possible to determine the positions of atoms not fixed by the crystal symmetry. In order to do so, from least-squares refinement of the diffracted x-ray intensities, single crystal methods have been required and at present the pressures for such studies has been limited to the region of 20 GPa. The majority of high-pressure single crystal studies have been performed in the fields of geophysics and geochemistry where mineralogists are concerned with the behaviour of minerals in the Earth's deep interior (Finger and Hazen (1991)). Neutron diffraction techniques have had a much more limited pressure range and it has not been possible to undertake diffraction studies above approximately 5 GPa, although powder diffraction, as well as single-crystal diffraction can be used. Compared to structural studies undertaken at ambient conditions, high-pressure structural-studies with both neutrons and x-rays have been of limited accuracy and have often been affected by systematic error, with the subtle structural changes with pressure being poorly determined (for example compare Kaldis *et al* (1989) and Nelmes *et al* (1990)). This is unfortunate since an understanding of the pressure dependence of many

physical properties may depend on only small variations in crystalline structure. Clearly then, it is essential that high-pressure diffraction techniques are improved so that crystal-structure determination can be made with greater accuracy and more reliability.

1.2 Objectives

Over the past five years members of the Condensed Matter Physics Group at The University of Edinburgh have been involved in the development of new techniques for crystal structure determination at high pressure. The project was planned to not only develop the existing programme of single-crystal neutron and x-ray diffraction studies, which the group has undertaken since the late 1970's, but also to develop new powder-diffraction techniques for high-pressure structure determination at spallation-neutron and synchrotron x-ray sources. The principal aims of this new project are to identify the factors limiting the accuracy of high-pressure structure determination and to introduce new methods, or new high-pressure equipment, so that these factors are minimised, or eliminated. These aims are motivated by the desire to determine the subtle structural changes that many materials exhibit with pressure, and that have only a relatively small effect on the diffracted intensities, and to extend accurate determination of high-pressure structures to weakly scattering (low Z) materials.

This thesis describes the author's involvement in this broadly based project. The central purpose has been to gain experience across the full range of diffraction techniques — using both single-crystal and powder samples and working with both x-ray and neutron radiation — whilst at the same time developing a specialisation in one of them, namely single-crystal x-ray diffraction. This is reflected in the structure of the thesis: the largest part is devoted to single-crystal x-ray diffraction studies, but state-of-the-art work and developments are also presented using single-crystal neutron diffraction and powder diffraction techniques. For completeness, developments not principally involving the author will be described and reviewed. However, it must be emphasised that the author has been closely connected with all the work presented. These include the single-crystal techniques

of section 3.2, the basic beam-line techniques for angle-dispersive x-ray powder-diffraction described in section 3.3, and the development of the Paris-Edinburgh cell described in section 3.4.

1.3 Thesis Outline

The thesis is organised in the following manner:

Chapter 2 serves as an introduction to the principles of diffraction for crystal structures using both x-ray and neutron radiation with powder and single-crystal techniques. It also reviews the equipment and techniques for high-pressure diffraction and details recent technique developments.

Chapter 3 describes the work of the Condensed Matter Physics Group at The University of Edinburgh to improve the accuracy and scope of high-pressure structural studies through the development of new techniques and equipment, and to improve high-pressure techniques already established. The work described covers single-crystal x-ray diffraction, neutron powder-diffraction and the development of an imaging-plate system for high-pressure x-ray powder-diffraction.

Chapter 4 describes the application of high-pressure single-crystal techniques, using x-ray radiation, to the study of the nonlinear optical material $KTiOPO_4$ (KTP). KTP is a particularly important material in the field of opto-electronics and, among its many technological applications, is an extremely efficient second-harmonic generator (SHG) of Nd-YAG laser light. The structure of KTP assumes the acentric $Pna2_1$ spacegroup at atmospheric pressure and is characterised by a framework of TiO_6 octahedra and PO_4 tetrahedra, which encloses the weakly bound potassium atoms. It is the anomalously short Ti-O bonds within the highly distorted TiO_6 octahedra that have been associated with the non-linear optical properties of the crystal. Recently, it has been demonstrated by Kourouklis *et al* (1987) that KTP exhibits a structural phase transition at a pressure of 5.5 GPa. Their high-pressure Raman study shows that there is an increase in the number of detectable modes at 5.5 GPa, which was interpreted as a lowering of the crystal

symmetry into an antiferroelectric phase. The purpose of the high-pressure structural study, described in chapter 3, was to establish the major structural changes as the phase transition is approached and to determine the structure of the high-pressure phase. A relationship between the structural changes with pressure and the effect they may possibly have on the SHG characteristics of the crystal is also explored. This chapter describes a substantial part of the experimental work presented in the thesis and has been published in the form of three papers (Allan *et al* (1991), Allan *et al* (1992), Allan and Nelmes (1992)).

Chapter 5 describes the application of high-pressure single-crystal techniques, using neutron radiation, to the study of the ferroelectric KH_2PO_4 (KDP), which is a well known representative of hydrogen-bonded materials which exhibit phase transitions. The phase transition in KDP is associated with the hydrogen atoms, which are 50/50 disordered over two sites in O—H...H—O bonds above T_c. Upon cooling through T_c, the hydrogen atoms order onto one site in asymmetric O—H...O bonds. The transition temperature is sensitive to the substitution of the hydrogen atom with its heavier isotope deuterium, and also to the application of hydrostatic pressure. At atmospheric pressure the transition temperature is 122K, which can be reduced to 0K under a pressure of 1.7 GPa. The reduction of T_c with pressure has been associated with the decrease of the H...H site separation (δ), which is determined by the oxygen-oxygen distance (2R) between adjacent PO_4 tetrahedra (McMahon *et al* (1990.)). Matsushita and Matsubara (1982) have modelled the potential between the O—H...H—O bonds and have calculated that for a sufficiently large 2R the hydrogen atom resides in a potential with two minima. At a 2R calculated to be 2.47Å the model predicts that the two minima merge to produce a single minimum. It has also been calculated that for a 2R close to 2.4Å the hydrogen atom resides at the midpoint of the two oxygens (Coulson (1961)). Recently, Endo *et al* (1989) demonstrated, from a single-crystal high-pressure x-ray diffraction study of KDP, that 2R decreases to a value of 2.45Å at 2.6 GPa (ambient temperature) and then increases again for higher pressures. They attributed this behaviour to a structural phase transition, close to 2.7 GPa, and asserted that the hydrogen atom was located at the centre of the hydrogen bond above the transition (although they could not observe this directly from the x-ray data). The high-pressure neutron-diffraction structural study, described in chapter 4, was performed to measure accurately the oxygen-oxygen distance

of KDP close to 2.7 GPa and to determine the H...H site separation (δ) at this pressure, for the first time.

Chapter 6 details the application of high-pressure powder diffraction techniques, using both x-ray and neutron radiation, and high-pressure x-ray single-crystal techniques for the study of the icosohedral boron-rich materials boron carbide (B_4C) and α-boron. The icosohedral boron-rich solids are refractory materials exhibiting a range of unique and potentially useful electronic, thermal and transport properties (Emin (1987)). They are characterised by having unusual twelve-atom icosohedral units within their crystal structures. The exceptional properties are believed to be closely associated with the nature of these structural units. The crystal structures of B_4C and α-boron are very similar and relatively simple. For B_4C, disordered $B_{11}C$ icosahedra are arranged on a rhombohedral lattice with an interconnecting C-B-C chain crossing the unit cell parallel to the [1 1 1] direction. In the case of α-boron the three atom chain is lost leaving only B_{12} icosahedra. Bonding theory and indirect experimental evidence suggest that the inter-icosahedral bonding is stronger and stiffer than that of the intra-icosahedral bonding (Bullett (1982), Gieske *et al* (1990)). This proposed nature of the bonding has been used to interpret the observed decrease in the electrical conductivity of B_4C with pressure (Samara *et al* (1985)). The interpretation is based on conduction by hopping of small-bipolarons between $B_{11}C$ icosahedra and the decrease in the conductivity has been attributed to the icosahedra being more compressible than the rest of the structure. However, there is no direct structural evidence to support this assumption. In this chapter a series of high-pressure structural studies are described which were undertaken to determine the structures of B_4C and α-boron as a function of pressure, so that the compressibility of the twelve-atom icosahedra could be determined.

Finally, Chapter 7 draws conclusions from the work presented in the preceding chapters and discusses future advances that can possibly be made in the determination of crystal structures at high pressure.

Chapter 2

A Review of High-Pressure Diffraction Techniques

2.1 Introduction

The purpose of this chapter is to serve as a detailed introduction to the methods of crystal structure determination at high pressure, by reviewing the current state-of-the-art high-pressure techniques, and to highlight their limitations for reliable crystal structure studies.

This chapter is arranged in the following manner. Section 2 describes the techniques employed for crystal-structure determination at both ambient pressure and high pressure, and considers the factors affecting the reliability of diffraction data. Sections 3 and 4 review all aspects of high-pressure diffraction apparatus and techniques, whether using powders or single crystals and neutron or x-ray radiation. Finally, section 5 discusses the limitations of high-pressure instrumentation and techniques presented in the preceeding sections.

2.2 The Determination of Crystal Structures by X-ray and Neutron Diffraction

2.2.1 Diffraction Techniques

A great deal of the present knowledge about the sub-microscopic structure of crystalline materials has been derived from studies of the diffraction of x-rays by crystals. This method was first used by W. L. Bragg in 1913 to determine the crystal structure of sodium chloride. Since then both x-ray and neutron diffraction techniques have advanced rapidly and have been used to establish the structural features of many kinds of stable chemical species, from the simplest, containing only a few atoms in the unit-cell to those containing many thousands of atoms, such as proteins and viruses. However, although there has been significant technical advances over the years, the basic principles, upon which crystal-structure determination is based, have remained the same.

Bragg was the first to associate the diffracted x-ray beams, or 'reflections', with planes within the unit cell of the crystal structure, defined by the Miller indices h, k and l. From this relationship he was then able to derive an equation, known as Bragg's law, which gives the necessary condition for diffraction

$$\lambda = 2dsin(\theta) \tag{2.1}$$

where λ is the wavelength of the incident radiation, d is the spacing between the crystal planes that are in the diffraction condition, and θ is half the angle through which the incident radiation is diffracted. The relative intensities of these reflections give detailed information about the atomic positions within the unit cell through the structure factor, F. The intensity of each reflection is related to F^2, where F is defined by

$$F = \sum_{n=1}^{N} f_n exp2\pi i(hx_n + ky_n + lz_n) \tag{2.2}$$

where N is the number of atoms in the unit cell, f_n and x_n, y_n, z_n are the scattering factor and fractional coordinates of the n^{th} atom respectively. Therefore, the crystal structure of a material can be determined by measuring sets of reflections. The size and shape of the unit cell (the lattice type) can be derived from the d-spacings of each reflection, calculated from θ using Bragg's law (equation 2.1), and the positions of the atoms, within this unit cell, can be determined from the intensities of the reflections, using equation 2.2. Although they have been described in an extremely simplified manner, these principles form the basis for all x-ray and neutron diffraction structural studies of which there are two distinct types.

In the first, the wavelength of the incident radiation is fixed and the reflections are measured by moving the detector through θ. This 'angle-dispersive' approach is the most successful, and the most widely used, method for the determination of crystal structures at ambient pressure and is applied routinely for single-crystal and powder techniques with both x-ray and neutron radiation. The single-crystal technique is the most favoured for the determination of accurate crystal structures and detailed structural information, such as electron density or anharmonic thermal motion, since the reflections are measured individually and are generally not affected by other reflections, unless the sample is twinned or there is strong multiple diffraction. For powder methods, on the other hand, the reflections are inevitably overlapped, especially at short d-spacing, and the intensities of individual reflections cannot be readily determined. Although structural refinement of powder data has been improved by the procedure of Rietveld (1969), where a curve is fitted through the entire powder pattern rather than attempt to fit the intensities extracted from isolated peaks, the significant loss of information at short d-spacing (high θ) limits the resolution of the powder technique. Powder techniques have also generally not been favoured for the solution of unknown crystal structures due to both the intensity correlation between overlapping reflections and the loss of three dimensional structural information. Of the choice between x-ray and neutron radiation, it is generally considered that neutrons give the more accurate structural information for both the atomic positions and thermal motion. This is due to the difference in the nature of x-ray and neutron scattering. For x-rays, the scattering occurs from the shells of electrons which have a radius comparable with the x-ray wavelength. Interference therefore oc-

curs between the x-ray radiation scattered from different parts of the atom so that the atomic scattering factor decreases as $\sin\theta/\lambda$ increases (figure 2.1). Additionally, an intensity variation is also introduced by a polarization factor which has an angular dependence of $(\frac{1}{2}+\frac{1}{2}\cos^2(2\theta))^{\frac{1}{2}}$ for unpolarized incident radiation (McKie and McKie (1986)). This reduction in intensity at high angles, coupled with the reduction due to thermal motion, ultimately limits the resolution of x-ray data. On the other hand, there is no polarization factor involved in neutron scattering and, since the radius of the nucleus is very small compared to the neutron wavelength, the nuclear form factor does not decrease as a function of scattering angle (figure 2.1). Therefore, neutron radiation is more favourable for high-resolution structural studies or those requiring detailed information about atomic thermal motion. The nuclear scattering power also varies irregularly with atomic number, unlike the atomic scattering power which shows a regular increase with atomic number, and, consequently, neutrons allow the accurate location of light (low Z) atoms. However, since the absolute nuclear scattering power for an atom is smaller than its corresponding atomic scattering power, and since neutron sources are weaker than those for x-rays, it is necessary to use larger samples for neutron diffraction structural-studies. As will be shown in section 2.3.1, this ultimately limits the utility of neutron-diffraction for structural studies at very high pressures.

The second type of x-ray and neutron diffraction study is that which requires θ to be fixed and λ to be varied-the 'energy-dispersive' mode. In this technique, the detector is usually fixed and a white, or polychromatic, incident beam bathes the sample. The crystal planes diffract the appropriate wavelength (according to Bragg's law) into the detector and individual reflections have their intensities determined by analysing the energy distribution of the detected radiation. This technique has been used rarely, until fairly recently, since it requires a radiation source producing a smooth and continuous spectrum over a range of wavelengths suitable for crystallographic studies. It has been with the advent of synchrotron x-ray sources and spallation neutron sources, which both produce the required spectrum at sufficient intensity, that the energy-dispersive technique has been used more frequently. Of the two possible sample types, powder-techniques have proved to be the most popular. Indeed, energy-dispersive powder-diffraction using neutrons has been widely used for crystal-structure studies. The pulsed nature of

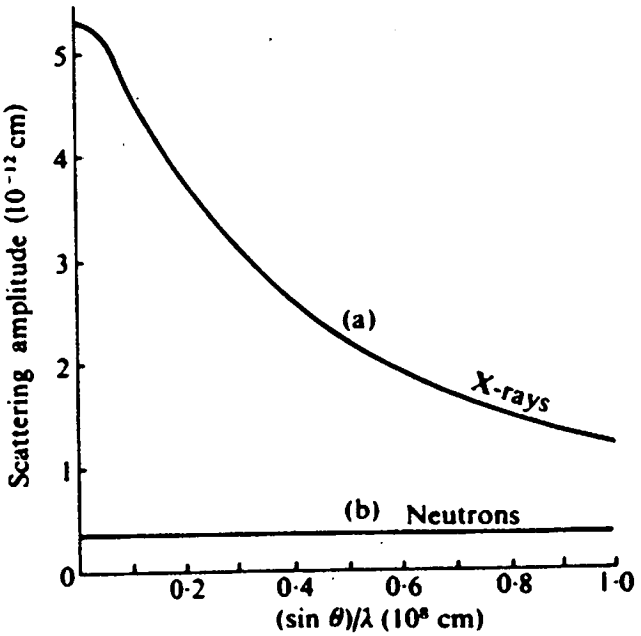

Figure 2.1: The neutron and x-ray scattering amplitudes for potassium as functions of $\sin(\theta)/\lambda$ (from Bacon (1975)).

the spallation source beam allows the time-of-flight of a neutron to be determined very accurately which, from a knowledge of its flight path through the instrument, can be used to determine its wavelength, by the de-Broglie equation, $\lambda=h/mv$, where h is Planck's constant, m is the mass of the neutron and v is its velocity. The peak shapes are well determined and sharp, allowing full structure refinement with the Rietveld method. In contrast, energy-dispersive x-ray powder diffraction has been used very rarely for structure refinement. This is mainly due to the poor powder patterns that can be measured with this method. The sample peaks are broad, due to the limited energy resolution of the semiconductor detectors, and are overlapped by fluorescence peaks from the sample and electronic escape peaks from the detector itself. In order to carry out full profile refinement it is necessary to correct the data for these effects, which has achieved only limited success (see for example Neuling and Holzapfel (1992)). Therefore, despite the fact that many x-ray diffraction studies at high pressure have used this technique they have generally been limited to the determination of unit-cell dimensions and spacegroup.

Single-crystal studies using energy-dispersive techniques, the Laue method, have been used extensively, over recent years, in the protein crystallography community. This method is well suited for the solution of complex protein structures since it allows the simultaneous measurement of many thousands of reflections on film, or some other area detector, in exposure times which can be considerably less than one second (see for example Helliwell (1989)). From comparative studies of the Laue and monochromatic x-ray diffraction techniques, the data were shown to give similar results, although the monochromatic data was of a generally higher quality (Gomez de Andrez *et al* (1989)). The use of the Laue method for neutron diffraction, however, has not yet been widely used for crystal-structure determination, although the two-dimensional position-sensitive detectors permit the measurement of a large volume in reciprocal space simultaneously, the third dimension being time-of-flight. However, the need to take wavelength-dependent factors into account, such as extinction and absorption in the sample, the incident radiation spectrum, and detector efficiency make quantitative Laue neutron-diffraction experiments (as in all energy-dispersive experiments whether using x-rays or neutrons, powders or single crystals) more difficult than standard angle-dispersive techniques (Jauch *et al* (1988)). Nevertheless, some success has been achieved (Alkire *et al* (1984), Harrison *et al* (1990)).

Although some of the methods described above offer clear advantages, the choice of technique may ultimately depend on the nature of the material being studied. The material may, for example, be difficult to grow as a single crystal, or have a pulverising first-order phase transition, necessitating powder diffraction techniques to be employed. The choice of whether to use x-ray or neutron radiation may also depend on the difficulty in producing sufficient quantities of the material, or other factors such as absorption, the presence of light atoms, such as hydrogen, and the ability to observe weak structural effects, such as difference reflections, if the atomic or nuclear scattering factors are similar. It is, therefore, essential that a range of diffraction techniques are developed for high-pressure diffraction involving all the methods described.

2.2.2 The Factors Affecting Accurate Crystal-Structure Determination

Before establishing how these diffraction techniques have been applied to the determination of crystal structures at high-pressure, it is important that the factors affecting the reliability of diffraction data, for accurate crystal-structure determination, are understood. These factors have been studied in great detail for many years (for example Ardnt and Mathieson (1969), Blessing (1987)) and it is not the authors intention to examine this subject at length. However, some of these factors are particularly relevant to high-pressure diffraction and are summarised below.

Single-Crystal Diffraction

(a) The data set should contain all independent Bragg reflections (including a number of their symmetry equivalents) up to the required resolution limit, in $\sin\theta/\lambda$. The reflections should also cover a uniform and reasonably isotropic volume of reciprocal space to avoid biassing the refined structure.

(b) The background should be low and smoothly varying so that the intensity of each reflection can be integrated accurately.

(c) The intensity of each reflection should be corrected for the effects of absorption from the sample itself and any absorbing sample environment, such as a cryostat.

(d) The sample crystal should be completely bathed, and well centred, in the incident beam of radiation to avoid intensity variations at different settings of the diffractometer.

Powder-Diffraction

(a) As full a powder pattern as possible should be collected, at least as high as the required resolution limit.

(b) For the Rietveld refinement method to extract accurate intensities from the

diffraction peaks, the background should be smoothly varying in θ so that it can be easily fitted. The pattern should also be free of contaminant peaks from foreign material.

(c) The powder pattern should be corrected for the effects of absorption.

(d) The orientation of the crystallites within the sample should be highly randomised to avoid preferred orientation. This is often achieved by using a relatively large volume of finely ground sample which is rotated in the incident beam.

The equipment and techniques that have been developed to achieve these criteria, for high-pressure structural studies, are discussed in the following two sections.

2.3 High-Pressure Apparatus

2.3.1 Pressure Cells

The development of apparatus to maintain materials at high hydrostatic pressure has been an active area of research for many years. From the pioneering work of Bridgman, during the early part of this century (Bridgman (1971)), until the late 1960's, massive hydraulicly driven Bridgman anvil and piston-cylinder devices dominated high-pressure science. Although there were later improvements in design (such as multiple-anvil devices) it was not until the advent of the gasketed diamond-anvil pressure cell, in the mid 1960's, that high-pressure studies of materials were possible in non-specialised laboratories. Indeed, over the last few years, the gasketed diamond-anvil cell (DAC) has become the standard tool for the generation of high pressures and has been applied in many kinds of experimental investigation, such as Brillouin scattering (Whitfield *et al* (1976)), Raman spectroscopy (Sharma *et al* (1989)), NMR measurements (Lee *et al* (1987)) and x-ray diffraction. The essential details of a DAC are shown in figure (2.2) and the principles upon which it operates are extremely simple.

The sample is placed in a pressure chamber created between the flat parallel

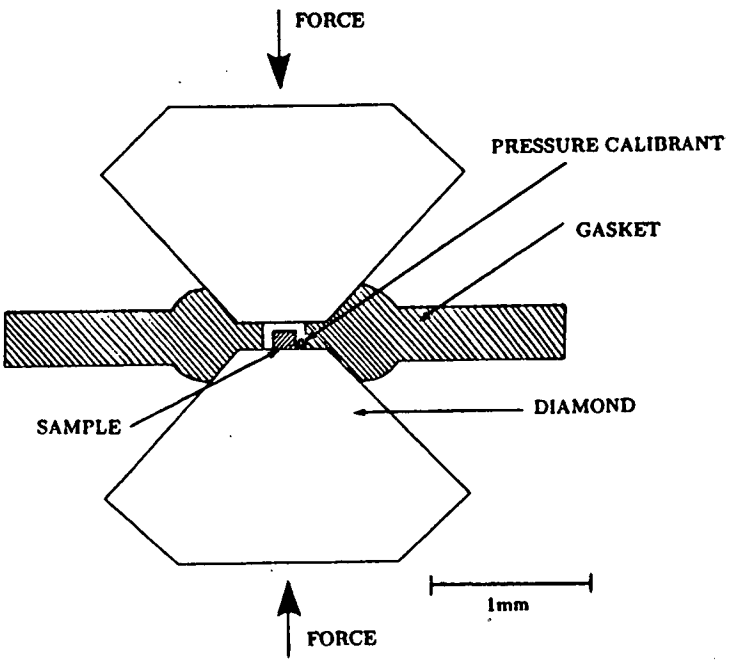

Figure 2.2: The essential details of a gasketed diamond-anvil pressure cell (DAC).

faces (culets) of two opposed diamond anvils and the hole penetrating a hardened metal gasket. A pressure calibrant is placed beside the sample and the free volume, within the pressure chamber, is flooded with pressure-transmitting fluid. Pressure is applied by forcing the diamonds together which causes the gasket to extrude around the diamond culets, sealing the pressure chamber. The force required is not large, for even the highest pressures attainable, and can be achieved, in some cases, with a simple clamp arrangement or by the tightening of Allen bolts.

The volume of the pressure chamber in a DAC, even for fairly modest pressures is such that a DAC can only be used for x-ray diffraction studies, the sample volume being insufficient for neutron-diffraction techniques. Therefore, neutron diffraction pressure cells often have designs more in common with piston-cylinder equipment and, even when they adopt design features similar to those of the DAC, require hydraulic rams to apply the pressure. Consequently, the large majority of high-pressure structural studies to date have been performed using x-ray diffraction techniques, and a variety of DAC designs exist for both single-crystal and powder-diffraction. The number of such designs is considerable and it is not possible to describe each in great detail here. However, there are general aspects of x-

ray (and neutron) pressure cell design that have a bearing on the quality of the diffraction data. These aspects, and their possible effect on the accuracy of the refined structure, will be described. Since the majority of high-pressure structural studies have been performed on standard laboratory x-ray sources with single-crystal techniques, the pressure cells used in these studies will be examined first.

Single-Crystal X-ray Diffraction

The development of the DAC for single-crystal x-ray diffraction was initiated at the National Bureau of Standards (NBS) from a simple modification of earlier DAC designs (Weir *et al* (1965)) and, although some structural studies were undertaken using adapted precession cameras (Weir *et al* (1969)), it was not until the advent of the Merrill-Bassett pressure cell (Merrill and Bassett (1974)) that routine high-pressure structural studies became possible. The pressure cell had an extremely simple construction and did not incorporate the spring actuated lever arm of the earlier design. This meant that the cell was small enough, and light enough, to be mounted on single crystal goniometers and could be used on most cameras and diffractometers without modification. The design of the Merrill-Bassett (M-B) cell is illustrated in figure 2.3 and, since most of its design features have been included in many recent designs, it is worth examining in detail.

The diamonds are mounted on two small triangular platens that are drawn together by three bolts. In the construction of the platens, beryllium discs, which serve as x-ray windows, are used to support the diamonds and the discs themselves are press-fitted into stainless steel housings. Conical apertures in the steel housings, each of 50° half angle, permit the measurement of 2θ angles up to a maximum of 100°. When fully assembled, the cell is 32mm in diameter and 16mm thick, and possess both mirror and cylindrical symmetry. The latter feature allows the absorption correction, for the incident and diffracted beams passing through the diamonds and beryllium discs, to be dependent only on the angles α_i and α_d (see section 2.4.3). The beryllium discs each have a 1mm hole drilled through their centres to provide optical ports to the diamonds. This allows observation of the sample in the pressure chamber, simplifying initial alignment on the diffractometer or camera, and also allows the use of the ruby fluorescence method for pressure calibration (Forman *et al* (1972), Barnett *et al* (1973)). Pressure is applied to the

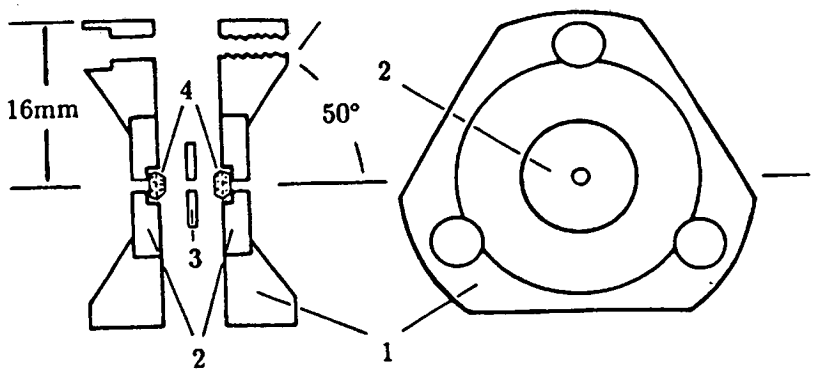

Figure 2.3: A diagram of the Merrill-Bassett DAC. (1) — Stainless steel platens; (2) — beryllium discs; (3) — gasket; (4) diamond anvils. (From Merrill and Bassett (1974).)

sample by tightening the three bolts situated at the corners of the platens and care must be taken to ensure that each is advanced uniformly, so that the platens are kept as parallel as possible.

In this original design of the M-B cell, there is no means of adjusting the diamonds to ensure that their culets are centred on one another and absolutely parallel — a condition required to avoid failure of either the diamond-anvils or the gasket. Although the authors claimed that the diamond alignment was not critical up to pressures of 2.5 GPa (the pressure limit for the cell) and very few gasket failures resulted, almost all subsequent versions of the original M-B cell have some means of aligning the diamonds.

The desire to study minerals at higher pressure prompted Hazen and Finger (1977) to introduce a number of modifications to the M-B design. In order to make partial alignment of the diamonds possible, the well containing the beryllium disc in one of the steel housings is increased in diameter. The disc is then held in position by three grub-screws, which can be adjusted radially, so that the diamond mounted on this disc can be translated with respect to the other fixed diamond. Although there is no method of adjusting the diamond culets so that they can be made

absolutely parallel to one another, three guide pins are positioned symmetrically around the steel housings to ensure that the platens themselves are kept parallel during pressurization. A further modification to the steel housings is the reduction of the opening angle in the conical aperture, from 50° to 40° so that greater support is provided for the beryllium backing plates. This, however, reduces the number of observable reflections. With 1mm diamond culets, these modifications allow a substantially higher pressure, of approximately 6 GPa, to be attained. This cell has superseded the original M-B design and has become extremely popular due to both its low cost and ease of use.

Further modifications to the M-B cell have allowed structural studies at even higher pressure. The cell designed by Mao and Bell (1980), see figure 2.4, is an enlarged version of the M-B cell and, since it was originally intended for the cryogenic loading of gases, all steel parts are made from maraging steel due to its suitability for low-temperature applications. The platens are disc shaped and are drawn together by two pairs of left and right-handed bolts. Alignment is maintained by carefully tightening alternate pairs of oppositely threaded bolts, and is further aided by the provision of four guide pins. The conical apertures in the steel housing are now reduced to a 30° opening angle, which lends additional support to the beryllium backing discs, again at the expense of the number of observable reflections. Although one of the diamonds can be translated with respect to the other, there is no provision for parallel alignment of the diamond culets. Nevertheless, the pressure limit of the cell is greatly increased.

A simple, and elegant, modification to the M-B cell, which overcame the problem of parallel alignment of the diamond culets, was included in the design of Takeuchi (1986). In this cell, one of the diamonds can be rotated on a ball-and-socket arrangement which is formed from a hemispherically shaped backing plate mounted in a similarly shaped steel housing. Alignment can, therefore, be achieved by rotating the beryllium plate until the diamond faces are parallel.

In order to benefit from accurate diamond alignment, the DAC itself must have excellent alignment stability when a pressurising force is applied. For M-B pressure cells, this condition is difficult to achieve since all the bolts applying force to the platens must be advanced at a uniform rate. Although the guide pins prevent

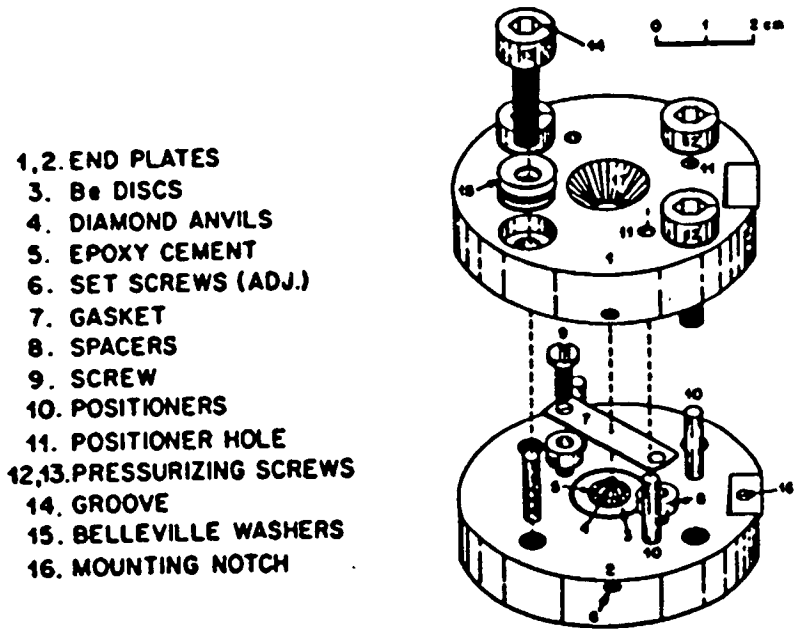

Figure 2.4: The single-crystal DAC of Mao and Bell (1980). (From Jayaraman (1983).)

gross misalignment, a loss of accurate culet alignment is inevitable. Consequently, many single-crystal x-ray diffraction cells, featuring both translational and rotational adjustments for the diamond anvils, are based on earlier piston and cylinder designs. For example, the DAC of Keller and Holzapfel (1977) is basically a modification of a pressure cell designed for optical studies (Huber *et al* (1977)) and is shown in figure 2.5. The cell body forms a cylinder and four horizontal screws, threaded through it, act on the lower beryllium backing plate, and provide precise translational centring of the diamonds. Four vertical screws, tapped into the piston, allow the upper beryllium plate to be rotated and enable parallel alignment of the diamond culets. Pressure is applied by advancing the tightly fitting piston downwards through the cell body. The force required to achieve this is provided by a compact system of levers whose geometry allows a large force multiplication factor. The hemispherical shape of the beryllium backing plates, together with the small beryllium plugs which close the central optical ports, reduce the problem of x-ray absorption to a constant angle-dependent factor. However, although this may also provide additional support for the diamonds, the increased volume of

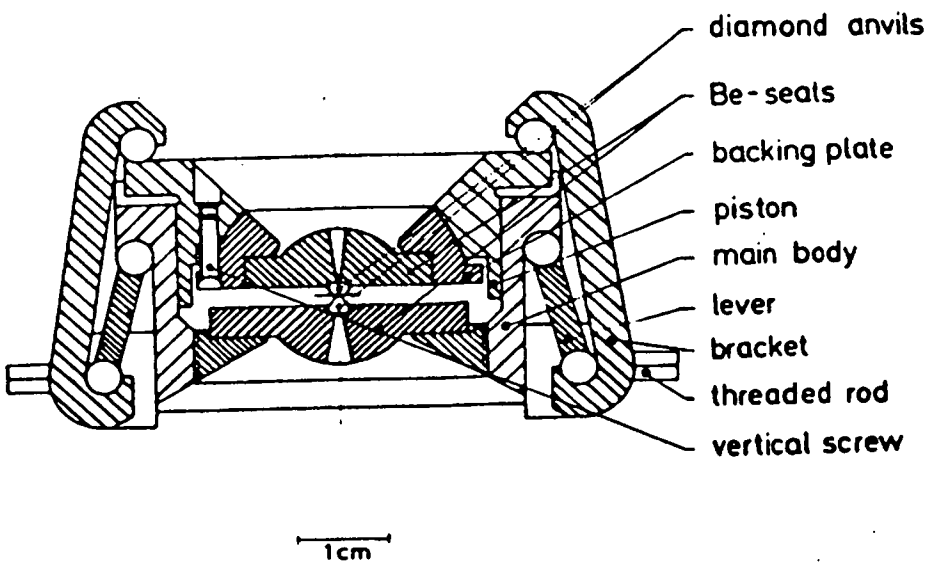

Figure 2.5: The single-crystal DAC of Keller and Holzapfel (1977). (From Keller and Holzapfel (1977).)

beryllium results in an enhanced absorption and background scatter, and these drawbacks will be discussed later. The diamonds themselves are not matched for culet size since the authors state this facilitates the centring and parallel-alignment procedures. Although the piston length-to-diameter ratio has been reduced to allow a large opening angle in the conical apertures of the steel housings, slightly degrading the angular alignment stability compared to the optical cell (Dunstan and Spain (1989)), pressures in excess of 10 GPa have been achieved.

The piston-cylinder arrangement is also adopted in a DAC (the DXR-4) recently designed by Adams (1992), see figure 2.6, and has many features derived from the Keller-Hozapfel cell (K-H). Alignment of the diamond culets is provided by sets of tilt and translation screws, situated in the titanium cell base, which bear on the mounting ring of the lower beryllium backing disc. The upper beryllium disc is set firmly into the piston. Each disc is shaped, in the same manner as the K-H cell, to provide angle independent x-ray absorption. A pressure plate advances the piston down the cylinder and is driven by two oppositely threaded bolts. Thus no net torque is applied to the cell when altering the sample pressure and, due to

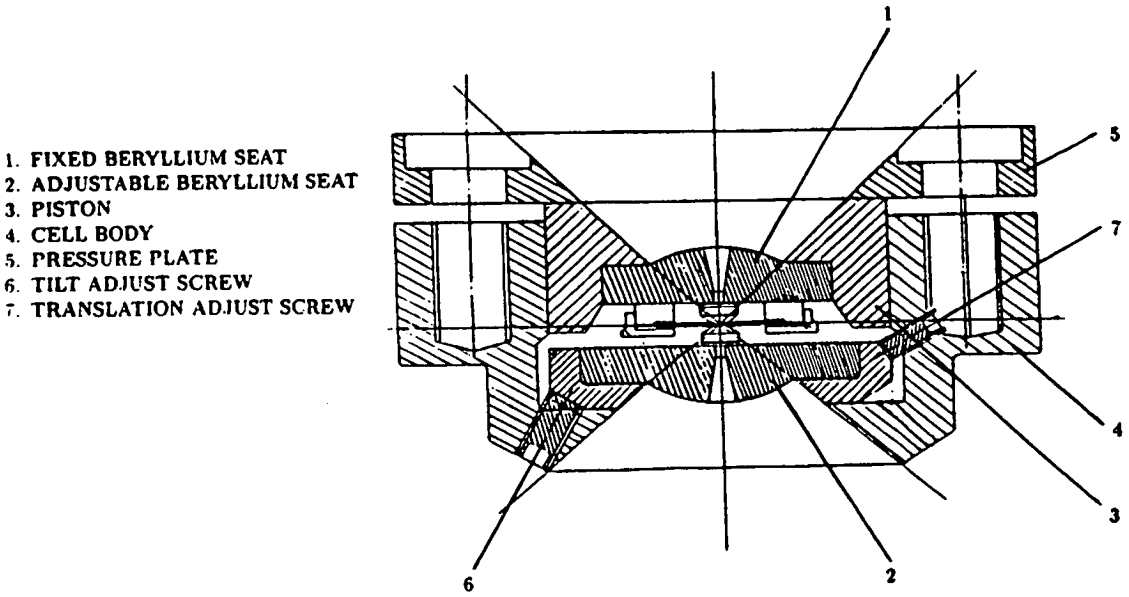

Figure 2.6: A cross-section of the DXR-4 design of DAC. (From Adams (1992).)

the much simpler force-generating system, the cell has much smaller dimensions than the K-H cell. Equipped with suitable diamond-anvils, it is claimed that the cell is probably capable of pressures close to 50 GPa.

All the cells that have been examined so far are those with the so called 'transmission geometry' where the incident and diffracted beams pass in through one anvil and out through the other. This technique offers a number of advantages, as can be seen from figure 2.7. Due to the cylindrical and mirror symmetry of these cells, absorption correction of the incident and diffracted beams (in the diamonds and beryllium) can be applied easily, satisfying the third criterion in section 2.2.2. Provided that the angle α_i is not too great the sample will not be shadowed by the gasket, satisfying the fourth criterion in section 2.2.2. As will be shown in section 2.4.2, the second criterion can also be satisfied provided that reflections in the proximity of the gasket or beryllium powder lines are not measured, or the type of scan, used to measure the reflections, is carefully selected. However, transmission-geometry cells have the drawback that only 40-50% of reciprocal space is accessible, this fraction depending on the opening angle of the conical apertures of the steel housings (Merrill and Bassett (1974)). As can be seen from

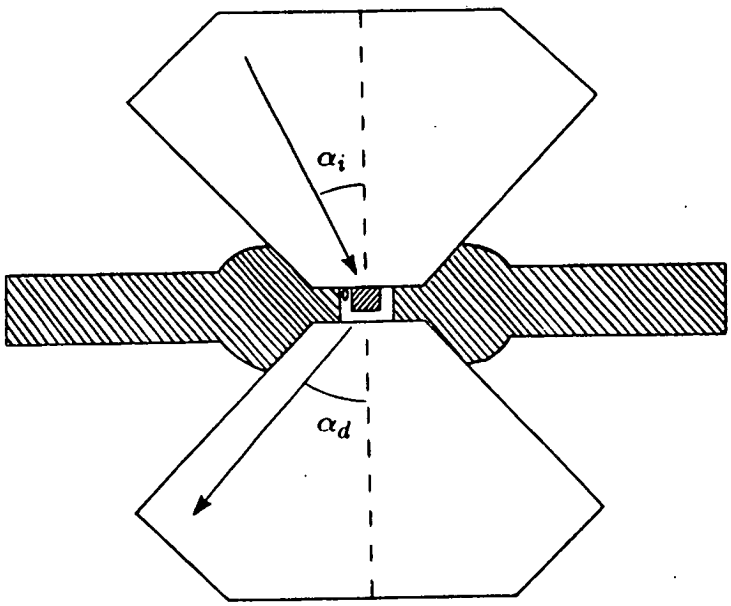

Figure 2.7: The definition of the angles α_i and α_d — the angles between the cell axis and the incident and diffracted beams respectively.

figure 2.8, the region of accessible reciprocal space is bounded by a toroidal surface whose rotational symmetry axis is parallel to the cell axis. The surface is defined by the equation

$$r_l = 2sin(\alpha - \phi)/\lambda \tag{2.3}$$

where $\mathbf{r}_l$ is a reciprocal lattice vector, α is the opening angle of the conical aperture and (90-ϕ) is the angle between a crystal-plane normal and the cell axis. Although the transmission-geometry DAC has been used in the majority of single-crystal x-ray diffraction studies, care has to be taken for each structure determination, that the first criterion in section 2.2.2 is satisfied.

In order to overcome the problem of limited access to reciprocal space (and thereby increase the number of observable reflections) a range of pressure cells with the transverse geometry has been developed. This design of DAC allows diffraction to occur approximately in the plane of the gasket, in a direction which is almost per-

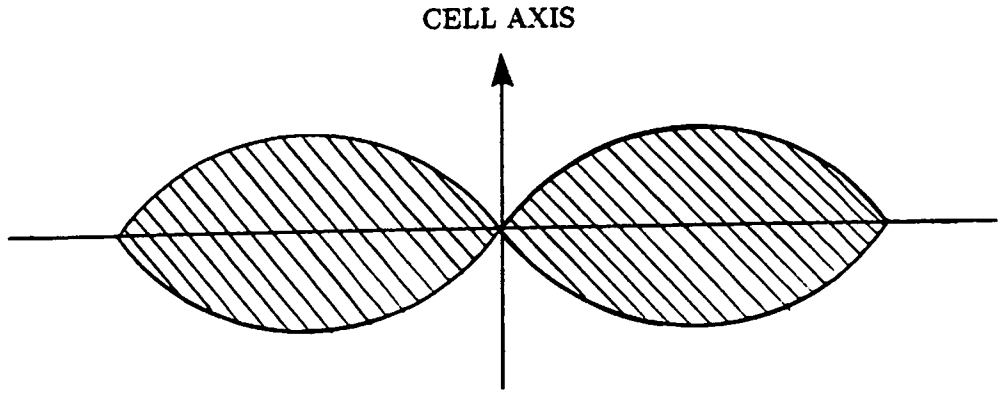

Figure 2.8: The region of reciprocal space accessible with a transmission-geometry DAC.

pendicular to the applied force (as can be seen from figure 2.9). The first example of a transverse-geometry cell was designed by Schiferl (1977) for the study of the pressure dependence of the As, Sb and Bi structures, and is shown schematically in figure 2.10. In this design, the incident and diffracted x-ray beams pass through the same anvil. This anvil is mounted on a beryllium cylinder which is rigidly set into a stainless steel cylinder. This cylinder is shaped to allow maximum access to the sample for both the incident and diffracted beams. The other diamond, which requires no x-ray access, is mounted on a bearing arrangement to allow the diamond culets to be aligned parallel to one another. There is no provision for translational centring of the diamonds. Pressure is applied by a lever system which forces a thrust rod against the back of the bearing. The lever system is extremely bulky and, consequently, the cell can only be mounted on specially adapted four-circle diffractometers. A later refinement of the cell (Schiferl *et al* (1978)) reduced the overall bulk of the pressure generating system, which made the cell suitable for use on several types of commercial four-circle diffractometer. The revised design allowed greater access to reciprocal space and a 'sliding diamond mount' provides translational alignment of the diamonds.

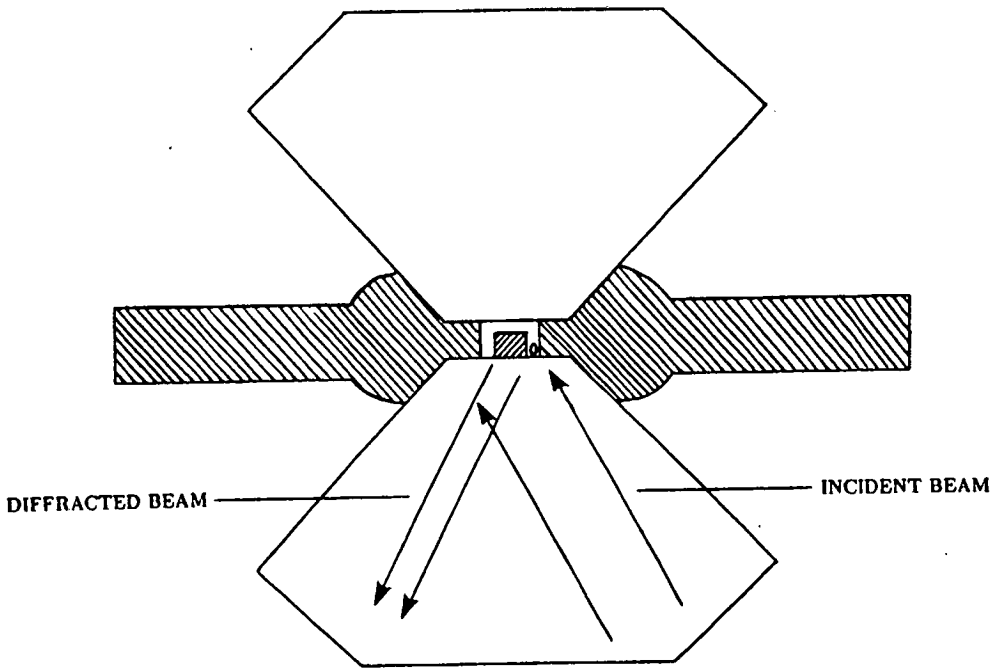

Figure 2.9: The diffraction condition in the transverse geometry design of DAC.

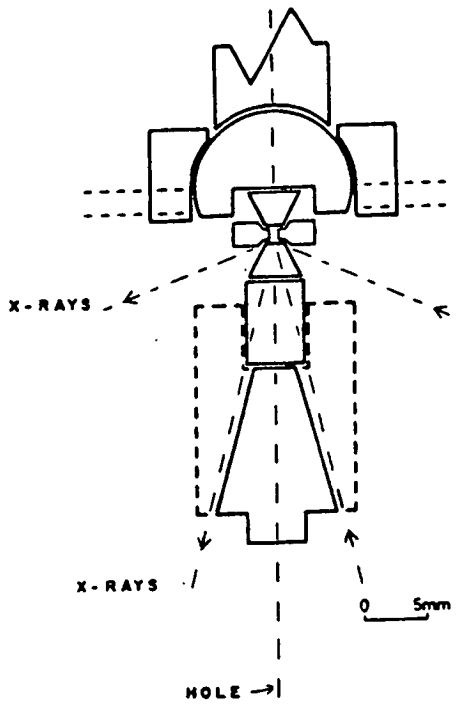

Figure 2.10: The transverse-geometry of Schiferl (1977) showing the angular access available for the incident and diffracted beams. (From Schiferl (1977).)

Further improvements were introduced by Koepke *et al* (1985) who developed a piston and cylinder device which is pressurised by a compact lever system, similar to that used in the K-H cell. In this version, except for two small sectors shadowed by support pillars, the lower half of a conical belt, with an opening angle of 45°, is accessible to the incident and diffracted beams. It was also found that the use of diamonds with different culet sizes (0.7 and 1.3mm) reduced absorption by the gasket. The unmatched culet sizes cause the gasket to deform in a nonuniform manner so that the smaller culet face indents the gasket further. Since the incident and diffracted x-ray beams pass through the lower diamond, which has the larger culet, smaller diffraction angles can be used without considerable absorption by the gasket material. Although pressures up to 50 GPa can be achieved with standard inconel nickel alloy gaskets (Ni:Cr:Fe=72:16:8), the high x-ray absorption in this gasket material inevitably causes shadowing of the sample. The effect of this 'occlusion' on the intensities of the measured reflections is difficult to correct for. Using beryllium gaskets, however, allows the use of simple analytic absorption correction although the pressure limit is reduced considerably to 2.3 GPa.

The pressure cell designed by Ahsbahs (1984a) also uses x-ray transparent gaskets. Its design, shown in figure 2.11, allows for a full conical belt, with an opening angle of 25°, to be accessible to the x-ray beams. The cell consists of two platens which are held apart by three support pillars. Diamond alignment is provided by an adjustable steel diamond seat housed in the upper platen. The lower diamond anvil is mounted on a steel piston, which produces a pressurising force by a system of buffer springs contained within the lower platen. A small hydraulic press is used to compress the springs and the applied force is held by a lock-nut. When the cell is used for data collection, and reflections are collected in the bisecting position (ω=θ), the limiting factor for reflections to be measurable is

$$\theta sin(\chi) \leq \beta \tag{2.4}$$

where β is the opening angle, in this case 25°. Therefore, for a θ limit of 25°, a uniform sphere of reciprocal space is accessible. Although the beryllium gasket material allows this relatively free access to reciprocal space, it suffers the major disadvantage of limiting the pressure that the cell can achieve to around 3.5 GPa.

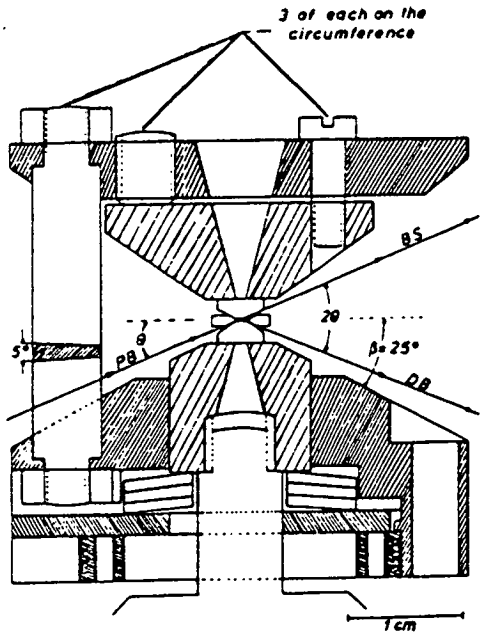

Figure 2.11: The Ahsbahs transverse-geometry design of DAC showing the primary beam (PB), diffracted beam (DB) and the opening angle β. (From Ahsbahs (1984).)

A final example, of single-crystal x-ray diffraction pressure cells, is that of Malinowski (1987). This cell combines features of the transverse and transmission-geometry cells and allows more than 85% of reciprocal space to be accessed. As shown in figure 2.12, the body of the cell is very similar to that of the K-H cell, since it adopts the same lever-driven piston-and-cylinder arrangement and also includes alignment facilities for the diamond culets. However, the lower beryllium disc of the K-H cell has been replaced by a beryllium beam supported by two steel fingers, thereby removing almost all the absorbing steel from the lower half of the cell. Therefore, this cell allows both kinds of diffraction geometry to be available simultaneously. To reduce gasket occlusion when the cell is used in the transverse mode, the diamond culets are not matched for size so that the gasket distortions, discussed for the Keopke cell, are induced. Although the cell has been used for the study of cell dimensions (Malinowski *et al* (1986)) it has not yet been used for a full structural study.

Although the transverse geometry offers a large accessible volume of reciprocal space and, therefore, easily satisfies the first criterion of section 2.2.2, the problems caused by gasket occlusion do not allow reliable intensity measurements. This limitation is a consequence of the very complex absorption paths of the x-

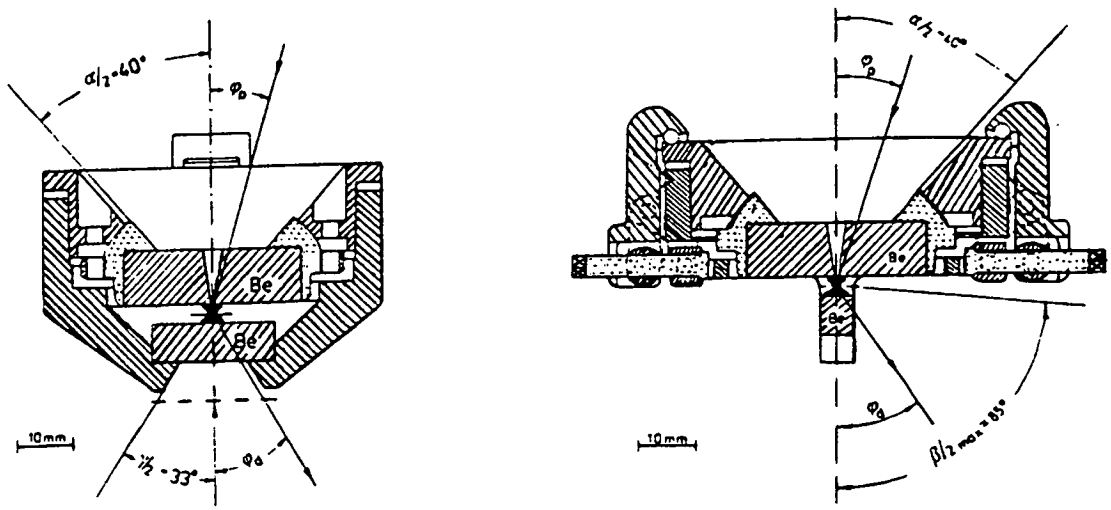

(a) (b)

Figure 2.12: Two perpendicular views of the Malinowski DAC, showing (a) the transmission diffraction geometry and (b) the transverse diffraction geometry. (From Malinowski (1987).)

rays passing through the gasket, diamonds and beryllium components. Therefore, most high-pressure single-crystal structural studies using x-rays are performed with transmission-geometry cells, and if additional reflections are required, for a complex crystal structure, an alternative orientation of the crystal, within the pressure cell can always be used.

X-ray Powder Diffraction

Of all the diffraction techniques, x-ray powder diffraction has been employed at the highest pressures and, although this technique has been used very rarely for full crystal structure investigations, it is, nevertheless, important that the design aspects of pressure cells used in this method of study are examined.

Since the advent of synchrotron x-ray sources, the energy-dispersive diffraction (EDD) technique has become the most frequently used for high-pressure studies of polycrystalline materials, as its fixed scattering geometry is well suited to the restrictions imposed by high-pressure cells. A typical design of DAC employed in these studies is that of Piermarini and Block (1975), which is shown in figure 2.13. The cell design is very similar to that of Weir *et al* (1965) with the exception

that all the beryllium parts have been replaced by hardened steel. The main body of the cell consists of a rectangular steel plate and contains an aperture at one end to act as a cylinder (approximately 2cm in length) for the sliding-piston diamond mount. The stationary diamond mount contains translational adjustments for diamond centring, while the short piston contains a hemispherical mount for parallel-alignment. Since the diamond mounts themselves are not transparent to x-rays they contain ports with suitable opening angles for EDD techniques (approximately 10°). Force is applied through a lever, when the system of Belville spring washers are compressed, and pressures up to 50 GPa can be generated. A later version of EDD cell (Mao and Bell (1978a)), with an improved piston length-to-diameter ratio (the piston length now being approximately 5cm) extended the available pressure range into the Mbar region. For alignment, this cell contains two tungsten carbide half-cylinders (Dunstan and Spain (1989)) whose axes are set perpendicular to each other and which can be translated or tilted. These tungsten carbide half-cylinders act as the diamond backing plates and have ports for the incident and diffracted x-ray beams, again with suitable opening angles for the 2θ range usually employed for EDD studies (typically 10°). A Belville washer driven lever-arm, similar to that of the Piermarini and Block, provides the pressurizing force.

Pressure cells designed for the angle-dispersive technique adopt similar features to those for EDD studies. For example, the cell used by Yu *et al* (1985), in their study of high-pressure phase transitions in group III-V and II-VI semiconductors, is a piston-and-cylinder design and has the same half-cylinder diamond-alignment mechanism of the Mao and Bell cell, described above. However, the half-cylinder mounted in the stationary diamond backing plate is modified to provide a 70° exit slot for the diffracted x-ray beams (figure 2.14). More recently, the membrane diamond anvil cell (MDAC) of Letoullec *et al* (1988), shown in figure 2.15, has been modified by Jephcoat *et al* (1992) for angle-dispersive powder-diffraction. In this design of cell, pressures are generated by driving the piston with an inflatable stainless-steel membrane coupled to a nitrogen, or helium, gas cylinder. The membrane ensures that the force exerted on the piston is symmetrical, so that diamond alignment is maintained under pressure, and offers the additional advantage that the force can be varied smoothly, and remotely, by changing the gas pressure on the membrane with a system of microvalves. The design of Jeph-

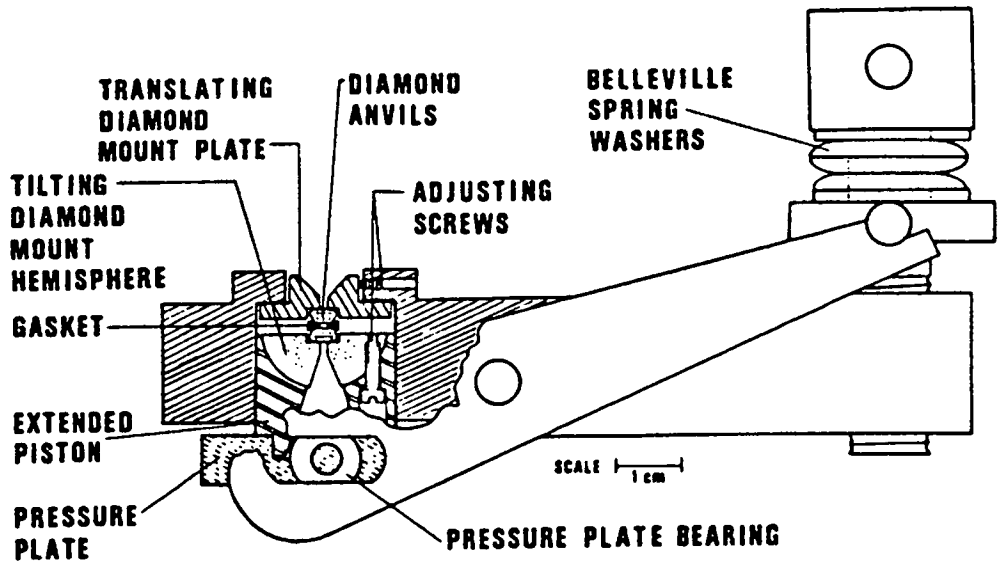

Figure 2.13: Cutaway cross-sectional drawing of the DAC of Piermarini and Block (1975). (From Piermarini and Block (1975).)

coat *et al* is very similar to that shown in figure 2.15 with the exception that the stationary diamond-seat has a tapered slot to provide a 0-40° 2θ diffraction angle for the diffracted x-ray beams.

EDD pressure cells, of similar design to that of Mao and Bell (1978), have recently been taken to pressures in excess of 438 GPa (Ruoff (1992)) and powder patterns free from contaminant gasket powder lines have been obtained. Even with the very small gasket-hole dimensions required for such pressures, the highly-collimated nature of the synchrotron beam, with additional accurately controlled collimation (Schiferl *et al* (1983), Spain *et al* (1984)), allows illumination of the sample without simultaneous illumination of the gasket. Therefore, with careful alignment of the x-ray optics, the second criterion in section 2.2.2 can be satisfied for both the energy-dispersive and angle-dispersive diffraction techniques. Since the cells have the transmission geometry and there are no complex x-ray absorption paths, a simple absorption correction can be applied to the diffracted beams, satisfying the third criterion in section 2.2.2. However, the very small sample volume available with a DAC, often in the order of 100μm in diameter and 50μm thick and

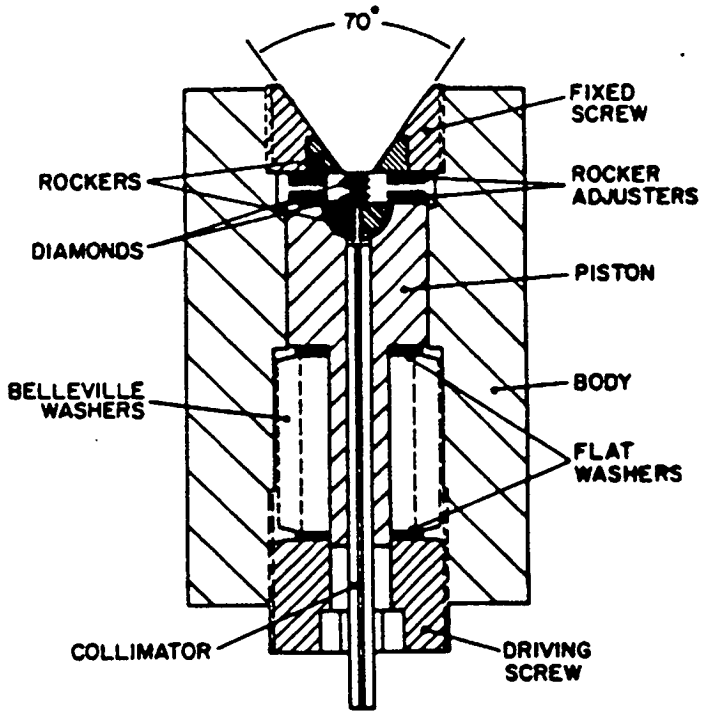

Figure 2.14: Cross-section of the DAC of Yu *et al* (1985) showing the modified half-cylinder (rocker). (From Yu *et al* (1985).)

1. GAS INLET
2. MEMBRANE
3. PISTON
4. CELL BODY
5. HALF-SPHERE DIAMOND SEATS

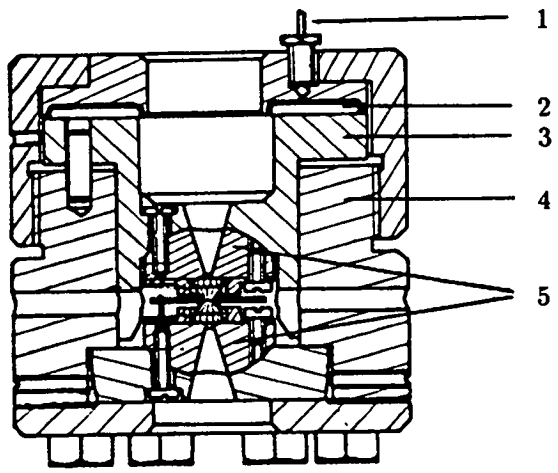

Figure 2.15: Cross-section of the Letoullec design of membrane DAC. (From Letoullec *et al* (1988).)

substantially less for studies to 1 Mbar, results in a poor powder average. This is further accentuated in the EDD technique by the high degree of collimation required between the sample and the detector, with the consequence that only a few crystallites are observed in the diffraction condition. Hence, with current x-ray powder diffraction techniques using DACs it is generally not possible to satisfy the fourth criterion.

Although large volume high-pressure devices, such as the multianvil press, hold sufficient material to eliminate the problems of obtaining a good powder average, comparatively little structural work has been undertaken with them. These devices are mainly used for high-pressure materials synthesis, such as industrial diamond and cubic boron nitride production, where a large pressurized volume and stable high-temperature are crucial (Besson *et al* (1992)). However, over recent years, with the development of powerful synchrotron x-ray sources, multianvil devices have become more widely used for high-pressure x-ray powder-diffraction. For example, the cubic-type MAX80 press, stationed at the KEK Photon Factory in Japan, has been used in energy-dispersive and, more recently, angle-dispersive diffraction studies. In this device a single hydraulic ram exerts a compressive force on a series of anvil blocks which then exert a uniform, and approximately isotropic, pressure on an octahedral gasket. The sample, contained within the gasket, has a volume of approximately 1 mm^3 and, with the appropriate anvil dimensions, can be sustained above 20 GPa at 800°C (Kikegawa (1992)). The main drawback with such systems, apart from their overall size and mass, is their complex anvil geometry. As can be seen from figure 2.16, which shows the anvil arrangement for the MAX80 press, the incident and diffracted beams must pass between the inner and outer tungsten carbide anvils. Although one of the inner anvils is constructed from sintered diamond to act as an x-ray window for the diffracted beam, the diffraction geometry is extremely restricted and results in a 2θ diffraction angle limit of approximately 12°. Such limits, on the the diffraction geometry, severly reduce the utility of multi-anvil devices for accurate angle-dispersive powder-diffraction studies (see the first criterion in section 2.2.2). At all pressures contaminant x-ray scatter from the gasket material is inevitable and, unless the incident beam is carefully collimated, the anvils themselves will produce contaminant powder-lines as the sample pressure is increased. This contaminant scatter and the complex x-ray absorption path lengths make quantitative measurements of the diffracted

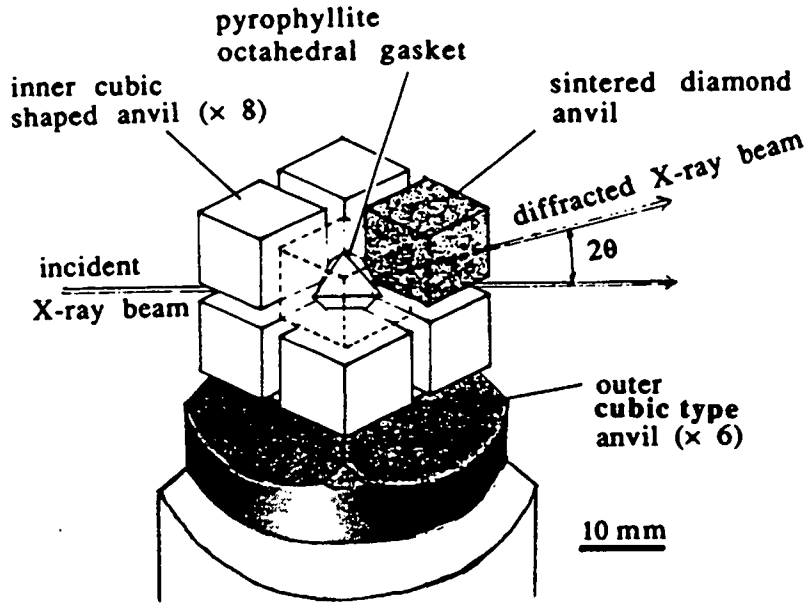

Figure 2.16: Schematic diagram of the 6-8 type double-stage multi-anvil system with a sintered diamond anvil window. (From Kikegawa (1992).)

intensities extremely difficult.

Neutron-Diffraction Pressure Cells

Compared with x-ray diffraction techniques, relatively few structural studies have been performed with neutron diffraction at high pressure. However, a number of different pressure cells have been designed for both the single-crystal and powder-diffraction techniques and some of these will be examined in this section.

Many of the pressure cells designed for neutron-diffraction structural studies have been based on simple piston-and-cylinder devices, and are pressurised hydraulicly. The cell designed by McWhan *et al* (1974) is a typical example. As shown in figure 2.17a, the pressure vessel is formed from a cylinder of sintered alumina (Al_2O_3), since this material has a relatively high transparency to neutrons. Although sintered alumina has a high compressive strength, its low tensile strength makes it necessary to balance the radial support of the cylinder carefully. This is achieved by shaping the outer surface of the cylinder into two opposed truncated cones and

compressing it between two conicly shaped support rings driven by a hydraulic ram, figure 2.17b. The resulting external radial compression is increased at a constant rate relative to the internal pressure of the cylinder. The internal pressure is produced by advancing a tungsten carbide piston into the cylinder by means of a second hydraulic ram. A window is formed between the conical support rings and gives 360° access to the sample in the horizontal plane (except for the support columns of the press). This geometry allows the cell to be used for both the time-of-flight and angle-dispersive powder diffraction techniques although, for single-crystal studies, it allows observation of only reflections lying in the plane perpendicular to the cell axis.

A later design of cell (Block *et al* (1976)), adopting the same diffraction geometry, has been employed for structural studies up to 3 GPa in the temperature range of 4-300K. In order to allow the cell to be operated in standard cryostats, or furnaces, its overall dimensions are smaller than those of the McWhan cell and the system of hydraulic rams are not included. The sintered alumina barrel is stressed, in the same manner as the McWhan cell, to reduce the internal forces acting on it, although this is achieved before the sample pressure is applied. The stress is created by mounting the cell on a hydraulic press and screwing the conical support bands, with small increments, into the threaded cell sleeve at progressively higher applied loads. The maximum load is fixed at a value just below that required to rupture the barrel. The sample is then pressurised by advancing two identical tungsten carbide pistons, by a system of 'force applicators', into the pressure-chamber formed by the barrel. When the required pressure is reached, the force applicators are clamped and the cell is removed from the hydraulic press. As with the McWhan design, this cell can be used for both single-crystal and powder-diffraction studies, although the diffraction geometry, again, allows observation of only those reflections lying close to the plane perpendicular to the cell axis.

Although the pressure cells described above are capable of operating in the region of 5 GPa (McWhan *et al* (1974)), the relatively small sample volumes they provide, at such pressures, necessitate a long data collection period. For the McWhan cell, a typical powder pattern requires at least 24 hours to collect. In order to increase the sample volume, an alternative design of pressure cell has been developed where helium gas is used to pressurise the sample directly. These so called 'gas cells',

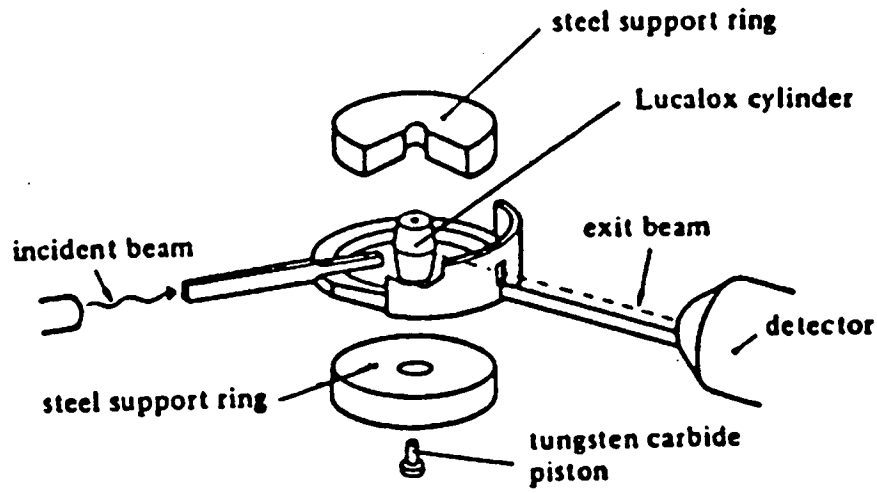

(a)

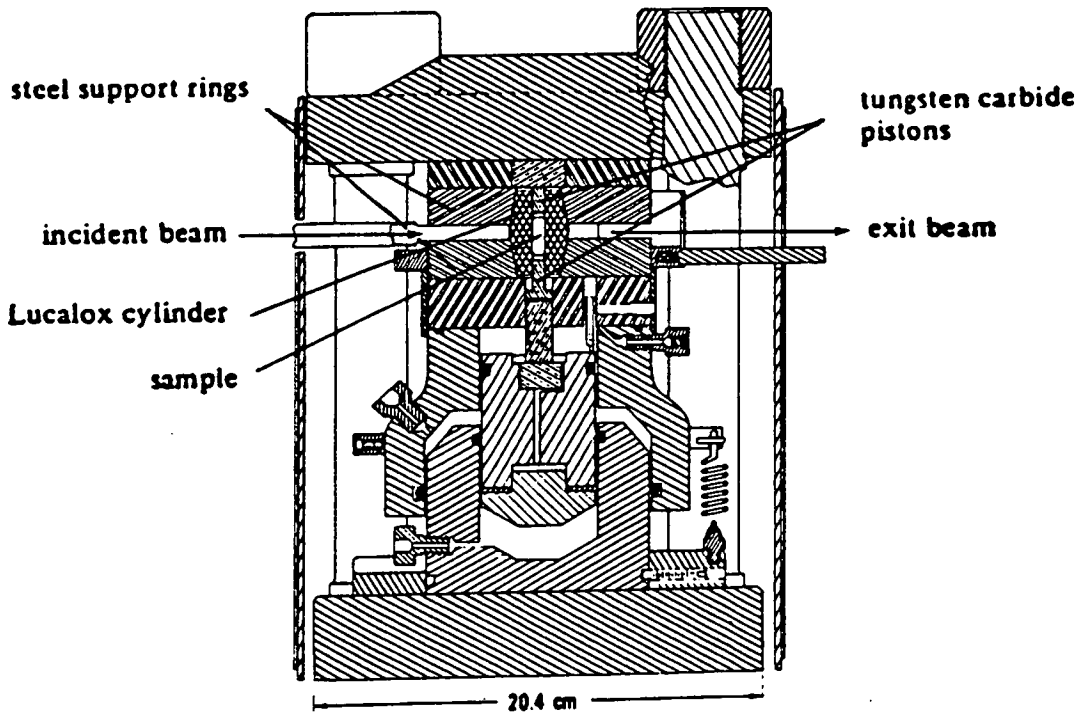

(b)

Figure 2.17: (a)Exploded, and (b) cross-sectional view of the directly pressurised supported cylinder cell of McWhan *et al* (1974). (From McWhan *et al* (1974).)

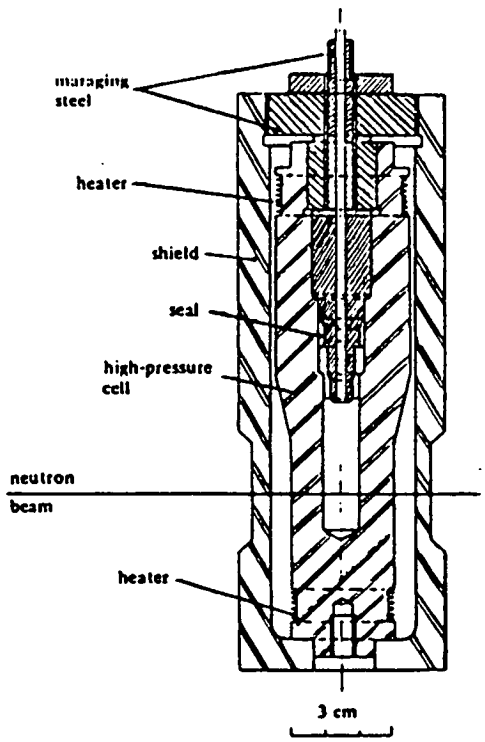

Figure 2.18: The helium gas pressure cell of Paureau and Vettier (1975). (From Carlile and Slater (1978).)

although capable of much lower pressures than the piston-and-cylinder devices, maintain the sample in perfectly hydrostatic conditions and at an extremely well determined pressure.

An example of this type of cell is that designed by Paureau and Vettier (1975), shown in figure 2.18, which has an upper pressure limit of 0.6 GPa and is capable of operating at 4.2K, the freezing temperature of the helium pressurising gas. The cell body is constructed from aluminium, which is relatively transparent to neutrons, with an outer shield made from high-tensile alloy, suitably thinned at the level of the pressure chamber to provide a neutron window. The pressure chamber has a volume of 5000mm^3 which is 25 times larger than that of the McWhan cell. Helium gas is pumped into the pressure chamber through high-pressure capillary tubing and its pressure can be controlled to within .5 bar.

The Paureau-Vettier gas-cell was originally designed for monochromatic angle-dispersive powder-diffraction and the powder patterns collected using this cell often have contaminant powder lines from the cell components close to the pres-

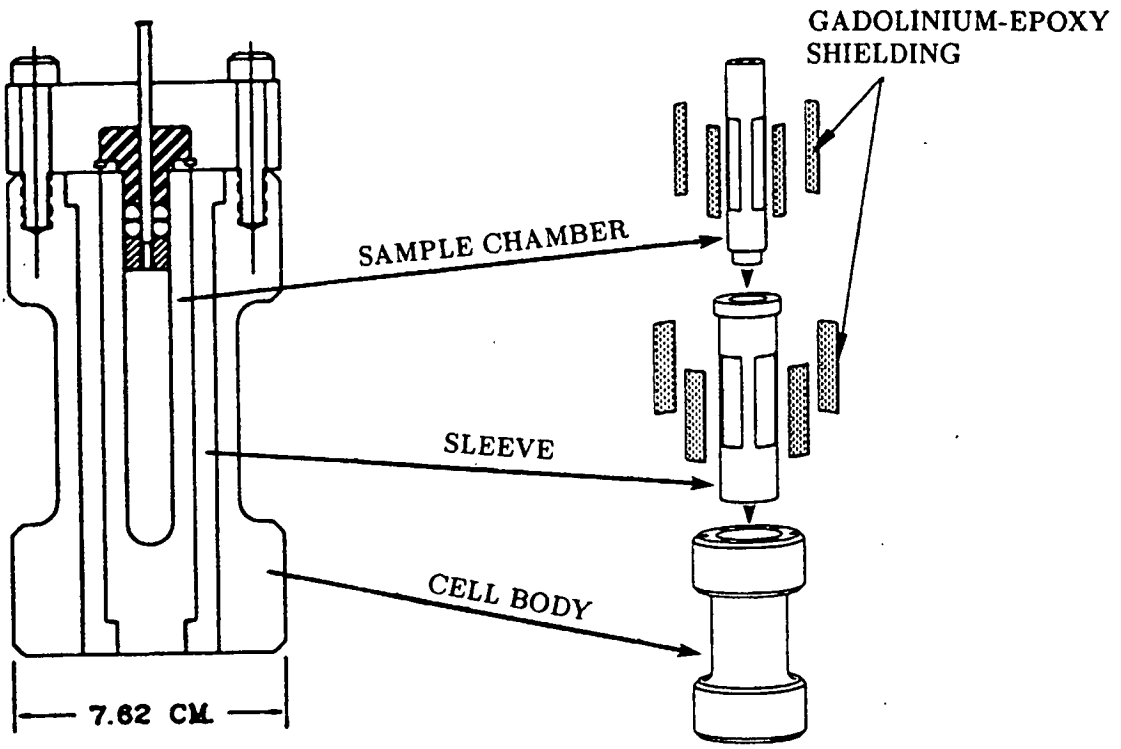

Figure 2.19: The IPNS helium gas pressure cell. (From Jorgenson (1991).)

sure vessel. In the gas-cell designed at the Argonne spallation neutron source (IPNS), for fixed geometry time-of-flight powder-diffraction, a layer of neutron absorbing material has been incorporated to reduce this contaminant scatter. As can be seen from figure 2.19, the pressure chamber is surrounded by a series of concentric neutron barriers which have windows for the incident and diffracted beams. These barriers, and the collimation pieces mounted on the outside of the cell, prevent any delayed neutrons (neutrons involved in multiple scattering from the cell components) reaching the detector. The cell, therefore, allows the collection of powder patterns free from contaminant features and with a low and smoothly varying background.

The successful application of the DAC to x-ray diffraction structural studies, and the ease with which they allow very high pressures to be attained, has prompted the use of suitably scaled up versions for neutron-diffraction studies. Indeed, a pressure cell has recently been constructed with 4 carat diamonds for neutron powder-diffraction at 20 GPa (Besedin *et al* (1990)). This pressure cell, however, has a sample volume that is relatively small and, considering that the anvils are broken during each experiment, is prohibitively expensive to operate. For cost

purposes, sapphire is often used as an anvil material and has been successfully applied in the single-crystal pressure cell designed by Ahsbahs (1984b), shown in figure 2.20. This cell is based on the x-ray design with the exception that the three steel pillars are replaced by a cylindrical aluminium sleeve, which has a low neutron absorption. The opening angle (β) of 25° in the original x-ray cell is increased to 37° or 45° (Ahsbahs (1984a)) to allow greater access to reciprocal space. Optical access to the sample is provided by ports through the upper and lower platens, and allow the ruby fluorescence method to be used for pressure calibration. The gasket material is a neutron permeable Ti-Zr null-matrix alloy which eliminates the parasitic coherent scatter and, therefore, no powder lines are produced by the gasket. If powder lines were produced, these would contaminate the background of the reflection profiles which, for neutron diffraction, must be measured with ω-2θ scans (see section 2.4.2). (A null-matrix material is produced by mixing elements, or isotopes, with positive and negative neutron scattering lengths so that the material has no overall coherent scattering length. Although the material no longer gives powder-diffraction lines, isotropic incoherent neutron scattering is produced.)

Compared to the piston-and-cylinder devices of McWhan and Block, the opposed anvil cell of Ahsbahs is much more satisfactory for single-crystal studies and offers almost unrestricted access to reciprocal space. Conversely, the piston-and-cylinder devices often allow the observation of only one layer of reflections and, although additional crystal mountings can be used, this severly limits the structural information that can be obtained. For example, the piston-and-cylinder design has often been used in high-pressure structure studies of KH_2PO_4 (KDP) and, when a second crystal mounting has not been possible, the structural parameters requiring information from reflections along the axis of the cell have had to be constrained in the refinements (see for example Tibballs *et al* (1982)). Clearly then, the Ahsbahs cell more readily satisfies the first criterion of section 2.2.2 and is to be preferred for accurate single-crystal structural studies using neutron radiation.

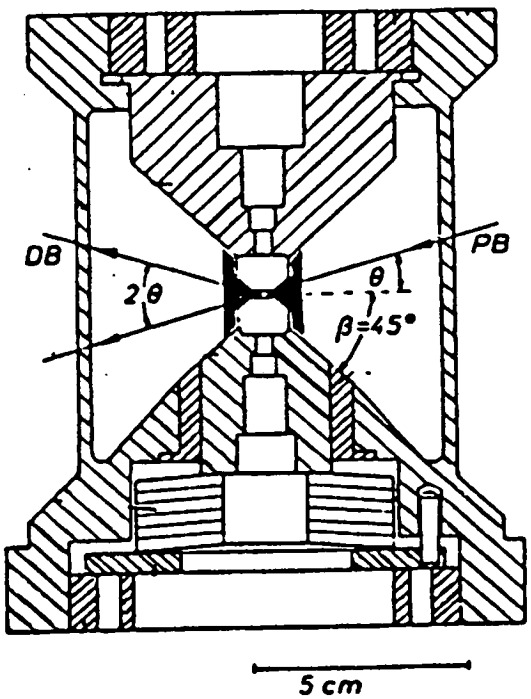

Figure 2.20: The Ahsbahs single-crystal pressure cell for neutron-diffraction studies. (From Ahsbahs (1984b))

2.3.2 Diamond Anvils

Diamond is chosen as an anvil material to generate very high pressures since it is the hardest substance known, and relatively transparent to electromagnetic radiation over a wide energy range, from the infrared through to hard x-rays. They are classified into two types (I and II) depending on the level and nature of their impurities (Seal (1984)). Type-I diamonds contain significant amounts of nitrogen impurity (0.1 at% or more) and are further classified into groups A and B depending on how the nitrogen impurities aggregate. The diamonds classified as type-II do not contain significant nitrogen impurity, although they do contain traces of a variety of impurities at the parts per million level, and are further classified into groups A and B, depending on their electrical conductivity. Since type-II diamonds do not show absorption bands in the ultraviolet and infrared regions, characteristic of the nitrogen impurities in type-I diamonds, they are better suited to high-pressure spectroscopic studies although they are more expensive. For most DAC applications type-I diamonds are usually sufficient (Dunstan and

Spain (1989)) and the nitrogen impurities are not important. Indeed, at very high pressures it has been demonstrated that type-I diamonds with platelet nitrogen aggregates are more resistant to plastic deformation and, therefore, may offer the best anvil material for DACs operating in the Mbar region (Mao *et al* (1979)).

The design of the anvils is a critical factor influencing the pressure a DAC can achieve. Many of the early designs were based on a modified brilliant cut where the diamond tips are polished to provide anvil culets, as shown in figure 2.21. Although this design is widely available on the gemstone market, with correspondingly low prices, it was originally developed to maximise back reflections and spectral dispersion, but is not necessarily the design which gives the optimum strength for DAC applications. More recently an alternative design has been made available which has proved to be extremely satisfactory for use in the DAC (Seal (1984)). This design, the so called Drukker-cut, has an enlarged table diameter, over that of the brilliant cut diamond of the same weight, and has an increased anvil angle. The tightly stressed shoulders of the brilliant-cut have also been removed. With the above modifications the anvil is capable of withstanding greater applied loads and can, therefore, achieve higher pressures. For work at very high pressures, the diamond culets are usually bevelled (Mao *et al* (1979), Mao and Bell (1978b)) so that stress concentration at the sharp corners are reduced and the support to the culets by the gasket is optimised (Bruno and Dunn (1984)).

For x-ray diffraction structure studies, the anvil dimensions are an important consideration. In order to minimise the effects of absorption of the x-ray beams and to reduce the incoherent background produced by Compton scattering from the diamonds, the anvils should be made as thin as possible. There is a limit to how thin the diamonds can be made, however, and this depends critically on the thickness to table-diameter ratio. If this is reduced, the tensile stresses in the base are increased, resulting in the diamond failing at lower pressures (Adams and Shaw (1982)). Although the table itself can be made smaller to compensate for this effect, it cannot be reduced significantly otherwise the anvil will begin to indent the backing plate at fairly modest loads (Dunstan and Spain (1989)) and, if the culet size remains the same, the pressure multiplication produced by the anvil will be reduced. The anvil dimensions are, therefore, a comprimise between several competing factors such as the minimum sample volume, the required

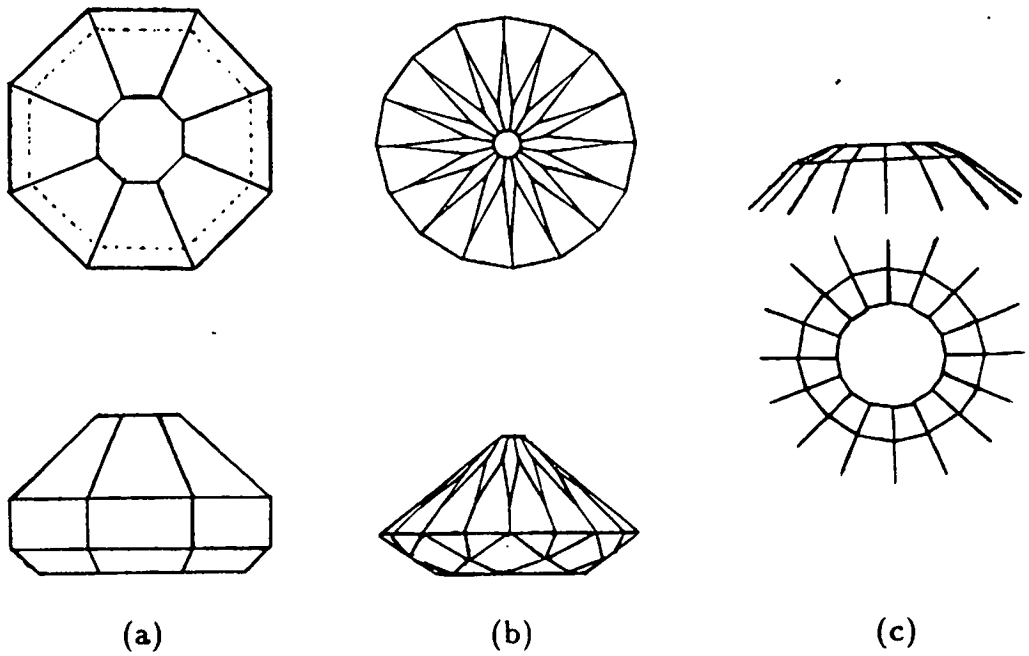

Figure 2.21: (a) The Drukker cut anvil, (b) the modified brilliant cut anvil and (c) the bevelled cut anvil. (From Sherman and Stadtmuller (1987).)

pressure, absorption and background effects, and cost. However, diamond anvils typically used for x-ray diffraction studies are approximately $\frac{1}{3}$carat (1carat=$\frac{1}{15}g$) a thickness of 2 mm, and a table and culet diameter of about 3 mm and 0.6mm respectively (Dunstan and Spain (1989)). The culet diameter has a critical effect on the maximum pressure that can be achieved and, for example, the culets used by Ruoff (1992), for the study of Mo at 438 GPa, were only 0.02mm (20μm) in diameter.

Although it would be desirable to use diamond anvils for high-pressure neutron diffraction studies, the sample size is limited by the availability of natural or synthetic diamonds with the necessary dimensions. The price of mono-crystalline diamonds suitable for anvil material, increases as the seventh power of their dimensions and, even if diamonds large enough for neutron-diffraction could be mined or grown, their price would be prohibitively expensive (Besson *et al* (1992)). For this reason, single-crystal sapphire is often used as an anvil material in neutron pressure cells (Ahsbahs (1984b)).

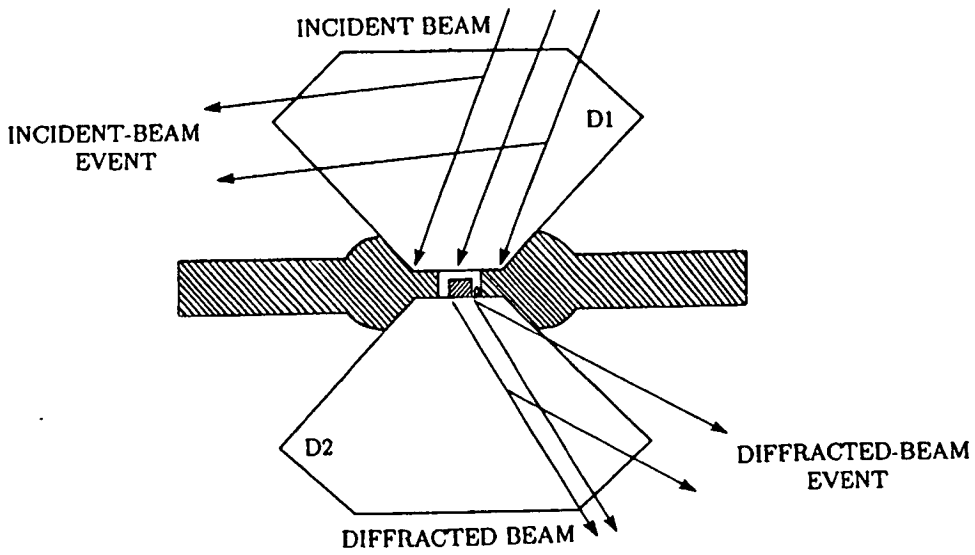

Figure 2.22: A cross-section of the opposed anvils showing the x-ray paths for simultaneous diffraction (i) by the diamond (D1) in the incident beam, and (ii) by the diamond (D2) in the beam diffracted by the sample.

Apart from the increased background from Compton scattering and the x-ray absorption in the diamonds, single-crystal data can also be affected by simultaneous diffraction from the diamond anvils. When this occurs, the intensity of a reflection can be underestimated since either the incident beam, or the diffracted beam from the sample, can be diffracted in the diamonds, see figure 2.22. In some cases a diamond reflection may also intersect the detector aperture, during a scan, and cause the intensity of the reflection to be overestimated. High-pressure experimental techniques have been developed to identify reflections affected by simultaneous diamond reflection, and these will be presented in section 3.2.3.

2.3.3 Gaskets

Although the gasket forms a critical part of the pressure chamber in a DAC, its preparation and its effects on the intensity data have received only limited

attention. Indeed, the choice of gasket material, and the gasket hole dimensions, play a significant part in determining the pressure a DAC can achieve and whether the incident or diffracted x-ray beams are shadowed.

The gaskets are generally prepared from a metal foil approximately 250μm thick which are preindented between the anvils to the required thickness. A sample hole is then drilled into the centre of the preindented area and its diameter is chosen to suit the culet size (typically $\frac{1}{3}$ of the culet diameter). The pressure the gasket can support is dependent upon the diameter of the hole, the thickness of the gasket and also the shear strength of the gasket material (Dunstan (1989)). Suitable gasket materials are hardened stainless-steel, tool-steel or alloys such as Cu-Be or inconel (Ni:Cr:Fe=72:16:8) (Spain and Dunstan (1989)). For single-crystal studies, the sample should have a diameter approximately $\frac{1}{3}$ that of the gasket hole, so that occlusion of sample reflections is prevented, or at least reduced. An additional method of reducing gasket occlusion has been proposed by Katrusiak and Nelmes (1986). To eliminate the shadowing of the incident or diffracted beams, they modified the edge of the gasket hole, furthest from the sample, so that it had a conical shape (figure 2.23). This simple modification allows reflections to be measured at a greater diffraction angle before gasket occlusion begins, although it is only useful up to limited pressures.

For transmission geometry DACs, the use of a large (1x1cm^2) gasket, which is made of a highly absorbing material, shields the detector from a considerable fraction of the background scatter produced by the cell components. The contaminant scatter is then only generated on the detector side of the cell by the beryllium and diamond illuminated by the diffracted beam and the part of the incident beam passing through the gasket hole.

The transverse geometry DAC does not benefit from the background shielding effect of the gasket, even when highly absorbing gasket materials are used. Indeed, gaskets made from materials with a low x-ray absorption are often employed to overcome shadowing of the incident or diffracted beams at low diffraction angles. Although beryllium is generally used its mechanical properties make it unsuitable for sustaining very high pressures, and to achieve pressures close to 10 GPa the initial gasket hole diameter can only be around 40μm at maximum (Macavei and

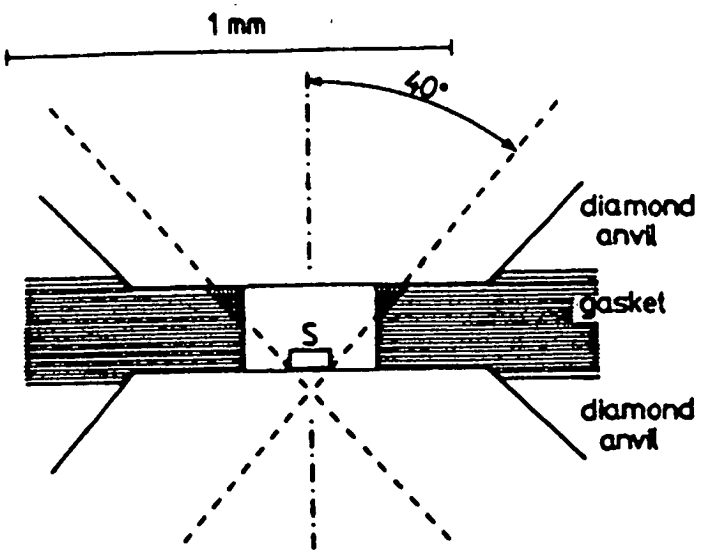

Figure 2.23: The high-pressure chamber in the Merrill-Bassett DAC. The dashed lines represent the limit of accessible angles. The edge of the gasket which has been removed in the modified version is indicated by the cross-hatched shading. (From Katrusiak and Nelmes (1986).)

Schulz (1989)), severly limiting the sample size.

2.3.4 Hydrostatic Pressure Transmitting Media

In order to determine the structural parameters of a crystalline material accurately at high pressure it is essential that the sample is contained within a hydrostatic (zero shear stress) environment. Although solids, with relatively low shear strength, such as AgCl or NaCl, produce quasihydrostatic pressures up to 10 GPa, the presence of an unknown magnitude of stress in the sample can cast serious doubt on the reliability of diffraction data, or on the interpretation of some other physical measurement (Piermarini *et al* (1973)). Therefore, to maintain hydrostatic conditions, in high-pressure sample environments, it is important that the pressure transmitting medium should remain a fluid.

The most frequently used pressure transmitting fluid in a DAC is the alcohol mixture of methanol and ethanol, in the ratio 4:1. This mixture was found to

remain fluid to a glass transition located at a pressure of 10.4 GPa (Piermarini *et al* (1973)). A small addition of water, in the proportion 16:3:1 methanol-ethanol to H_2O, appears to delay the glass transition of the alcohol mixture to 14.5 GPa. For neutron diffraction the incoherent background scatter from the hydrogen atoms make alcohol based pressure transmitting fluids unfavorable. Although deuterated forms of ethanol and methanol can be used (Jorgenson (1978)) their cost is often prohibitive and fluorinated hydrocarbons, such as Fluorinert (McWhan (1975)) are regularly employed. However, these fluorinated hydrocarbon fluids solidify at much lower pressures — in the case of Fluorinert about 1.7 GPa (Sherman and Stadtmuller (1987)).

More recently, the rare-gas solids have been found to be convenient pressure transmitting media since they retain low shear strength even at very high pressure, and low temperature (Toule (1967), Bell and Mao (1977, 1981)). A convenient method of filling the gasket hole with the pressure medium is to cool the DAC below the gas liquifying temperature. The gas can then be introduced into the gasket hole, in the form of a liquid, and trapped there by closing the DAC remotely (for example see Liebenberg (1979)). An alternative approach is to introduce the gas at high pressure (Mills *et al* (1980)). This technique has the advantage that a density higher than that of the fluid can be achieved (He gas at 0.5 GPa is 2.3 times more dense than liquid He) and allows higher pressures to be reached for less gasket deformation (Jayaraman (1983)).

2.4 High-Pressure Diffraction Techniques

Although apparatus has been developed to allow both x-ray and neutron structural studies to be performed at high pressure, there are a number of factors affecting the data quality which require specialised diffraction techniques to minimise, or to correct. These high-pressure diffraction techniques will be described in this section.

2.4.1 Optimising the Data Set

The limited volume of reciprocal space accessible when using a pressure cell reduces the number of reflections that can be measured and, therefore, diminishes the accuracy of any high-pressure structure determination. Indeed, the reduction of measurable data is significantly worse at higher pressure since the angular access to the sample is further reduced to provide improved support for the stressed cell components. With the popularity of the DAC for single-crystal x-ray diffraction studies a number of techniques have been introduced to increase the volume of accessible reciprocal space. This has led to the development of the transverse-geometry DAC and new diffraction techniques to optimise the use of the transmission-geometry DACs.

Although Merrill and Bassett (1974) calculated that, for a 2θ limit of 60°, their cell allowed 55% of reciprocal space to be accessible, they assumed that each reflection was measured with the cylindrical axis of the DAC in the diffraction plane. On a three-circle diffractometer, which was employed in their own structural studies, and on four-circle diffractometers operated in the bisecting position (ω=θ), this ideal condition is violated. Consequently, the accessible volume of reciprocal space is considerably smaller than that predicted by Merrill and Bassett (equation 2.3). However, four-circle instruments allow a reflection to be measured at almost any angle (ψ) around its scattering vector and this property has been exploited by Finger and King (1978) to increase the number of observable reflections.

In their technique, the ϕ-axis is fixed equal to zero (or some other value defined by the direction of the cylindrical axis of the cell) and each reflection is brought into the diffraction condition by rotating around ψ, with the ω and χ motors. By measuring the reflections in this way the cylindrical axis of the cell is constrained to lie in the diffraction plane of the diffractometer and the ideal geometry of Merrill and Bassett is realised. The maximum number of reflections can be observed in this geometry and trial calculations, performed by Finger and King (1978), indicate that this number is as much as 40% greater than that measured in the standard bisecting position. As an additional benefit, the path length of the x-rays through the diamonds and beryllium are reduced, leading to lower absorption and background scatter (see section 2.4.3). For these reasons the fixed-ϕ procedure of

Finger and King is widely used.

Recently Hazen and Finger (1989) have further optimised high-pressure single-crystal data collection by adopting the 'leverage' procedure of Prince and Nicholson (1985). In this procedure, the subset of reflections most influenced by the structural parameters of interest is collected with relatively slow scan rates. By improving the counting statistics of these selected reflections, the number of well determined reflections is increased and the precision of the refined structural parameters are improved. This technique is particularly useful where there are a large number of relatively weak reflections and, therefore, is suitable for crystals that are too small or too weakly scattering for conventional high-pressure crystal structure studies. The leverage procedure was implemented by Hazen and Finger (1989) in their high-pressure study of the mineral andradite. With conventional high-pressure techniques, although a complete data set with 1131 reflections was collected, the resulting refinement was found to give unacceptably large errors. However, using the leverage procedure an optimised set of only 32 reflections was collected, with longer scan periods, and found to give a 'dramatic' improvement in the quality of the refinement.

2.4.2 Minimising the Effects of an Irregular Background and Parasitic Scattering

As the incident beam of x-rays, or neutrons, passes through components of the pressure cell a strong and structured background is generated, which makes reliable measurement of the diffracted intensities extremely difficult. This has led to the development of a number of techniques to overcome the background effects and to improve the quality of high-pressure diffraction data.

For single-crystal x-ray diffraction at ambient pressure the intensity of a reflection is usually recorded with an ω-2θ scan, where both the sample crystal and detector are rotated simultaneously. Although this type of scan ensures that the diffracted x-ray beam strikes the centre of the detector throughout the scan, if the crystal is mounted inside a pressure cell, the detector will sweep across the powder lines generated by the beryllium components and the gasket. The powder lines will

appear as extra peaks in the reflection profiles and, therefore, make it extremely difficult to integrate the intensities of the sample reflections accurately. Indeed, when ω-2θ scans have been adopted for data collection, reflections in 2θ regions where background powder lines appear have often been removed from the structural refinement (see for example Endo *et al* (1989)). If, on the other hand, the detector is held stationary during the scan so that only the sample is rotated, this problem can be overcome (King (1981)). In this so called ω-scan the reflections are scanned parallel to the powder lines and, therefore, their profiles appear on a relatively flat background. The ω scan, however, does require a larger horizontal detector aperture so that all the sample intensity is recorded over the full scan range. Although this results in the reflections being measured on a higher background, the lower signal-to-noise ratio can be compensated for by increasing the counting time for each scan and, since the level of the flat background can be determined accurately, the ω-scan method is widely used in high-pressure structural studies.

The ω-2θ scan is essential for single-crystal neutron-diffraction studies since the wavelength spread for even a monochromated beam is such that the detector has to be moved to intercept all the radiation diffracted from the sample. Although some designs of pressure cells, such as that of Ahsbahs, incorporate null-matrix alloys immediately around the sample to eliminate most of the powder lines, the detection of powder lines produced by steel or aluminium cell components is inevitable. This is certainly the case for neutron pressure cells containing an Al_2O_3 pressure-vessel where a large number of powder lines are generated. When a standard single-detector is used, the 2θ regions affected by powder lines must be avoided. Alternatively, the background level can be estimated by slightly offsetting the sample from the diffraction condition immediately after a reflection has been measured, and then performing an identical scan through the background. This allows the background profile and reflection profiles to be determined independently of one another at almost identical diffractometer settings.

Although it is inevitable that a subset of reflections within a data set will be affected by powder lines from the pressure cell or gasket, simultaneous measurement of sample reflections and those produced by the diamond, or sapphire, anvils can be avoided. In the technique developed by Denner *et al* (1978), from their earlier

work on twinned crystals (Denner *et al* (1977)), the orientation matrices of the sample, anvils and pressure calibrating crystal are determined, and for each sample reflection a test is performed to ensure that only diffracted radiation from the sample passes through the detector aperture. If the test indicates that the sample reflection will overlap with a reflection from any other crystal in the pressure cell, it will be omitted, or collected at a different ψ-angle where no overlap occurs.

For single-crystal x-ray diffraction the number of overlapping reflections produced by the diamond anvils is limited since the diamond has a small lattice parameter and a large number of systematic absences, making the reflections relatively sparse in reciprocal space. Reflections from diamond anvils are also extremely easy to identify due to their high intensity, and the provision of energy discrimination on the detector allows $\frac{\lambda}{2}$ and $\frac{\lambda}{3}$ diamond reflections, which are fairly weak and could be confused for sample reflections, to be rejected automatically. However, for single-crystal neutron diffraction the problems encountered with sapphire reflections are much more serious. Since sapphire has a larger unit cell than diamond, the reflections arising from the anvils in a neutron pressure cell are far more numerous than those from a DAC. The lack of energy discrimination on standard neutron single-crystal detectors can also lead to relatively weak $\frac{\lambda}{2}$ and $\frac{\lambda}{3}$ reflections being difficult to distinguish from those of the sample and, therefore, make the initial determination of the sample orientation matrix extremely difficult. However, the recent development of a small two-dimensional position-sensitive detector for single-crystal neutron-diffraction (Lehmann *et al* (1989)) has eased these problems, and allowed the collection of data free from the effects of pressure-cell powder lines and overlapping reflections from the sapphire anvils.

The position sensitive detector (PSD), of Lehmann *et al* (1989), was originally designed for single-crystal neutron-diffraction studies of crystals with relatively small unit cells. Although standard single-detectors are usually employed for such studies, an area-detector, or PSD, offers several advantages if the sample is twinned, has satellite reflections or crystallizes poorly, since the overlapping reflections are sampled over a three-dimensional grid in reciprocal space and the form of twinning or incommensuration may be readily identified (Lehmann *et al* (1989)). The surface of the detector has a 32×32 pixel layout and each pixel has dimensions of 2x2mm. Under normal sample conditions, with a typical sample to detector

distance of 45cm (for a diffractometer at the Institut Laue-Langevin), the dimensions of a Bragg peak at the detector will be around 8mm and, therefore, it will cover several pixels in either direction across the detector surface. For the intensity measurement of single reflections, an ω-scan can be employed, as the detector surface is also large enough to accomodate the full horizontal motion of the Bragg peak. As discussed above, the use of ω-scans for high-pressure structural studies has considerable advantages since it allows scans to be performed along parasitic powder lines rather than across them. As can be seen from figure 2.24a, the two-dimensional nature of the PSD also allows the spacial separation of the powder lines and sample reflection recorded in the same scan. The powder lines appear as sheets of intensity and can be easily excluded from the intensity integration of the ellipsoid shaped sample reflection, unless there is a strong overlap. In the same manner, the number of reflections that are badly affected by sapphire reflections is considerably less when using a PSD, rather than a single-detector, as can be seen from figure 2.24b. Indeed, since the diffracted intensities have unambiguous spatial separation, a comparative study conducted by Kuhs *et al* (1989) indicated that more than 30% of the single-detector scans suffering from sapphire reflections could be recovered readily using PSD data.

An additional advantage of the PSD is the ability to determine the orientation angles of a reflection rapidly. In the case of a single-detector, the diffractometer angles 2θ, ω, χ and ϕ are scanned in an iterative manner so that the intensity maximum of a reflection passes through the centre of the detector aperture. To make the reflection centring as accurate as possible the aperture is much smaller than that used for intensity data collection. With the PSD, on the other hand, only the ω motor is scanned to find the maximum intensity and the remaining diffractometer angles are determined from the (X,Y) position of the reflection on the detector surface. Since a small detector aperture is not required, the full intensity of the sample reflection can be used and, therefore, reduce the counting time for the centring procedure. For high-pressure studies this is an important consideration since the sample size is relatively small and, consequently, the time spent centring reflections with a single-detector can consume an excessive fraction of limited experimental time.

The PSD also allows relatively weak reflections to be determined with greater pre-

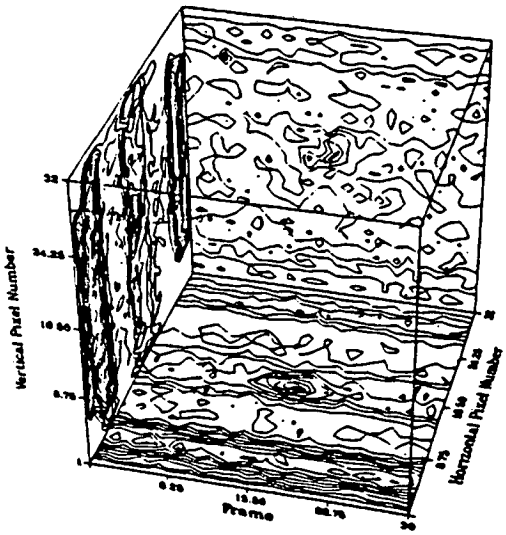

(a)

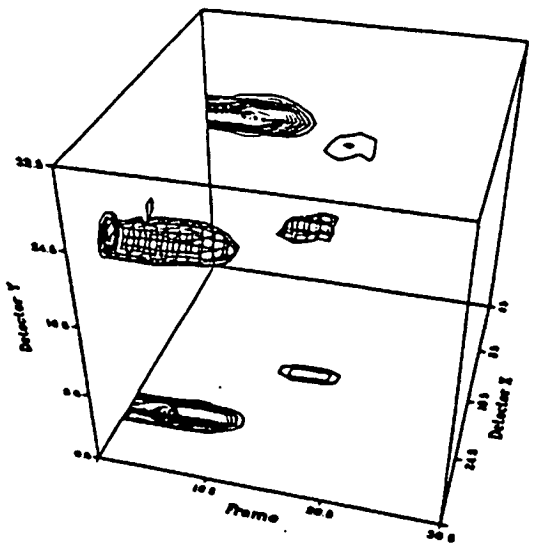

(b)

Figure 2.24: Three-dimensional representations of sample reflections affected by (a) powder lines from the pressure cell and (b) a reflection from one of the sapphire anvils of the Ahsbahs cell. The axes are the scan-step in ω (frame) and the horizontal (X) and vertical (Y) detector axes. The reflection at the centre of both scans (in X,Y and ω) is from the sample.

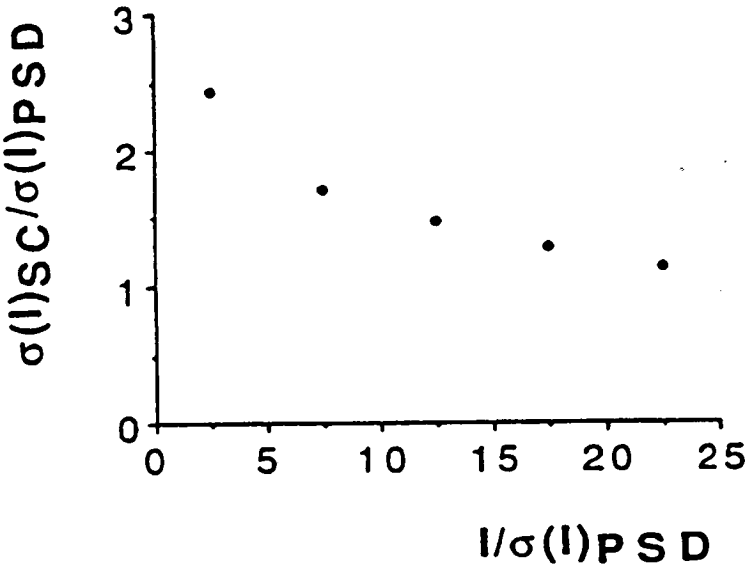

Figure 2.25: The ratio of estimated standard deviation, σ(I), for two sets of data recorded on ice VI at high-pressure, versus the strength of the reflection, expressed as I/σ(I). SC stands for single detector, while PSD stands for the two-dimensional detector. (From Lehmann *et al* (1989).)

cision than can be achieved with a standard single-detector. As can be seen from figure 2.25, which shows a comparison of single-detector and PSD data (Lehmann *et al* (1989)), the gain in precision can be as much as a factor of 2.5 for the weaker sample reflections. Although the scan period of the single-detector can be increased to compensate for its lower precision, the number of reflections that can be collected in the experimental time will be reduced. Therefore, the improved precision that the PSD allows for weak reflections is extremely important for high-pressure studies using small samples, and it is clear that the study of KDP at 2.9 GPa, described in chapter 4, would have been extremely difficult without the use of a PSD.

2.4.3 Absorption Correction

If an accurate high-pressure crystal-structure refinement is to be performed, it is important that the measured reflection intensities are corrected for absorption in the components of the pressure cell. For high-pressure neutron-diffraction, the ab-

sorption of the incident and diffracted beams will be relatively small since the materials used in the construction of the pressure cell have low absorption coefficients. Indeed, for some designs of pressure cell, such as that of Block for single-crystal diffraction and that of Paureau and Vettier for angle-dispersive powder-diffraction, no absorption correction may be required since the absorption pathlengths of the incident and diffracted beams through the cell will be the same, independent of diffraction angle. If this is not the case, such as in the Ahsbahs cell, the pathlengths of the incident and diffracted beams can be determined using a simple graphical approach, where the absorption paths for each reflection are estimated from an expanded drawing of the cell components (see for example figure 5.5). Although the pathlengths for each reflection through a pressure cell used in time-of-flight neutron diffraction techniques may be the same, the absorption correction is more difficult to apply since wavelength dependent absorption coefficients must be taken into account. In this case, the correction is usually determined empirically by monitoring the wavelength spectrum of the incident beam both before and after it passes through the pressure cell. Provided that the diffracted beam passes through a similar absorption path, the difference between the 'up-stream' and 'down-stream' spectra will yield the absorption correction for the pressure cell.

For high-pressure x-ray diffraction techniques, absorption in the pressure cell components can be appreciable and it is, therefore, essential to determine the absorption correction for each reflection accurately. This requirement has led to the development of several absorption correction techniques. The first such technique was introduced by Santoro *et al* (1968) for the correction of high-pressure single-crystal intensity data collected on a precession camera. By applying an analytic absorption correction, it was found that the internal consistency of Br_2 data, collected at 1.0 GPa, could be improved significantly. A later absorption correction technique was developed by Denner *et al* (1978) for intensity data collection on four-circle diffractometers. In this method, which is based on the technique of Flack (1974) for ambient studies of highly absorbing samples or those of an arbitrary shape, a model is developed for the absorption of the pressure cell in terms of the diffractometer angles from a series of azimuthal ψ-scans performed around a number of different sample reflections. Before an intensity measurement is performed on a sample reflection, during data collection, the model is used

to determine the optimum ψ value at which the absorption correction will be a minimum. The reflection is then collected at this optimum ψ position and the correction for cell absorption applied. However, this technique requires considerable experimental time and does not necessarily allow the maximum number of accessible reflections to be measured.

Another, simpler, absorption correction technique was introduced by Finger and King (1978) for the fixed-ϕ diffraction geometry.This technique, as was described in section 2.4.1, allows the maximum number of reflections to be accessible and reduces the pathlengths of both the incident and diffracted x-ray beams to a minimum. As can be seen from figure 2.7, the absorption correction can be parameterised in terms of the angles α_i and α_d, which the incident and diffracted beams subtend with the cylindrical symmetry axis of the cell. In principle, the absorption can be calculated analytically from a knowledge of the size, shape and absorption coefficients of the pressure cell components and from the angles α_i and α_d for each reflection. However, Hazen (1976) found that this approach failed to determine the observed absorption accurately and attributed this to uncertainties in the measured pathlengths and inaccuracies in the mass absorption coefficients of carbon and beryllium. An alternative approach was later adopted by empirically determining the absorption of the pressure cell as a function of α (Finger and King (1978)). This was achieved by measuring the attenuation of the direct beam for values of ω from -45° to 45° for χ equal to 0°, 45° and 90°. The three scans were averaged, as the cell is radially symmetric, and fitted with a polynomial to allow the absorption to be calculated for any angle α. A reflection can be corrected for absorption, therefore, by assuming that each half of the pressure cell has the same attenuation polynomial and from a knowledge of the angles α_i and α_d. If the fixed-ϕ geometry is used, α_i and α_d are given by ω and 2θ-ω respectively. The fixed-ϕ geometry also ensures that α_i and α_d are minimised for each reflection and so reduces the absorption of the incident and diffracted beams through the pressure cell.

A further absorption correction procedure involves a comparison between the integrated intensities measured for a crystal mounted in the cell, at a very low pressure, and the same crystal mounted in the normal fashion outside the cell (Hazen (1976)). The results obtained with this technique are in good agreement

with those obtained by measuring the attenuation of the direct beam, and the absorption corrections for both methods as a function of α are very similar. The same approach has also been adopted for transverse-geometry cells where the complex absorption path lengths make absorption correction by any other means extremely difficult (Schiferl (1977)). However, this method is likely to be less accurate, when the pressure is increased, since a different fraction of the sample will be occluded as the highly-absorbing gasket deforms.

2.4.4 Sample Centring

For accurate crystal-structure determination, using single-crystal techniques, it is extremely important that the sample should be completely bathed in the incident beam of radiation to avoid intensity variations at different settings of the diffractometer. This requires the sample to be accurately centred on the diffractometer so that it is placed in the uniform central region of the incident beam. At ambient pressure, accurate centring can be achieved optically by viewing the sample, with a microscope, at various settings of the diffractometer circles. However, when the sample is mounted inside a pressure cell the centring procedure is more difficult since optical access to the sample is extremely limited. To overcome this difficulty for high-pressure single-crystal x-ray diffraction, King and Finger (1979) have generalised Hamilton's eight-position method (Hamilton (1974a)) to enable diffracted beam crystal centring in the non-bisecting geometry. By measuring a reflection's angular position at eight different diffractometer settings the deviation of the crystal from the centre of the diffractometer can be determined as well as the alignment errors of the diffractometer itself. The procedure is also useful for the determination of accurate unit-cell parameters since the averaged reflection angles are effectively corrected for the positional errors of the sample and misalignment of the diffractometer, an essential condition if accurate equations-of-state are to be measured. However, for the technique to be effective the initial crystal centring errors must be relatively small. This can be achieved with a DAC by alternately viewing the sample through opposite optical ports in the diamond backing discs and, provided the diamonds are optically matched, sample alignment along the cylindrical axis of the cell can be obtained by iteratively translating the DAC so that the sample remains focused for both viewing positions (King (1981)). For

single-crystal studies with neutron radiation it is generally not possible to perform the initial sample centring with optical techniques and photographic methods are often employed. By placing a polaroid film in the 'down-stream' section of the incident beam, the position of the sample, or more usually the sample environment, can be determined from shadowed regions on the film. The sample can then be aligned with sufficient accuracy for diffraction centring techniques to be used. However, since most neutron diffractometers do not allow the detector arm to be driven to negative 2θ values the eight-position method cannot be employed and the centring errors must be determined from the setting angles of carefully selected reflections.

For energy-dispersive x-ray powder-diffraction techniques, the pressure cell can be accurately positioned so that the highly collimated incident beam passes through the centre of the gasket hole, even at the highest pressures. Since a relatively small diffraction angle is used (typically 2θ=10°), the peak locations in the powder patterns are relatively insensitive to positioning errors of the sample along the direction of the beam and, therefore, the energy-dispersive technique is well suited for determining accurate compressibilities. The time-of-flight neutron powder-diffraction technique is also relatively insensitive to centring errors, as the sample displacement will be much smaller than the total flight-path of the neutrons. Therefore, the corresponding flight-time errors will be extremely small allowing small changes in the unit-cell dimensions to be determined accurately. However, angle-dispersive neutron powder-diffraction studies require accurate alignment of the sample, at the centre of the diffractometer, since even a small misalignment will introduce a systematic error in the 2θ values of the diffraction peaks. Although such errors will offset the measured cell dimensions from their true values, accurate relative changes can be determined if the pressure can be increased without changing the position of the pressure cell.

2.5 Concluding Remarks

Over recent years, the DAC has allowed considerable improvements to be made in the quality of high-pressure intensity data collected using single-crystal x-ray

diffraction techniques. With the use of the techniques outlined in the preceeding sections — to optimise the data set, minimise the background and parasitic scatter, minimise and accurately correct for absorption in the DAC components, and reduce the intensity variations and errors in the unit cell dimensions due to inaccurate crystal centring — structures can be refined in which the esd's on the parameters are only a factor of two or three larger than those obtained at atmospheric pressure (see for example Levein *et al* (1980)). This quality of refinement, however, has been available only with the transmission-geometry cells, such as that of Merrill and Bassett, and, to date, very little structural work has been undertaken with the transverse-geometry DACs, despite the advantages they offer of an increased access to reciprocal space. As was described above, this may be due to the difficulty in correcting for the complex absorption path lengths through the cell components. It would, therefore, appear that the most accurate high-pressure structural studies using a DAC can be achieved with those adopting the transmission geometry.

Although x-ray single-crystal techniques have had considerable success for crystal-structure determination at high-pressure, powder-diffraction techniques have been used very rarely for full structure refinement and have been usually limited to the determination of unit cell and spacegroup. This is unfortunate since x-ray powder-diffraction DACs are capable of pressures significantly higher than those used for single-crystal studies. Therefore, there is clearly a need for techniques to allow the accurate measurement of diffracted x-ray intensities from polycrystalline samples contained within a DAC to enable full structural refinement at very high pressure.

Despite the significant advantages that neutron radiation allows at ambient pressure for high-resolution structural studies or those requiring detailed information about atomic thermal motion, relatively few high-pressure single-crystal structural studies have been performed with neutron radiation compared with single-crystal x-ray diffraction. This may be partly due to the relatively low pressures that can be achieved and the severly limited access to reciprocal space that many neutron-diffraction pressure cells provide. As was described in section 2.3.1, many of these designs allow only a single layer of reflections to be measured and, therefore, in order that single-crystal neutron-diffraction can realize its full potential, a more three-dimensional access to reciprocal space is required so that low-symmetry crys-

tal structures can be studied. In this respect, the neutron-diffraction version of the Ahsbahs cell, with its transverse geometry allowing a large volume of reciprocal space to be accessible, would appear to offer great advantages. Although restricted to an upper pressure limit of around 3 GPa, the combined use of the Ahsbahs cell and the position sensitive detector provides the most accurate means of determining crystal structures at high-pressure, using neutron-diffraction, currently available.

For high-pressure neutron powder-diffraction, the time-of-flight technique appears to offer significant advantages over the angle-dispersive technique. The powder patterns collected with angle-dispersive techniques are often contaminated by powder lines generated by the pressure cell components and problems also arise from centring errors which make the determination of structural changes with pressure extremely difficult. However, with time-of-flight techniques the 90° scattering geometry allows contaminant scatter from the pressure cell to be shielded from the detector and the measured powder patterns themselves are relatively insensitive to miscentring of the sample. Although piston-and-cylinder devices, such as those described in section 2.3.1, have generally been limited to pressures in the region of 5 GPa (McWhan *et al* (1974)), the use of a fixed scattering geometry also offers the prospect of extending the use of time-of-flight techniques to very much higher pressures through the development of specialised pressure cells.

Chapter 3

Technique Development

3.1 Introduction

The previous chapter has attempted to describe the apparatus and techniques employed in the determination of crystal structures at high pressure and how the problems associated with collecting reliable diffraction data can be reduced or eliminated. There are, however, a number of important limitations in the outlined state-of-the-art techniques and these will be examined in detail here, along with the techniques developed by the Condensed Matter Physics Group at The University of Edinburgh to overcome them. Although, as was stated previously, the author has not been principally involved with some of this development work, many of the new techniques have been implemented in the high-pressure structural studies of chapters 4, 5 and 6 and are presented here both for completeness and to serve as a detailed description of some of the experimental procedures.

3.2 Single-Crystal X-ray Diffraction

3.2.1 Introduction

Although high-pressure single-crystal x-ray diffraction is the most widely used, and the most highly developed technique for high-pressure crystal-structure studies, the techniques described in the following two parts of this section have allowed the collection of diffraction data with greater accuracy than has previously been possible. The first part describes the application of tungsten gaskets to allow high quality data to be collected with AgKα radiation. In the second part, the effects of simultaneous diffraction from the diamond anvils on the intensity of sample reflections are described and a data collection procedure is presented to identify those reflections affected.

3.2.2 The Use of Tungsten Gaskets and AgKα Radiation

Although diamond and beryllium have low absorption coefficients, the relatively long pathlengths of the incident and diffracted beams through a DAC require that either MoKα (λ=0.71Å) or AgKα (λ=0.56Å) radiation are used, on standard laboratory sources, in preference to CuKα (λ=1.54Å) radiation, which is too highly absorbed. Of the two possible choices of radiation for high-pressure x-ray diffraction, AgKα would appear to offer distinct advantages.

(1) The shorter wavelength of AgKα radiation makes a larger fraction of the reciprocal lattice accessible, allowing structural information to be determined at higher resolution.

(2) The linear-absorption coefficients for AgKα radiation are smaller than those for MoKα and, therefore, the effects of absorption in both the sample and the pressure cell will be less significant.

However, despite these advantages, AgKα radiation has been used very rarely for high-pressure structure determination, and those that have been performed have

given significantly poorer results than equivalent studies employing MoKα x-rays. For example, in the study of the crystal-structure of quartz at high pressure Levien *et al* (1980) found that refinement of the 3.1 GPa data, collected with AgKα radiation, resulted in R values three times larger than those of similar MoKα data sets. There are a number of factors which may lead to this reduction in data quality.

(1) Although x-ray photons at the AgKα wavelength have a higher energy than those at the MoKα wavelength, all x-ray tubes are operated at similar voltage and current settings, irrespective of the target material, and, as a result, the intensity produced by a Ag-target x-ray tube is less than that for a Mo-target tube.

(2) The counting efficiency of scintillation detectors, used on most commercial diffractometers, is poorer for AgKα radiation than for MoKα radiation.

(3) The atomic scattering power has a λ^3 dependence and is therefore smaller for the AgKα wavelength.

(4) Absorption of AgKα x-rays in the gasket is less than that for MoKα and, therefore, the gasket will be less efficient at shielding the detector form contaminant background produced by illuminated pressure cell components (see section 2.3.3).

The combination of these effects is to reduce the signal-to-noise ratio for reflections measured with AgKα radiation, making the measurement of accurate integrated intensities extremely difficult. Although the scan period can be increased to partly compensate for the poorer counting statistics, a reduction in the data quality is inevitable. However, with the advantages that the use of a shorter wavelength offers and the development of single-crystal diffraction techniques on synchrotron sources, which provide both high intensity at short wavelengths and the possibility of achieving higher pressures by reducing the sample size, it is important that a means is found of improving the quality of diffraction data collected with relatively short x-ray wavelengths.

When AgKα radiation is used the degradation of data quality is due to both a decrease in the signal, despite the reduction in DAC and sample absorption, and

an increase in the noise from the augmented background. Although it is not possible to significantly increase the signal using standard laboratory-based equipment (both sealed tubes and rotating-anode sources require lower currents when operating with targets made from Ag rather than Mo), the noise can be diminished if the enhanced transmission through the gasket material can be reduced. This is particularly important at higher pressure since the gasket material between the diamonds will get thinner, leading to greater transmission of the primary beam through the gasket and an increase in the background by the illuminated cell components.

As was explained in section 2.3.3, typical gasket materials used for high-pressure x-ray diffraction are Inconel, a nickel alloy, and forms of hardened steel which have linear absorption coefficients of $320cm^{-1}$ (Macavei and Schulz (1990)) and $303cm^{-1}$ respectively for MoKα radiation and significantly lower values of $164cm^{-1}$ and $155cm^{-1}$ respectively for AgKα radiation. Since the transmission of a material is determined by $e^{-\mu x}$, where μ is the absorption coefficient and x is the pathlength, the transmission of a 100μm gasket, composed of either Inconel or Steel, will be increased from approximately 4.5% to around 20% if the radiation is changed from MoKα to AgKα, corresponding to a reduction by about a factor of 4 in the absorption for both materials. In this respect it is extremely important that a highly absorbing material is used for AgKα wavelengths.

The linear absorption coefficient of tungsten is $1913cm^{-1}$ for MoKα radiation and $1023cm^{-1}$ for AgKα radiation giving an absorption for a 100μm thickness which is approximately 8,000,000 times and 5,000 times greater than Inconel for the MoKα and AgKα wavelengths respectively. Clearly then, the significantly higher absorption offered by tungsten gaskets would appear to allow a large reduction of the background generated by illuminated components of the pressure cell. In order to test this effect, Dr M.I. McMahon and Dr J.S Loveday, of this department, measured the background produced by a Merrill-Bassett DAC with a series of 2θ scans using two different gasket materials, inconel and tungsten, and using MoKα and AgKα radiation.

An inconel gasket, 250μm thick and with a 250μm sample hole, was mounted, on one platen of a Merrill-Bassett pressure cell and carefully positioned so that

the sample hole was centered on the culet face. The platen was then mounted on a CAD4 diffractometer with the beryllium backing plate and diamond anvil on the detector side of the gasket. After centering the gasket hole in the MoKα x-ray beam (graphite monochromator), a series of long 2θ scans were performed through the powder pattern generated by the illuminated beryllium. The platen was removed from the diffractometer and a second platen mounted, which contained a similar, although not identical, gasket made of tungsten. Another series of long 2θ scans were performed to measure the powder pattern generated when using this gasket. The x-ray tube was then replaced with a tube containing a Ag-target and the measurements repeated for both gasket materials.

Although it was attempted to measure the background generated by the two different gaskets under almost identical experimental conditions, in practice it was found extremely difficult to produce gaskets with the same dimensions. Since different pressure cell platens were also used it is not possible to compare the results obtained with different gaskets directly. However, identical experimental conditions were maintaned for the study of the same gasket at different wavelengths and a direct comparison of changing the wavelength for each gasket can be made.

The results of this study are shown in figures 3.1a and 3.1b, which compare the powder patterns measured with MoKα and AgKα radiation for both gasket materials. As can be seen from figure 3.1a, which shows the powder patterns collected with the Inconel gasket, although the Ag-target tube has a lower intensity and the efficiency of the detector is poorer, the intensity of the beryllium powder lines and the general level of the background is significantly higher when AgKα radiation is used. This pronounced increase in the structured background combined with the reduced intensity of the sample reflections would appear to explain the poor data quality obtained with AgKα radiation. However, upon examination of figure 3.1b, which shows the powder patterns collected with the tungsten gasket, it is clear that the intensities of the powder patterns measured with the different wavelengths are very similar and, although the background obtained with AgKα radiation is slightly higher, the tungsten gasket has effectively reduced the background level of the AgKα radiation to the same level as that of MoKα.

Although this study has demonstrated the value of tungsten gaskets for the reduc-

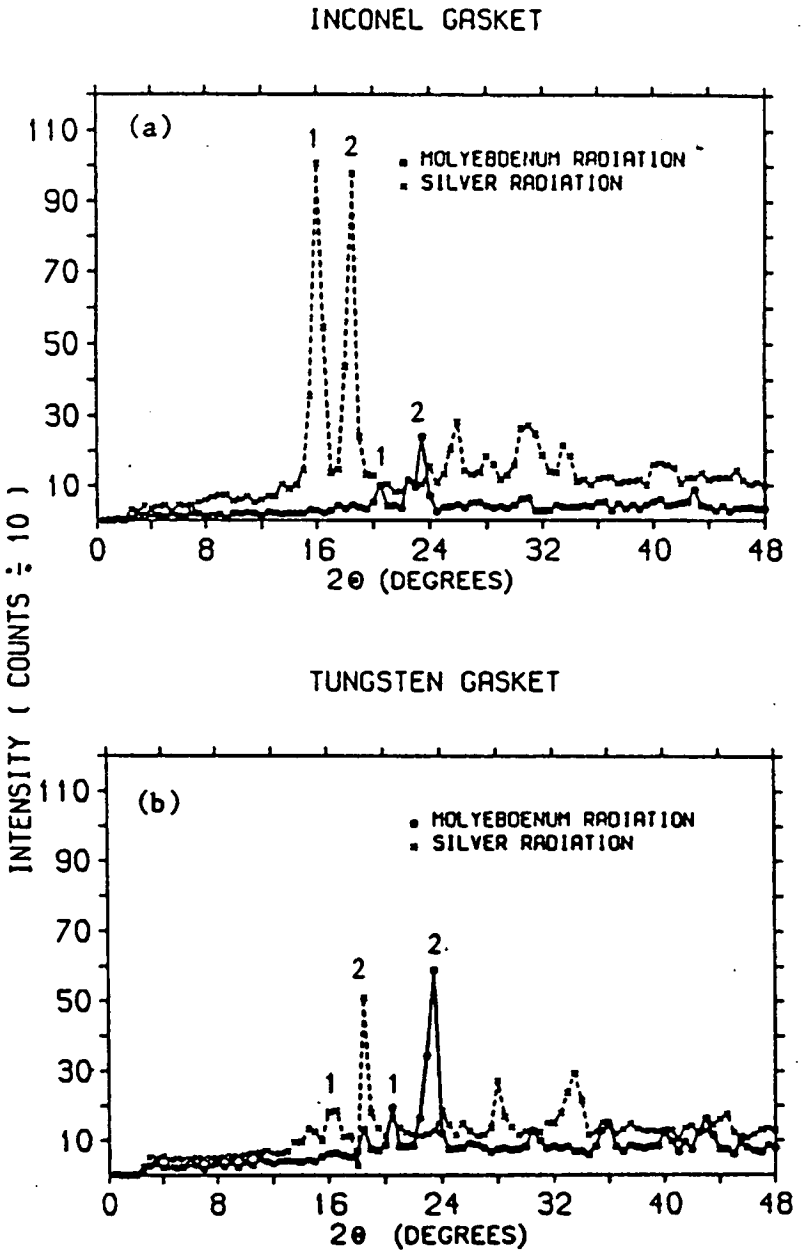

Figure 3.1: A 2θ-scan through the powder pattern produced by the incident beam passing through the beryllium components of half a Merrill-Bassett DAC for (a) an Inconel gasket using MoKα (□) and AgKα (×) radiation, and (b) for a tungsten gasket using MoKα (□) and AgKα (×) radiation. The peaks labelled 1 and 2 in (a) and (b) are from the same group of reflections but are shifted in 2θ due to the different wavelengths.

tion of the background generated by AgKα radiation, a number of important considerations have not been investigated. For example, quantitative measurements are required to compare the background intensities for gaskets of identical dimensions prepared from Inconel and tungsten, and to determine the dependence of the background intensity with gasket thickness and sample hole diameter. However, it is clear that the background intensity is significantly reduced by using tungsten as gasket material, particularly for AgKα radiation, and, for this reason, tungsten gaskets have been used in the structural studies of $KTiOPO_4$ and α-boron in chapters 4 and 6 respectively.

3.2.3 Simultaneous Diffraction by the Diamond Anvils

Although, as described in section 2.4.2, procedures have been developed to avoid the simultaneous measurement of sample and diamond anvil reflections, by ensuring that only diffracted radiation from the sample passes through the detector aperture, a phenomenon that has not previously been considered is the removal of intensity from either the incident or diffracted beams of the sample reflection by diffraction in the diamond anvils. In the following study (which has been described in more detail elsewhere (Loveday *et al* (1990)), it is demonstrated that this 'simultaneous diffraction' process can produce a remarkably large effect on the accuracy of the intensity measurements.

As can be seen from figure 3.2, there are two possible types of simultaneous diffraction process. In the first, a fraction of the incident beam is diffracted by the diamond-anvil between the sample and the x-ray source, reducing the intensity of the beam before it reaches the sample (the incident-beam event). In the second process, a fraction of the intensity diffracted by the sample is further diffracted by the diamond-anvil between the sample and the detector (the diffracted-beam event), reducing the intensity of the radiation reaching the detector.

Preliminary evidence for such simultaneous diffraction effects was established from variations in sample reflection intensity measurements as the reflection was rotated about its scattering vector (a ψ-scan), for a crystal contained within a DAC. These measurements were made on a crystal of the cubic perovskite $KMnF_3$ mounted in

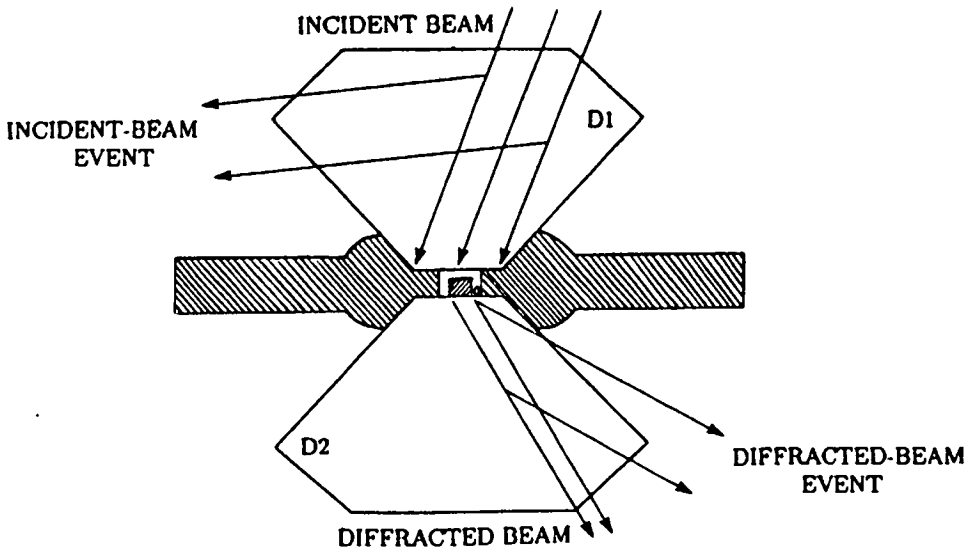

Figure 3.2: A cross-section of the Merrill-Bassett DAC illustrating the x-ray paths for simultaneous diffraction (i) by the diamond (D1) for the incident beam, and (ii) by the diamond (D2) for the beam diffracted by the sample.

a Merrill-Bassett DAC, using a CAD4 diffractometer and MoKα radiation. Figure 3.3 illustrates the integrated intensity of the (2 0 0) reflection measured using ω-2θ scans performed at successive steps of 0.1° in ψ. In addition to the broad peak due to the variation of of the DAC and sample absorption with ψ, the intensity of the (2 0 0) reflection also exhibits several sharp 'dips', of up to 50%, which were attributed to simultaneous diffraction events in the diamond anvils. However, the magnitude of the dips was difficult to explain since the initial studies with single diamond anvils had shown that the maximum intensity scattered was only 1% of the direct beam.

To be confident that these dips were due to simultaneous diffraction in the diamond anvils it was necessary to investigate whether the diamonds in the loaded DAC (at a relatively low pressure of 0.25 GPa) reflected a significant fraction of the incident beam. The CAD4 detector was set to monitor the suitably attenuated direct beam and intensity measurements were made as the diamond on the detector side of the DAC was driven by the ω-motor through its (2 2 0) reflection. As can be seen from figure 3.4, even with the fairly modest applied pressure of 0.25 GPa the effective scattering power of the diamond has increased, causing a 10% reduction of the direct beam intensity. This was confirmed by using the CAD4

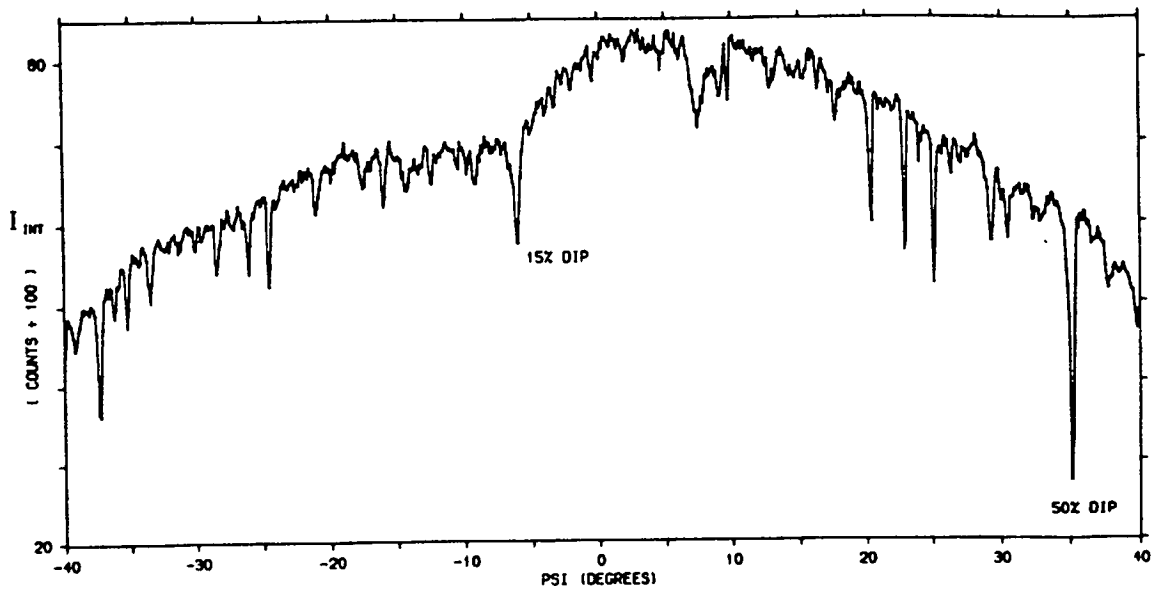

Figure 3.3: The integrated intensity, I_{INT}, versus ψ for the (2 0 0) reflection of a $KMnF_3$ sample under pressure in a Merrill-Bassett diamond-anvil cell (DAC). I_{INT} is the total integrated counts at each point, divided by 100.

detector to measure the intensity of the (2 2 0) reflection itself, and is shown as the circular symbols on the dashed line in figure 3.4. There is a clear correspondence in both intensity and ω-position between the dip in the direct beam and the diamond reflection. The same techniques was then used to monitor the scattering power (the percentage of the direct beam scattered) for several classes of diamond reflections under the same conditions. It was found that only the five strongest classes had a significant effect on the primary beam — the (1 1 1) class by 20-30%, the (2 2 0) class by 10-15%, the (3 1 1) class by approximately 7%, and the (4 4 0) and (4 0 0) classes by about 4%.

Since it had been shown that the diamond anvils are capable of diffracting a significant fraction of the primary beam, it was necessary to determine whether this was responsible for all the dips in a ψ-scan. The orientation matrices of the sample and the diamonds were used to predict the ψ value at which significant incident- and diffracted-beam events, involving the five strongest classes of diamond reflections listed above, would occur. Figure 3.5 shows a section of the ψ scan for the $KMnF_3$ (1 1 0) reflection and the the vertical lines below the scan mark the positions of simultaneous diffraction events, predicted using a program written by Dr J. S. Loveday, of this department. The relative strengths of these predicted events

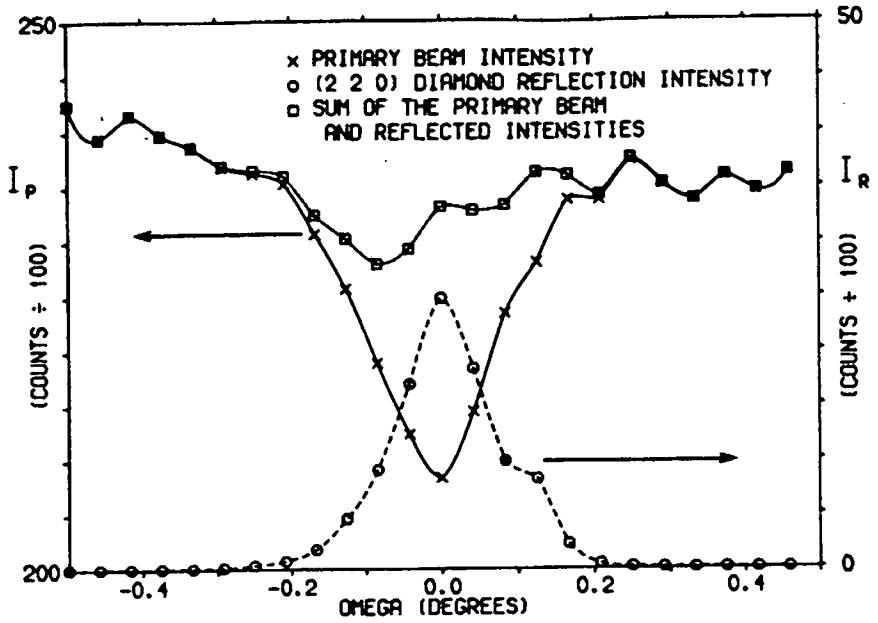

Figure 3.4: An ω scan through a (2 2 0) diamond reflection from a DAC under pressure (○), setting ω=0 at peak, and the intensity of the primary beam (×) measured for each step through the reflection. The sum of the primary beam intensity (I_p) and the intensity in the reflection (I_R) is also shown (□). I_p and I_R are the recorded counts at each point, divided by 10.

are represented by the lengths of the vertical lines. As can be seen from figure 3.5, there is a good general agreement between the observed dips and the predicted events, in terms of both position and relative magnitude. The small discrepancies of up to 2-3° in ψ between calculated and observed positions are due to errors in the orientation matrices of the diamonds, since an orientation matrix can only calculate the diffraction angles accurately if the crystal is well centered on the diffractometer — a condition not satisfied by either diamond anvil.

As a final confirmation, tests were performed to directly relate the observed dips in the ψ-scans and simultaneous diffraction events. In the case of the incident-beam events, the direct-beam intensity was monitored as the sample ψ-scan passed through a dip. For all cases studied, the direct-beam intensity exhibited a reduction in magnitude consistent with the class of diamond reflection predicted to be involved and, furthermore, the magnitude of the dip in the measured sample reflection was simply the percentage reduction of the primary beam intensity. The diffracted-beam events were measured with a second detector, placed out of the diffraction plane of the diffractometer, since it is not generally possible to inter-

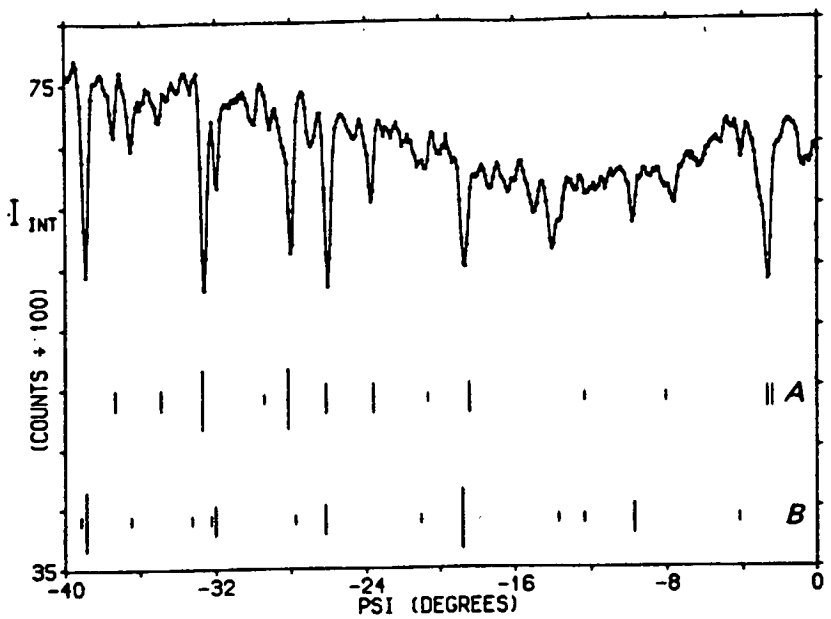

Figure 3.5: The integrated intensity, I_{INT}, versus ψ for the (1 1 0) $KMnF_3$ reflection, at a pressure of 0.25 GPa. The vertical marks show the predicted positions of the incident-beam events (labelled A) and diffracted-beam events (B). The lengths of the marks represent the relative scattering powers of the diamond reflections, as given in the text — the longest for (1 1 1)-type reflections, the next for (2 2 0), the next for (3 1 1) and the shortest for both (4 0 0) and (4 4 0).

cept the diffracted beam from the diamond with the CAD4 detector. Figure 3.6 shows a diffracted-beam event due to the diamond (2 2 0) reflection, successfully recorded at the predicted position of the detector and the dip in intensity of the sample reflection (recorded with the same detector to ensure the intensities were on the same scale) is also shown. Although there is a slight offset due to the uncertainty of the diffractometer setting (0.1° in ψ) and a small difference in magnitude due to the differences in absorption for the diamond and sample reflections, there is a good correspondence between the dip in the sample reflection intensity and diamond reflection in terms of both magnitude and ψ value.

Since there was a pronounced difference in scattering power between an unstressed diamond and the diamonds in a DAC at low pressure (this effect attributed to an increase in their mosaic width), the measurements were repeated with the cell at 3.0 GPa and ambient pressure. To look for evidence of wavelength dependence measurements were also performed with AgKα radiation as well as MoKα radiation. The results confirmed that the diamonds had a very small scattering power

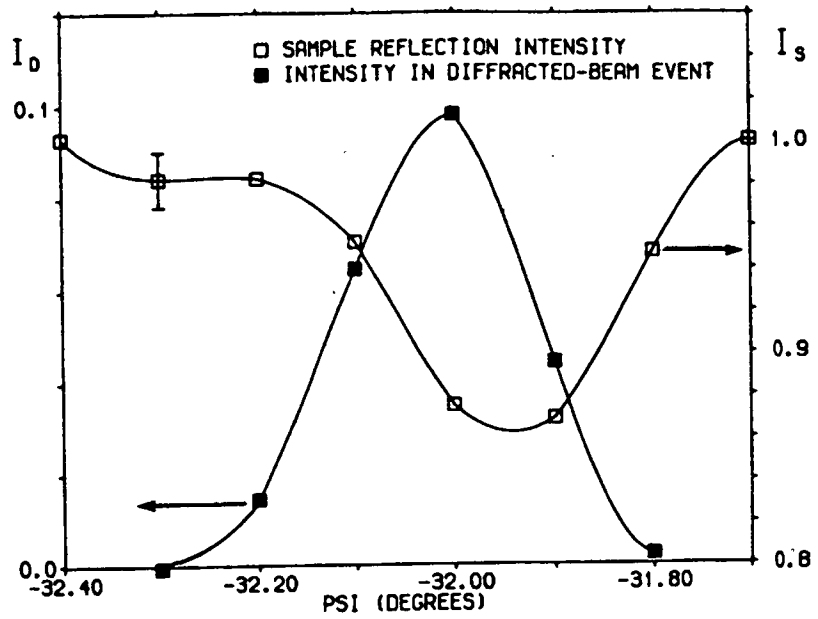

Figure 3.6: The peak intensity of a (2 0 0) $KMnF_3$ sample reflection, I_S, and the peak intensity of a diffracted beam event involving a (2 2 0) diamond reflection, I_D, as a function of ψ at a pressure of 0.25 GPa. I_S and I_D were measured with the same detector and have been put a common scale normalised to 1.00 at the maximum sample intensity. A typical error bar is shown for one of the points.

at ambient pressure and showed that the increased scattering power at 0.25 GPa was the same as that at 3.0 GPa. Therefore, the dramatic effect of pressure on the scattering power is achieved in the first 0.1 or 0.2 GPa of applied load and is not increased significantly at higher pressures. The scattering power was also found to be unaffected by wavelength, and since the same five classes of reflections were found to give significant diffraction events, the overall density of dips is not affected either.

Although it had been demonstrated that simultaneous diffraction can have a large effect on the measured intensity of a sample reflection, the number of reflections affected in a data set at the ψ-value, ψ_m, at which they are measured (usually determined by the fixed-ϕ technique, see section 2.4.1) had not been determined. This was investigated by developing a simple data-collection strategy to avoid simultaneous diffraction. A full data set was collected on the CAD4 diffractometer measuring each reflection at three values of ψ at 0.5° intervals from ψ_m. This three-point ψ-scan provided a method of detecting those reflections affected by simultaneous diffraction and indicated that about 20% of all reflections had their

integrated intensity reduced by more than two standard deviations from their initial measuring position, in a data set collected to a $\frac{\sigma(I)}{I}$ of 3%. A similar result may be expected for any sample, irrespective of unit-cell dimensions, since the unit-cell dimensions of diamond determine the average separation of the dips as a function of ψ.

The points at which dips appear in a ψ-scan appear to be almost randomly distributed and so the consequence of ignoring simultaneous diffraction effects maybe to simply reduce the precision of a structural refinement. However, due to the larger angular separation of $K\alpha_1$ and $K\alpha_2$ components of a sample reflection at high 2θ, which prevents them both being diffracted by the same strong (and thus, low-2θ) diamond reflection, it is to be expected that the higher angle sample reflections will be less affected. Therefore, since the average magnitude of the dips decrease with increasing 2θ, the thermal parameters of the sample will be underestimated.

It is extremely important that the simple three-point ψ-scan procedure is adopted if reliable intensity data is to be collected, and, for this reason, it has been used in the structural studies of $KTiOPO_4$ and α-boron in chapters 4 and 6 respectively.

3.3 X-ray Powder-Diffraction

3.3.1 Introduction

As was discussed earlier in section 2.3.1, the very small sample volume offered by a DAC, often in the order of 100μm in diameter and 50μm thick, results in both a weak signal and a poor powder average and, therefore, prevents accurate crystal structure refinement of high-pressure x-ray diffraction data collected from polycrystalline samples. Although energy-dispersive x-ray diffraction studies have been performed on polycrystalline samples at pressures in excess of 100 GPa for many years and has overcome the problem of low signal by bathing the sample in intense polychromatic synchrotron radiation, the high degree of collimation required between the sample and detector enhances the problems of poor orienta-

tional averaging of the crystallites, giving peak intensities that are not generally reliable enough to refine accurate crystal structures. However, very recently, both of these problems have been overcome using a new type of area detector, an imaging plate (IP), which has allowed angle-dispersive powder-diffraction techniques to be employed for the determination of the crystal-structure of Br_2 to 80 GPa, from pioneering work at the Photon Factory (Fujii *et al* (1989)). Such a detector, whose dynamic range of 10^4-10^5 is two orders of magnitude better than that of film and intrinsic noise level is some 300 times less than the intrinsic fog of x-ray film, is ideally suited to angle-dispersive techniques and can be used to intercept a substantial proportion of the Debye-Scherrer rings; subsequent integration around the powder rings greatly increases the signal and improves the powder averaging. The integration process also greatly improves the signal-to-noise ratio.

For the past year the Condensed Matter Physics Group of The University of Edinburgh has been developing an IP system at the Synchrotron Radiation Source (SRS), Daresbury, UK, with the objective of performing full Rietveld refinement of crystal structures at high pressure. Such techniques require high-quality data free from contaminant powder rings and spurious diffraction spots, and that have a high signal-to-noise ratio with well defined peak shapes. To this end, great emphasis has been placed on obtaining diffraction patterns of the highest quality that are free from background scatter and contamination, and to develop an integration procedure for processing the data. The following sections describe the development of the Edinburgh-Daresbury IP system and the author's involvement in developing a revised alignment technique.

3.3.2 The Imaging Plate System

The IP system, which is shown schematically in figure 3.7, has been developed for use on station 9.1, which is situated 15m from the 5 Tesla superconducting wiggler at the SRS Daresbury. A water-cooled channel-cut Si(1 1 1) monochromator is used to select the required wavelength from the wiggler magnet spectrum and the monochromatic beam is reduced to the dimensions of 0.5x0.5mm^2 by tungsten-carbide slits. As the background produced by the monochromator vessel is significant, the beam passes through a Pb shield which prevents stray radiation

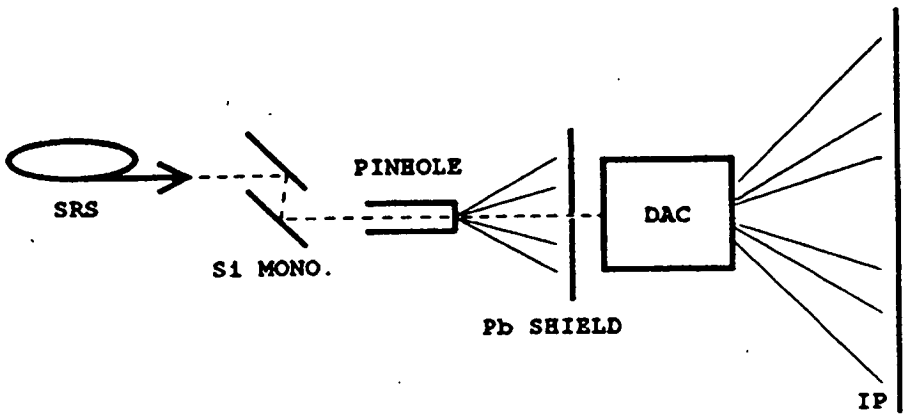

Figure 3.7: A schematic diagram of the beam line setup at the SRS. The incident white beam is monochromated before being collimated by a slit and pinhole system. A Pb shield placed between the pinhole and the pressure cell removes the λ and $\frac{\lambda}{3}$ powder lines from the pinhole material. The collimated beam passes through a hole in this shield before striking the sample in the DAC. The clean diffraction from the sample is then intercepted by the IP.

being detected by the image plate. To remove scatter and fluorescence induced by the incident beam itself, further Pb shielding completely encloses the monochromatic beam until it is finally collimated to a circular cross-section of 50-100μm in diameter by a pinhole mounted on the end of a tungsten-carbide tube. This pinhole assembly is mounted on a motorized XYZ stage to allow the pinhole to be accurately positioned in the centre of the monochromatic beam.

The pinholes, which can be readily interchanged for different beam diameters with the minimum of realignment, are constructed from a sheet of 300μm of platinum bonded to a 250μm sheet of tungsten. Platinum offers a number of advantages as a pinhole material: it is strongly absorbent of x-rays due to its high atomic number and high density; it is relatively easy to drill small, accurately circular holes through; and, fortuitously, as the platinum K-absorption edge is at 0.15817Å, for wavelengths shorter than 0.4745Å the $\frac{\lambda}{3}$ harmonic from the monochromator is greatly attenuated. The latter feature is particularly important as contaminant powder lines would otherwise result from illumination of the pressure cell gasket by the 0.5x0.5mm^2 sheath of $\frac{\lambda}{3}$ radiation surrounding the collimated incident beam. Although the incident beam also contains a $\frac{\lambda}{4}$ component, parasitic scatter from this harmonic is considerably weaker than that from $\frac{\lambda}{3}$ due to both the λ^3 term in

the scattering power and the reduced flux of the $\frac{\lambda}{4}$ wavelength in the white beam. For wavelengths longer than 0.4745Å other materials, such as W, Ir, Re and Os, can be used in much the same manner, although it is considerably more difficult to drill holes of a suitable diameter through these materials. The layer of tungsten, which is bonded to the platinum pinhole, has a spark eroded hole approximately 300μm in diameter and is used to restrict the dimensions of any remaining $\frac{\lambda}{3}$ sheath surrounding the collimated beam without introducing additional alignment difficulties.

Although the pinhole prevents contaminant powder lines being produced by the gasket material, illuminated by stray $\frac{\lambda}{3}$ radiation, illumination of the pinhole edges by the incident beam generates both a λ and $\frac{\lambda}{3}$ powder pattern from the platinum. This is a serious problem when DACs with large x-ray transparent beryllium windows are used, since the platinum powder pattern will easily penetrate the cell and contaminate the sample powder pattern recorded on the IP. To overcome this problem, a 5mm thick lead shield is placed immediately in front of the pressure cell and a small (approximately 1mm) hole drilled through it allows the collimated beam to bathe the sample while the shield is far enough away (approximately 30mm) from the pinhole to allow the diffracted beams from the platinum to diverge sufficiently to be intercepted.

The plates are mounted on the beam line in a light-tight holder which can be tilted or rotated with respect to the incident beam. A Pb beam stop is secured to the front of the holder, which is thin enough to allow a small fraction of the incident beam to penetrate so that the powder pattern centre can be determined accurately for subsequent integration, and is mounted close enough to the IP surface to avoid contaminant Pb powder lines.

Finally, as the general background in the station hutch is significant, principally due to fluorescence induced by hard radiation escaping from the monochromator vessel, great care has to be taken to ensure that the IP is shielded from all sources of background scatter in the beam line environment. This is achieved by enclosing the entire beam line assembly, from the initial Pb shielding at the monochromator housing to the image plate, in a steel frame draped with Pb-loaded rubber sheeting.

The image plate itself consists of a Kodak Storage Phosphor Screen (BaFBr:Eu phosphors) bonded onto a flat aluminium backing plate. X-ray photons incident on the image plate create trapped electron states (colour centers) which are stabilised by the Br vacancies. The image plate is highly sensitive to the short wavelengths (in the order of 0.7Å) that are necessary to penetrate the pressure cell; for a phosphor coat 150μm thick, the x-ray absorption is 100% for wavelengths greater than 1Å and is still 70% for a wavelength of 0.5Å. After exposure, the plate is placed in a Molecular Dynamics 400A Phosphor Imager for reading. An He-Ne laser is used to stimulate the phosphor with the emitted light (caused by the decay of the colour centers) being collected by a fibre-optic bundle and detected with a photomultiplier tube. The amplified and digitally encoded signal is stored on a microcomputer, that also controls the translational motion of the image plate and the galvanometer mirror which rasters the laser beam across the plate. The reading of a standard 250x200mm image plate takes 9 minutes and creates an 11-Mbyte data file consisting of approximately 2800x2000 pixels each of 88x86μm in size. The resolution of the reader is determined by the point spread function of the laser beam on the surface of the IP and results in peak widths (full width half maximum) for NBS standard samples (Si, Al_2O_3 and CeO_2) of 5-7 pixels, a figure well suited to the Rietveld refinement method. As the half-width of the powder lines, in terms of pixels, is ultimately determined by the reader itself, rather than the divergence of the incident beam, the peakwidth remains relatively constant for different distances between the sample and the plate. Therefore, the angular resolution of the patterns can be increased by simply increasing the sample to image plate distance, providing an effective means of separating closely spaced groups of reflections into well resolved individual peaks. The sample to plate distance can be varied from 150 to 800mm, although a distance of 250mm proves satisfactory for most experiments.

In order to determine the sample to plate distance accurately, for subsequent conversion of the digitized image into a standard 1-dimensional powder pattern expressed in terms of 2θ, the following procedure has been adopted. During an experimental run, a powder pattern is collected at the standard sample to plate distance of around 250mm so that as much of the powder pattern as possible is intercepted, and a second exposure is taken at a longer sample to plate distance in order to maximize the angular resolution, as described above. Using a 20μm

thick nickel foil as a calibrant, a nickel powder pattern is collected at both plate positions which can be used to determine the foil to plate distance in each case, from a knowledge of the nickel lattice parameter, and hence the difference, Δ, in the sample to plate distances. As the same sample powder pattern is collected at each of the two plate positions, the sample to plate distance can be calculated in both cases knowing only the distance Δ and the dimensions of the pixels on the integrated images. Provided that the sample to plate distance is the same in all instances, other exposures of the sample, taken at different pressures, can also be calibrated.

In order to benefit from the 2-dimensional nature of the image plate, the DACs that have been used exclusively to date are those designed for single-crystal diffraction, which offer a large angular access to the sample. For low pressure studies ($\leq$6 GPa) Merrill-Bassett DACs have been used which contain a relatively large sample volume and allow data to be collected to a maximum 2θ angle of approximately 40°. To extend the pressure range to 25 GPa, an Adams cell (the DXR-4 cell described in section 2.3.1) has been employed which also has a conical aperture and which permits reflections with a maximum 2θ angle of 50° to be observed. The full conical aperture of these cell designs, as opposed to the slit aperture of many ultrahigh pressure powder-diffraction DACs, allow the entire Debye-Scherrer ring pattern to be observed. This feature not only allows integration around the full powder ring, resulting in a superior powder average and improved signal-to-noise, but also permits the 2-dimensional nature of the image plate to be used to its full advantage. For example, the ability to observe a large portion of the complete powder pattern can also aid the interpretation of the data, as can be seen from figure 3.8 which shows a section of the diffraction pattern of InSb at 3 GPa. On close inspection it can be observed that the pattern is composed of two distinct types of powder ring, one characterised by spots from relatively large sample crystallites, and the other by relatively smooth lines. This behaviour indicates that the sample is a mixture of two phases. Assigning the powder lines to each of these phases has allowed the successful unit cell indexing of both structures in a relatively straightforward manner, a task that would have been very much harder, if not impossible, without the full 2-dimensional image.

The 2-dimensional image of the powder pattern also allows contaminant features of

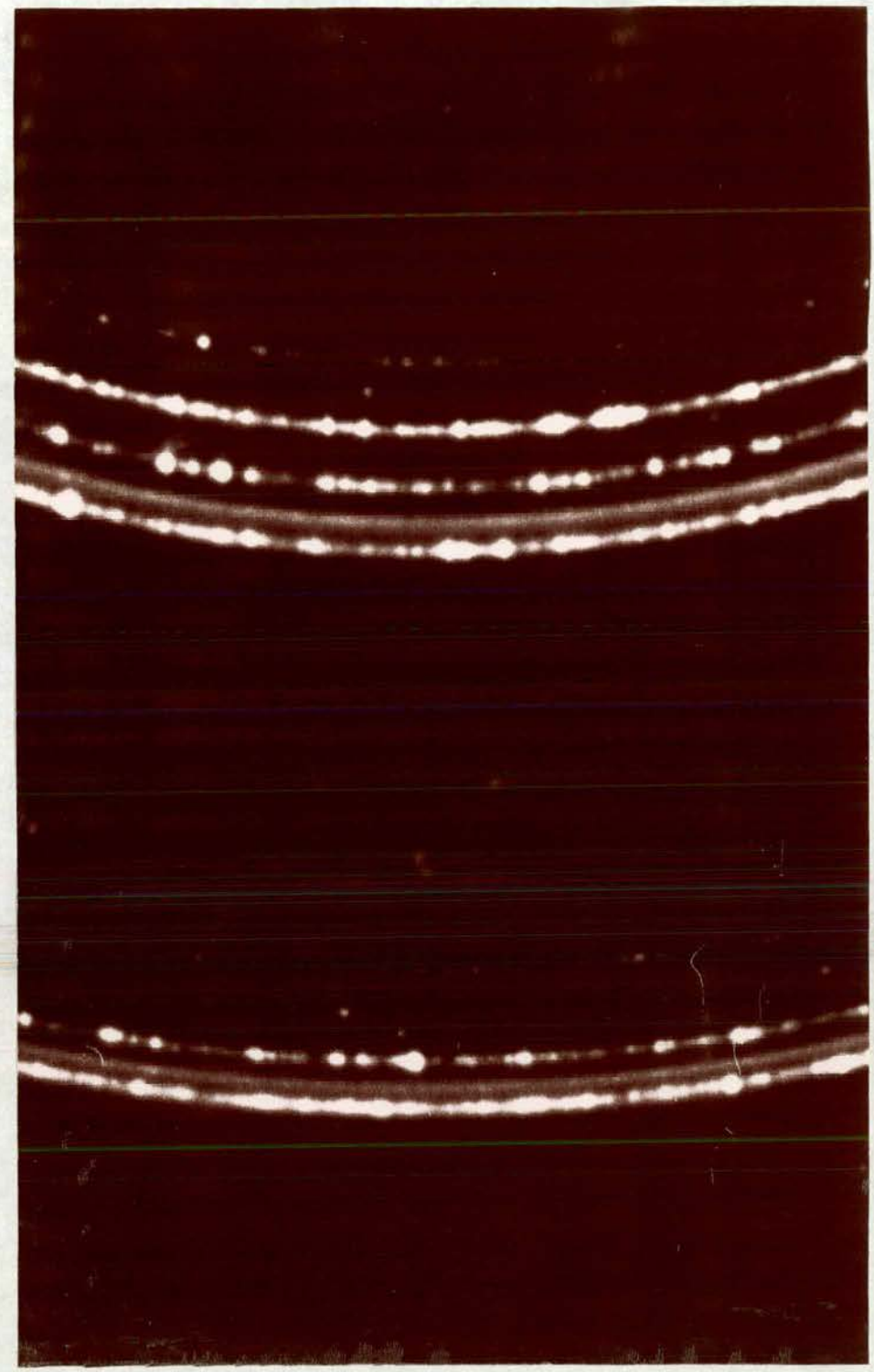

Figure 3.8: Part of the diffraction pattern obtained from InSb at approximately 3 GPa showing the distinct smooth and spotty nature of the different diffraction rings.

the pressure cell components to be easily identified. As can be seen from figure 3.9, the characteristic preferred-orientation of the metal gasket is very obvious in the low-angle powder-line and can, therefore, be excluded from Reitv eld refinement of the data or, as will be explained in the following section, can be removed from the powder pattern integration altogether.

3.3.3 Integration of the Image-Plate Data

In order to benefit from the improved powder averaging and the large gain in the signal-to-noise ratio that the integration around the Debye-Sherrer rings allow, it is important that the integration procedure is extremely accurate so that the peaks are not broadened and a systematic error is not introduced into the 2θ determination. Previous methods of integrating 2-dimensional area detector data have attempted to avoid these problems by determining the pattern centre, and any tilts of the detector relative to the beam, from the position of maximum intensity of each Debye-Sherrer ring on the detector surface before integration proceeds (Meade and Jeanloz (1990), Shimomura *et al* (1990)). However, the application of such methods to high-pressure powder-diffraction is quite difficult, due to the structured background generated by the DAC and the poor quality of the powder pattern. As an alternative, a more general integration algorithm has been developed for the Edinburgh-Daresbury IP system which refines the pattern centre and plate tilts as part of the integration process. Before the data can be integrated, an approximate position for the pattern centre is required and, in most cases, can be determined from the point on the IP surface illuminated by the fraction of the direct beam penetrating the beam-stop. The 2-dimensional image of the diffraction pattern is then partitioned into 160 sectors around this initial pattern centre and the pixels within each sector are rebinned in terms of the distance in pixels from the centre point, thus creating 160 conventional 1-dimensional powder patterns. By refining the diffraction pattern centre and the plate tilts, all 160 patterns can be aligned with respect to each other — a condition in which the sum of the sectors (the integrated pattern) is defined as being maximally sharp. From a knowledge of the sample-to-plate distance, determined using the method described above, the rebinned and sharpened powder pattern can then be calibrated in terms of 2θ.

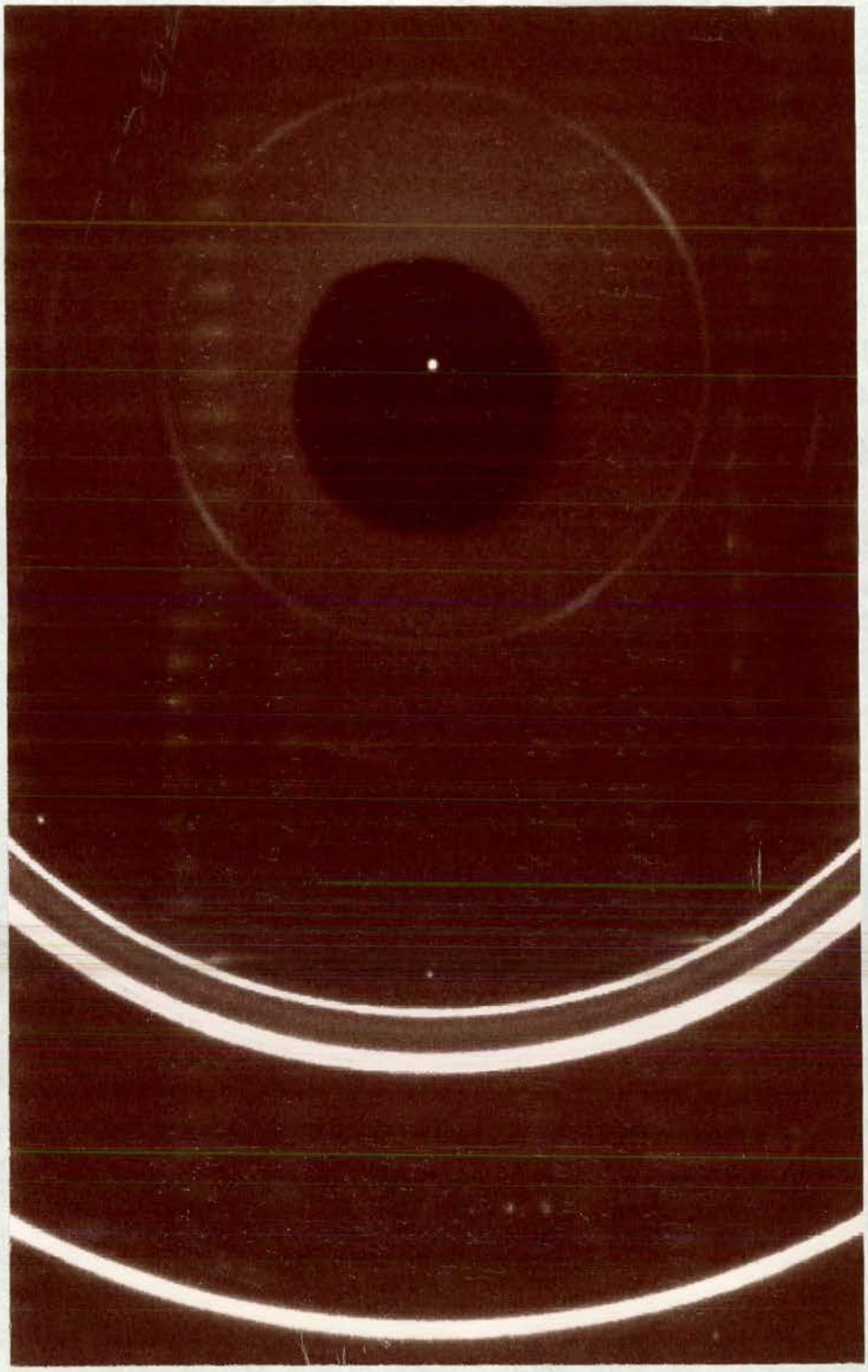

Figure 3.9: Part of the diffraction pattern of InSb at approximately 8 GPa showing the charactersitic preferred-orientation of the low-angle ($\frac{\lambda}{3}$) powder-line from the gasket.

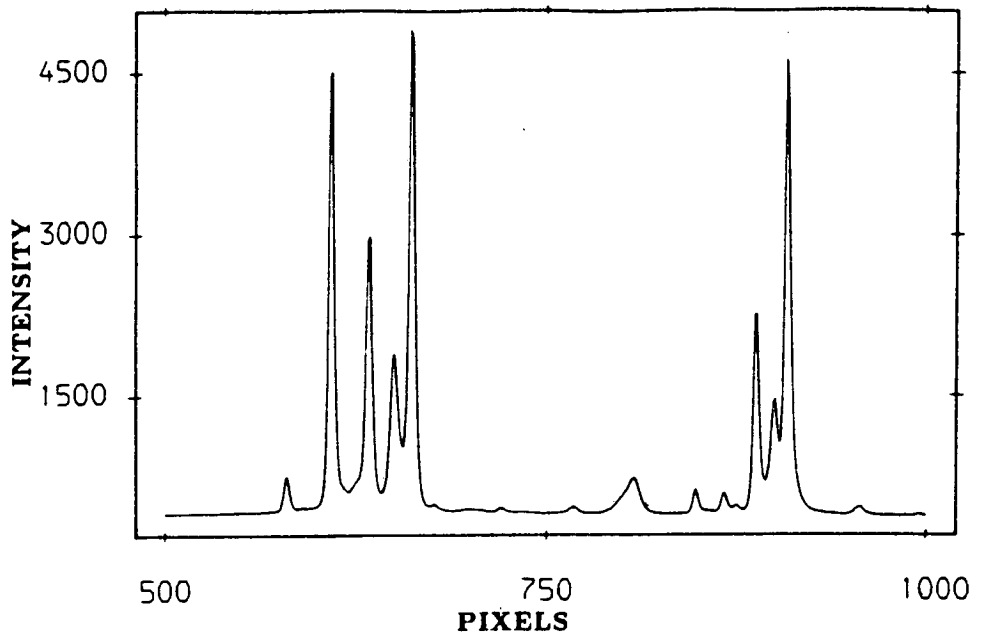

Figure 3.10: The fully integrated profile of the InSb pattern shown in figure 3.8 All distinction between the smooth and spotty phases is lost in the integrated profile.

This integration routine has been tested rigorously and has shown itself to be very robust, even when the starting values for the plate tilts and pattern centre are offset significantly from their true values (such as an error of $\pm 10°$ in the tilts and 50 pixels in the pattern centre). As can be seen from figure 3.10, which shows the integrated profile of the mixed-phase pattern of figure 3.8, the integration algorithm copes easily with the spotty nature of the pattern while the final integrated profile gives relative intensities that can be refined for both coexisting structures despite the very high intensity of some of the spots. It should be noted that it is no longer possible to distinguish between the spotty and smooth lines in the integrated profile and, as was described above, the assignment of powder lines to each of the phases would have been much more difficult without reference to the full 2-dimensional image.

One of the main advantages of the integration process is the significant improvement that can be obtained in the signal-to-noise ratio and in the signal itself. Indeed, it is these improvements that make the use of the angle-dispersive technique for high-pressure powder-diffraction, with its relatively low count rates, feasible at all. The improvement in the signal-to-noise ratio is illustrated in figure 3.11, which shows the effect on a section of a B_4C pattern when the integration range is

increased from a width of 200 pixels (the typical integration width available with a slot aperture cell), and then to a full integration over the entire image (a width of approximately 4500 pixels). A comparison of the integrated profiles with the simulation indicates that many of the weak B_4C powder lines are only visible when the full integration range is used. The use of a full conical aperture DAC ensures that the full Debye-Sherrer ring pattern can be intercepted and that the number of pixels included in the integration increases in proportion to 2θ (although for a large sample-to-plate distance this may not be the case as the rectangular shape of the plate will not cover the full range of the high-angle powder lines). This pronounced increase in the integration range, and the accompanying improvement in the signal-to-noise ratio, is in contrast to the use of a slot-aperture DAC where a smaller and smaller proportion of the diffraction rings can be integrated as 2θ increases.

Although the integration procedure effectively averages the intensity of any spurious diffraction features, such as λ and $\frac{\lambda}{3}$ diamond reflections, into the background, the potential of the image plate system for measuring extremely weak sample lines make it highly desirable that any residual intensity is removed from the integrated profile. To facilitate this, the integration software allows those pixels affected by contaminant diffraction to be removed from the image prior to integration. However, this procedure is less effective for extended features, such as contaminant powder lines from the gasket, as a relatively large number of pixels at the same 2θ will be affected and, due to the restricted integration range, a discontinuity will be produced in the background of the integrated profile. Since contamination from gasket powder lines has been found to be a common occurrence, a revised technique for aligning the DAC, and thus the sample, relative to the incident beam has been developed so that the gasket is no longer accidently illuminated.

3.3.4 A Revised Alignment Technique

Until fairly recently, the method developed at the Photon Factory has been employed on the Edinburgh-Daresbury IP system to align the sample in the beam. In this method, a high-power ($\times 40$ to $\times 80$) telescope, placed between the pressure cell and the image plate, is focused on the sample. The pressure cell is then

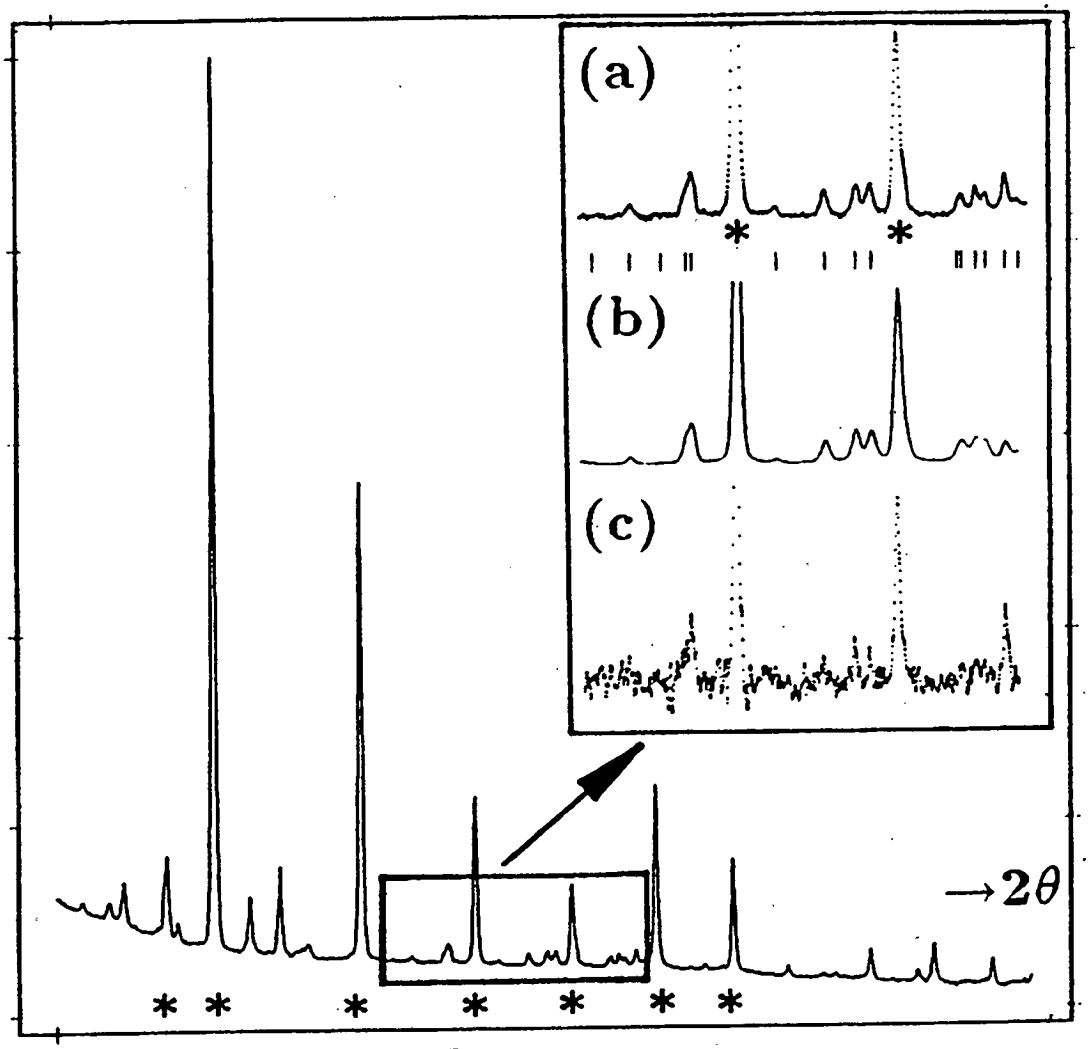

Figure 3.11: An integration of the image obtained from a mixture of a B_4C sample and an NaCl pressure calibrant (see section 6.2.2). The inset illustrates the improvement in the signal to noise ratio for the the mid-angle region of the pattern as the integration range is increased from (c) 200 pixels to (a) a full integration and the profile labelled (b) is from a calculation. The peaks labelled with a * are from the NaCl pressure calibrant.

replaced with an aluminium block holding a sheet of x-ray sensitive paper which is carefully positioned along the direction of the beam so that the surface of the paper is in focus when viewed through the telescope. After exposing the paper to the collimated beam for approximately one minute, the telescope is translated so that the graticule crosswires are accurately centered on the circular mark created by the beam. Without adjusting the telescope focus, the paper holder is then removed and replaced with the pressure cell which is translated manually (perpendicular to the beam) so that the sample appears to be centered on the crosswires of the telescope graticule.

Although the majority of powder patterns collected with this technique are free of spurious diffraction features from the pressure cell, an unacceptably large proportion of patterns have been found to be affected by contaminant gasket lines. As can be seen from figure 3.12, such features can often have intensities comparable to those of the strongest sample powder lines and can make analysis of the data extremely difficult, if not impossible. Since the incident beam is collimated to a diameter smaller than that of the gasket hole, the accidental illumination must be due to alignment errors of the sample with respect to the beam. There are two possible sources of such errors and both are related to observing the sample through a diamond window, which has a very high refractive index.

In the first, which is illustrated in figure 3.13, the optical axis of the telescope is aligned so that it is accurately perpendicular to the lower face (table) of the diamond anvil but is misaligned with respect to the incident beam. Under these circumstances, although the sample may appear to be placed so that its centre coincides with that of the circular mark on the paper, the true position of the sample is significantly further along the optic axis, due to the optical path through the diamond, and, since the optic axis of the telescope is not aligned with the x-ray beam, the centre of the beam will not pass through the centre of the sample. The sample displacement (d) along the optic axis of the telescope is given by

$$d = t(1 - \frac{1}{n_d}) \tag{3.5}$$

where t and n_d are the thickness and refractive index of the diamond respectively.

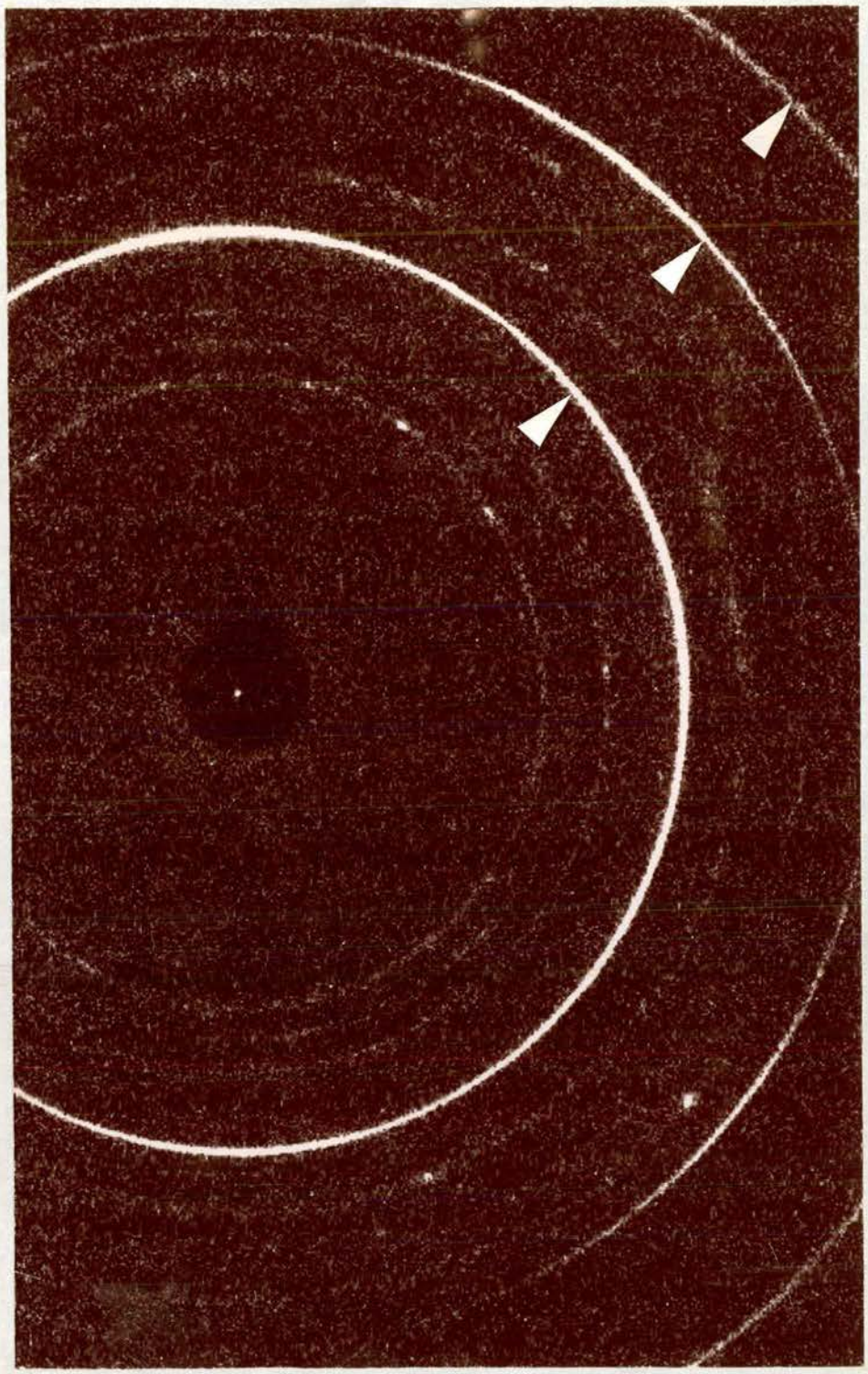

Figure 3.12: A portion of the diffraction pattern of Ge obtained at approximately 9 GPa with a wavelength of 0.4446(1)Å. The strong contaminant gasket lines have been indicated by the arrows.

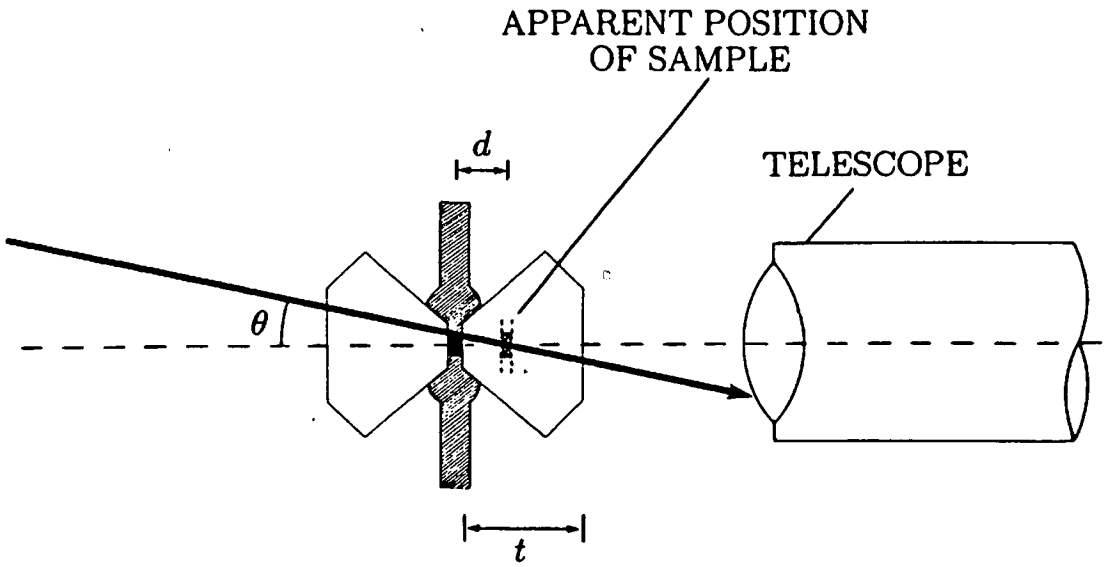

Figure 3.13: A schematic diagram illustrating how the incident beam can be made to accidentally strike the gasket when both the telescope and diamond anvils are misaligned with respect to the incident beam but are aligned with one another.

For a typical diamond thickness of 2 mm, with n_d=2.4, this displacement will be 1.2 mm. The shift of the sample in a direction perpendicular to the x-ray beam is simply $dsin\theta$ (where θ is the angle between the beam and the optic axis of the telescope) and, therefore, for a beam of 75 μm in diameter to pass cleanly through a 100 μm gasket hole the optic axis of the telescope must be aligned to within 0.57° with respect to the direct beam.

The second source of error, illustrated in figure 3.14, can occur when the optic axis of the telescope is parallel to the direct beam but is no longer perpendicular to the lower face of the diamond. In this situation the misalignment is due to the apparent shift δ of the sample, in a direction perpendicular to the optic axis of the telescope, given by

$$\delta = tsin\theta(1 - (\frac{1 - sin^2\theta}{n_d^2 - sin^2\theta})^{\frac{1}{2}}) \tag{3.6}$$

where θ is the angle between the diamond face normal and the optic axis of the telescope, and t and n_d are the thickness and refractive index of the diamond respectively. For $\theta \rightarrow 0$, and from equation 3.1, this can be simplified to

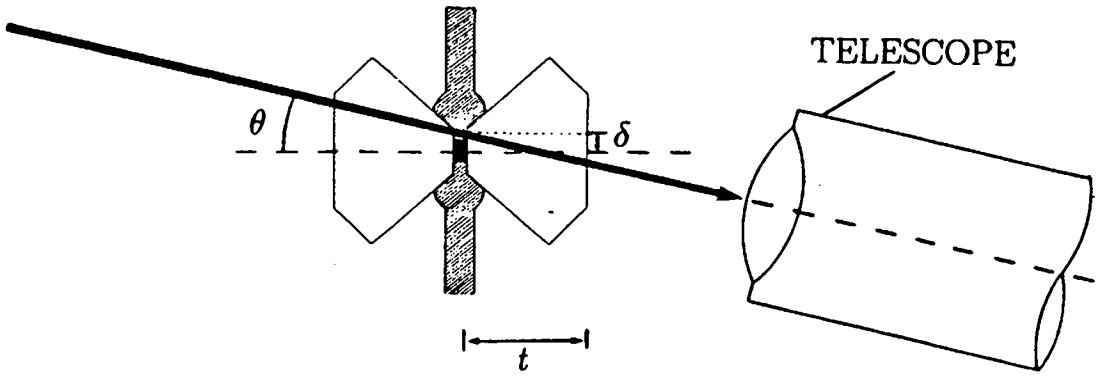

Figure 3.14: A schematic diagram illustrating how the incident beam can be made to accidentally strike the gasket when both the diamond anvils are misaligned with respect to the incident beam but the optic axis of the telescope is aligned parallel to the incident beam.

$$\delta = t\theta(1 - \frac{1}{n_d}) = \theta d \tag{3.7}$$

giving essentially the same result as that obtained for the first alignment error. Again, for a typical diamond thickness of 2 mm, and a typical gasket and beam diameters of 100 μm and 75 μm respectively, the normal to the face of the diamond must be aligned to within 0.01 radians, or 0.57 °, with respect to the optic axis of the telescope, so that the gasket is not illuminated.

For the beam line set up that has previously been used, illustrated in figure 3.7, there is no means of adjusting, or checking, the angular alignment of either the telescope or pressure cell with respect to the collimated x-ray beam, or with respect to each other, and, therefore, it is to be expected that the sample alignment errors will be due to a combination of the two effects described above. As the angular tolerances required for acceptable alignment are extremely small, even when their estimation has assumed some initial degree of angular alignment, it is extremely important that an accurate alignment procedure is developed.

In view of this, a relatively simple technique has been devised which allows the rapid alignment of both the pressure cell and telescope, between exposures, and is illustrated schematically in figure 3.15. The position of the x-ray beam is indicated by two lasers which direct highly collimated light both towards and away from the monochromator vessel. These lasers are aligned along the monochromated x-ray beam with the aid of two sheets of x-ray sensitive paper, spaced approximately 50cm apart along the optical bench, to define the position of the beam. Using the laser at the 'downstream' end of the optical bench, the pressure cell can be aligned to within approximately 0.04° to the laser beam (from estimates of the laser spot size at a distance of 1m between the laser and pressure cell) and, hence, with respect to the x-ray beam. The telescope is aligned in much the same manner by reflecting light from the 'upstream' laser off the objective lens , which defines the optic axis of the telescope (Hossack (1992)). Although the objective lens provides reasonably strong back-reflected light its curved surfaces result in the beam divergence being increased with an accompanying decrease in the alignment accuracy. To overcome this difficulty, a small mirror is used to replace the objective lens during the alignment procedure and has been found, in practice, to allow the same alignment accuracy for the telescope as that obtained for the pressure cell. The 'upstream' laser is extremely small (approximately 10mm in length) and can be placed between the monochromator vessel and the initial lead shield. Since its holder has a sliding shutter arrangement, the 'upstream' laser can be translated out of the x-ray beam during an exposure and subsequently repositioned to allow the telescope to be aligned for the next exposure. In this way, the laser can be mounted permanently, and non-obtrusively, on the optical bench. The 'downstream' laser is mounted behind the image plate holder and, therefore, does not interfere with exposures at any stage. This laser can, therefore, be used as a permanent reference to realign the upstream laser after successive exposures.

Although the revised alignment system has only recently been implemented, initial tests have indicated that powder patterns free from contaminant gasket lines can be readily obtained and that the collimated beam can be placed extremely accurately at the centre of the gasket hole.

In order to benefit from the ability to accurately align the pressure cell with respect to the incident beam, it is extremely important that the pressure cell can

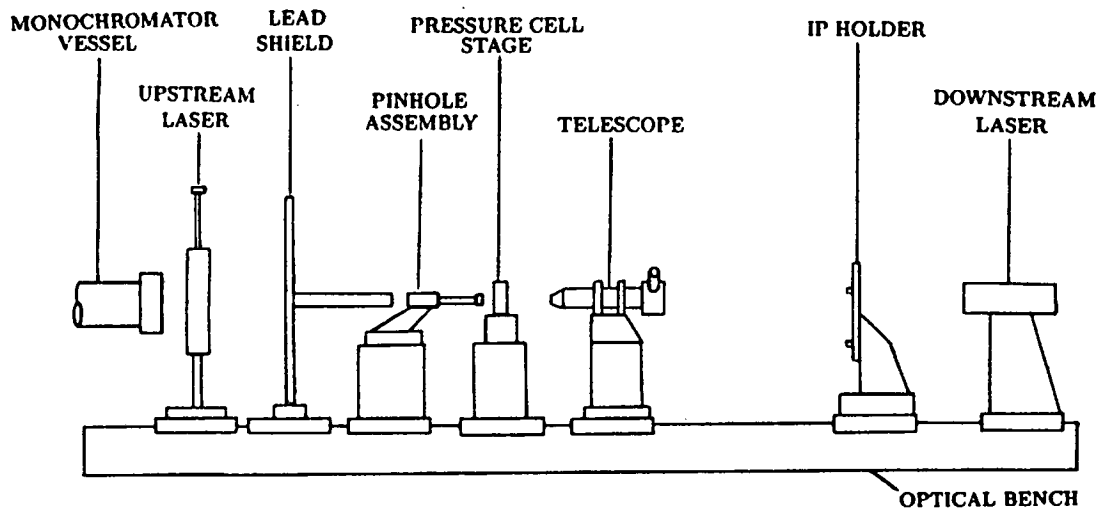

Figure 3.15: The revised beam line setup at the SRS. The role of each of the beam line components is described in the text.

be rotated so that the position of the sample both along and perpendicular to the beam is not altered. This is particularly important if an accurate sample to plate distance is to be maintained for a series of exposures on a sample at different pressures. It is also important to maintain the sample position if other contaminant features, such as diamond reflections, are to be removed from the powder patterns by rotating the diamond anvils out of the diffraction condition. As can be seen from figure 3.16, a diamond reflection from the anvil on the image plate side of the DAC can produce an extremely intense Bragg spot on the image and generate a series of accompanying powder lines as it passes through the beryllium backing plate. A diamond reflection, as was described in section 3.2.3 for single-crystal studies, can diffract as much as 50% of the incident beam (Loveday *et al* (1990)) and result in a corresponding loss of intensity from the powder pattern itself. Therefore, although the contaminant Bragg spot and beryllium powder lines produced by a diamond reflection on the monochromator side of the pressure cell will be absorbed in the gasket, the powder pattern will, nevertheless, still be affected and have poorer counting statistics than expected. If weakly scattering samples are being studied, such an effect will negate the use of lengthy exposures and waste limited beam-time.

Powder averaging will also be improved by rotating, or oscillating, the sample

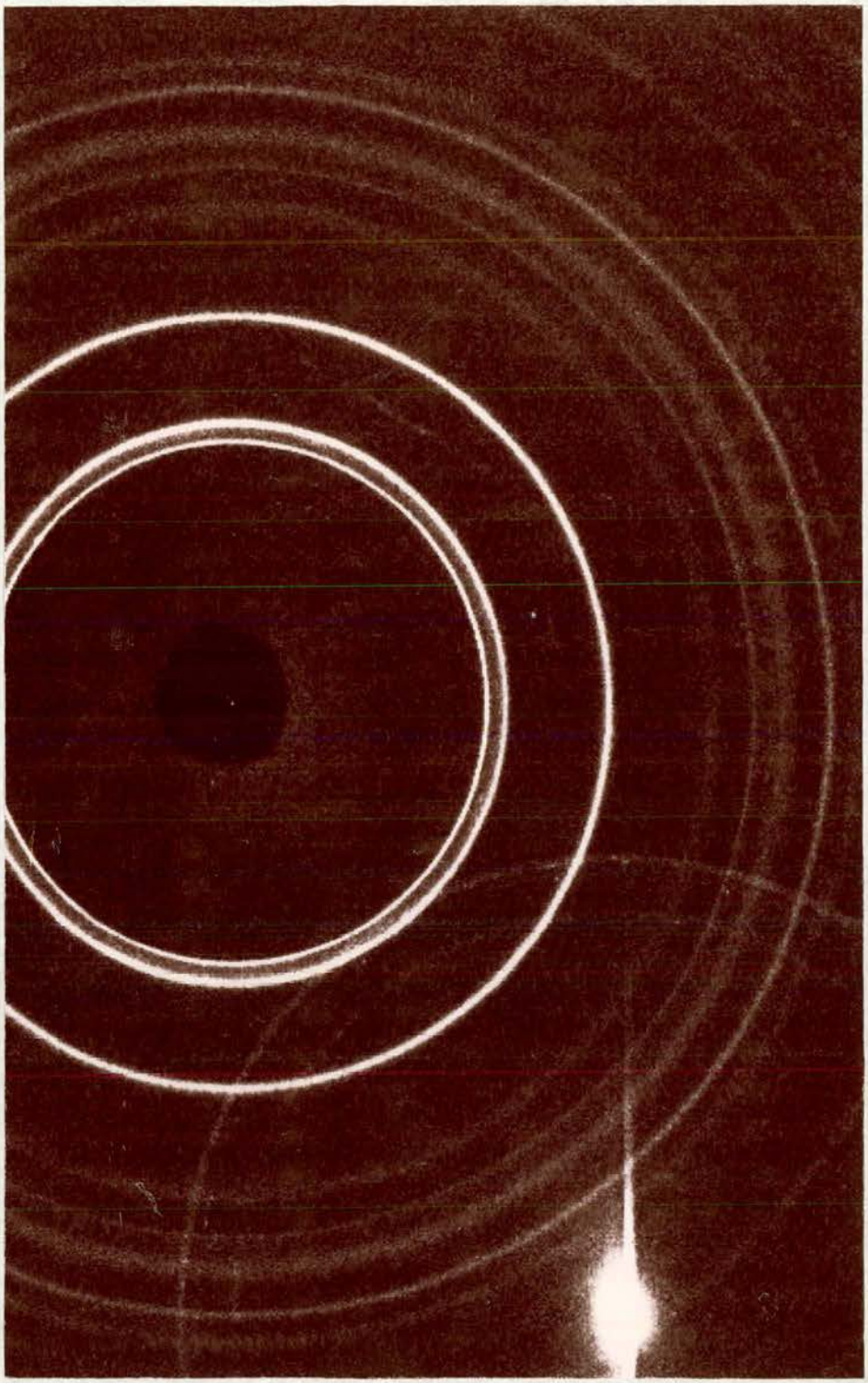

Figure 3.16: Part of the diffraction pattern of obtained from InSb at approximately 8 GPa showing a strong diamond spot with an accompanying series of beryllium powder lines.

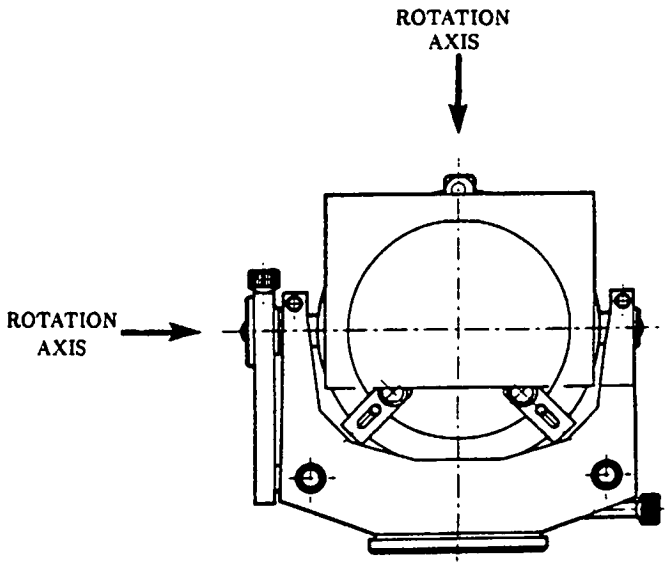

Figure 3.17: A cross-section of the proposed pressure cell mount which will allow the pressure cell to be tilted with respect to the incident beam.

during an exposure. If this is to be effective, however, the sample must not be translated by a significant amount over the oscillation range so that gasket illumination can be avoided. Therefore, in order to align the pressure cell with respect to the incident beam, avoid diamond reflections and to oscillate the sample to improve powder averaging, the pressure cell mount must be carefully designed. The mount currently being constructed for the Edinburgh-Daresbury IP system is shown in figure 3.17 and is expected to maintain the sample position within a sufficiently small tolerance to allow the oscillation of samples contained within a DAC without accidental gasket illumination.

Improvements such as those described above will allow the Edinburgh-Daresbury IP system, which has already proved itself to be an extremely sensitive and diagnostically powerful instrument (Nelmes *et al* (1992)), to collect powder patterns free from contaminant features and with a high degree of powder averaging for sample volumes considerably smaller than those used to date. Combined with the development of MDACs with conical apertures for the diffracted x-ray beams, the use of the imaging plate system for high-pressure powder diffraction may allow the determination of crystal structures, with the Rietveld refinement method, to pressures in the region of 1 Mbar. This challenging goal, although impossible to achieve just over a year ago, is now certainly within reach.

3.4 Neutron Powder-Diffraction

3.4.1 Introduction

Due to the large sample volumes required for crystal-structure determination using neutron powder-diffraction techniques, typically in the order of 10 to 100mm^3, the upper pressure limit for such studies has been restricted to around 2-3 GPa since the late 1960's. These large sample volumes, combined with the correspondingly large forces required to apply the pressure, have resulted in the construction of pressure cells with considerable mass offering only a limited angular access to the sample, for the incident and diffracted beams, with a relatively high and structured background. The use of time-of-flight techniques, with a fixed 90° diffraction geometry, is not hampered by the restricted angular access and has also allowed many of the background problems to be eliminated so that high-quality data can be collected. Although these techniques have been developed almost exclusively at the IPNS spallation source, Argonne, where successful structural studies have been performed for pressures of up to 2 GPa (see for example Jorgenson (1978)), the neutron flux at this, and other, pulsed neutron sources has been insufficient to allow work at higher pressures, which would require smaller sample volumes.

However, the very high flux available from the recently commissioned ISIS spallation neutron source, at the Rutherford Appleton Laboratory, would allow sample volumes to be reduced while still enabling high-quality powder patterns to be collected. With this and recent advances in anvil design and fabrication, a pressure cell designed specifically for neutron-diffraction with a 90° scattering geometry has been constructed, in association with the high-pressure group from the Universite Marie-Curie, Paris, with the aim of collecting powder diffraction data, suitable for full Reitveld refinement, at pressures in excess of 10 GPa. This has allowed accurate structural studies of materials containing light atoms, such as hydrogen, and the prospect of studying detailed thermal motion and magnetism, at pressures previously associated with x-ray diffraction studies in DACs. The details of the cell design and the work undertaken so far to reduce background and contaminant scatter are described in the following section.

3.4.2 The Paris-Edinburgh Cell

The layout of the Paris-Edinburgh cell is shown in figure 3.18a, with an enlarged view of the novel opposed-anvil geometry shown in figure 3.18b. The anvils are constructed from tungsten carbide or, for the highest pressures, sintered-diamond compacts and are machined to provide a spherical sample space with a typical diameter of 6mm. A toroidal groove is also machined around the sample space to provide lateral support for the gasket. Lateral support for the anvils themselves is provided by heat-treated maraging steel binding rings, where the anvils are pressed into the rings, on a 1.5° angle, to the maximum tensile strength of the steel. The tungsten-carbide anvil seats, which are also laterally supported by pre-stressed maraging steel binding rings, have central holes to provide ports for the incident neutron beam, and the anvils are partly hollowed out at the back to further reduce neutron absorption. The gaskets are formed from a composite of three concentric layers of metal. Soft beryllium-copper outer gaskets are machined to the correct cross section, then shaped by compression in the toroidal grooves, and subsequently heat treated to full hardness. The middle layer of gasket material is formed from pyrophyllite which is varied in thickness from 1 to 2mm depending on the required pressure. Finally, an inner ring of Ti-Zr null-matrix alloy surrounds the sample to prevent contaminant gasket lines being produced, as the gasket extrudes into the incident neutron beam, at the highest pressures. The gasket is sufficiently permeable to neutrons so that it forms a window for the diffracted neutron beams, which can be collected over a 12° angle in 2θ (90°±6°) since the faces of the anvil binding rings are suitably tapered.

The second element of the Paris-Edinburgh pressure cell setup is the 250MN (250 tonnes) press. As space is limited in the ISIS powder diffractometer hutches and the setup has to be removed, tilted, and otherwise manipulated in the loading and unloading operations, the press must be $\lesssim$ 40cm in all dimensions and not too massive to be handled by an average operator. Since standard presses of the same capacity have masses of over 1000kg and are extremely large pieces of equipment, a more suitable press, of dimensions 200×200×270mm and with a mass of only 50kg, has been purpose built. As can be seen from figure 3.18a, the press itself consists of two parts held together by four steel tie rods. The upper steel platen holds the breech which provides a flat resting surface for the upper

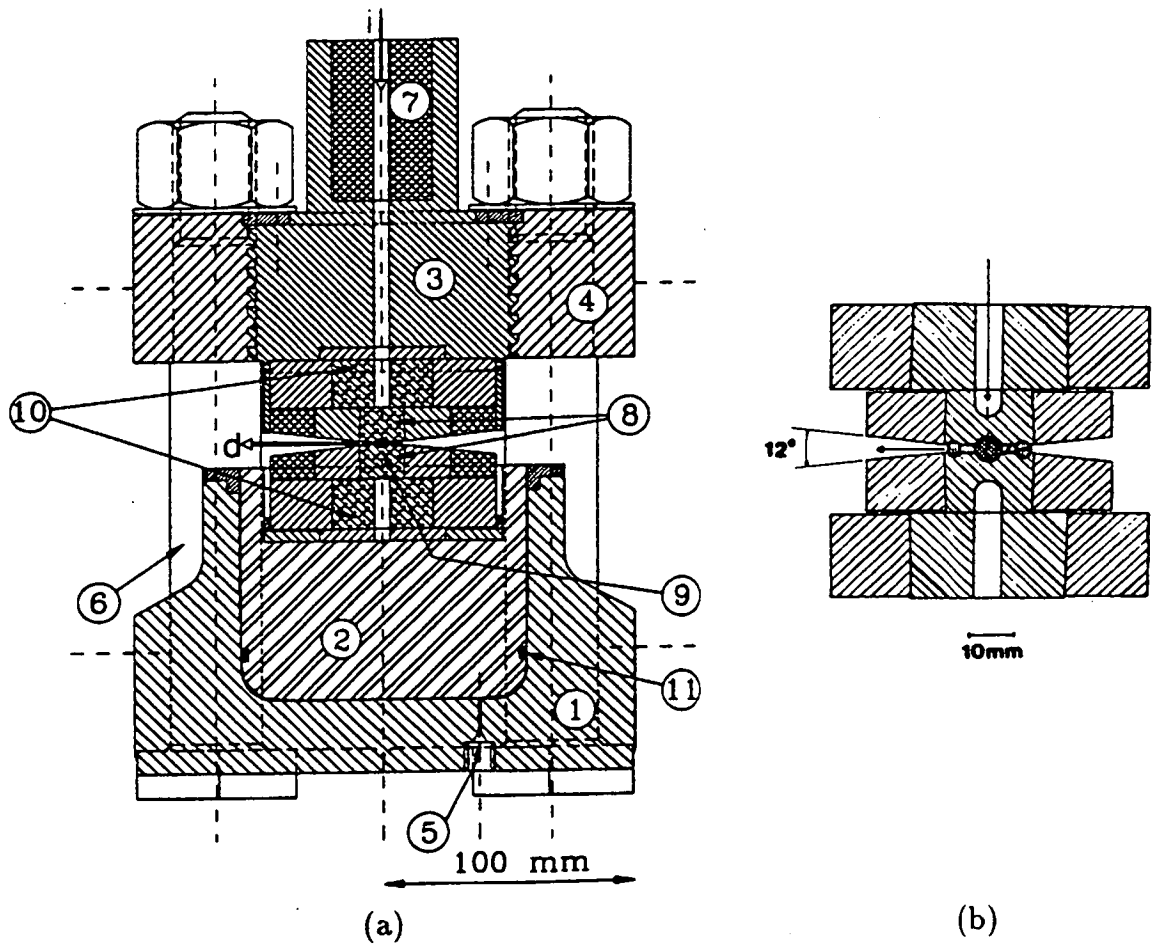

Figure 3.18: (a) — A cross section of the Paris-Edinburgh press and anvil assembly showing; the hydraulic ram cylinder (1), the ram piston (100 cm^2 in area) (2), the breech (3), the platen (4), the hydraulic fluid inlet (280 MPa) (5), the tie rods (6), the boron carbide collimator (7), the tungsten carbide anvils and their steel supporting rings (8), the sample volume (9), the tungsten carbide anvil seats (10) and the 'O' ring oil seal (11). The directions for the incident (i) and diffracted (d) beams are also shown. (b) — An enlarged cross section of the high pressure anvils and anvil seats showing the toroidal gasket.

tungsten carbide anvil seat. The breech is threaded into the upper steel platen to make it possible to assemble the sample, gasket and anvils without disassembling the tie rods. A hydraulic ram is contained within the lower half of the press and bears directly on the lower anvil. Its unusual shape has been calculated, by finite element analysis (Besson *et al* (1992)), to provide compensation for strains under applied load so that the oil chamber is leak tight to oil pressures exceeding the practical working limits of the press. The hydraulic oil pressure is provided by a small hand pump, rated to 280MPa, and allows *in situ* variation of the pressure.

To date, the press has been used almost entirely on the Polaris station of the ISIS facility, with a specially constructed jig holding the cell so that its axis lies in the horizontal plane. The whole assembly of mounting jig and pressure cell is designed to fit within the Polaris tank and give reproducible alignment with respect to the incident beam and the detectors between loadings.

In order to reduce the background and optimise the signal-to-noise ratio, a multi-stage approach to collimation has been used to eliminate the effects of scattering from the pressure cell materials immediately around the sample. Initially, the incident beam is reduced to the dimensions of $2\times1\text{cm}^2$ by a series of slits placed in the beam line. A B_4C collimator mounted directly onto the breech (see figure 3.18a) then reduces the beam to a circular cross section with a diameter of 4-6mm, depending on sample size and anvil configuration. Collimation of the diffracted beam is provided by coating the faces and sides of the anvil binding rings with neutron absorbing paint (Gd_2O_3-doped epoxy), which also shields the 90° bank of detectors from contaminant peaks produced by illuminated anvil material. Further collimation of the diffracted beam is provided by slits mounted on the side of the cell, and on the outside of the sample tank, to restrict the region viewed by the detectors to that immediately around the sample. To eliminate the background generated by multiple scattering of neutrons from the steel components of the pressure cell assembly, highly absorbing borated-polythene blocks are bolted to the sides of the cell mounting jig. Finally, the detector itself is shielded by B_4C sheets surrounded by borated-polythene blocks, forming a channel from the sample tank wall to the detector bank, to reduce the detected background from the environment of the Polaris hutch. The detector bank itself consists of an array of 20 ^{4}He tubes, each 2cm in diameter, at a distance of 2m from the sample, giving a resolution ($\frac{\Delta d}{d}$)

of about $7x10^{-3}$ (Besson *et al* (1992)). For samples of typical scattering powers and dimensions, an exposure time of approximately 4 to 6 hours is required to collect a pattern of sufficient quality for Rietveld refinement.

Although powder patterns can be collected that are relatively free from contaminant powder lines, the data must be corrected for wavelength-dependent absorption in the pressure cell components so that accurate structural studies can be performed. To measure this correction, powder patterns were collected from reference iron pellets (chosen as a readily available strongly scattering material) mounted both inside and outside the cell. From a comparison of the in-cell and out-of-cell patterns a set of empirical attenuation coefficients were determined, which have subsequently been shown, in conjunction with finite element calculations, to provide a suitable means of correcting raw powder-diffraction data for cell absorption (Nelmes *et al* (1991)). Since the attenuation of the gasket is likely to vary as it deforms under increasing pressure, a small laser arrangement has recently been mounted on the cell so that the separation of the anvils can be measured during an experiment. Although the system has yet to be fully calibrated, it is expected that a knowledge of the distance between the anvils will allow the deformation of the gasket, and hence the cell attenuation, to be more accurately modeled as a function of pressure. Nevertheless, with the existing techniques described above, the Paris-Edinburgh cell has been used, for example, to successfully determine the structural changes of ice VIII between the pressures of 2.5 and 12.5 GPa at a temperature of -5°C (Nelmes *et al* (1993)).

Very recently, a new 90° bank of detectors has been installed on the Polaris diffractometer to increase the angular coverage of the detectors encircling the sample — in the plane perpendicular to the incident beam — from an azimuthal angle of 20° (4° in 2θ) of the old detector bank to an azimuthal angle of around 132° (14° in 2θ). The increased area of coverage and the improved efficiency of the new detectors has produced a 16 fold increase in the detected signal (Loveday (1993)), providing an opportunity to decrease the sample volume, without a degradation of the powder pattern quality, so that higher pressures can be achieved. With this new development, it may be possible to obtain refinable powder patterns at pressures above the 23 GPa attained so far, and when combined with variable temperature, will provide unrivaled opportunities in high-pressure neutron powder-diffraction.

Chapter 4

A High-Pressure Structural Study of Potassium Titanyl Phosphate (KTP)

4.1 Introduction

Potassium titanyl phosphate, $KTiOPO_4$ (KTP), and its family of structural analogues form a unique class of non-linear optical materials. KTP is an extremely efficient second-harmonic generator (SHG) of Nd-YAG laser light (Bierlein and Vanherzeele (1989)) and is a particularly important material for many opto-electronic applications. At room temperature the structure of KTP assumes the acentric $Pna2_1$ space group with lattice parameters a=12.819(3)Å, b=6.399(1)Å, c=10.584(2)Å, V=868.1Å^3 (Thomas *et al* (1990)). The principal structural origin of this non-linear optical behaviour has been considered to be the anomalously short Ti-O bonds in the highly distorted TiO_6 octahedra (Tordjman *et al* (1974)), which form characteristic chains in the [0 1 1] and [0 $\bar{1}$ 1] directions, linked by alternately long and short Ti-O bonds (e.g. the chain A, B, C, D, E in figure 4.1). Several structural analogues of KTP have been reported where K is substituted by (for example) Rb or Tl (Masse and Grenier (1971)), P by As (El Brahimi and Durand (1986)) and more recently where Ti is substituted by (for example) Sn (Slobodyanik *et al* (1987)) or Fe (Phillips *et al* (1989)). All of these have been extensively reviewed (Stucky *et al* (1989)). The KTP structure exhibits a strong pseudosymmetry derived from the centric Pnan spacegroup and it has been reported that the isomorphous thallium analogue $TlTiOPO_4$ (TlTP) under-

goes a second-order transition into this Pnan symmetry at 923K (Harrison *et al* (1990)). In addition to this, a high-pressure Raman study of KTP, carried out by Kourouklis *et al* (1987), provides evidence of a phase transition at 5.5 GPa to an uncharacterised phase. This Raman study shows that there is an increase in the number of modes at the 5.5 GPa phase transition, which was taken to indicate a lowering of the crystal symmetry, or a multiplication of the unit cell, into an antiferroelectric phase. The mechanism of the transition is proposed to be polyhedral tilting in the TiO_6-PO_4 framework being driven by the softening Raman mode near $56cm^{-1}$. This mode, which has been associated with the potassium atoms (Pisarev *et al* (1990)), has a small discontinuity at the phase transition, indicating that the transition is first order in character. On release of pressure the original Raman spectrum appears with no change in the appearance of the sample. This indicates that although the transition is first order it is reversible. In contrast, Serhane *et al* (1991) have located a phase transition in TlTP at 6 GPa where the number of Raman modes *decreases* by about a factor of two. They postulate that TlTP adopts a centrosymmetric phase which is paraelectric and closely related to the high-temperature phase. It is clearly of considerable interest to determine what relationship these high-pressure phases have to the high-temperature phase, and whether the high-pressure phases of KTP and TlTP have different structures.

A high-pressure structural study of KTP was mentioned briefly towards the end of a review article by Stucky *et al* (1989) although it has not been reported in more detail elsewhere. No structural results are given except an angle change of 6.1° at 1 GPa for an unspecified P-O-Ti linking bond. In the absence of any other information regarding the pressure dependence of KTP the present investigation was undertaken to establish the major structural changes occurring as the phase transition at 5.5 GPa is approached, and to determine the structure of the high-pressure phase. The details of this high-pressure single-crystal x-ray diffraction study are presented in the following sections.

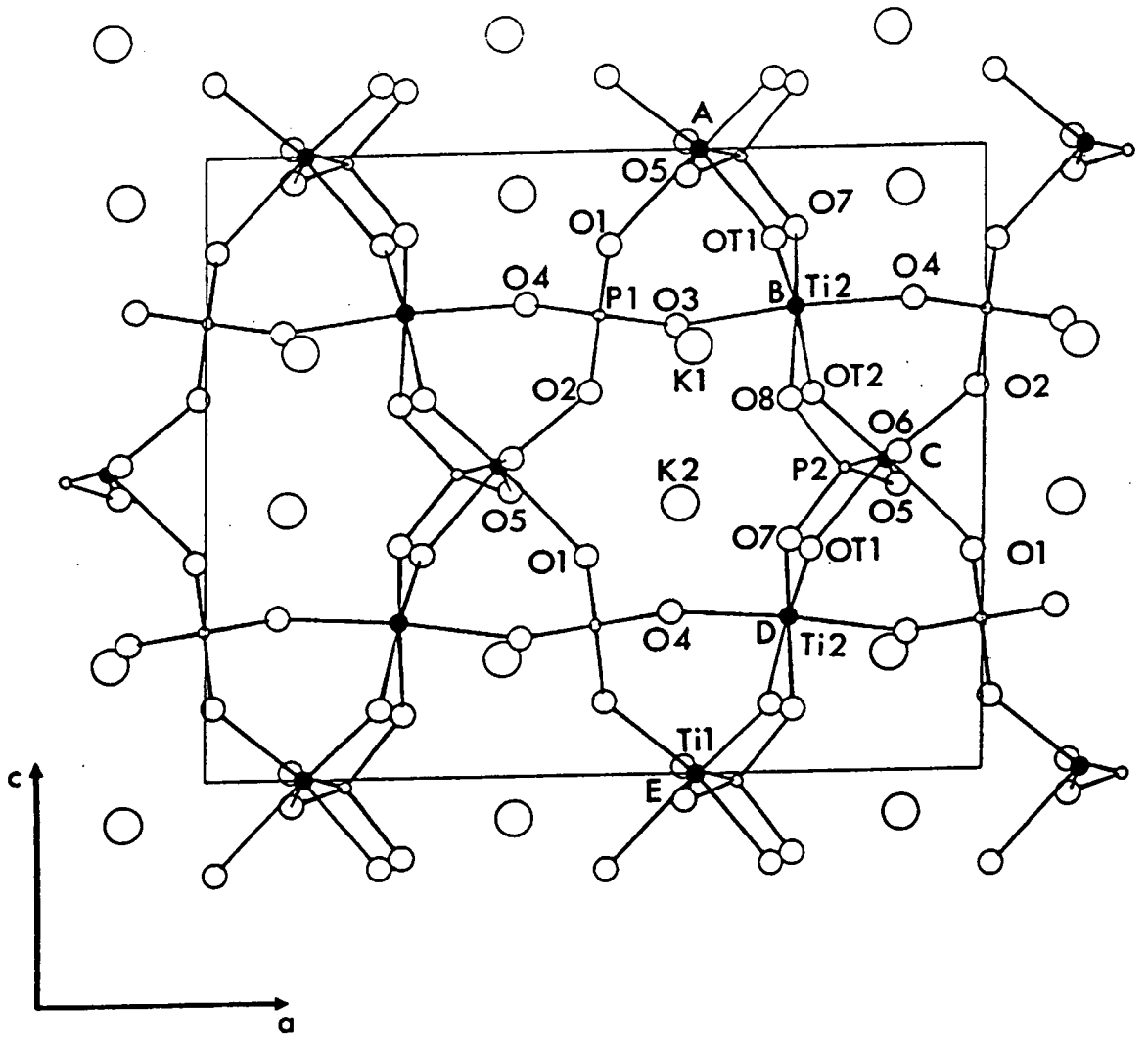

Figure 4.1: The structure of $KTiOPO_4$ viewed along the b-axis. The shaded circles represent the titanium atoms and the atoms labelled A, B, C, D, E are titanium atoms forming a chain linked by alternately long and short Ti-OT bonds.

4.2 The Pressure Dependence of the Structure as the Phase Transition is Approached

4.2.1 The Experiment and Data Analysis

A single crystal of flux-grown KTP was cut to the approximate dimensions of 100 $\times$ 100 $\times$ 100 μm^3, from a sample supplied by Dr P. A. Thomas of The University of Warwick, and the resulting fragment was mounted on the Physics Department's CAD4 four-circle diffractometer. The crystal quality was then checked and the crystallographic axes determined relative to the somewhat irregular crystal shape. To ensure that the crystal shape had been adequately characterised, for finite-element absorption correction, a series of ψ scans were performed on selected reflections. The absorption corrected intensities of these reflections were found to remain constant (to within 2σ) for each point measured around the scattering vector. The data were to be collected using a Merrill-Bassett diamond-anvil pressure cell (DAC) which limits the region of accessible reflections to that lying close to the reciprocal lattice plane parallel to the diamond-anvil faces (see section 2.3.1). Since the atoms of the KTP structure occupy general positions, such that their x-, y- and z-coordinates are not restricted by symmetry, it was not clear how the sample should be oriented within the DAC to reduce parameter correlations. Therefore, in order to determine the most satisfactory crystal orientation a series of trial refinements was performed on a previously collected three-dimensional ambient data set, taking the structural parameters of Thomas *et al* (1990) as starting values. Regions of inaccessible reflections were removed from the data to simulate the crystal mounted with either the a-, b- or c-axes perpendicular to the plane of the diamond anvil face. The refinements indicated that the lowest correlations between the positional parameters were observed for the a-axis setting and it was also found that the errors for the x-coordinates were not significantly higher than those for the y- and z-coordinates despite the a-axis being the direction of lowest resolution in the restricted data set. Therefore, it was decided to mount the crystal with its a-axis perpendicular to the diamond-anvil face.

The sample was secured to the face of one diamond-anvil, using petroleum jelly as

a glue, with chips of ruby placed beside it for pressure calibration. The DAC was then assembled with a tungsten gasket confining the sample and a 4:1 methanol-ethanol fluid (which had been dried with a molecular sieve) used to transmit the pressure. Initially the cell was taken to a relatively low pressure of 0.2 GPa (measured to ±0.05 GPa using the ruby fluorescence method) which is just sufficient to ensure the cell is firmly sealed and the crystal mounting secure. The DAC was mounted on the CAD4 and the sample carefully centered using the four-equivalent-settings procedure of King and Finger (1979) with graphite-monochromated Ag Kα x-rays. This wavelength was chosen due to the superior resolution and lower absorption it offers over Mo Kα (see section 3.2.2).

A low-pressure reference data set was then collected, measuring each reflection with the ω-scan method at the position of least attenuation by the pressure cell, according to the procedure of Finger and King (1978). The reflections were also measured at three positions over a narrow range around the scattering vector to detect and eliminate errors due to simultaneous diffraction by the diamond anvils (Loveday *et al.* (1990)), see section 3.2.3. Initially data were carefully collected in the region of $0° < \theta < 15°$ and, with a slightly increased scan speed, in the region of $15° < \theta < 30°$. At least two equivalents were present (±h,-k,±l) in both shells. Reflections for which either the incident or diffracted beam lay beyond 37° from the cylindrical symmetry axis of the cell were not collected, leaving a small safety margin on the limit (40°) imposed by the steel mounting of the beryllium discs (Merrill and Bassett (1974)). After applying a correction for the absorption of both the pressure cell and the sample (Finger and King (1978), Zucker *et al* (1983)), the data were averaged over repeated measurements and reflections affected by simultaneous diamond reflections removed from the data set. The data were then used for an initial least-squares refinement of the structure, including an extinction correction, using the Prometheus crystallographic programs (Zucker *et al.* (1983)). The structural parameters obtained by Thomas *et al* (1990) were taken as starting values. It became apparent that since many of the reflections were relatively weak, particularly for the second shell, it was very important that the most structurally sensitive of these weak reflections were identified and their intensities measured more accurately. This was achieved with the 'leverage' procedure (Prince and Nicholson (1985)), discussed in section 2.4.1, which uses the derivatives calculated by the least-squares program to identify reflections most

sensitive to the variable parameters of interest. The intensities of the 'leveraged' reflections were then remeasured with increased counting times, to improve their precision, and added to the data set. Structure factors were calculated for the remaining accessible reflections and for reflections whose intensities had not already been measured accurately. The strong and intermediate reflections predicted from these calculations were measured, as accurately as the 'leveraged' reflections, and added to the data set. All of the poorly determined reflections ($I < 3\sigma(I)$) present in the second shell were removed from the refinement. This had little effect on either the refined coordinates or on the magnitude of the errors. The resulting data set, which covers the whole range of accessible reflections (up to $\sin\theta/\lambda$=1.0 $Å^{-1}$), was then used for a final least-squares structural refinement. As for the initial refinement, all the reflections not rejected due to simultaneous diamond reflections were corrected for pressure cell and sample absorption and averaged over identical reflections. In order to assign weights correctly to the reflections in the data set, averaging over the equivalent reflections and leveraged reflections only occurred after the final structural refinement. In the least-squares refinement each reflection was assigned a weight $w=1/[\sigma^2(F_o)+f]$, where $\sigma(F_o)$ is the esd for the observed structure factor and f is an estimate of the irreducible uncertainties in the measurement of intensities (Lehmann (1975)) (taken in this case to be 3% of the observed intensity of each reflection). Averaging over the equivalent reflections after the refinement allowed the internal consistency of the data to be determined.

The positional parameters for all the atoms refined stably with no significant correlations between them. However, due to the rather limited data set, this was not found to be the case for the thermal parameters, and various constraints had to be applied. For all except the potassium atoms, only isotropic temperature factors were refined. This seems appropriate since the ambient structural study, carried out by Thomas *et al.* (1990), demonstrates that the potassiums are the only atoms exhibiting significantly anisotropic thermal motion: the other atoms, which form the TiO_6-PO_4 framework, have thermal motions which are almost isotropic. A further constraint was introduced by fixing the anisotropic thermal parameters directed along a (the direction of lowest resolution in the data) to their ambient values. With all these constraints applied, the refinement converged and gave physically reasonable thermal parameters for the K, Ti and P atoms.

However, the oxygen atoms were less well defined and additional constraints had to be applied to them. Since the oxygen atoms all have similar environments, their isotropic thermal parameters were all constrained to be the same, except for those involved in the short Ti-O bonds (labelled OT1 and OT2). The parameters for these two atoms were kept the same as each other, but allowed to differ from the other oxygens. In order to determine the effect of these further constraints, Hamilton's R-factor test (Hamilton (1974b)) was applied between refinements where the oxygen thermal parameters were refined freely and where they were constrained. The test revealed that the constraints changed the R-factor by less than the 90% confidence limit and are therefore not statistically significant for the data (Hamilton (1964)). The refined positional parameters were also found to agree to within 1.5σ or better, indicating that the constraints had not biased the refinement significantly. Physically reasonable values were obtained for all the thermal parameters although the errors were fairly large. The anisotropic thermal parameters for the potassium atoms agreed with the values of Thomas *et al* (1990) to within 20% while the isotropic thermal parameters for the other atoms agreed with Trodjman *et al* (1974) to within a factor of two. As a final check that the thermal-parameter constraints did not affect the positional parameters, a full data set, measured at ambient pressure, was refined with anisotropic thermal parameters for all the atoms. The results were compared with a second refinement where the above constraints had all been applied, and there were no significant differences between the positional parameters for the two refinements (all agreeing to within σ).

The purpose of the low-pressure reference data set was to determine to what extent (if at all) the restrictions imposed by the pressure cell bias the data, as well as establishing a reasonable data-collection strategy. Any bias in the data may result in some small offsets in the refined positional parameters from their ambient pressure values. The low-pressure reference data set therefore provides a secure starting point from which any changes in the structure can be determined from data measured at higher pressures.

Data were collected for pressures of 2.2, 3.7 and 4.7 GPa following the strategy already outlined for the 0.2 GPa reference data and at each pressure, including 0.2 GPa, (i) the unit-cell dimensions were determined accurately by the four-

equivalent-settings-procedure of King and Finger (1979) which corrects for any sample miscentring (see section 2.4.4.), and (ii) the pressure was remeasured after the data collection to ensure it had remained constant. Again the data were corrected for pressure-cell and crystal absorption and averaged over identical reflections. As already explained, averaging over equivalent reflections was carried out after the final refinements and allowed the internal consistency of each data set to be determined.

4.2.2 Results and discussion

Table 4.1 presents the refined atomic coordinates, the measured unit-cell dimensions and unit-cell volume, the number of independent reflections, the number of refined parameters, the weighted R-factor and the goodness-of-fit. The results of the atmospheric study conducted by Thomas *et al.* (1990) are also given for comparison. All the R-factors for the high-pressure data are similar and the refined scale factors (not given) show only a small monotonic variation in the sequence in which the data were collected. The bond lengths of the K cages, Ti octahedra and P tetrahedra derived from these refinements are given in table 4.2.

The unit-cell volume is plotted as a function of pressure in figure 4.2. A Murnaghan fit to the values, using the Volfit program (Ida (1985)), gives a bulk modulus B_0=58±8 GPa with a curvature of B'=15±4. The unit-cell volume decreases by 2.8(1)% at 2.2 GPa, comparable with that of the anorthite feldspar ($CaAl_2Si_2O_8$) which exhibits a decrease of 2.8(1)% at 2.5 GPa (Angel (1988)). Anorthite has similar structural properties to those of KTP and will be described in more detail later.

From table 4.1 it is clear that the K2 atom exhibits a shift under pressure while the K1 atom remains relatively stationary. To illustrate this, their fractional coordinates are plotted as a function of pressure in figure 4.3. The potassium atoms occupy cavities, or cages, in the TiO_6-PO_4 framework and are loosely held in the structure. The movement of the K2 atom suggests that its cage exhibits a significant pressure dependence. This pressure dependence will manifest itself as a relative movement in the TiO_6-PO_4 framework and, upon examination of

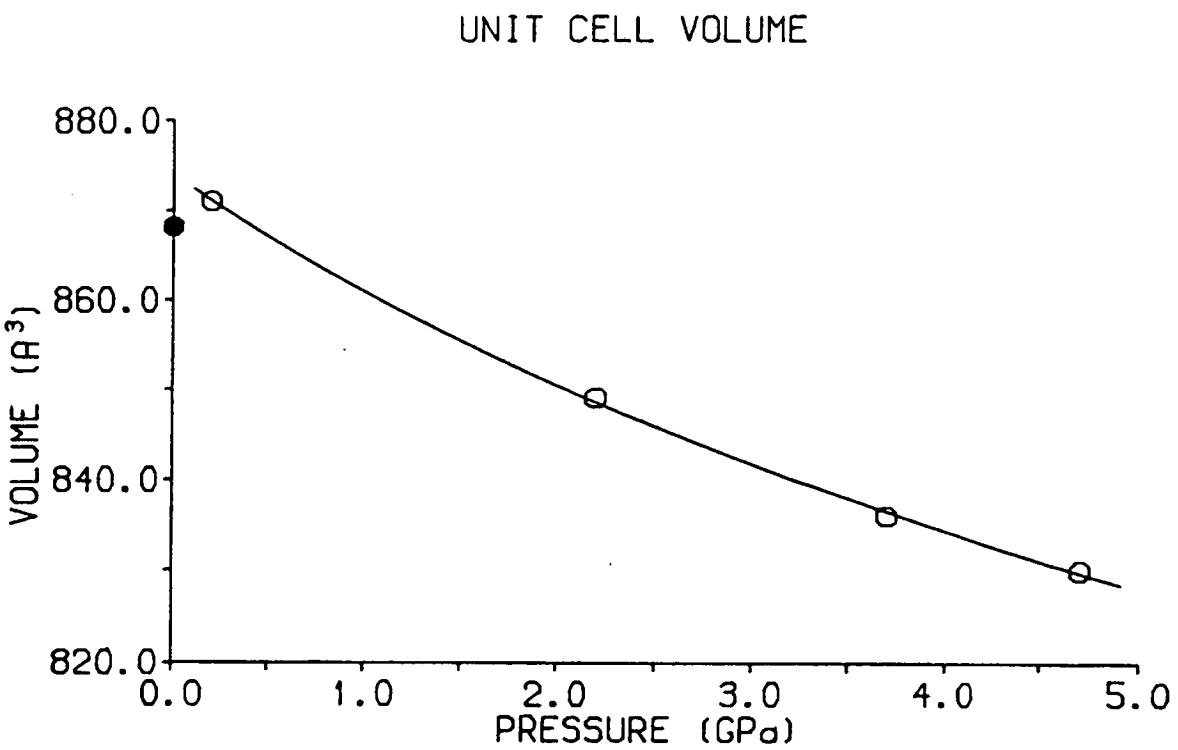

Figure 4.2: The unit-cell volume of $KTiOPO_4$ as a function of pressure. The atmospheric-pressure value shown as ●, is calculated from the unit-cell dimensions of Thomas *et al* (1990). Note that the errors are smaller than the symbols shown. The line is fitted to the high-pressure points using a Murnaghan function.

table 4.1, it is evident that the P1, P2 and O3 atoms undergo clear shifts. To illustrate the shifts, the fractional coordinate changes for the P1 and O3 atoms are also shown in figure 4.4 (note that P2 has a shift of similar magnitude to that of P1 and is not shown in the figure). The small but significant offset of the O3 y-coordinate at 0.2 GPa from the atmospheric-pressure value illustrates the need for the low-pressure reference data set in determining trends in the structure.

		AP	0.2 GPa	2.2 GPa	3.7 GPa	4.7 GPa
	a(Å)	12.819(3)	12.832(7)	12.705(7)	12.639(7)	12.620(8)
	b(Å)	6.399(1)	6.412(3)	6.363(2)	6.331(2)	6.315(4)
	c(Å)	10.584(2)	10.586(4)	10.505(4)	10.447(4)	10.417(5)
	V(Å^3)	868.1(4)	871(1)	849(1)	836(1)	830(1)
K1	x	0.37807(8)	0.3795(5)	0.3813(5)	0.3815(5)	0.3818(4)
	y	0.7806(1)	0.7799(5)	0.7796(5)	0.7807(5)	0.7819(5)
	z	0.6880(1)	0.6867(4)	0.6860(4)	0.6855(4)	0.6853(5)
K2	x	0.10526(7)	0.1049(6)	0.1049(6)	0.1045(5)	0.1046(4)
	y	0.6990(1)	0.6989(5)	0.6946(5)	0.6921(4)	0.6911(5)
	z	0.9332(1)	0.9331(6)	0.9325(5)	0.9332(5)	0.9320(6)
Ti1	x	0.37290(4)	0.3737(4)	0.3728(3)	0.3733(3)	0.3743(3)
	y	0.5001(1)	0.5013(5)	0.5004(4)	0.5013(4)	0.5006(4)
	z	-0.00040(8)	-0.0004	-0.0004	-0.0004	-0.0004
Ti2	x	0.24658(6)	0.2450(6)	0.2450(5)	0.2467(5)	0.2461(4)
	y	0.2695(5)	0.2697(4)	0.2690(4)	0.2686(3)	0.2685(3)
	z	0.74836(9)	0.7483(5)	0.7480(5)	0.7484(5)	0.7486(6)
P1	x	0.49808(8)	0.4986(8)	0.4981(8)	0.4980(7)	0.4970(6)
	y	0.3363(1)	0.3360(4)	0.3338(4)	0.3318(4)	0.3318(4)
	z	0.7397(1)	0.7409(6)	0.7419(6)	0.7409(5)	0.7404(6)
P2	x	0.18079(7)	0.1822(6)	0.1815(6)	0.1805(5)	0.1797(5)
	y	0.5020(1)	0.5000(9)	0.5003(7)	0.5029(8)	0.5024(6)
	z	0.4872(1)	0.4882(6)	0.4874(5)	0.4882(5)	0.4891(6)
O1	x	0.4859(2)	0.4852(14)	0.4873(12)	0.4868(13)	0.4890(12)
	y	0.4867(5)	0.4894(12)	0.4863(12)	0.4873(12)	0.4857(13)
	z	0.8497(2)	0.8478(9)	0.8522(8)	0.8500(9)	0.8481(11)

		AP	0.2 GPa	2.2 GPa	3.7 GPa	4.7 GPa
O2	x	0.5103(2)	0.5142(17)	0.5087(13)	0.5094(14)	0.5100(10)
	y	0.4657(5)	0.4616(12)	0.4604(12)	0.4583(13)	0.4600(13)
	z	0.6170(2)	0.6168(8)	0.6146(8)	0.6162(8)	0.6174(11)
O3	x	0.4004(2)	0.4009(12)	0.4023(12)	0.4009(12)	0.4004(9)
	y	0.1986(4)	0.2037(13)	0.1981(14)	0.1920(14)	0.1897(13)
	z	0.7208(2)	0.7192(10)	0.7234(9)	0.7226(10)	0.7272(13)
O4	x	0.5934(2)	0.5908(15)	0.5929(14)	0.5918(14)	0.5917(11)
	y	0.1930(4)	0.1888(13)	0.1851(13)	0.1836(13)	0.1840(14)
	z	0.7589(2)	0.7572(9)	0.7590(9)	0.7583(10)	0.7574(11)
OT1	x	0.2248(2)	0.2226(14)	0.2233(14)	0.2273(13)	0.2274(12)
	y	0.9653(4)	0.9694(16)	0.9714(15)	0.9737(14)	0.9703(15)
	z	0.3561(2)	0.3537(10)	0.3537(9)	0.3354(9)	0.3566(11)
OT2	x	0.2232(2)	0.2195(17)	0.2205(14)	0.2218(14)	0.2219(12)
	y	0.0413(5)	0.0423(18)	0.0388(17)	0.0428(15)	0.0407(15)
	z	0.6097(2)	0.6088(12)	0.6097(11)	0.6119(10)	0.6126(11)
O5	x	0.1126(2)	0.1118(14)	0.1089(14)	0.1126(11)	0.1094(10)
	y	0.3106(4)	0.3162(13)	0.3141(12)	0.3177(12)	0.3143(12)
	z	0.4585(2)	0.4560(10)	0.4545(9)	0.4574(10)	0.4594(15)
O6	x	0.1113(2)	0.1119(15)	0.1120(15)	0.1087(15)	0.1083(13)
	y	0.6918(4)	0.6938(13)	0.6904(12)	0.6961(12)	0.6937(13)
	z	0.5117(3)	0.5129(11)	0.5127(9)	0.5124(10)	0.5126(12)

		AP	0.2 GPa	2.2 GPa	3.7 GPa	4.7 GPa
O7	x	0.2525(2)	0.2506(17)	0.2551(17)	0.2575(15)	0.2560(13)
	y	0.5402(5)	0.5420(16)	0.5415(15)	0.5364(15)	0.5419(15)
	z	0.3718(2)	0.3713(10)	0.3720(9)	0.3734(10)	0.3747(11)
O8	x	0.2528(2)	0.2522(14)	0.2560(11)	0.2542(12)	0.2536(12)
	y	0.4619(5)	0.4598(16)	0.4598(14)	0.4602(15)	0.4602(16)
	z	0.6008(2)	0.6014(12)	0.6003(10)	0.6015(11)	0.6006(12)
	N_i	2158	490	491	496	417
	N_r	145	65	65	65	65
	R_w	0.024	0.044	0.042	0.047	0.051
	Gf	-	1.38	1.33	1.44	1.80

Table 4.1: Unit-cell dimensions (Å), unit-cell volume (Å^3) and refined atomic fractional coordinates of $KTiOPO_4$ as a function of pressure. The number of independent reflections (N_i), the number of refined parameters (N_r), the weighted R-factor (R_w) and the goodness-of-fit (Gf) are also given. The estimated standard deviations (esd's) for each of the values are given in parentheses. Note that the Prometheus refinement program requires that one atom be fixed along the polar axis. The Ti1 z-coordinate was chosen to be fixed, and so no esd is quoted for it. The ambient pressure (AP) values were calculated from the refined atomic fractional coordinates of Thomas *et al* (1990).

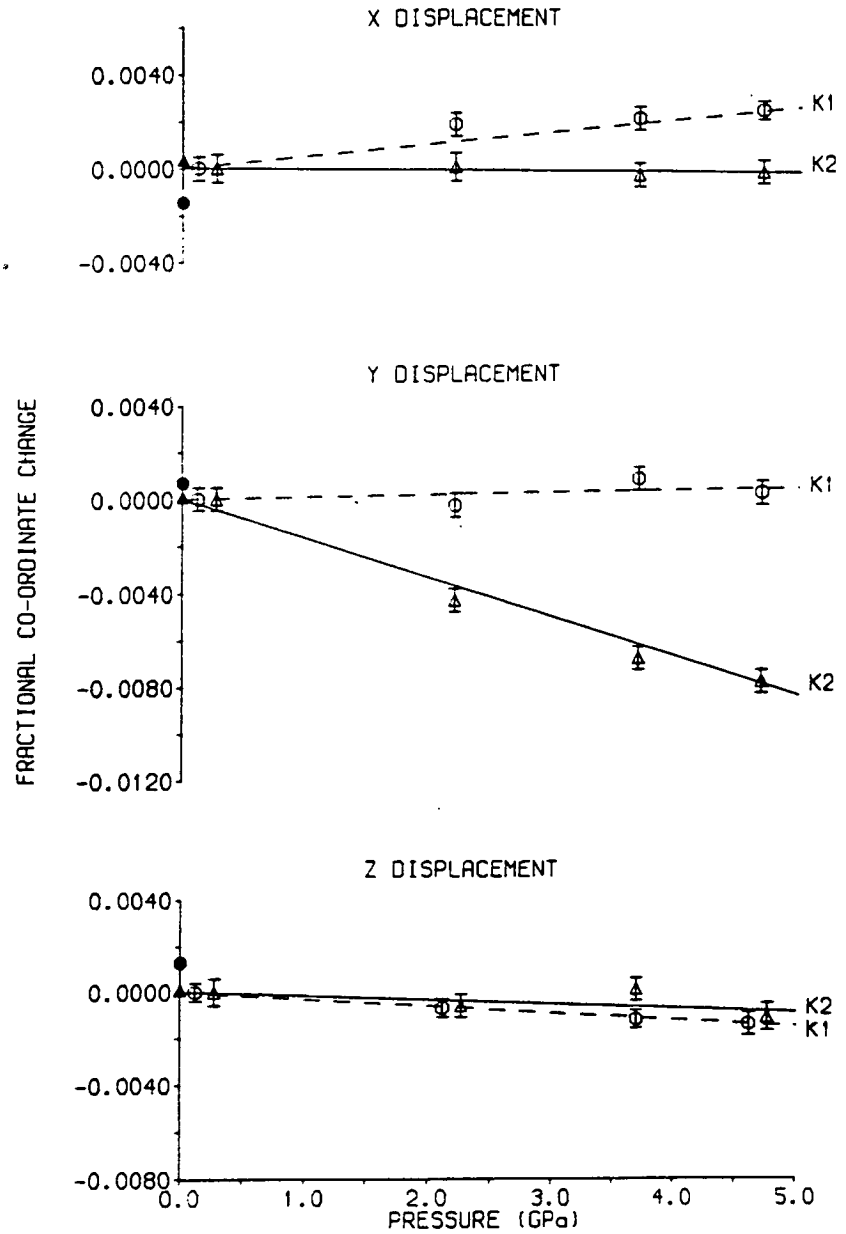

Figure 4.3: Fractional coordinate changes for the K1 (○) and K2 (△) atoms in $KTiOPO_4$ relative to the 0.2 GPa values. The ambient-pressure values, shown as and ▲, are from Thomas *et al* (1990). Note that some of the points have been translated slightly along the pressure axis to avoid overlap. The dashed and solid lines represent the movements of the K1 and K2 atoms, respectively, and are a guide to the eye only.

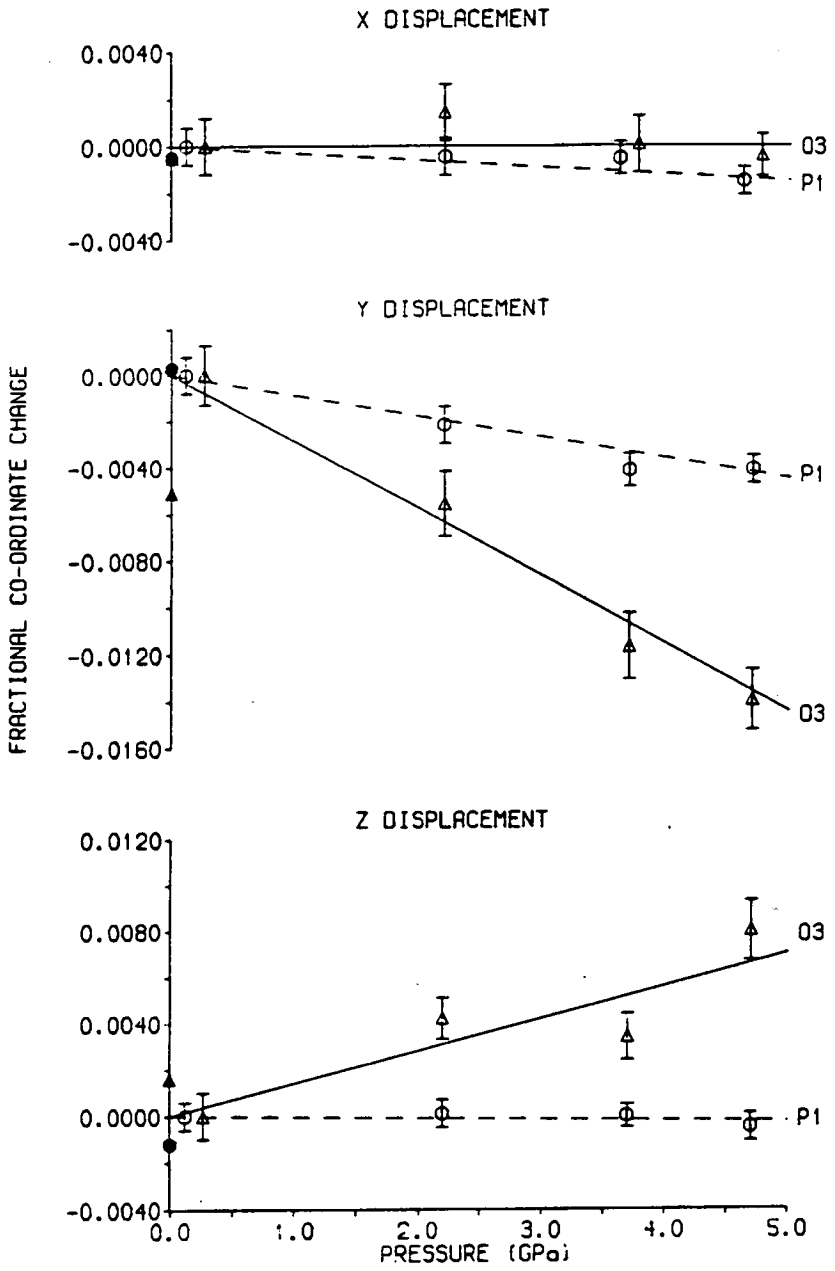

Figure 4.4: Fractional coordinate changes for the P1 (○) and O3 (△) atoms in $KTiOPO_4$ relative to the 0.2 GPa values. The ambient-pressure values, shown as and ▲, are from Thomas *et al* (1990). Note that some of the points have been translated slightly along the pressure axis to avoid overlap. The dashed and solid lines represent the movements of the P1 and O3 atoms, respectively, and are a guide to the eye only.

	AP	0.2 GPa	2.2 GPa	3.7 GPa	4.7 GPa
$K(1)O_8$					
K1-O1	2.894(4)	2.867(12)	2.889(11)	2.859(11)	2.865(12)
K1-O2	2.738(4)	2.775(16)	2.703(13)	2.702(14)	2.693(12)
K1-O3	2.712(3)	2.753(10)	2.705(10)	2.644(10)	2.622(10)
K1-O5	2.872(3)	2.862(10)	2.832(9)	2.851(10)	2.864(15)
K1-O7	3.057(3)	3.071(14)	3.099(15)	3.092(12)	3.100(13)
K1-O8	2.755(4)	2.774(15)	2.736(11)	2.734(13)	2.743(13)
K1-OT1	2.995(3)	2.967(12)	2.953(12)	2.969(11)	2.992(12)
K1-OT2	2.722(4)	2.780(19)	2.745(16)	2.724(16)	2.705(13)
$K(2)O_9$					
K2-O1	2.677(3)	2.677(12)	2.658(12)	2.663(15)	2.656(11)
K2-O2	2.982(3)	2.991(14)	2.933(11)	2.927(12)	2.950(12)
K2-O3	3.045(3)	3.029(11)	3.057(10)	3.024(11)	3.075(12)
K2-O4	3.117(3)	3.112(9)	3.031(8)	3.003(9)	2.991(10)
K2-O5	2.806(3)	2.793(19)	2.727(18)	2.757(16)	2.717(14)
K2-O7	2.918(4)	2.951(15)	2.905(14)	2.861(14)	2.891(13)
K2-O8	3.048(4)	3.055(16)	3.013(14)	3.027(14)	3.028(14)
K2-OT1	2.765(4)	2.789(15)	2.733(15)	2.663(15)	2.656(15)
K2-OT2	3.057(4)	3.089(22)	3.062(17)	3.033(17)	3.039(15)
$Ti(1)O_6$					
Ti1-O1	2.150(3)	2.153(13)	2.126(12)	2.123(13)	2.144(14)
Ti1-O2	1.958(3)	1.915(17)	1.946(14)	1.936(15)	1.923(13)
Ti1-O5	2.042(3)	2.079(8)	2.065(8)	2.058(8)	2.035(9)
Ti1-O6	1.987(3)	1.985(8)	1.986(8)	1.950(8)	1.956(9)
Ti1-OT1	1.981(3)	1.988(14)	1.968(13)	1.978(13)	1.975(13)
Ti1-OT2	1.716(3)	1.684(17)	1.675(13)	1.700(13)	1.710(13)

	AP	0.2 GPa	2.2 GPa	3.7 GPa	4.7 GPa
$Ti(2)O_6$					
Ti2-O3	2.044(3)	2.067(15)	2.065(16)	2.026(15)	2.022(11)
Ti2-O4	1.981(3)	1.999(16)	1.958(17)	1.983(17)	1.974(13)
Ti2-O7	1.965(3)	1.957(11)	1.948(10)	1.967(10)	1.942(10)
Ti2-O8	1.990(3)	1.978(11)	1.975(10)	1.958(10)	1.963(11)
Ti2-OT1	1.733(3)	1.749(12)	1.748(10)	1.745(10)	1.732(11)
Ti2-OT2	2.092(3)	2.101(12)	2.086(11)	2.043(11)	2.042(11)
$P(1)O_4$					
P1-O1	1.519(3)	1.509(10)	1.517(9)	1.513(9)	1.489(12)
P1-O2	1.548(3)	1.554(9)	1.567(9)	1.537(9)	1.525(12)
P1-O3	1.544(3)	1.531(15)	1.505(15)	1.525(14)	1.520(12)
P1-O4	1.541(3)	1.523(17)	1.542(18)	1.523(17)	1.527(13)
$P(2)O_4$					
P2-O5	1.535(3)	1.523(15)	1.540(14)	1.488(13)	1.515(10)
P2-O6	1.528(3)	1.557(14)	1.521(15)	1.544(15)	1.526(12)
P2-O7	1.548(3)	1.541(15)	1.553(16)	1.559(14)	1.553(14)
P2-O8	1.537(3)	1.520(13)	1.539(12)	1.530(13)	1.513(13)

Table 4.2: The bond lengths (Å) of the K cages, Ti octahedra and P tetrahedra in $KTiOPO_4$ as a function of pressure. The ambient pressure (AP) values were calculated from the refined atomic fractional coordinates of Thomas *et al* (1990).

In order to determine the relative compressibilities of the K cages, the PO_4 tetrahedra and the TiO_6 octahedra, their volumes were calculated for all four pressures by dividing each unit into constituent irregular tetrahedra. The PO_4 tetrahedra and TiO_6 octahedra require one and four such tetrahedra respectively, with an oxygen atom at each vertex. For the K cage sites the constituent tetrahedra were determined by placing a K atom at one vertex and neighbouring oxygen atoms at the remaining three vertices. Describing the volume of the cage sites in this way requires twelve and fourteen such tetrahedra for the $K(1)O_8$ and $K(2)_9$ cages respectively. The volume of each of the irregular tetrahedra can be readily calculated from the appropriate bond lengths and bond angles and then summed to yield the volume of each structural unit. As can be seen from table 4.3, all the units show a decrease in volume under pressure, although their relative volume changes are quite different: the K cages have a 5.7±1% reduction in volume at 4.7 GPa, while the Ti octahedra and P tetrahedra have 2.8±2% and 2.4±2% reductions respectively. Therefore, it seems that the large potassium cage sites are readily compressible and absorb a significant fraction of the overall 4.7±0.2% reduction in the unit-cell volume at 4.7 GPa. The average volume change of the K cage sites is plotted in figure 4.5 along with the change in the unit-cell volume. It is evident from figure 4.5 that the curvature of the pressure-volume relationship is significantly greater for the K cages than for the unit-cell.

From figure 4.1, which presents the structure of KTP projected along the b-axis, it is evident that the environments for the K1 and K2 atoms are quite different. The $K(2)O_9$ cage forms a channel, parallel to the b-axis, which runs through the entire crystal structure and along which the K2 atom may be expected to move relatively freely; and it is seen from figure 4.3 that the only significant movement of the K2 atom with increasing pressure is along the b-axis (i.e. along the channel). On the other hand, the K1 atom is constrained from a similar motion by the confinement of the $P(1)O_4$-$Ti(2)O_6$ chain which restricts movement of the K1 atom along the b-axis (see figure 4.1). It is interesting to note that although the K1 cage forms a channel which runs parallel to the a-axis, the K1 atom does not show a significant movement along the a-axis with increasing pressure. The apparent difference in behaviour may be partly due to the greater restriction offered by the K1 cage environment, which has a volume 25% smaller than that of the K2 cage. There is also a significant difference in compressibilty in the average K-O bond lengths

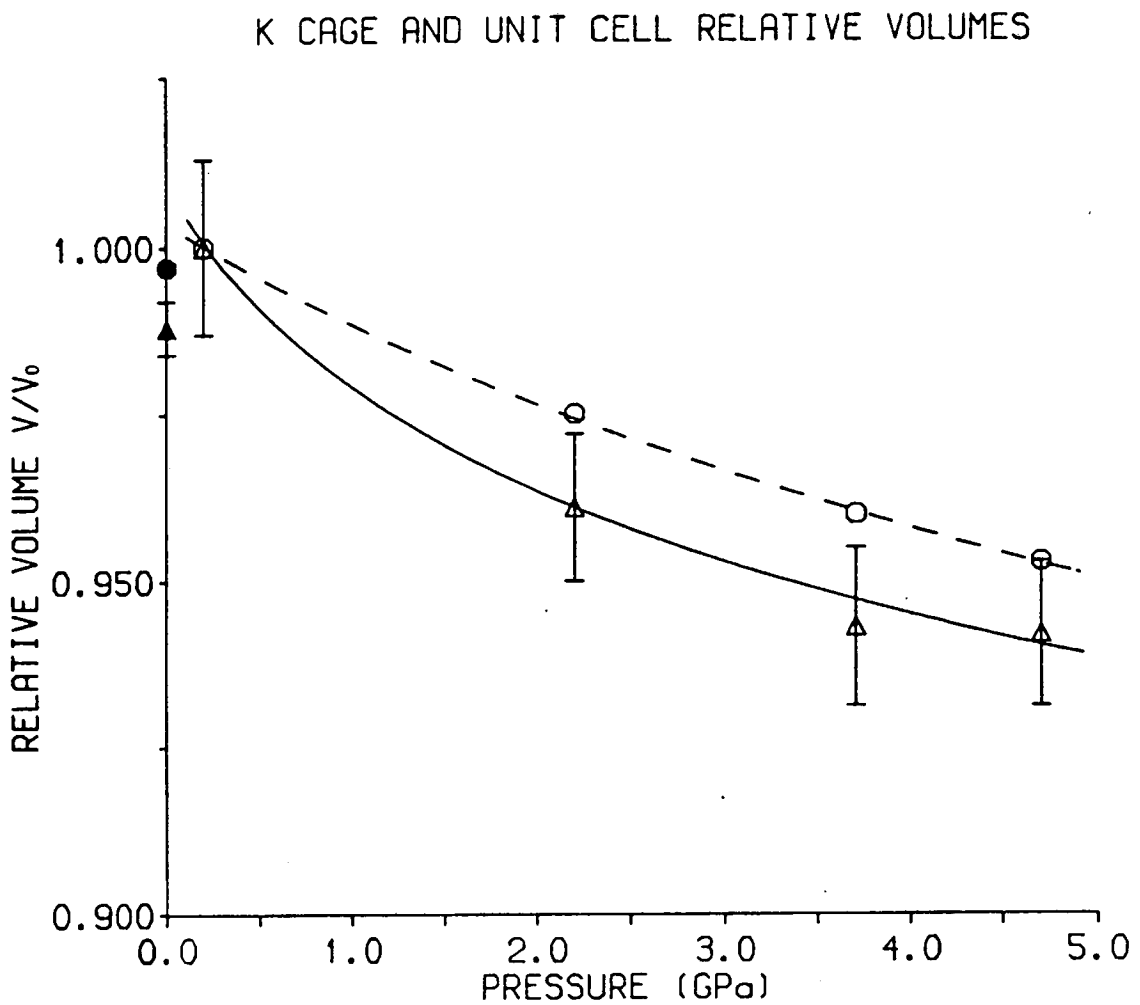

Figure 4.5: The relative volumes (V/V_o) of the unit-cell volume (○) and K cages (△) (the K1 and K2 cages averaged) in $KTiOPO_4$ as a function of pressure, referred to the value V_o at 0.2 GPa. The ambient-pressure values, shown as and ▲, are calculated from the unit-cell dimensions and the fractional coordinates of Thomas *et al* (1990). Note that where error bars are not shown the errors are smaller than the circular symbols. The dashed and solid lines are from Murnaghan fits to the relative volumes of the unit cell and the K cages respectively.

	AP	0.2 GPa	2.2 GPa	3.7 GPa	4.7 GPa
TiO_6 octahedra					
average bond length (Å)	1.970(3)	1.971(13)	1.962(12)	1.956(12)	1.952(12)
volume (Å^3)	10.08(5)	10.08(18)	9.94(17)	9.86(17)	9.80(16)
PO_4 tetrahedra					
average bond length (Å)	1.537(3)	1.532(13)	1.534(13)	1.527(13)	1.521(12)
volume (Å^3)	1.86(1)	1.84(5)	1.86(5)	1.83(5)	1.80(4)
K1 cage					
average bond length (Å)	2.843(4)	2.856(14)	2.833(12)	2.822(12)	2.823(12)
volume (Å^3)	26.15(6)	26.46(36)	25.72(33)	25.14(34)	25.00(31)
K2 cage					
average bond length (Å)	2.934(3)	2.943(15)	2.902(13)	2.884(14)	2.889(13)
volume (Å^3)	34.71(7)	35.12(45)	33.46(45)	32.91(45)	33.03(45)

Table 4.3: The pressure dependence of the average M-O bond lengths (Å) in the TiO_6 octahedra, PO_4 tetrahedra and K cages of $KTiOPO_4$ and of the volumes (Å^3) of these structural units. The definition of the volumes is discussed in the text. The ambient pressure (AP) values were calculated from the refined atomic fractional coordinates of Thomas *et al* (1990).

which reduce by 1.2±0.3% and 1.8±0.2% for the K1 and K2 cages respectively.

As the $P(1)O_4$-$Ti(2)_6$ chain deforms under pressure, the motion of the O3 atom, combined with that of the P1 atom, results in a reduction of the P1-O3-Ti2 bond angle by approximately 3° between 0.2 and 4.7 GPa (see table 4.4). This bond links the chain of alternate $P(1)O_4$ tetrahedra and $Ti(1)O_6$ octahedra which is directed along the a-axis (see figure 4.1). The most significant TiO_6-PO_4 linking angle change, however, is in the P2-O7-Ti2 bond which reduces by approximately

	AP	0.2 GPa	2.2 GPa	3.7 GPa	4.7 GPa
PO_4-TiO_8 linking angles					
P1-O3-Ti2	129.6(2)	131.0(7)	129.8(7)	128.2(7)	128.1(5)
P2-O7-Ti2	130.3(2)	132.9(9)	130.3(9)	126.6(9)	128.9(9)
P1-O4-Ti2	134.8(2)	132.9(7)	132.3(7)	131.9(7)	132.4(6)
P2-O6-Ti1	135.9(2)	136.6(9)	136.1(9)	134.8(9)	134.8(9)
Ti1-OT2-Ti2	133.4(2)	134.6(9)	133.6(8)	134.3(8)	133.5(7)

Table 4.4: Selected P-O-Ti and Ti-OT-Ti bond angles (°) in $KTiOPO_4$ as a function of pressure. The ambient pressure (AP) values were calculated from the refined atomic fractional coordinates of Thomas *et al* (1990).

5° over the same pressure range (see table 4.4). (This is less than 20% of the angular change of 6.1° at 1 Gpa reported by Stucky *et al* (1989) for an unspecified P-O-Ti bond.) All the other P-O-Ti bonds have angular changes of approximately 2° or less, as do the Ti-OT-Ti bonds which link the titanium octahedra (the P1-O4-Ti2, P2-O6-Ti1 and Ti1-OT2-Ti2 linking bonds are given as examples in table 4.4).

The overall distortion of the $Ti(1)O_6$ and $Ti(2)O_6$ octahedra appears to be retained up to 4.7 GPa in as much as the general pattern of long and short Ti-O bond lengths remains the same (as can be seen from table 4.2) and the O-Ti-O bonds, within the octahedra, have angular changes of only 2° or less. The anomalously short Ti-OT bonds within the highly distorted TiO_6 octahedra have been considered to be linked to the non-linear optical properties of KTP and are consequently of great interest(Tordjman *et al* (1974)). From table 4.2 it is evident

that the Ti1-OT2 and Ti2-OT2 bond lengths both undergo systematic changes under pressure. The longer of the two, Ti2-OT2, clearly reduces in length while the shorter one, Ti1-OT2, appears to increase slightly, as shown in figure 4.6. (In the case of Ti1-OT2 there is a significant offset between the values obtained at ambient pressure and 0.2 GPa. The trend in this bond length is taken relative to the 0.2 GPa reference point.) These changes reduce the difference between the Ti1-OT2 and the Ti2-OT2 bond lengths by around 20%, but the Ti1-OT1 and the Ti2-OT1 bonds appear to retain their bond length difference; it would now be of interest to find out whether there is any accompanying variation in the second-harmonic generating (SHG) properties as a function of pressure. From table 4.2, it is also evident that the relatively long Ti1-O5 and Ti2-O3 bonds undergo significant shortening under pressure (relative to the 0.2 GPa values). As indicated above, however, the shortening of these bonds does not significantly reduce the overall distortions of the TiO_6 octahedra.

The orientation of the Ti-O bonds, as well as the variation of their bond lengths is also considered to be important for the non-linear optical properties of the KTP structure (Thomas *et al* (1990), Hansen *et al* (1988), Sastry (1991)). In the calculation of the geometrical contribution of the structure to the non-linear tensor coefficients, the orientations of the bonds participate through products of their direction cosines. Briefly summarized, a tensor component of the second-order susceptibility is given by

$$d_{ijk} = \sum_{b}^{cell} g_{ijk}^{b} p^{b} / V \tag{4.8}$$

where V is the volume of the unit cell, p^b is the longitudinal bond polarizability of the bth bond (with the transverse component set to zero) and the g_{ijk}^b term for a bond is given by

$$g_{ijk}^{b} = cos(\nu_i) cos(\nu_j) cos(\nu_k) \tag{4.9}$$

where the direction cosines are calculated with respect to the crystallographic axis. For the KTP structure there is a strong inherent asymmetry in the summation

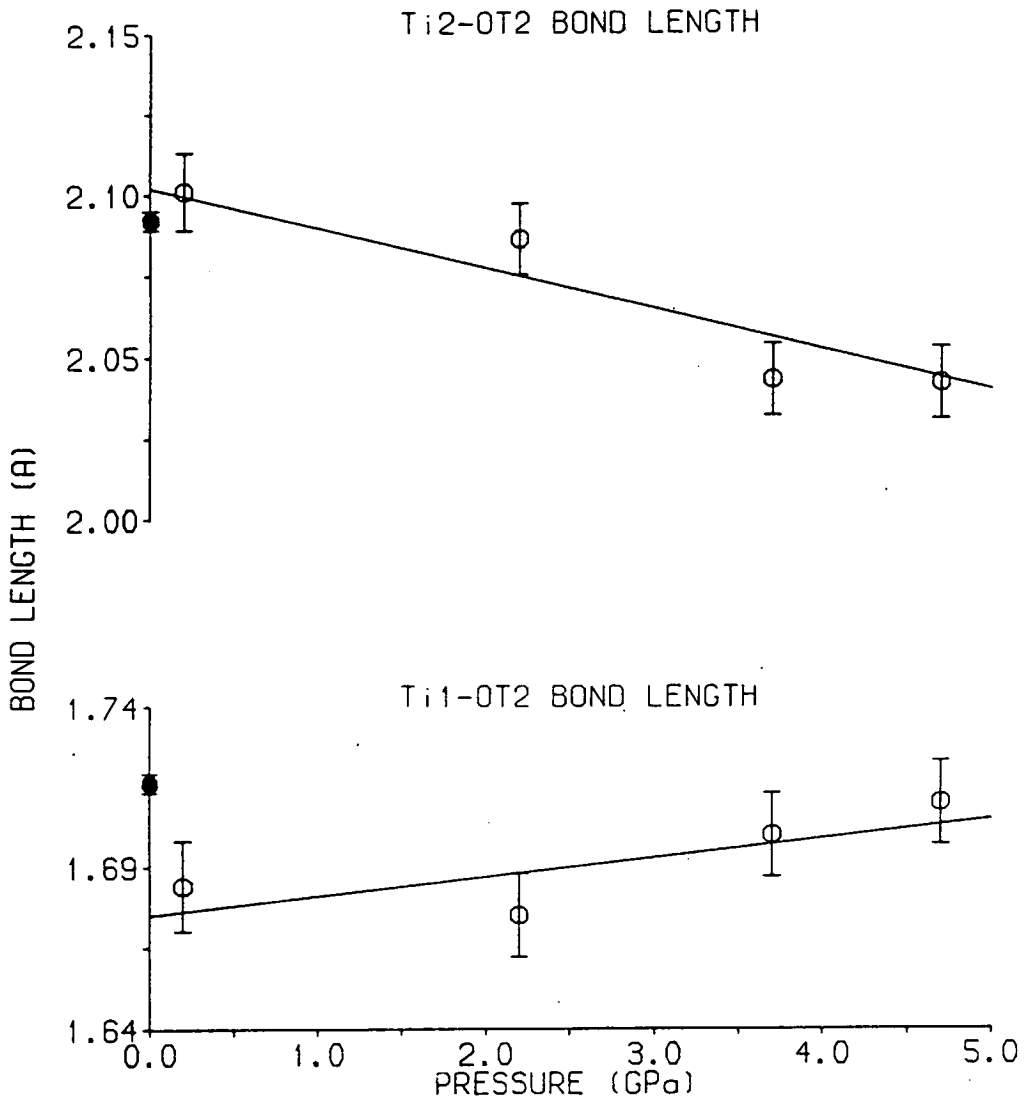

Figure 4.6: The Ti2-OT2 and Ti1-OT2 bond lengths in $KTiOPO_4$ as a function of pressure. The ambient pressure values, shown as ●, are calculated from the fractional coordinates of Thomas *et al* (1990). The lines indicate the changes in the bonds and are a guide to the eye only.

over the g^{b}_{ijk} terms due to the presence of the long and short Ti-O bonds in the highly distorted TiO_6 octahedra. In the calculations performed by Hansen *et al* (1988), this asymmetry was exploited by including only five of the six Ti-O bonds in each octahedra (omitting the 2.150 and 2.094Å bonds) and assigning the anomalously short Ti-O bonds as higher contributors. With this approach, the tensor component d_{333} is given by a two term equation of the form

$$d_{333} = [-2.34p^{(1)} + 1.64p^{(2)}]/V_{KTP} \tag{4.10}$$

where $p^{(1)}$ and $p^{(2)}$ refer to the bond polarizabilities of the short- and medium-length Ti-O bonds respectively, neglecting the K-O and the P-O bonds which are not expected to contribute significantly (Zumsteg *at al* (1976)). From experimentally determined values of the single-crystal d_{ijk}, Hansen *et al* (1988) calculated that $p^{(1)}$=$14 \times p^{(2)}$ and, therefore, the contribution of the anomalously short Ti-O bonds to d_{333} is significantly greater than the other bonds in the TiO_6 octahedra. At the pressures of 0.2, 2.2, 3.7 and 4.7 GPa the pre-multiplier of $p^{(1)}$ has the values -2.34, -2.35, -2.37 and -2.40 respectively, giving an overall change of only 2.5% as the phase transition is approached. Therefore, although the TiO_6 octahedra appear to be tilting with respect to the PO_4 tetrahedra, the magnitude of this re-orientation does not affect the summation of the direction cosines for the anomalously short Ti-O bonds significantly.

As already outlined, the KTP structure assumes a pronounced pseudosymmetry derived from the centric Pnan space group (Thomas *et al* (1990)), and it is of interest to examine how the structure moves with respect to this space group as the phase transition at 5.5 GPa is approached. In order to do so the Missym computer program (Thomas *et al* (1990), Le Page (1988)) was utilized to compare the refined coordinates with the pseudosymetry at all four pressures. The degree of pseudosymmetry was found to remain almost constant and, therefore, the structure neither appeared to be moving significantly towards or away from the prototypic Pnan phase. It is also interesting to note that the Missym program did not indicate an approach towards any other pseudosymmetries at 4.7 GPa, suggesting that the structural transition is first-order in character.

The deformation of the TiO_6-PO_4 framework is not accompanied by a significant movement of the titanium atoms (table 4.1) although, as already indicated, there is a clear movement of the phosphorus atoms and a change in the P-O-Ti bond angles. Since the O-Ti-O angles show changes of 2° or less (to 4.7 GPa) the titanium octahedra remain fairly rigid in shape. Therefore, the movement of the phosphorus atoms relative to the stationary titanium atoms, coupled with the angular changes in the P-O-Ti linking bond angles, suggest that the TiO_6 octahedra are tilting relative to the PO_4 tetrahedra.

The observed structural changes of KTP as it approaches its phase transition are similar in kind to those of the plagioclase feldspar anorthite $CaAl_2Si_2O_8$ which exhibits a first-order structural phase transition at 2.6 GPa (Angel (1988)). Although the refinements of the low-pressure structure were undertaken in the $I\bar{1}$ symmetry, so that the reported bond-lengths and bond-angles are an average of two parts of the structure which are nearly, but not quite, related by an I-lattice vector $(\frac{1}{2}, \frac{1}{2}, \frac{1}{2})$ and are not true values, it is, nevertheless, instructive to examine the general structural changes both before and after the phase transition. All of the feldspars have crystal structures consisting of a three-dimensional framework of corner-linked AlO_4 and SiO_4 tetrahedra. In the case of anorthite, cavities formed in the framework, which are analogous to the cage sites of KTP, contain Ca atoms. The mechanism for the transition, from the low pressure $P\bar{1}$ structure to the $I\bar{1}$ high-pressure structure, is tilting of the essentially rigid tetrahedra of the framework. The resulting deformation of the framework from the ambient structure apparently reflects a need to accommodate both the applied pressure and the large Ca cations within the cavities of the framework. Initially the volumes of the cavities, as defined by the eight closest oxygen positions, decrease under pressure in a manner similar to that of the cage sites in KTP. After the transition the volume of the cavities increases again as the framework tetrahedra suddenly tilt into new orientations. The tilting of the tetrahedra manifests itself as a change of the T-O-T (Al,Si-O-Al,Si) bond angles, which link neighbouring tetrahedra. The magnitudes of the T-O-T bond angle changes between atmospheric pressure and the phase transition are of the same order as those for the P-O-Ti linking bonds of KTP. After the transition in anorthite, however, there is a sudden angular change of the linking bonds with one such bond exhibiting an increase of 17°, where it had initially decreased by only 2° as the phase transition was approached. It is also

interesting to note that the Ca atom environments, or rather the potential well within each cavity, show a marked change above the phase transition. In the low-pressure phase the potential within the cavities is wide and relatively flat while above the transition the potential becomes significantly sharper. Although the KTP cage sites are quite different from the anorthite cavities, the high-pressure Raman study and the present high-pressure structural study both indicate that the potential well within the cage sites also becomes sharper after the transition, in as much as the initially softening 56cm^{-1} mode becomes stiffer. However, as will be shown later in this chapter, the K-cage sites exhibit a behaviour quite different from that shown by anorthite, where the volume of the Ca cavities remained about the same, if not increased.

The observed decrease of the K-cage site volumes under pressure intuitively suggests that the potential experienced by the K atoms will sharpen under pressure, thereby coupling the motion of the K atoms more closely to that of the cage oxygens. But in the absence of a detailed analysis of the phonon spectrum it is not possible to relate the observed structural changes of KTP with pressure to the softening 56cm^{-1} A_1 mode. However, the tilting of the TiO_6 octahedra relative to the PO_4 tetrahedra does generally agree with the behaviour proposed by Kourouklis *et al* (1987) as the phase transition is approached.

4.3 The Crystal Structure of Potassium Titanyl Phosphate (KTP) in its high-pressure phase

4.3.1 The Experiment and Data Collection

In order to achieve the 5.5 GPa required to place KTP into its high-pressure phase, it was found necessary to use a cell of alternative design to that of Merrill and Bassett. Although the Merrill-Bassett cell was capable of pressures just in excess of 6.0 GPa the pressure was found to be unstable and could not be sustained above the required 5.5 GPa. This behaviour was observed in several loadings of the cell and was attributed to the diamond seats indenting the beryllium backing

plates. A cell of more robust construction (the DXR-4 designed by D. Adams, see section 2.3.1) was loaded with a freshly prepared sample of KTP. The crystal was cleaved to the dimensions 50 × 100 × 100 μm^3, from the same bulk sample of KTP used in the first part of the experiment, and the sample mounted on the CAD4 diffractometer. The quality of the crystal was then checked and the crystallographic axes determined relative to its regular box-like shape. It was found that the faces of the crystal were perpendicular to the crystallographic axes and the crystal shape could, therefore, be easily characterised for sample absorption correction. The crystal was mounted in the cell with its b- and c-axes parallel to the diamond-anvil faces. From the previous study of the low-pressure phase, section 4.2, this orientation of the sample was found to give the lowest correlations and e.s.d's for the restricted data. A tungsten gasket was used to enclose the sample and the ethanol-methanol pressure transmitting fluid. The pressure cell was then taken to a pressure of 6.2±0.1 GPa (measured using the ruby fluorescence method) to place the sample crystal into the high-pressure phase. The cell was mounted on the CAD4 diffractometer and oriented using the same indexing scheme as that used for the low-pressure phase, and a search was made along the [1 0 0], [1 1 0] and [1 1 1] directions for new reflections. No new reflections were found in the survey; the unit cell appears to remain primitive, with axes parallel to the low-pressure phase.

As a final check that the unit-cell had been determined correctly, the pressure cell was oriented on the diffractometer so that the unit-cell of the sample was aligned with respect to the goniometer-head and a series of precession photographs were taken, with exposure times of approximately 48 hours. The photographs, for reciprocal lattice layers parallel to the (0 k l) plane, showed no new reflections strong enough to be detected on film although a number of reflections exhibited very large intensity changes after the transition. The original Merrill-Bassett cell loading also gave a useful exposure of the (h 0 l) reciprocal lattice plane. As the cell could only hold the sample in the high-pressure phase for only a few hours, the exposure time was limited to approximately 12 hours, nevertheless, no new reflections were apparent and the intensities of several reflections showed significant intensity differences compared to corresponding reflections in precession photographs taken just below the transition. A comparison of the above and below the transition photographs also indicated that the c-axis had undergone a

relatively large contraction which was estimated to be, from the measurement of the distance between spots on the photographs, in the order of 0.5Å.

The unit-cell dimensions were then determined accurately, on the diffractometer, by the four-equivalent-settings procedure of King and Finger (1979) and found to be a=12.477(9)Å b=6.322(3)Å c=10.058(4)Å giving a unit-cell volume V=793(1)Å^3. Comparing these values with an extrapolation to 6.2 GPa from the unit-cell measurements of the low-pressure phase (table 4.1, figure 4.7) indicates that there is a 4.2±0.2% volume reduction at the phase transition. The transition is, therefore, strongly first-order. Intensity data were collected with the ω-scan method at the position of least attenuation of the pressure cell, according to the fixed-ϕ technique (Finger and King (1978)). All accessible reflections in the hemisphere ±h, k,±l up to a maximum $\sin\theta/\lambda$ of 0.59Å^{-1}, totalling 1056, were measured with graphite-monochromated MoKα radiation. Although it would have been desirable to collect the data with Ag Kα radiation this was not possible due to the inadequate shielding of the CAD4 diffractometer, belonging to the Chemistry Department of The University of Edinburgh, which had been borrowed for the experiment. A time constraint also prevented the use of the three-point ψ-scan procedure (described in section 3.2.3) to detect those reflections affected by simultaneous diffraction by the diamond anvils. However, as will be shown in the following section, the data proved to be of sufficient quality, and resolution, to allow the full structure to be determined with good precision on the structural parameters.

4.3.2 Data Analysis and Structure Solution

The intensities were extracted from the reflection profiles using the method of Lehmann and Larsen (1974) and corrected for sample absorption. The reflections were then grouped into (0 k l), (h 0 l) and (h k 0) layers and the following systematic absences observed:-

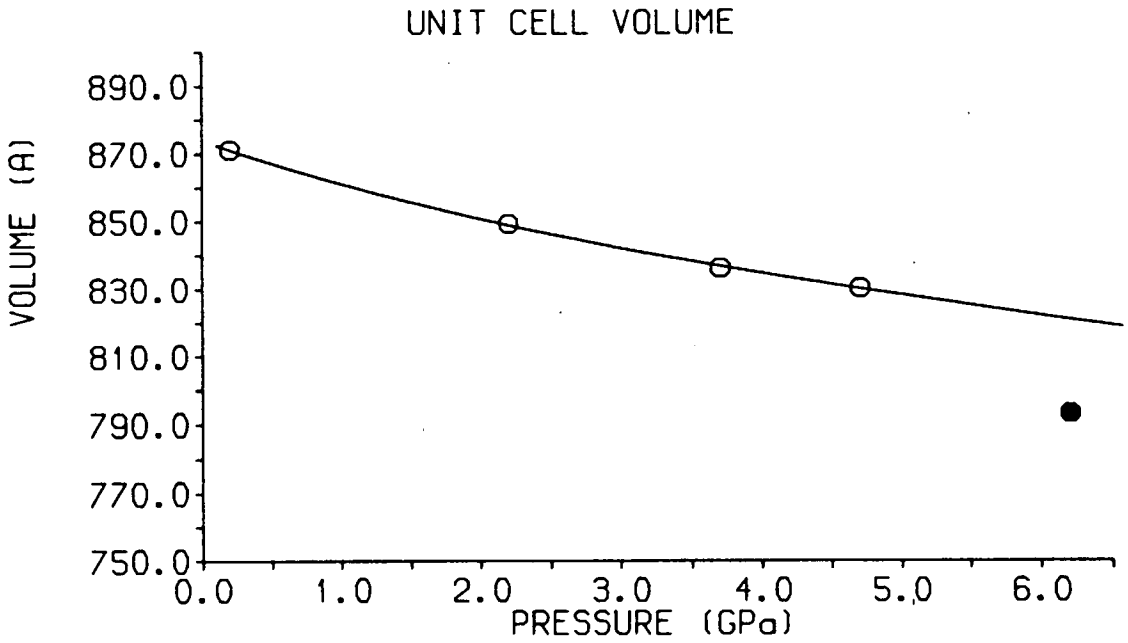

Figure 4.7: The unit-cell volume of $KTiOPO_4$ as a function of pressure both above (●) and below (○) the phase transition. Note that errors are smaller than the symbols shown. The line is fitted to the points measured in the low-pressure phase using a Murnaghan function.

reflections	absence condition
h k l	no condition
0 k l	k + l = 2n + 1
h 0 l	h = 2n + 1
h k 0	no condition
h 0 0	h = 2n + 1
0 k 0	k = 2n + 1
0 0 l	l = 2n + 1

The systematic absences appear to be consistent with either the $Pna2_1$ or Pnam space groups. Although the orientation of the sample within the pressure cell restricted observation of the h 0 l layer of reflections, a sufficient number of systematic absences could be scanned to suggest that the a-glide was present. At this stage an attempt was made to develop a model with the Pnam space group. However, a satisfactory model could not be found since the atoms would have to undergo unrealistically large movements to conform to the mirror plane. These movements would require severe disruption of the TiO_6-PO_4 framework and the breaking of several bonds. For example, if the mirror plane is placed through the $Ti(2)O_8$-$P(1)O_4$ chain the $Ti(1)O_8$-$P(2)O_4$ chain must be translated parallel to the a-axis to conform with the mirror symmetry. This translation would require a shift of at least 1.6Å for the Ti1 and P2 atoms and the break up of the P-O-Ti and Ti-O-Ti linking bonds.

If the Pnam spacegroup is discounted, the systematic absences suggest that the structure retains the $Pna2_1$ symmetry (or has a very strong $Pna2_1$ pseudosymmetry) and the structure of the high-pressure phase may be closely related to that of the low-pressure phase. It therefore seems reasonable, at least as a first attempt, to refine the 6.2 GPa data in the $Pna2_1$ spacegroup with the fractional coordinates of the 4.7 GPa structure as starting values. However, such a refinement was found to be unstable, and Rw and Gf could not be reduced to less than 0.26 and 5.78 respectively. The structural model derived from the 4.7 GPa data was, therefore, not sufficiently close to allow convergence of the least-squares refinement and the Patterson method would be required to develop a suitable starting model for the high-pressure phase. The Patterson function is usually expressed in the form

$$P(u,v,w) = \frac{1}{V}\sum\sum\sum_{-\infty}^{\infty}|F(hkl)|^2 cos2\pi(hu + kv + lw) \qquad (4.11)$$

where V is the volume of the unit cell, F(hkl) is the structure-factor, and u, v, w are vector components within the unit cell, and gives information about atomic distances, but not about atomic positions. The derivation and use of the Patterson function has been described elsewhere (see for example Lipson and Cochran (1966)) and it is not the author's intention to examine it in great detail here. However, the use of projected Patterson maps, calculated directly from the Patterson function itself, to aid the solution of the high-pressure structure will be described below.

After transforming the observed intensities into structure factors (using the Prometheus refinement program of Zucker *et al* (1983)) the (0 k l) layer of reflections was used to generate a Patterson projection in the (0 v w) plane. A number of reflections were removed from the data so that the list of reflections, within the (0 k l) layer, was identical to that of the 0.2 GPa data. This ensured that the 6.2 GPa Patterson projection could be compared directly with those of the low-pressure data and any differences in the projections arose only from the intensities of the reflections. At this stage, the data were not averaged and care had to be taken to ensure that any reflections with Friedel mates contributed correctly to the projections. To be confident that the contributions had been assigned correctly, the projections were calculated using a Fortran program written by the author, which averaged the Friedel pairs before the Patterson function was applied. The Patterson projections were normalised to give an origin height of 11120 and calculated over a grid of spacing $\frac{b}{20}$ and $\frac{c}{20}$. Figures 4.8a and 4.8b show the Patterson projections for the 0.2 GPa and 6.2 GPa data respectively. (The 4.7 GPa Patterson projection is almost indistinguishable from that of the 0.2 GPa data and is, therefore, not shown.)

To identify the peaks present in figure 4.8a the 0.2 GPa Patterson projection was compared to a structural diagram projected onto the (1 0 0) plane. From this structural projection, shown in figure 4.9, it is clear that the peaks observed in the 0.2 GPa Patterson projection arise from sets of overlapping vectors. The peak labeled (b) arises from vectors between atoms in the $Ti(1)O_6$-$P(2)O_4$ and $Ti(2)O_6$-

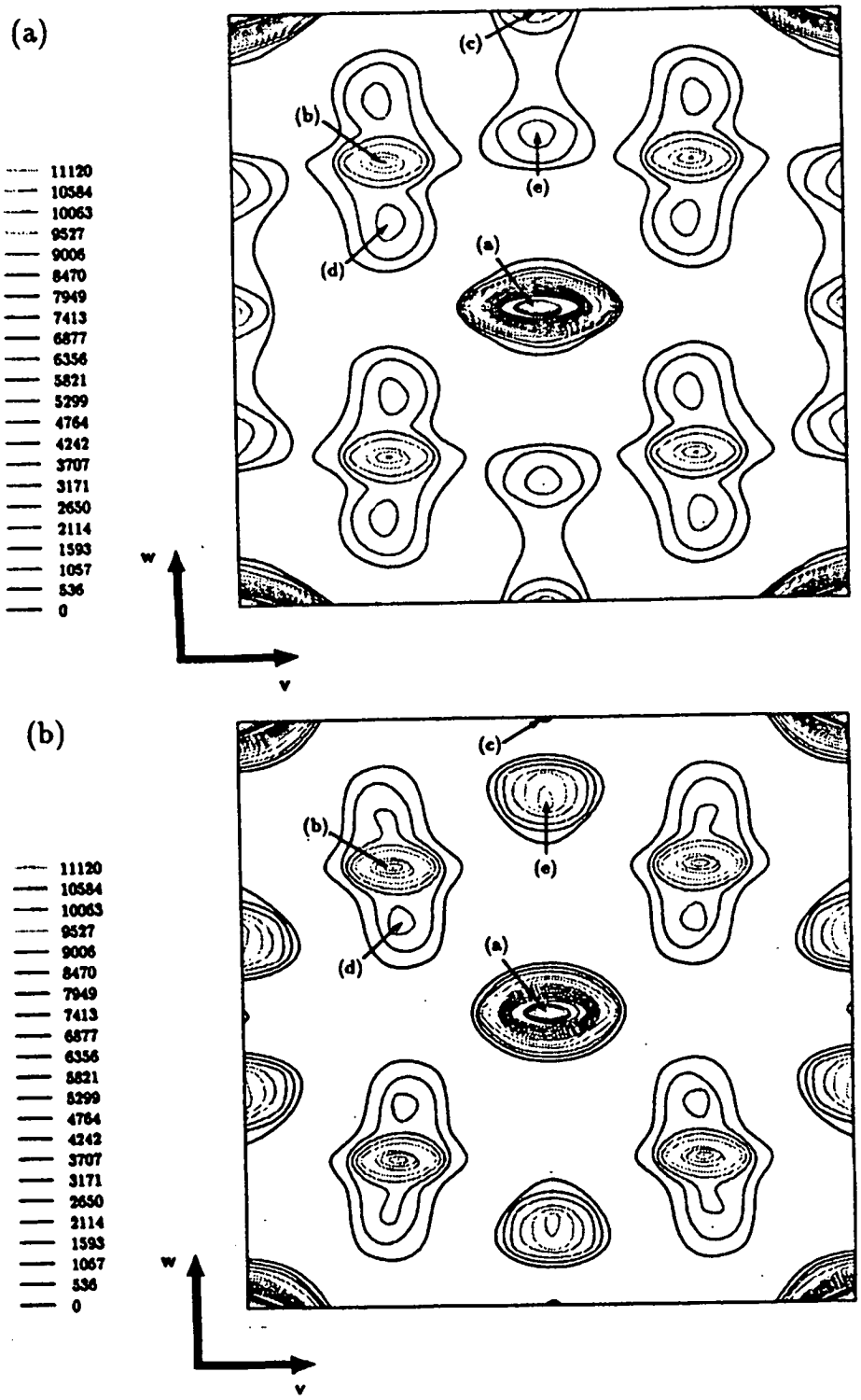

Figure 4.8: Patterson projections in the (0 v w) plane for (a) the 0.2 GPa data and (b) for the 6.2 GPa data. The origin of the peaks labelled (a), (b), (c), (d) and (e) is given in the text.

$P(1)O_4$ chains, while peak (c) arises from vectors between atoms in neighbouring $Ti(1)O_6$-$P(2)O_4$ chains overlapping with (Ti,P,O)—K vectors. The other features in the Patterson projection, labeled (d) and (e), are formed from several sets of overlapping (K,Ti,P,O)—K vectors.

If the Patterson projection for the 6.2 GPa data (figure 4.8b) is now examined it is apparent that many of the features of the 0.2 GPa projection are retained. As expected, the projections both have mirror symmetry perpendicular to the v and w directions, indicating that the Laue symmetry is mmm, and the positions of the origin peaks are consistent with an n-glide perpendicular to the a-axis. However, it is apparent that there are some differences in the positions and heights of the Patterson peaks themselves. Perhaps the most obvious changes can be observed in the peaks labeled (c) and (e) which both show pronounced changes in height. The height of peak (e) has increased by 1593 and the height of peak (c) has decreased by a similar magnitude. Indeed, it appears that some of the vectors associated with peak (c) have merged with those of peak (e), which has also shifted significantly along the w-direction. As was explained above, both of these peaks arise from sets of overlapping vectors involving the potassium atoms and, therefore, it can be expected that the potassium atoms undergo pronounced shifts in the structure. In order to determine the magnitudes of these shifts, a series of Patterson projections were simulated from the fractional coordinates of the 0.2 GPa model. The z-coordinates of the potassium atoms were varied so that the simulated Patterson projections could be matched as closely as possible to that of the 6.2 GPa data. Figure 4.10 shows the Patterson projection obtained by shifting both the K1 and K2 atoms along the z-axis by 0.03 (in terms of fractional coordinates) from their 0.2 GPa values. Although there are some differences in the peak shapes, the position and height of the peaks are now much closer to what was observed with the 6.2 GPa data and indicates that the y- and z-coordinates must be in reasonable agreement with their true values.

The (0 k l) layer of data was now refined using the fractional coordinates of the simulated Patterson projection as starting values. Refining only the scale and the y- and z-coordinates, an Rw of 0.087 and a Gf of 1.97 were achieved. The Patterson projection obtained from the calculated structure factors is shown in figure 4.11. Comparing figure 4.11 with figure 4.8b, it is clear that an excellent

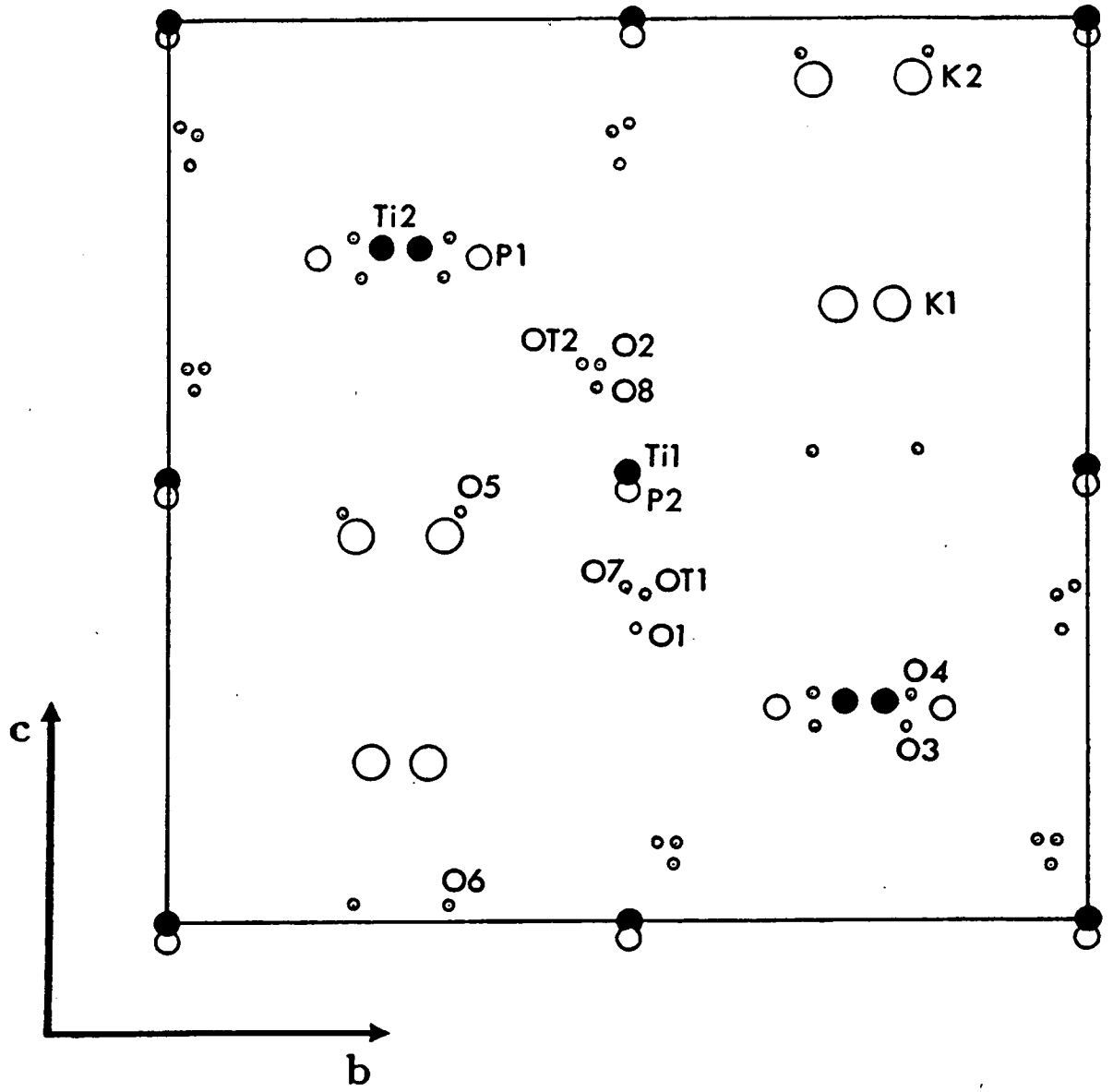

Figure 4.9: The structure of $KTiOPO_4$ viewed along the a-axis. The shaded circles represent the titanium atoms. Note that the bonds have been omitted for clarity. As the Patterson projections are drawn so that the v and w axes have the same length, the lengths of the b and c axes are also set to be the same so that a direct comparison can be made between the low-pressure structure and the 0.2 GPa Patterson projection shown in figure 4.8(a).

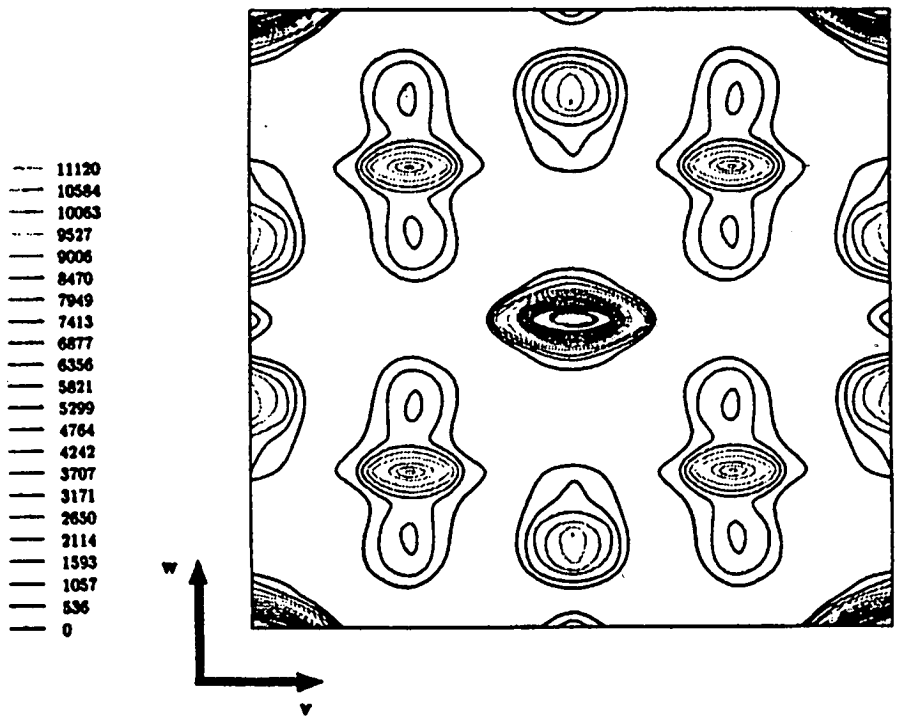

Figure 4.10: Simulated Patterson projection in the (0 v w) plane for both the K1 and K2 atoms shifted along the z-axis by 0.03 (in terms of fractional coordintes) from their 0.2 GPa values.

agreement has been obtained and only very minor differences remain in the peak shapes. Indeed, an examination of the Fourier difference map for the (0 k l) layer of data (see figures 4.12a and 4.12b) indicates no significant features above the general background noise. With the projected structure essentially determined, the full data set was now re-examined.

Although it would have been desirable to determine the x-coordinates from Patterson projections of the (h k 0) or the (h 0 l) layers of data, the restrictions imposed by the pressure cell, on the number of observable reflections (see section 2.3.1), gave an appreciable loss of information from the projections. The resolution along the u-direction was also severly limited. To gain Patterson projections of acceptable quality would have required another data collection with the crystal mounted with either the b- or c-axis perpendicular to the diamond-anvil face, so that a complete layer of data could be collected. However, a further data collection was not required since it was found that the full data set could now be refined successfully. For this refinement the y- and z-coordinates determined from refinement of the (0 k l) data and the x-coordinates from the 0.2 GPa structure were

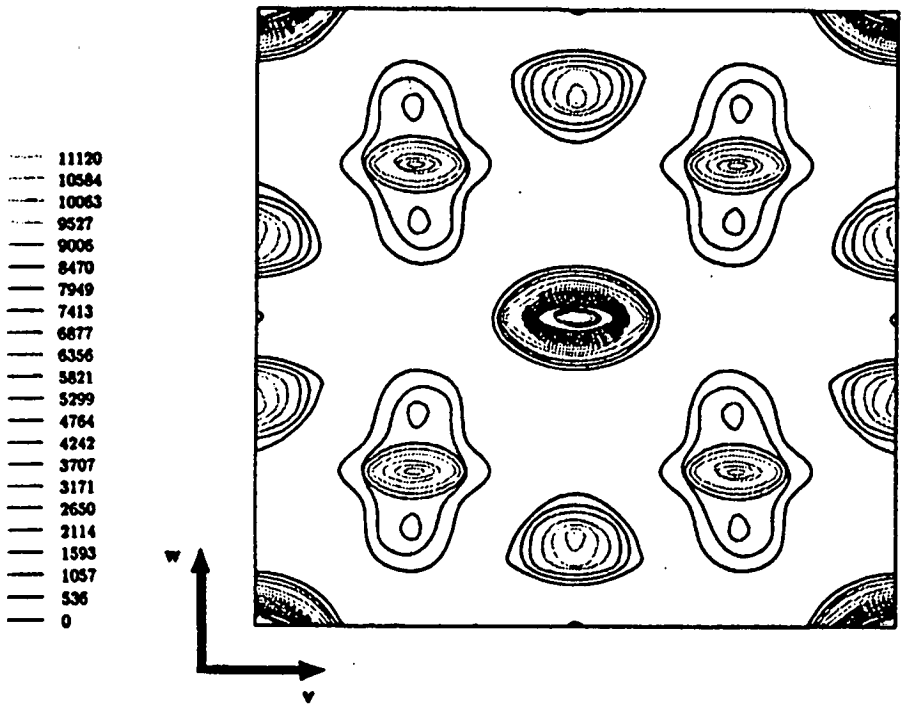

Figure 4.11: Patterson projection in the (0 v w) plane from the calculated structure factors obtained from the refinement of the (0 k l) layer of data.

taken as starting values. Varying only the fractional coordinates and the scale, the refinement converged to give an Rw and Gf of 0.11 and 2.52 respectively. Since a reasonable fit to the full data set had been been achieved, thermal parameters and an extinction correction were now refined. The potassium atoms were refined with anisotropic thermal parameters (the parameters for the atomic motion directed along a, the direction of lowest resolution in the data, were constrained to their ambient values) and the other atoms were refined with isotropic thermal parameters. After further refinement the data were searched for reflections affected by gasket occlusion and simultaneous diamond reflection. A total of 55 reflections, approximately 5% of the data, were found to be affected in this way and were excluded from the refinements. The fit had now been improved considerably and an Rw of 0.054 and a Gf of 1.24 were obtained.

In order to check that the refined structure was sensible, bond lengths and bond angles were calculated for the TiO_6 octahedra and PO_4 tetrahedra. These structural units were found to have internal bond lengths and bond angles very similar to those of the low-pressure structure. The refinement was also repeated with the same list of reflections as that of the 0.2 GPa data set and with the same

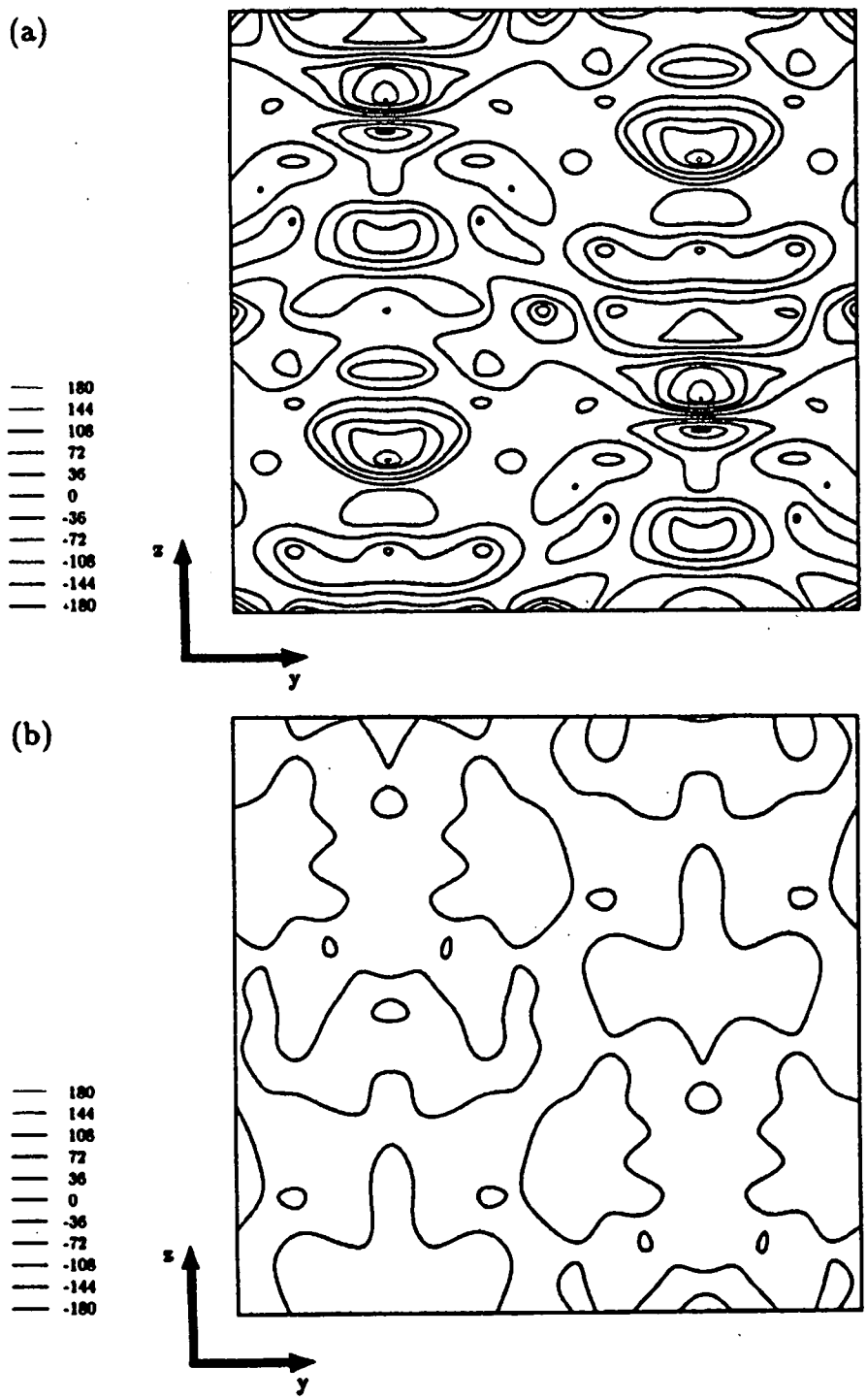

Figure 4.12: Fourier difference maps for (a) the 0.2 GPa structure, and (b) for the refinement where only the y- and z-coordinates were varied, with respect to the 6.2 GPa (0 k l) layer of data.

constraints on the thermal parameters. The fit to the data, for this refinement, compared well with the fits obtained from refinements of the low-pressure phase. At this stage the structure was considered to be fully determined (at least as an average structure) and attention was now turned to other possible space groups of lower symmetry.

If the true symmetry of KTP were lower than $Pna2_1$ as proposed by Kourouklis *et al* (1987) from their high-pressure Raman study, the structure would have to be only slightly distorted from the one refined in the $Pna2_1$ space group so that the apparently absent reflections are in fact present but too weak to be observed. The only space groups allowing such a small distortion of the structure, and not introducing further reflection conditions, are monoclinic Pn, Pa and $P2_1$.(Note that Pn and Pa are different settings of the monoclinic space group Pc.) Using the coordinates refined with the $Pna2_1$ space group, model structures were generated for all three of these space groups, which each required twice the number of refinable atoms. The additional atoms were generated by performing one of the missing symmetry operators from the $Pna2_1$ space group. The model structures were then refined using the same list of reflections, and with the same types of thermal parameters, as that for the $Pna2_1$ refinement. However, the refinements did not give a significantly better fit to the data and the atomic positions differed by less than 0.1Å from their $Pna2_1$ positions. It appears, then, that the $Pna2_1$ space group is retained after the phase transition, unless there is twinning not resolvable in this experiment.

The $Pna2_1$ refinement was completed by removing the systematically absent reflections from the data and averaging over symmetry-equivalent reflections, after their intensities had been corrected for extinction. The oxygen atoms were all refined with isotropic thermal parameters while the potassium, titanium and phosphorus atoms were refined with anisotropic thermal parameters (the parameters for the atomic motion directed along a were constrained to their ambient values). Similar constraints were applied to the low-pressure refinements (section 4.2.1) and were shown not to bias the refinement of the positional parameters significantly. The final cycle of refinement resulted in an Rw and Gf of 3.6 and 1.13 respectively for 533 independent reflections and 88 refinable parameters.

4.3.3 Results and Discussion

Table 4.5 presents the refined atomic coordinates and the structure is shown in figure 4.13. In order to allow a direct comparison of the ambient and high-pressure structures, the orientation of figure 4.13 has been made the same as that of figure 4.1. The bond lengths of the K cages, Ti octahedra and P tetrahedra derived from the refinement are given in table 4.6.

The main structural changes involve the n-glide related $Ti(2)O_6$-$P(1)O_4$ chains (labelled CH1 and CH2 in figure 4.13), which exhibit parallel/ antiparallel translations along the a-axis. The cross-linking $Ti(1)O_6$-$P(2)O_4$ chains (which are directed along the b-axis) are rotated by the relative shifts of the $Ti(2)O_6$-$P(1)O_4$ chains. Within the chains there is a pronounced tilting of the TiO_6 octahedra with respect to the PO_4 tetrahedra, with a considerably larger change in their relative orientation than is observed between ambient pressure and the phase transition. For example, as can be seen from table 4.7, the P1-O2-Ti1 and the P2-O8-Ti2 bonds exhibit an angular change of 4.0° and 5.7° respectively at the phase transition where they had only shown angular changes of approximately 1.5° and 2.0° as the transition is approached. It is also interesting to note that the Ti1-OT2-Ti2 bond, which links neighbouring TiO_6 octahedra, exhibits a 6.5° angular change at the transition which is significantly larger than 0.3° change shown between 0.2 and 4.7 GPa (see table 4.7).

The overall shape and distortions of the TiO_6 octahedra remain almost unchanged by the phase transition and the distribution of the long, intermediate and short bonds is the same as in the low-pressure phase. In particular the anomalously short bonds are retained, although the transition has reduced the difference between the Ti1-OT1 and Ti2-OT1 bonds and the difference between the Ti1-OT2 and Ti2-OT2 bonds by about 30% and 15% respectively from their 4.7 GPa values. The pronounced tilting of the TiO_6 octahedra with respect to the PO_4 tetrahedra, combined with some significant bond angle changes *within* the TiO_6 octahedra themselves, results in a re-orientation of the anomalously short Ti-O bonds which is significantly larger than that observed as the phase transition is approached. Indeed, the pre-multiplier of $p^{(1)}$ (see equation 4.3) is reduced to a value of -1.20, corresponding to a reduction of about 50% with respect to the 4.7 GPa value.

	x	y	z
K1	0.3953(7)	0.7780(4)	0.6314(4)
K2	0.1146(6)	0.7001(4)	0.8667(4)
Ti1	0.3718(4)	0.4894(3)	-0.0004
Ti2	0.2800(5)	0.2572(3)	0.7240(3)
P1	0.5296(8)	0.3218(4)	0.7623(4)
P2	0.1798(6)	0.4810(4)	0.4784(3)
O1	0.5134(15)	0.4177(11)	0.8973(7)
O2	0.5452(15)	0.5043(10)	0.6625(7)
O3	0.4373(21)	0.1848(11)	0.7130(9)
O4	0.6246(19)	0.1795(12)	0.7590(9)
OT1	0.1913(16)	0.9728(9)	0.3269(6)
OT2	0.2510(17)	0.0398(9)	0.5783(7)
O5	0.0998(15)	0.2982(11)	0.4702(7)
O6	0.1218(15)	0.6777(12)	0.5285(8)
O7	0.2300(16)	0.5126(9)	0.3390(7)
O8	0.2754(15)	0.4380(9)	0.5672(6)

Table 4.5: Atomic coordinates of $KTIOPO_4$ at 6.2 GPa. The estimated standard deviations (ESDs) are given in parentheses. Note that the Prometheus refinement program requires that one atom is fixed along the polar axis. The Ti1 z coordinate was chosen to be fixed to the same value used in the low-pressure study, and so no ESD is quoted for it.

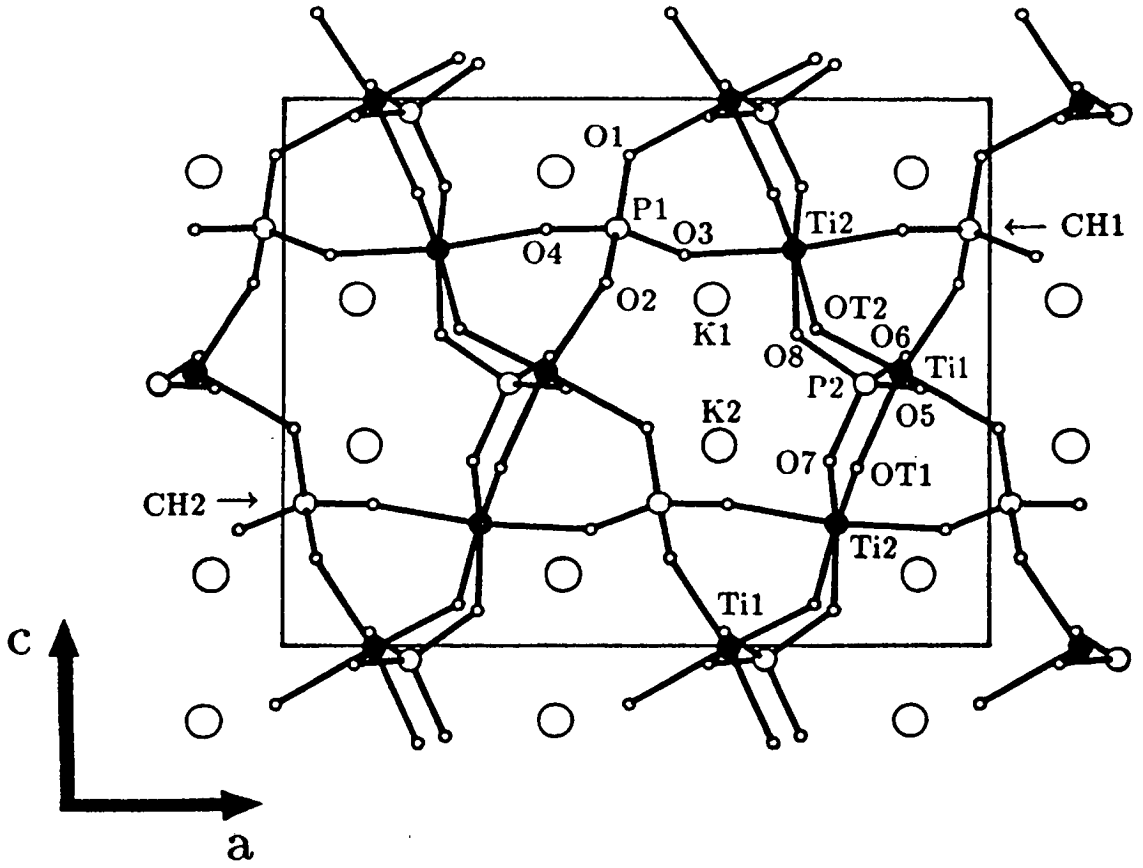

Figure 4.13: The high-pressure structure of $KTiOPO_4$ viewed along the b-axis. The shaded circles represent the titanium atoms and the TiO_6-PO_4 chains labelled CH1 and CH2 exhibit parallel/antiparallel translations along the a-axis, in the directions indicated by the arrows. This figure can be compared directly with figure 4.1 to reveal the deformation of the potassium cage site environments and the pronounced movements of the potassium atoms along the c-axis.

$K(1)O_8$		$K(2)O_9$	
K1-O1	2.893(10)	K2-O1	2.744(12)
K1-O2	2.567(15)	K2-O2	2.909(10)
K1-O3	2.749(9)	K2-O3	3.634(18)
K1-O5	3.410(8)	K2-O4	2.636(8)
K1-O7	3.000(12)	K2-O5	2.870(19)
K1-O8	2.698(12)	K2-O7	2.782(15)
K1-OT1	2.959(10)	K2-O8	2.865(11)
K1-OT2	2.504(18)	K2-OT1	2.844(19)
		K2-OT2	2.892(14)
$Ti(1)O_6$		$Ti(2)O_6$	
Ti1-O1	2.094(17)	Ti2-O3	2.019(26)
Ti1-O2	1.934(12)	Ti2-O4	2.010(23)
Ti1-O5	2.006(7)	Ti2-O7	1.935(6)
Ti1-O6	1.994(7)	Ti2-O8	1.949(6)
Ti1-OT1	1.911(10)	Ti2-OT1	1.748(7)
Ti1-OT2	1.754(19)	Ti2-OT2	2.042(8)
$P(1)O_4$		$P(2)O_4$	
P1-O1	1.501(8)	P2-O5	1.529(15)
P1-O2	1.541(7)	P2-O6	1.525(12)
P1-O3	1.524(20)	P2-O7	1.548(11)
P1-O4	1.489(20)	P2-O8	1.514(16)

Table 4.6: The bond lengths (Å) of the K cages, Ti octahedra, and P tetrahedra in $KTiOPO_4$ at 6.2 GPa.

	4.7 GPa	6.2 GPa
PO_4-TiO_8 linking angles		
P1-O2-Ti1	133.3(8)	129.3(7)
P2-O8-Ti2	133.0(9)	127.3(9)
Ti1-OT2-Ti2	133.5(7)	126.93(9)

Table 4.7: Selected P-O-Ti and Ti-OT-Ti bond angles (°) in $KTiOPO_4$ at 6.2 GPa.

Therefore, from the geometrical contribution of the anomalously short Ti-O bonds alone, neglecting the effects of the relatively large bond length changes, it is to be expected that the high-pressure structure will have a significantly poorer SHG performance than that of the low-pressure structure.

Although there are a number of bond-length and bond-angle changes in the TiO_6 octahedra at the transition this gives rise to only a 0.1±2% reduction in the average volume of the two octahedra. The PO_4 tetrahedra, whose internal bond-lengths and bond-angles exhibit almost no change, have an average volume reduction of a similar magnitude. It appears then that the potassium cage sites, which show an average volume reduction of 11.9±1%, absorb most of the 4.2±0.2% reduction in the unit cell volume at the transition. As was found with the pressure dependence of the low-pressure structure, the compression of the K-cages is accompanied by significant movements of the potassium atoms themselves along the polar c-axis. These movements, which are in the order of 0.5Å with respect to the TiO_6-PO_4 framework, correspond to the K(1) and the K(2) atoms adopting positions that are closely n-glide related i.e. if the pseudo n-glide, through z=0, were present there would be only one independent K atom described by the average of the K(1) and K(2) positions (Thomas (1992)). The distance, Δ, between the K(2) atomic

	Δ_x(Å)	Δ_y(Å)	Δ_z(Å)	Δ(Å)
Ambient	-0.2128	-0.1305	-1.2826	1.3066
6.2 GPa	0.1235	-0.1384	0.0191	0.1865

Table 4.8: The displacements Δ_x, Δ_y, Δ_z (Å) of the K(2) atomic position from the pseudo-n-glide related K(1) atomic position, with respect to the crystallograpic axis. The distance Δ (Å) between these positions is calculated from $\Delta = (\Delta_x^2 + \Delta_y^2 + \Delta_z^2)^{\frac{1}{2}}$. The calculations have assumed a pseudo n-glide through z=0.

position and the pseudo n-glide related K(1) atomic position is given in table 4.8 for both the ambient and high-pressure crystal structures.

As can be seen from table 4.8, the distance between the pseudo-n-glide related K(1) and K(2) positions is reduced to only 0.1865Å in the 6.2 GPa structure from a distance of 1.3066Å in the ambient pressure structure. Much of this reduction can be attributed to the shifts along the c-axis exhibited by both the K(1) and K(2) atoms. This significantly decreases the Δ_z displacement which has the largest contribution to the 'distortion' away from the Pnan pseudosymmetry of the whole ambient structure, including the TiO_6-PO_4 framework atoms (Thomas *et al* (1990)). In contrast, the framework atoms of the high-pressure structure adopt positions that generally increase the distortion from the Pnan pseudosymmetry. For example, the distance, Δ, for pseudo-n-glide related Ti(2) atoms increases from 0.2668Å at ambient pressure to 0.9177Å at 6.2 GPa. This increase can be attributed almost exclusively to the relatively large parallel/ antiparallel shifts of the Ti(2)O_6-P(1)O_4 chains with respect to the a-axis. It appears then that at least the K-atoms move towards their Pnan-type positions in the high-pressure phase.

A possible explanation of this behaviour may be found from the recent identification of 'hole sites' in the ambient KTP structure (Thomas and Glazer (1991)).

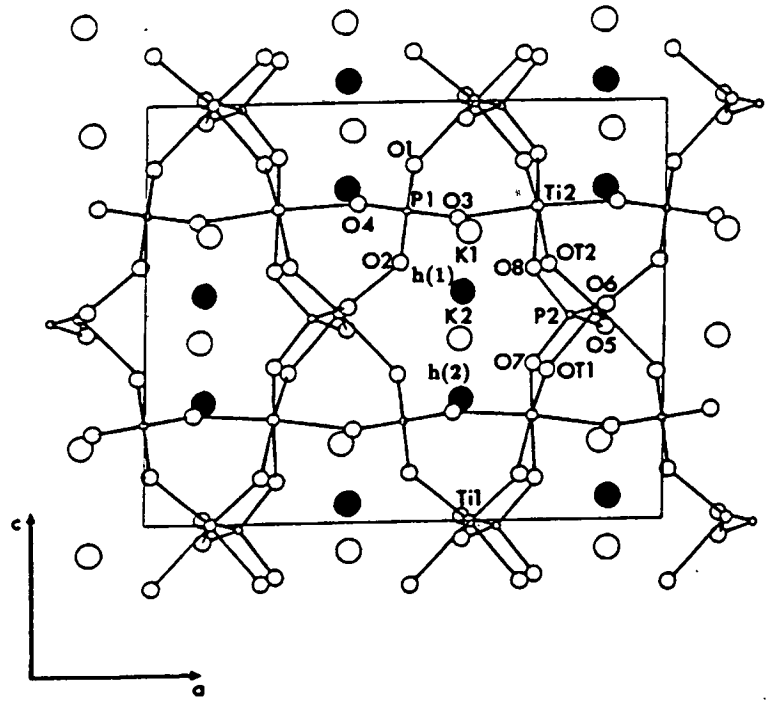

Figure 4.14: The ambient pressure structure of $KTiOPO_4$ viewed along the b-axis. The shaded circles represent the 'hole sites' (see text) labelled h(1) and h(2).

From inspection of the ambient KTP structure it was found that each K atom is highly asymmetrically coordinated by O atoms, and that at a short distance (about 1.5Å) along -c from each K atom there is a vacant site, a hole site (h(1) and h(2) in figure 4.14), of similar size and oxygen coordination to the K-site. In the high-temperature phase the presence of the n-glide plane causes the pseudo-symmetrically related K(1) and h(1) (K(2) and h(2)) sites to merge together along [0 0 1] at the average high-temperature K atom position. This new K-site would be characterised by the absence of the large 'hole' region present in the ambient structure. Although a different behaviour is to be expected at high-pressure, the smaller K-cage volumes of the high-pressure phase also corresponds to an absence of the hole-sites as does the corresponding shift of the K atoms to positions more closely related to the pseudo-symmetry (Thomas (1992)).

The absence of a symmetry change through the 5.5 GPa transition disagrees with the interpretation that Kourouklis *et al* (1987) make of their high-pressure Raman data. The apparent contradiction may be explained if the intensities of weak and previously unobserved Raman modes are augmented after the phase transition.

This would give rise to an apparent increase of the number of modes without changing the crystal symmetry. Although first-order phase transitions retaining the crystal symmetry are unusual a number of such transitions have been reported in a variety of different elements and compounds. For example, Makarova *et al* (1990) have recently reported a structural phase transition in the compound $(NH_2)_2Se_2O_5$ at 312K where the $P2_12_12_1$ spacegroup is retained, although the transition involves an N-H...O hydrogen bond being broken, with only a 0.6% reduction in the unit-cell volume. Other notable examples include the pressure-induced isostructural valence transitions of the rare-earth elements Ce, Sm, Eu and Yb and of compounds such as the Eu based $EuPd_2Si_2$, $EuNi_2P_2$ and $EuCu_2Si_2$ (Chandran *et al* (1992)).

4.4 Conclusions

The principal changes of the KTP structure as the phase transition is approached are in the region of the relatively compressible K cages. The PO_4 and TiO_6 units remain rigid in size and shape, and the compression of the cages appears to be accommodated by significant buckling of the framework structure, accompanied by a pronounced movement of the K2 atom. The observed angular changes in the P-O-Ti linking bonds suggest that the deformation of the structure around the cage sites is principally achieved by tilting of the TiO_6 octahedra relative to the PO_4 tetrahedra. The other structural changes up to 4.7 GPa are relatively small. In particular, the TiO_6 octahedra were found to retain their general distortion although there are some small changes in Ti-O distances, including a reduction in the difference between the Ti1-OT2 and Ti2-OT2 bond lengths.

The structural phase transition has been shown to be strongly first-order in character with a re-orientation of the TiO_6 octahedra, with respect to both the PO_4 tetrahedra and the crystallographic axes, which is much larger in magnitude than that observed as the phase transition is approached. This re-orientation reduces the pre-multiplier of $p^{(1)}$ by approximately 50%, and is accompanied by significant reductions in the difference between the Ti1-OT1 and Ti2-OT1 bond lengths and the Ti1-OT2 and Ti2-OT2 bond lengths. Although from the geometrical con-

tribution of the anomalously short Ti-O bonds alone it would appear that the SHG performance will decrease, it is not known quantitatively how the structural changes with pressure will affect the SHG properties of the crystal. It is now clearly of interest to determine this, from direct optical measurements.

The behaviour of the K atoms within their cage sites is particularly interesting in as much as they appear to adopt positions more closely related to the Pnan pseudosymmetry, in contrast to the other atoms, within the TiO_6-PO_4 framework, which move away from their pseudo-symmetrically related positions. As it appears that the hole sites may play an important role in the phase transition (Thomas (1992)), it would now be of interest to establish the structural nature of the high-pressure phase transition in TlTP where the hole sites are expected to be smaller, due to the increased atomic volume of the Tl^+ cation over that of the K^+ cation. Certainly, from the Raman studies of Kourouklis *et al* (1987) and Serhane *et al* (1991), the nature of the high-pressure phase transitions in KTP and TlTP appear to be quite different.

Chapter 5

A High-Pressure Structural Study of Potassium Dihydrogen Phosphate (KDP)

5.1 Introduction

Potassium dihydrogen phosphate, KH_2PO_4 (KDP), is a well known representative of hydrogen-bonded materials which exhibit hydrogen-ordering structural phase transitions, from a paraelectric phase to a ferroelectric or antiferroelectric phase, on cooling through the phase transition temperature T_c. In KDP itself, the ambient-temperature paraelectric phase has a tetragonal crystal structure (space group $I\bar{4}2d$), shown in figure 5.1, and the transition to the orthorhombic ferroelectric phase (space group Fdd2) occurs at a T_c of 122K. Above T_c the H-atoms are 50:50 disordered over two sites in O—H...H—O bonds, linking neighbouring PO_4 groups. Upon cooling through T_c, the H-atoms order onto one site in asymmetric O—H...O bonds with an accompanying displacement of the heavy atoms along the c-axis (Nelmes (1987)).

The transition temperature is sensitive to the substitution of the hydrogen atom with its heavier isotope deuterium, rising to 229K on deuterating KDP to KD_2PO_4 (DKDP), and also to the application of hydrostatic pressure, T_c falling by 0.46 K/GPa in KDP (Samara (1987)). These changes in T_c, on deuteration and under the application of high pressure, have been explained using the tunnelling model for the transition (Blinc (1960)) where the H atoms (or the D atoms in DKDP) are

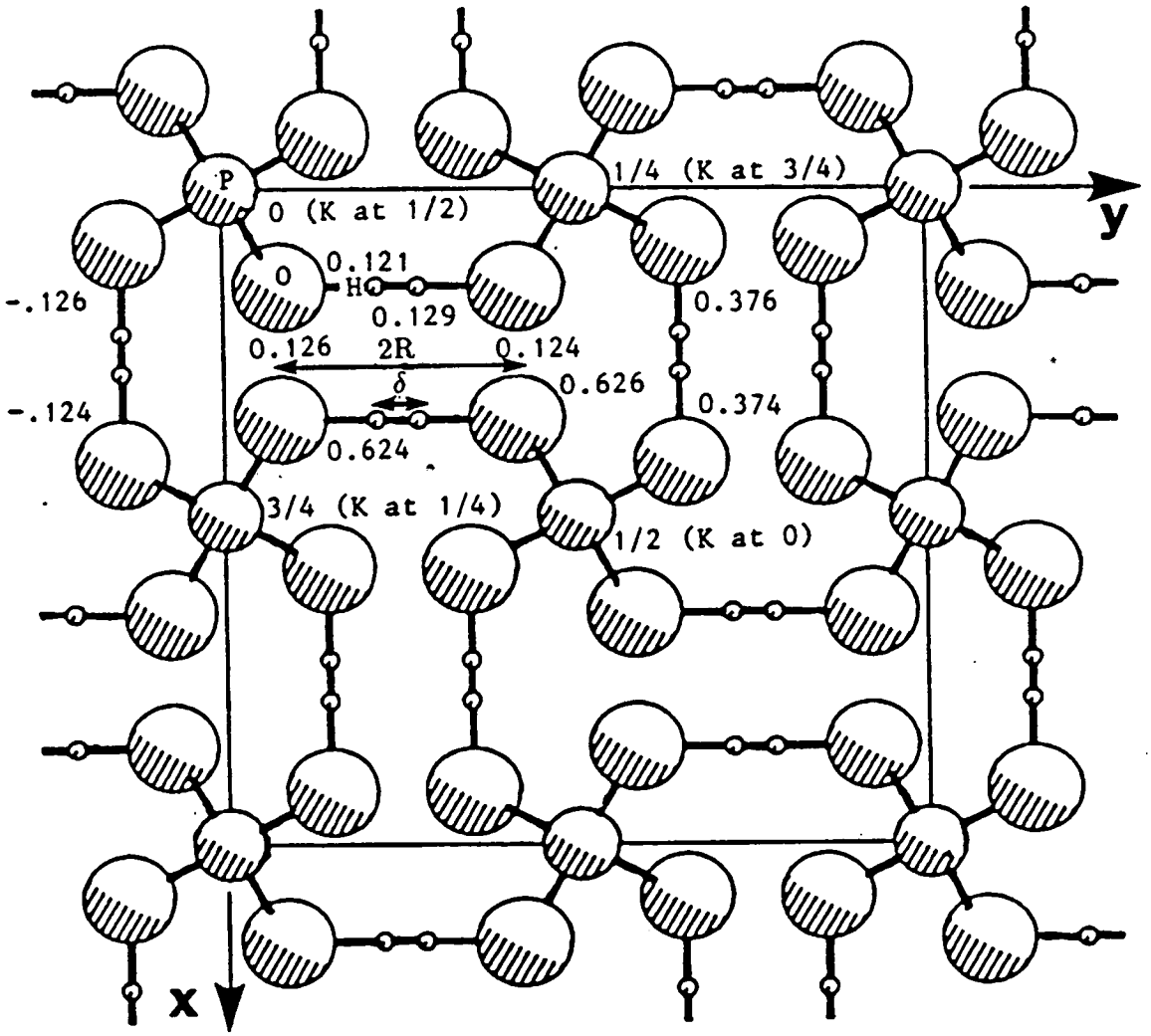

Figure 5.1: The tetragonal structure of KH_2PO_4 (KDP) viewed along the z axis. The K atoms, at positions displaced c/2 from each P atom, are superimposed onto the P atoms in this projection. Fractional coordinates along z (fixed by symmmetry for the K and P atoms) are given for some of the atoms. The bondlengths 2R and δ are also shown.

treated as being in a double-welled potential (figure 5.2) and the increase of T_c on deuteration is attributed to the heavier deuterons having a lower tunnelling frequency through the potential barrier, between the two minima, than the protons. This requires that the deuterated material orders at a higher temperature. The reduction of T_c with applied pressure has been assumed to be associated with a shortening of the H(D)-bonds which leads to a lower potential barrier separating the minima and a correspondingly higher tunnelling frequency. However, accurate single-crystal neutron-diffraction structural studies of KDP and DKDP (Nelmes (1987)) at both ambient and high pressure have cast doubt on this interpretation of the transition and has led to efforts to revise the theory. The structural studies have indicated a number of specific problems: the increase in T_c on deuteration is accompanied by significant increases in both the oxygen-oxygen distance (2R) and the H-H site separation (δ) which are not explicitly taken into account in the tunnelling model; both δ and 2R decrease under applied pressure, as does T_c, indicating, along with the effects of deuteration, that there could be a relationship between the H-bond dimensions and T_c; the reduction of the H(D)-bond length with pressure is significantly less than was expected, making the explanation for the pressure dependence of T_c uncertain. However, Ichikawa (1981) and Ichikawa *et al* (1987) have shown that for a number of hydrogen-ordering materials, and their deuterated isomorphs, their exists a simple empirical, and approximately linear, relationship between T_c and 2R. It was determined that the increase in T_c with deuteration was primarily due to the increase in 2R, without the need of tunnelling, and was referred to as the 'geometrical isotope effect' (Ichikawa (1978)). A more recent evaluation of high-resolution neutron diffraction results for KDP and DKDP (Nelmes (1988)), however, has shown that although the difference in T_c is significantly reduced when KDP and DKDP are compared at the same 2R it is still as much as 40K, as can be seen from figure 5.3a. If, on the other hand, the comparison is made at the same value of δ, then the difference in T_c is reduced to only 15K, or perhaps less given the uncertainties of the extrapolation, indicating that δ is possibly the more important geometrical determinant of T_c.

It is also apparent, from the extrapolated line on figure 5.3b, that δ will decrease to approximately 0.22Å as T_c approaches 0K, corresponding to a pressure of 1.71 GPa where the ordered ferroelectric phase of KDP was observed to vanish (Samara (1971)). From a recent high-pressure single-crystal neutron diffraction study of

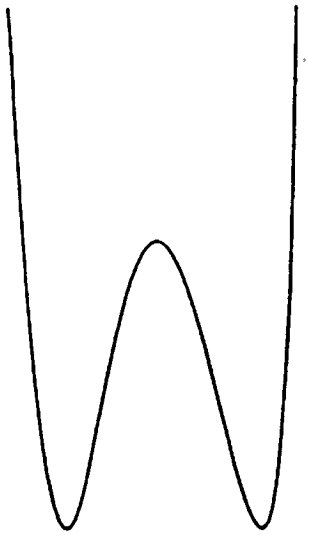

Figure 5.2: A schematic drawing of the double-welled potential in which the H atoms sit in the paraelectric phase of KH_2PO_4.

KDP, conducted at 1.65 GPa and 10K (McMahon (1990)), δ was determined to be 0.217(23)Å and, although the data were of insufficient resolution to show conclusively that the H-atom was either ordered or disordered, this is in excellent agreement with the extrapolated value. It was concluded that the along-bond zero-point thermal motion of each proton at 1.65 GPa and 10K is sufficient to carry the proton from one potential minimum to the other, preventing the system from ordering — a view consistent with predictions based on earlier high-pressure neutron diffraction structural studies (Tibbals *et al* (1982)). This observation contradicts the previous interpretation of the phase transition, based on high-pressure single-crystal x-ray diffraction studies (Morosin and Samara (1971)), where it was suggested that $\delta \rightarrow 0$Å as $T_c \rightarrow 0$K, the H-atoms becoming centered on a single site in a symmetric O—H—O bond.

However, very recently Endo *et al* (1989) have located a structural phase transition in KDP at a pressure of 2.7 GPa, at ambient temperature, and have asserted that the hydrogen atom is located at the centre of the hydrogen bond above the transition, although they could not observe this directly from their high-pressure single-crystal x-ray diffraction study. The assumption that the H-atoms become centered in O—H—O bonds, and hence $\delta \rightarrow 0$Å at the phase transition, is based on the observation that 2R decreases linearly to 2.45Å as the phase transition is approached (to subsequently increase again, at first by an abrupt

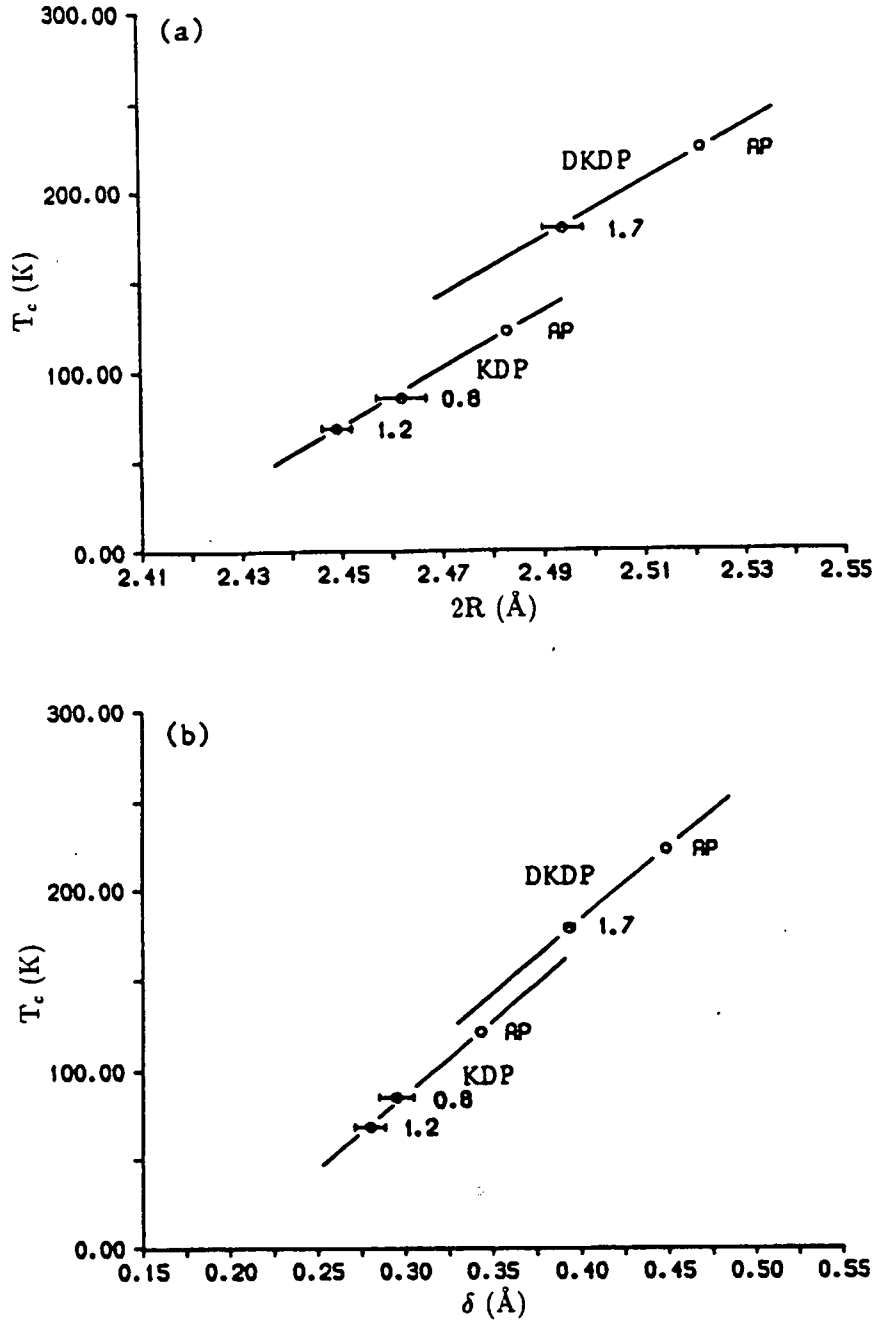

Figure 5.3: (a) The variation of T_c with the O—H—O bondlength, 2R, and (b) the variation of T_c with the H-site separation, δ, in KH_2PO_4 (KDP) and KD_2PO_4 (DKDP). The pressure is given against each point as AP (ambient pressure) or the number of GPa applied. Where error bars are not shown, the errors are smaller than the size of the symbols used to plot the point. The lines are guides for the eye only.

jump and then more gradually, as the pressure is increased), a value less than the 2.47Å that Matsushita and Matsubara (1982) have predicted, in their model of the hydrogen bond, that the two minima merge to produce an essentially symmetric potential with one minimum. The results also support the conclusions of Meyer *et al* (1980), which note that the decrease in 2R is smaller than would be expected from the contraction of the a-axis and that the effects of pressure are not confined to shortening the overall hydrogen bond length (an assumption made in earlier high-pressure studies (Morosin and Samara (1971)). Rather, a rotation of the PO_4 tetrahedra about their fourfold inversion ($\bar{4}$) axes (see figure 5.4) was found to take up to approximately 60% of the change in the unit cell dimension, a (Meyer *et al* (1980)). In the study conducted by Endo *et al*, the rotation angle of the PO_4 tetrahedra, represented as θ in figure 5.4, was found to increase over the whole pressure range with a small (approximately 1°) discontinuous increase at the phase transition. No significant pressure dependence was found for either the O-P-O bond angles within the tetrahedra or for the P-O bondlengths as the phase transition was approached, although the P-O bonds were observed to exhibit significant compression after the transition. The abrupt increase in 2R at the transition, and its more gradual increase at elevated pressures, was attributed to both a decrease in the P-O bondlengths and an increase in θ which counteract the progressive compression of the a-axis (see figure 5.4). Although the space group symmetry does not appear to change at the phase transition, a discontinuity in the compressibilty of the unit cell dimensions and, more recently, an anomaly in the capacitance of KDP at about 2.5 GPa, measured by Bao *et al* (1991), lend further evidence that a phase transition occurs.

In order to determine whether or not the H atoms do indeed become centered in symmetric O—H—O bonds, and to test the structural changes observed by Endo *et al* (1989) as the phase transition is approached, a single-crystal neutron-diffraction structural study was performed as close as possible to the pressure region in which the phase transition was expected to occur. This study, which was undertaken at the Institut Laue-Langevin, is presented in the following sections.

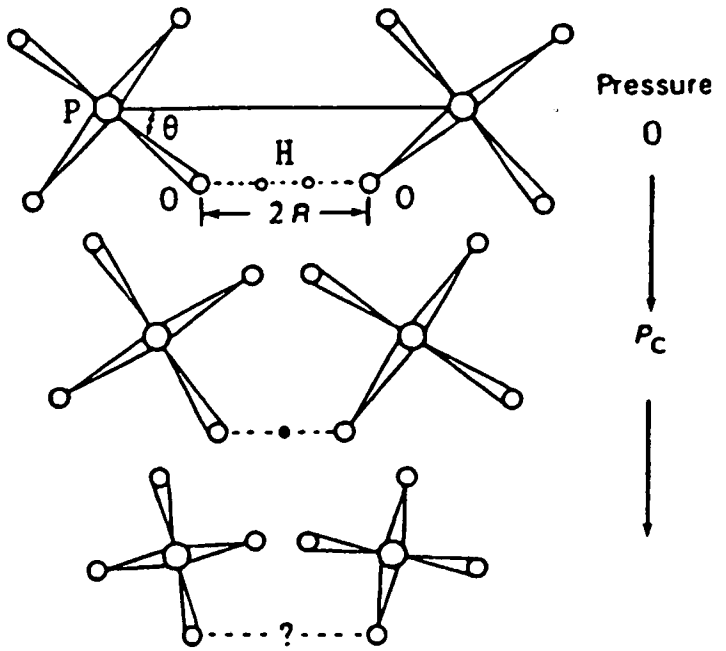

Figure 5.4: Schematic diagram showing the structural changes observed in KH_2PO_4 under pressure, viewed along the z axis. Only part of the structure is shown. (From Endo *et al* (1989).)

5.2 The Experiment and Data Analysis

The experiment was performed on the D9B diffractometer using the Ahsbahs design of pressure cell, described in section 2.3.1, and a PSD. The sample crystal was approximately cylindrical in shape, with a diameter of 1.1mm and a thickness of 0.7mm and was cut from a larger crystal purchased from Lasermetrics Incorporated, New Jersey. The sample was mounted in the cell with its crystallographic b-axis perpendicular to the anvils and a Ti-Zr gasket used to enclose both the sample and the deuterated methanol pressure transmitting fluid. As the pressure cell was equipped with steel anvils, to enable it to attain a pressure in the region of 3.0 GPa, the ruby fluorescence method could not be used to determine the pressure and, instead, the cell was loaded with a pressurizing force (on a hydraulic press in Marburg by Drs W.F. Kuhs and H. Ahsbahs) estimated to be sufficient to place the sample close to the phase transition. Subsequent measurements of the cell dimensions at the ILL would then allow the pressure to be determined from the known equation of state.

Before the cell was mounted on the D9B diffractometer the monochromator was set to give a wavelength of approximately 0.7Å. This was then calibrated accurately using the germanium standard crystal and found to be 0.6978(1)Å for a total of 40 centered reflections, including a number of reflections measured at negative θ values to allow the diffractometer offsets to be determined. With the detector monitoring the germanium (3 $\bar{3}$ 3) reflection, both the collimator and the PSD entrance aperture were adjusted to maximise the detected signal. As the standard crystal had been accurately centered on the diffractometer, using optical techniques, this ensured that the collimator and the detector aperture were directed at the centre of the goniometer circles.

With the wavelength calibrated and the diffractometer aligned, the Ahsbahs pressure cell was mounted on D9B and roughly centered using two micrometer gauges clamped to the χ circle. A search was then made for sample reflections and from these an initial UB derived. By monitoring the intensities of the (2 0 0), (0 $\bar{2}$ 0) and (0 0 8) reflections, using the micrometer gauges as a reference, the sample was carefully aligned on the diffractometer so that the maximum intensity for each reflection was recorded. The reflections were then recentered, along with a number of new reflections, and their setting angles, which deviated from their calculated values by the same magnitude (about 0.02°) as those from the germanium standard, confirmed that the sample had been placed accurately at the centre of the diffractometer. An improved UB was derived and from the refined unit cell dimensions, which had a relatively low precision at this early stage, the pressure was estimated to be in the region of about 2.7 GPa, a pressure deemed to place the sample sufficiently close to the phase transition for a data collection to be attempted with this loading of the cell. However, before data collection could proceed a number of tests had to be performed on the collimator aperture to ensure that the sample was completely bathed in a uniform beam of monochromated neutrons. This was achieved by performing a series of intensity measurements, on a number of selected reflections, with a range of different aperture diameters. From these measurements, it was determined that an aperture with a diameter of 4.1mm would be required to keep the signal to noise ratio to a minimum without affecting the sample illumination. Although it is common practice to test the detector aperture with the same procedure, this is only necessary for a single detector as the PSD allows an 'aperture' to be set electronically by restricting in-

tensity integration to pixels immediately around the sample reflection spot. The aperture placed in front of the PSD, therefore, is only used to ensure that the detection of background radiation is kept to a minimum but allowing each pixel on the detector surface to have an unrestricted view of the sample. In this experiment a detector aperture of 13mm was used.

Data were collected with ω-scans in a series of shells, covering a quarter of reciprocal space (+h, +k, ±l), for $0° \leq \theta \leq 15°$, $15° \leq \theta \leq 20°$ and $20° \leq \theta \leq 30°$, and, as the hydrogen bonds lie mainly in the plane perpendicular to the c-axis, (+h, +k, 0) reflections were collected to a slightly higher resolution for $0° \leq \theta \leq 45°$. The scan profiles were then converted into integrated intensities using the method of Wilkinson *et al* (1988). In order to allow the intensity of weak reflections to be integrated accurately, a library of strong reflections (whose ellipsoidal peakshapes were well defined and could be easily fitted) was updated at each stage of the data collection to provide reference peakshape parameters as a function of θ. By interpolating between these peakshape parameters, the integration region, in terms of pixels, can be defined for each of the intensity scans containing a weak reflection. The library of strong reflections can also be used to accurately refine both the UB matrix and the unit cell dimensions as each scan profile, collected with a PSD, contains all the information required to determine the reflections setting angles (see section 2.4.2).

Initial refinements of the data were undertaken with the tetragonal ($I\bar{4}2d$) crystal structure and indicated that high ±l indexed reflections gave a relatively poor fit with a number of reflections differing by more than 5σ from their calculated values, where σ is the estimated standard deviation (esd) from counting statistics. However, reflections close to the (h k 0) reciprocal lattice plane (i.e. those reflections near to the plane of the anvil faces) gave fits to an acceptable 2σ level and indicated that, although the data were of good quality, there were problems with the absorption correction for the pressure cell, particularly for reflections measured with χ close to ±90°. The absorption correction was initially determined by measuring the pathlengths of the incident and diffracted beams through the Ti-Zr gasket and steel anvils from an enlarged drawing (figure 5.5a), assuming that the gasket had not deformed significantly while the pressurising force had been applied. However, this assumption does not take account of the displacement of the

sample towards the midpoint of the gasket hole, when the anvils are advanced to increase the pressure, and will result in an erroneous estimation of the absorption correction for reflections measured at negative χ settings of the diffractometer. In order to determine how this sample displacement affected the pathlengths of the diffracted and incident beams through the anvil and gasket materials, several reflections were measured, at both negative and positive χ, for various values of γ (where $\gamma = sin^{-1}(sin\omega sin\chi)$ and is the angle that both the incident and diffracted beams subtend with the plane of the gasket). The background measurements for the positive and negative χ reflections, when compared at the same values of γ, were very similar, indicating that the path lengths through the gasket and anvils must be almost identical. This was taken to indicate that the sample was placed almost at the midpoint of the gasket so that it is close to bridging between the two anvils. A revised absorption correction diagram was then drawn (shown in figure 5.5b) where the gasket was assumed to be symmetrically compressed and the sample crystal was within about 100μm from the midpoint between the anvils. The resulting absorption correction, which was applied to the data by a program written by R. Dorwarth of The University of Karlsruhe, was much more satisfactory and eliminated the systematic errors in reflections with high $\pm$l indices.

Refinement of the data collected to this point were used to generate a list of the strongest reflections in the region $30° \leq \theta \leq 45°$ and those reflections which the leverage procedure (Prince and Nicholson (1985)) had shown to be most sensitive to the u_{ii} thermal parameters of the hydrogen atoms. These reflections were then collected to give a final total of 743 reflections, of which 677 were non-identical, measured to $\sin\theta/\lambda$=1.01Å^{-1}. After correcting the data for anisotropic extinction all reflections were averaged over their symmetry equivalents to yield a total of 216 independent reflections. The data were refined with anisotropic thermal parameters for all the atoms and with the hydrogen atoms modelled over two sites (each with a 50% occupancy), giving an Rw and Gf of 0.069 and 1.22 respectively for 19 refinable parameters. Finally, the library of strong reflections was used to refine the cell dimensions and, from the known compressibility of KDP, the pressure was found to be 2.9(1) GPa.

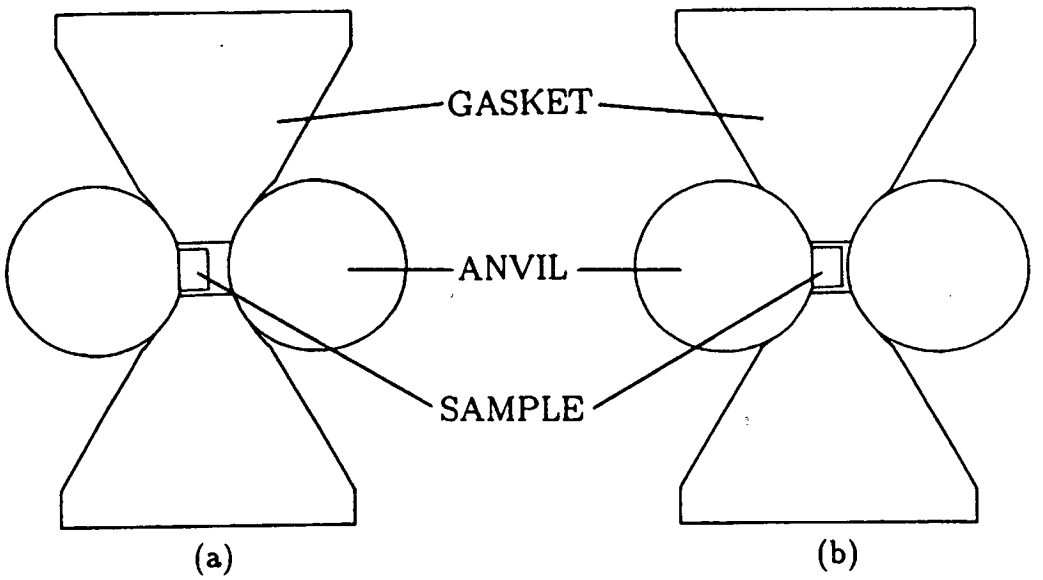

Figure 5.5: (a) The anvil and gasket geometry used for the initial absorption correction and (b) the anvil and gasket geometry used for the improved absorption correction (see text).

5.3 Results and Discussion

The unit cell dimensions, the refined atomic coordinates, the hydrogen bond dimensions and the P-O bond length are given in table 5.1 along with the single crystal neutron diffraction results of Tun *et al* (1988) and Tibbals *et al* (1982), at ambient pressure and 1.65 GPa respectively, for comparison. For completeness the results of the 2.6 GPa single-crystal x-ray diffraction study conducted by Endo *et al* (1989) are also given. The O-P-O bond angle and the structural parameters θ, ϕ and ψ, which will be defined later, are also given at the foot of table 5.1.

It is apparent, upon examination of table 5.1, that the refined positional parameters for the oxygen atoms are in excellent agreement with the 2.6 GPa values of Endo *et al* as is the oxygen-oxygen distance, 2R, all agreeing to within about σ. A close examination of Endo *et al's* data reveals that the discontinuous behaviour of the structure could occur between 2.6 GPa and 3.2 GPa and, therefore, the agreement between the refined values of the present study and the 2.6 GPa values

	AP	1.65 GPa	2.9 GPa	2.6 GPa
a (Å)	7.4521(4)	7.329(3)	7.2703(19)	7.278(2)
c (Å)	6.974(2)	6.856(3)	6.7877(30)	6.807(3)
x(O)	0.14839(4)	0.1526(1)	0.1536(6)	0.1539(15)
y(O)	0.08263(4)	0.0816(1)	0.0813(7)	0.0812(17)
z(O)	0.12586(5)	0.1267(2)	0.1288(11)	0.1297(15)
x(H)	0.14762(15)	0.1526	0.1588(15)	
y(H)	0.22582(20)	0.2286(7)	0.232(3)	
z(H)	0.12098(63)	0.1224(12)	0.121(9)	
2R (Å)	2.4946(6)	2.469(3)	2.452(9)	2.457(24)
δ (Å)	0.3647(28)	0.315(11)	0.27(4)	
P-O (Å)	1.5403(4)	1.537(2)	1.537(5)	1.544(11)
O-P-O (°)	110.52(3)	111.25(13)	110.75(50)	110.3(8)
θ (°)	60.89(1)	61.87(4)	62.11(29)	62.2(7)
ϕ (°)	0.265(19)	0.52(6)	1.16(36)	1.48(51)
ψ (°)	8.8(1.4)	6.6(2.9)	12(14)	

Table 5.1: The unit-cell dimensions, the refined atomic fractional coordinates, and selected interatomic distances and bond angles of KDP as a function of pressure. The strcuctural parameters θ, ϕ and ψ, defined in the text, are also given. The ambient pressure (AP), 1.65 GPa and 2.6 GPa values are taken from Tun *et al* (1988), Tibballs *et al* (1982) and Endo *et al* (1989) respectively. The estimated standard deviations (ESDs) for each of the values are given in parentheses.

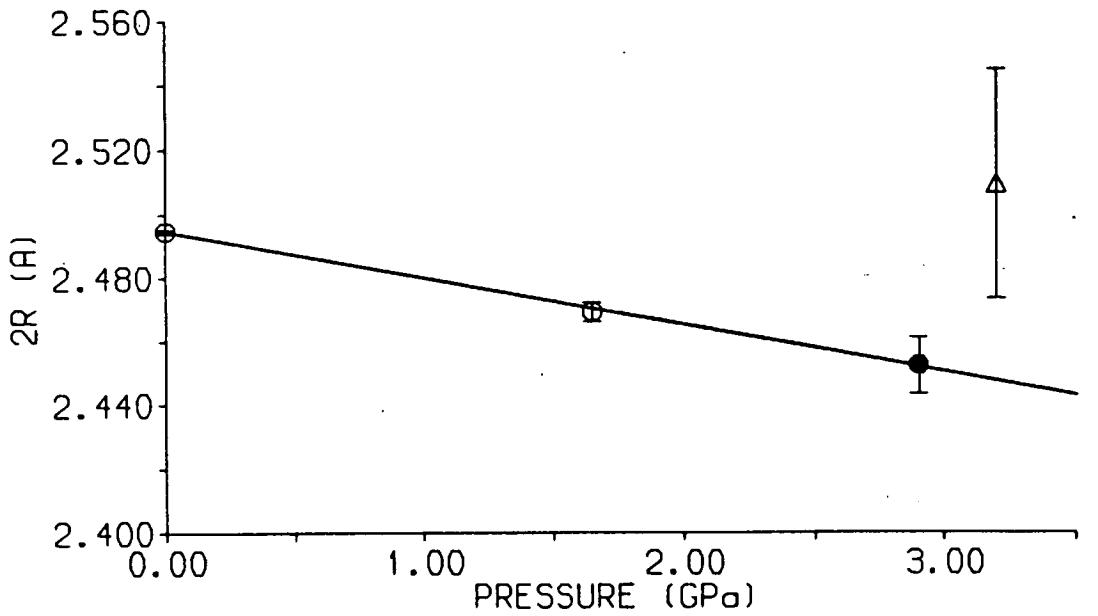

Figure 5.6: The pressure dependence of the O—H—O bondlength, 2R, in KH_2PO_4 from the study conducted by Tun *et al* (1988) and Tibballs *et al* (1982) (○), and from the present study (●). The point shown as △ is from the single-crystal x-ray diffraction study conducted by Endo *et al* (1989). The line is a guide to the eye only.

of Endo *et al* suggests that the phase transition has not yet been reached. This is confirmed in figure 5.6 where the value of 2R at 2.9 GPa lies on the line extrapolated from the ambient pressure and 1.65 GPa values and also re-affirms the linear decrease of 2R with pressure that was observed by Endo *et al* as the phase transition is approached. Certainly, the discontinuous increase of 2R to a value of 2.509(36) above the phase transition (Endo *et al* (1989)) is not observed, as can be seen in figure 5.6.

The linear decrease of 2R with pressure, as the phase transition is approached corresponds to a contraction of the oxygen-oxygen distance at a rate of 0.013(8)Å/GPa, or a reduction by about 1.7% from its ambient pressure value. On the other hand, the P-O bondlength and the O-P-O bond angle exhibit almost no change up to

2.9 GPa, within the accuracy of the refinement, and suggest that the PO_4 tetrahedra must remain relatively rigid in size and shape as the phase transition is approached. As the a-axis contracts by 2.4% at 2.9 GPa, with respect to its ambient pressure value, the reduction in 2R is much less than would be expected if the PO_4 tetrahedra are assumed to be unaffected by pressure i.e. if the main structural changes in the ab-plane are confined to only a compression of the oxygen-oxygen distance. However, as has already been mentioned in section 5.1, when the structure is compressed the P atoms necessarily move closer together, since they are at sites fixed by the $\bar{4}$ symmetry, but the PO_4 tetrahedra are free to rotate such that the oxygen-oxygen distance is preserved. This rotation of the PO_4 tetrahedra around the $\bar{4}$-axis manifests itself as an increase in the angle θ (previously defined in figure 5.4) and as can be seen in both table 5.1 and figure 5.7, is observed to increase over the whole pressure range up to the phase transition, in accordance with previous studies (see for example Meyer *et al* (1980)). The value of θ derived from the refinement of the 2.9 GPa data collected with the present experiment is in good agreement with the value of Endo *et al* and, given the relatively large esd's, forms an approximately linear relationship with the ambient pressure and 1.65 GPa values. Again, the discontinuous structural changes expected at the phase transition are not observed, as can be seen in figure 5.7, where the value of θ at 3.2 GPa (θ=63.64°) from Endo *et al* (1989) is also plotted to show the approximately 1° jump in its value.

As can be seen in figure 5.8, the hydrogen bond is inclined at an angle ϕ to the ab plane and, from the study of Endo *et al* (1989), this angle was observed to increase at progressively higher pressure, although the precision on the results was insufficient to show any anomalous behaviour at the phase transition. The results of the present study also indicate that ϕ increases with pressure as the phase transition is approached. However, the magnitude of this change, with respect to the ambient pressure value, is significantly less (by about 0.3°) than that observed by Endo it et al, as can be seen in table 5.1. This more gradual increase of ϕ with pressure is in better agreement with the 1.65 GPa value of Tibballs *et al* (1982), also shown in table 5.1, although it is still somewhat more than would be expected from a linear pressure dependence of ϕ.

The contraction of the oxygen-oxygen distance, 2R, to 2.452(9)Å is not accom-

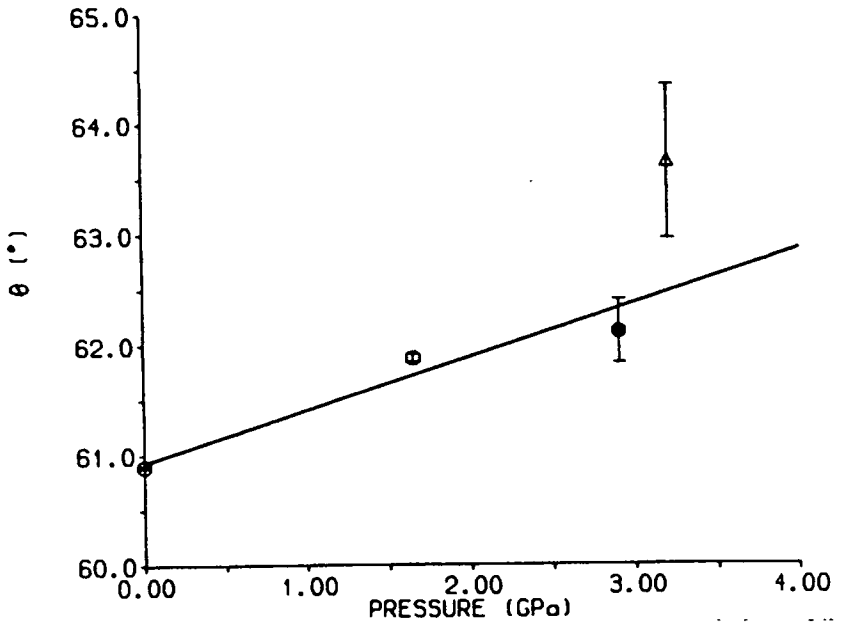

Figure 5.7: The pressure dependence of the rotation angle, θ, of the PO_4 tetrahedra around their $\bar{4}$-axis from the study conducted by Tun *et al* (1988) and Tibballs *et al* (1982) (○), and from the present study (●). The point shown as △ is from the single-crystal x-ray diffraction study conducted by Endo *et al* (1989). The line is a guide to the eye only.

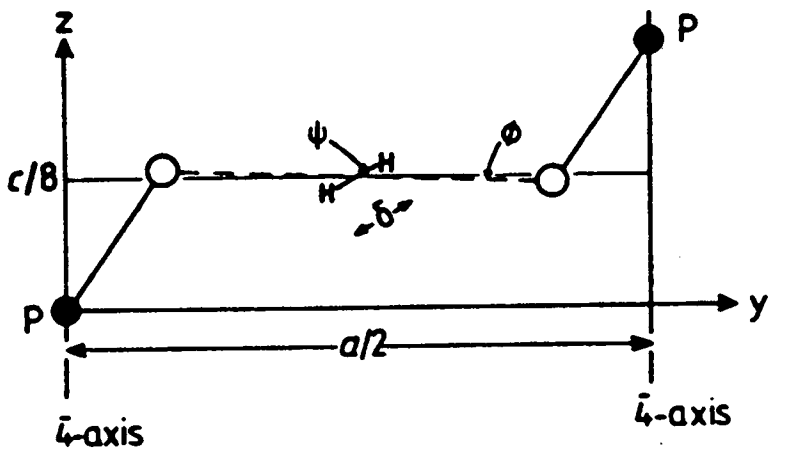

Figure 5.8: The hydrogen bond and adjoining atoms in the KH_2PO_4 structure seen in projection along the x-axis. The angles ϕ and ψ, respectively the inclination angles of the O...O and H...H lines to the XY plane, have been exaggerated by a factor of four. (From Nelmes *et al* (1982).)

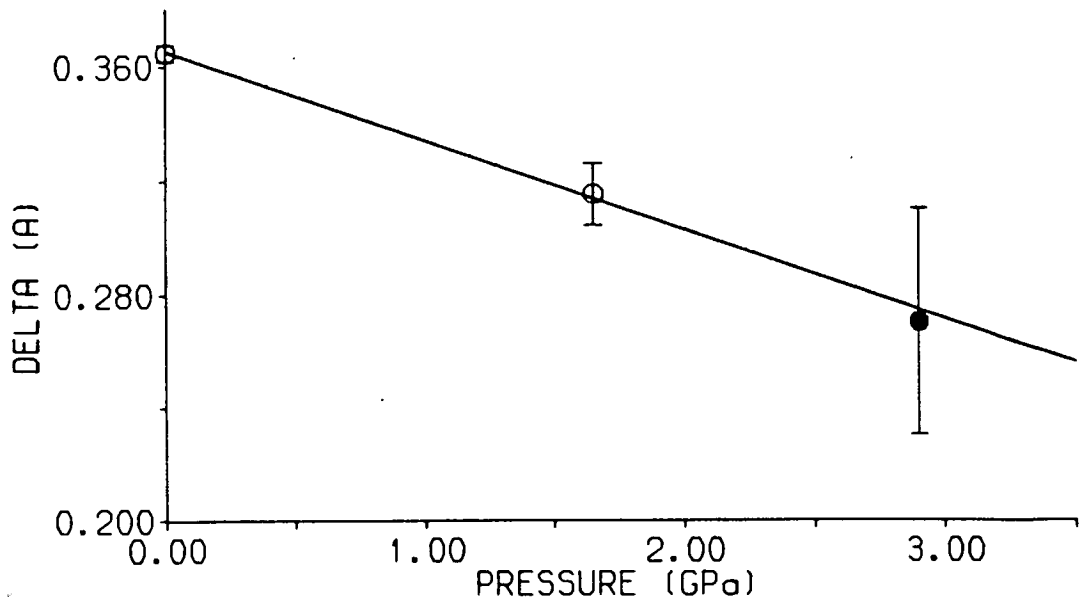

Figure 5.9: The pressure dependence of the H...H site separation, δ, in KH_2PO_4 from the study conducted by Tun *et al* (1988) and Tibballs *et al* (1982) (○), and from the present study (●). The line is a guide to the eye only.

panied by the hydrogen atom occupying the centre of a symmetric O-H-O bond, contrary to the assumptions of Endo *et al* (1989), since δ has a finite value at 2.9 GPa which is only about 25% smaller than that at ambient pressure. Indeed, comparing δ at 1.65 GPa with its ambient pressure value, as can be seen in figure 5.9, this reduction is no more than would be expected if δ decreases linearly with pressure at a rate of 0.033(14)Å/GPa. Although the hydrogen atom may become centered in an O-H-O type bond at the phase transition through some first-order effect, it is clear that the results of the present study disagree with the behaviour of the hydrogen bond expected by Endo *et al*, whose predictions were based on the calculations of Matsushita and Matsubara (1982). These calculations have also been shown to disagree with the behaviour of KDP at 1.65 GPa and 10K, in a recent high-pressure single-crystal neutron-diffraction study conducted by McMahon (1990). In this study, the hydrogen atoms were shown to be disordered over two sites, 0.217(23)Å apart, although a 2R of 2.442(3)Å was observed, which is significantly less than the 2.47Å calculated to give a hydrogen bond with a single minimum.

Finally, the line joining the hydrogen sites (H...H) is inclined at an angle ψ to the ab plane, as can be seen in figure 5.8, and, for completeness, the values of ψ are presented at the bottom of table 5.1. It is apparent that the precision on ψ is generally quite poor, particularly for the value derived from the present study. Although it is clearly not possible to show any significant pressure dependence of ψ as the phase transition is approached, it appears, nevertheless, that ψ remains finite at 2.9 GPa with a value comparable to those determined at ambient pressure and 1.65 GPa.

5.4 Conclusions

The principal changes in the structure of KDP, observed by Endo *et al* (1989), as the phase transition is approached are on the whole confirmed by the present high-pressure single-crystal neutron diffraction study. In particular, it appears that the oxygen-oxygen distance, 2R, undergoes a uniform compression to 2.9 GPa which is moderated by the rotation of the essentially rigid PO_4 tetrahedra around their $\bar{4}$-axes. The compression of 2R is also accompanied by a re-orientation of the hydrogen bond which is observed to increase its inclination with respect to the ab plane. However, the H...H site separation (δ) is not found to vanish as the phase transition is approached but, instead, exhibits a reduction which is no more than would be expected if δ decreases linearly with pressure. This result contradicts the assumptions made by Endo *et al* and leaves the structural mechanism for the transition unclear. It would, therefore, now be of interest to determine the structure at a higher pressure, using single-crystal neutron diffraction techniques, so that the behaviour of the hydrogen atoms in the high-pressure phase can be determined.

Although such a study was planned, the reactor at the ILL developed a serious mechanical fault, shortly after the experiment presented in this chapter was completed, which forced an extended shutdown of the reactor for major repair work. This is unfortunate as the D9B diffractometer, stationed on the 'hot source' of the ILL reactor, uniquely provides neutrons at both a suitable flux and at a short enough wavelength for the collection of high-pressure single-crystal data in a rea-

sonably short time and to an adequate resolution limit. Nelmes (1987) suggests that for KDP a resolution of $\sin\theta/\lambda > 1.0 \text{Å}^{-1}$ is required for an accurate determination of δ.) In contrast, other reactor based four-circle diffractometers have insufficient flux at short enough wavelengths to make high resolution structural studies of KDP practical. For example, the monochromator of the E5 diffractometer at the Hahn Meitner Institute, Berlin, can only provide three fixed wavelengths, of which $\lambda = 0.9$Å is the shortest, and is limited to a resolution of only $\sin\theta/\lambda = 0.88 \text{Å}^{-1}$. As the repairs to the ILL reactor are expected to be completed by 1994, at the earliest, it will be some time before the detailed behaviour of the hydrogen atoms in the high-pressure phase of KDP is known.

Chapter 6

High-Pressure Structural Studies of α-Rhombohedral Boron and Boron Carbide

6.1 Introduction

Icosohedral boron-rich solids are refractory materials with melting temperatures up to 2400°C, a thousand degrees higher than silicons, and exhibit a range of unique structural, electronic and thermal properties that are not only of scientific interest but are potentially useful in a variety of technological applications (Emin (1987)). In addition, the combination of these materials' lightness, strength and stability have made them invaluable thermal neutron absorbers in control rods and biological shields for fission reactors.

The principal boron polymorphs, of which there may be as many as 16 different types (Donahue (1974)), together with a number of boron-rich compounds, are all characterised by three-dimensional networks of boron atoms which are often built up from 12-atom icosahedra (figure 6.1). Of all these structures, α-rhombohedral boron (α-boron) has the simplest form and is composed of units of nearly regular icosahedra in a slightly deformed cubic close packed (face centered cubic) arrangement. As the ideal five-fold symmetry of the regular icosahedron cannot propagate through the crystal lattice, the distortion of each icosahedra, away from the five-fold symmetry, is accompanied by a translation of the close packed layers so that a rhombohedral unit cell is formed with an icosahedron at each vertex and

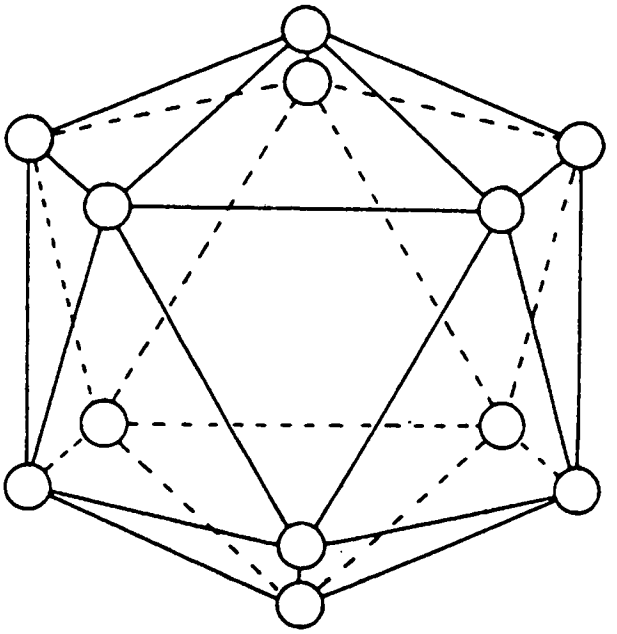

Figure 6.1: The B_{12} boron icosahedron, viewed from a direction close to a threefold axis. (From Bullett (1981).)

with a rhombohedral angle of α=58° (see figure 6.2): perfect cubic close packing would correspond to α=60°. Within the icosahedra, each boron atom has five neighbouring atoms and, therefore, in terms of conventional (two-centre) covalent bonding each boron atom must supply five electrons to form bonds with all its neighbours. However, as each boron atom has only three valence electrons in the second shell available for bonding, and as some electrons are also required for bonding between the icosahedra, the internal bonding of the icosahedra cannot be based on the usual two-centre bonding arrangement (Emin (1987)). Instead of forming the conventional two-centre bonds, where the bonding pair of electrons reside at the midpoint between the pair of bonded atoms, a 'three-centre' bond is formed, illustrated in figure 6.3, in which a pair of electrons is shared by three neighbouring atoms and, as a result, a charge accumulation occurs at the centre of the triangle formed by the three bonded atoms. High-resolution x-ray diffraction studies of α-boron show that there is a pronounced peaking of the electron density within the triangular faces of the icosahedra and, therefore, lend support to this model of the bonding (Emin (1987), Will (1987)). The B_{12} icosahedral units are

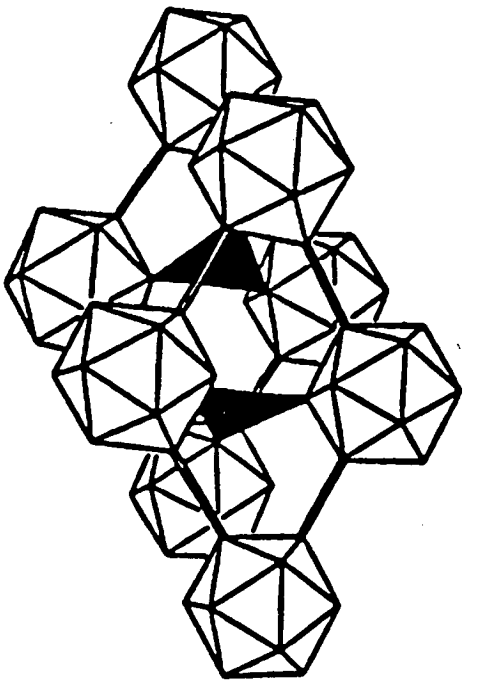

Figure 6.2: The structure of α-rhombohedral boron. The shaded triangles represent the intralayer intericosahedral three-centre bonds. (From Aselage *et al* (1990).)

linked by conventional two-centre bonds, which are parallel to the edges of the rhomohedral cell, and by intralayer intericosahedral three-centre bonds, shown as the shaded triangles in figure 6.2. The B-B distance in these three-centre bonds is 2.01Å, compared to the bond lengths of 1.75-1.81Å within each icosahedra and the 1.67Å for the two-centre intericosahedral links. It is these relatively long, and relatively weak (Seongbok (1990)), intralayer three-centre bonds which are believed to be associated with the high reactivity of α-boron and its transformation into the complex β-rhombohedral form above 1500K (Bullett (1982)).

The electronic properties of α-boron, which is an insulator, can be significantly altered by the addition of other atomic constituents between the icosahedra so that the intralayer intericosahedral three-centre bonds are replaced by conventional two-centre bonds linking the non-boron atoms to the icosahedra. The icosahedral boron pnictides, $B_{12}P_2$ and $B_{12}As_2$, and the boron carbides are notable examples. Of these, the boron carbides have received much scientific attention over recent years due to their distinctive electronic transport properties. Apparently,

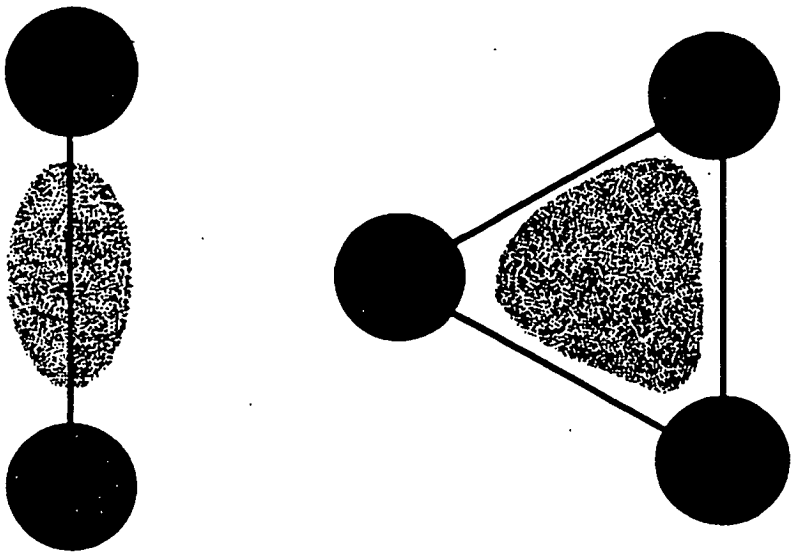

Figure 6.3: A schematic representation of (a) a two-centre bond and (b) a three-centre bond. The shaded regions show the dominant parts of the electronic charge distribution. (From Emin (1987).)

the boron carbides exist as single-phase materials over a range of carbon concentrations from about 8% to about 20% (Emin (1988)) and are characterised by a three-atom intericosahedral chain which is parallel to the [1 1 1] direction in the rhombohedral unit cell, as can be seen in figure 6.4. Depending on the composition, one, two or all of the atoms in this chain may be carbon atoms so that C-B-B, C-B-C and C-C-C chains can be formed. In addition, a boron atom may be replaced by a carbon atom within the icosahedra, forming disordered $B_{11}C$ icosahedral structural units i.e. the icosahedral carbon atom is distributed among many, if not all, icosahedral positions. At the highest concentration, B_4C (20% C), it is believed that the structure is composed of these disordered $B_{11}C$ icosahedra linked mainly by C-B-C chains, that is, three-atom chains with a boron atom placed between the two carbon atoms (Emin (1988)). As the carbon concentration is reduced, Aslage *et al* (1990) have observed that the structure initially expands along the [1 1 1] direction of the unit cell as the C-B-C chains are replaced by more weakly bonded C-B-B chains. At carbon concentrations below 13%, $B_{13}C_2$, no further expansion along the [1 1 1] direction of the unit cell was observed and this behaviour was attributed to the supply of C-B-C chains becoming exhausted so that further substitution of B for C occurs within the icosahedra, with

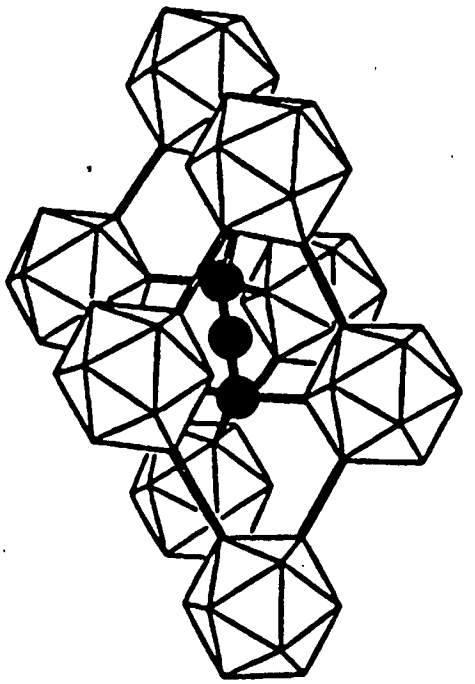

Figure 6.4: The structure of boron carbide. The shaded circles represent the three-atom intericosahedral chain which runs parallel to the [1 1 1] direction of the rhombohedral unit cell. (From Aselage *et al* (1990).)

a significantly smaller effect on the structure.

This simple model for the composition dependence of the structure is given additional support from measurements of the velocity of longitudinal and shear acoustic waves as a function of carbon concentration (Gieski *et al* (1990)). It was found that there was a pronounced decrease in the bulk modulus, derived from the sound velocity measurements, below the $B_{13}C_2$ concentration and was associated with a change in the stiffness of the most compressible structural unit, assumed to be the icosahedron, as the $B_{11}C$ icosahedra are replaced by 'softer' B_{12} icosahedra.

The $B_{11}C$ icosahedra are believed to be involved in the unusual electronic transport properties of boron carbide, which may make them a suitable material for efficient thermoelectric generators and, more generally, for very-high-temperature semiconductors. In boron carbide, the electronic charge carriers are singlet small bipolarons — pairs of electrons with oppositely aligned spins that are bound together by the distortions of the crystal structure that their presence induces —

which move between $B_{11}C$ icosahedra by a succession of phonon assisted hops (Emin (1982)). Although such pairing of electrons is rarely observed, in the boron carbides there are two factors that favour small bipolaron formation: the excess charges are distributed over the surface of the $B_{11}C$ icosahedra so that the coulomb repulsion between a pair of charge carriers is considerably smaller than that associated with placing them on a single atomic site; the attractive force associated with the carrier-induced atomic displacements is relatively large as the strong bonding, and small atomic radii, yield especially strong coupling between electrons and the crystal lattice (Emin (1987)). Therefore, the boron carbide structure is particularly suited to electronic conduction by the hopping of small bipolarons. Under the application of high hydrostatic pressure, however, the conductivity of boron carbide exhibits an anomalous behaviour. Although compression of a solid generally increases the hopping mobility and thus the conductivity (by enhancing the electronic overlap between the hopping sites and by increasing the atomic vibrational frequencies), Samara *et al* (1985) have observed that the conductivity of boron carbide decreases with pressure. This behaviour has been linked to the compression of the icosahedra which causes the hopping activation energy to increase at the expense of the increased vibrational frequencies and electronic overlap. The results of Samara *et al's* study were taken to indicate that, with pressure, the sites (icosahedra) are compressed more than the intersite (intericosahedral) separations: a view consistent with bonding theory (Bullett (1982)) and indirect experimental evidence (Emin (1990)) which suggest that the icosahedra are the most compressible parts of the structure. However, there is no direct structural evidence to support this assumption.

It is, therefore, clearly of interest to determine whether or not the 12-atom icosahedra are indeed the most compressible parts of the structure and to establish the difference in compressibility between B_{12} icosahedra and $B_{11}C$ icosahedra. In the following sections of this chapter parallel studies of the pressure dependence of both the α-boron and B_4C structures will be described, allowing the direct comparison of the relative compressiblities of the B_{12} icosahedra and $B_{11}C$ icosahedra for the first time.

6.2 The Experiments and Data Analysis

6.2.1 X-ray Single-Crystal Studies of α-Rhombohedral Boron

As boron has a low atomic number, with a correspondingly low electron density and x-ray scattering power, a high-pressure structural study of α-boron would appear to be more ideally suited to the techniques of neutron-diffraction rather than those of x-ray diffraction. However, it is extremely difficult to produce large quantities of chemically pure α-boron, certainly in sufficient quantities for a neutron-diffraction experiment, and, as a consequence, it was necessary to resort to single-crystal x-ray diffraction techniques instead.

The sample crystal was provided by Drs B. Morosin and T.L. Aselage of Sandia Laboratories, Albuquerque, New Mexico, and found to be an extremely thin platelet, or slab, of dimensions 425 $\times$ 150 $\times$ 13 μm^3 with the [1 1 1] direction of the rhomohedral unit cell (the c-axis in the hexagonal setting) perpendicular to the plane of the slab. A piece, of dimensions 75 $\times$ 75 $\times$ 13 μm^3, was cut from the sample crystal and loaded into a Merrill-Bassett DAC so that the face of the platelet was as close to being perpendicular to the diamond anvil culets as possible — a task made all the more difficult by the thinness of the sample. This sample orientation was chosen to minimise positional parameter correlations, during subsequent refinements of the restricted data, and to ensure that their was sufficient resolution in each of the crystallographic directions. (Ideally, for the hexagonal setting of the unit cell, the ($\bar{1}$ 1 0) would be parallel to the diamond-anvil culets.) The cell was assembled using a tungsten gasket to enclose the sample and the 4:1 methanol-ethanol pressure transmitting fluid, and initially taken to a pressure of 0.50(5) GPa, measured using the ruby fluorescence method.

The cell was then mounted on the Physics Departments CAD4 four-circle diffractometer which had been equipped with a graphite monochromated Ag-target x-ray tube. After centering the sample roughly on the diffractometer, using adapted optical techniques (King (1981)), a polaroid rotation photograph was exposed for 12 hours so that the sample reflections could be located. However, it was found that the sample reflections had insufficient intensity to be recorded on the polaroid

film. In order to enhance the intensity of the sample reflections, from the λ^3 term in the scattering power (Bacon (1975)), the x-ray tube was replaced with another containing a Mo-target. After carefully re-aligning the diffractometer, the pressure cell was remounted and another polaroid rotation photograph exposed. As the generator voltage had been reduced to 40kV, so that $\frac{\lambda}{2}$ reflections from the diamonds could be eliminated, the exposure time was extended to 18 hours. This photograph had successfully recorded a number of very faint spots which allowed the 2θ, ω and χ values of two sample reflections to be determined. However, the CAD4's automatic search routine was unable to find these reflections and the diffractometer had to be driven manually. By setting the 2θ, ω and χ circles at their calculated values the ϕ motor was slowly rotated until a rise in the detected intensity (approximately 0.5° wide in ϕ) was located. The other motors were then adjusted iteratively to maximise the signal. With the reflection roughly centered the automatic centering routine was now able to determine the reflections setting angles accurately, although it took approximately 45 minutes to do so (with the tube set back to its optimum voltage and current settings). The second reflection was centered with the same procedure and, after successfully indexing both reflections (with the rhomohedral unit cell), an initial UB matrix was derived. From this UB matrix a further nine 'strong' reflections were located and their setting angles subsequently determined using the automatic centering procedure. The diffractometer took over an hour to centre the faintest of these reflections.

The sample was then accurately centered on the diffractometer using the four-position method of Finger and King (1979) on four reflections. Having accurately centered the sample, the four-position method was used to determine the setting angles for all of the reflections, so that any residual sample mis-centering could be corrected for, and the results were used to refine the cell dimensions with the program Rafin, which allows the constraints imposed by the unit cell symmetry to be applied.

After measuring the profiles of selected reflections to determine the peak widths (which also indicated that the sample was a good quality single crystal) and determining the optimum detector aperture parameters, all accessible reflections were collected, using ω-scans, to a 2θ limit of approximately 80° ($\sin\theta/\lambda$=0.91Å^{-1}). The data were collected in the fixed-ϕ geometry at three positions 0.5° apart around

the scattering vector to detect simultaneous diffraction by the diamond anvils (section 3.2.3). After applying a correction for the absorption of both the pressure cell and sample (Finger and King (1978), Zucker *et al* (1983)), the data were averaged over repeated measurements and reflections affected by simultaneous diamond reflections removed from the data set. The data were then used for an initial least-squares refinement of the structure, including an isotropic extinction correction, using the Prometheus crystallographic programs (Zucker *et al* (1983)). The structural parameters obtained by Will *at al* (1987) were taken as starting values. Comparison of the calculated and measured intensities showed that a number of reflections had intensities significantly weaker than their calculated values. Analysis of the angles subtended by the incident and diffracted beams to the cell axis (ω and 2θ-ω respectively) showed that these reflections were partially occluded by the gasket, and were subsequently removed from the data set. As many of the reflections were relatively weak, the leverage procedure of Prince and Nicholson (1985) (see section 2.4.1) was used to identify those reflections most sensitive to the refinable structural parameters so that their intensities could be measured with improved precision. These reflections were then remeasured with increased counting times and added to the data set. The resulting data set was then used for a final structural refinement. As for the initial refinement, all reflections not rejected due to simultaneous diamond reflections and gasket occlusion were corrected for both pressure cell and sample absorption and averaged over identical reflections. In order to assign weights correctly to the reflections in the data set, averaging over equivalent reflections and leveraged reflections only occurred after the final structural refinement (following the same procedure as that used for the KTP experiment (section (4.2.1)) and allowed the internal consistency of the data to be determined. The positional parameters refined stably with no significant correlations between them and the isotropic thermal parameters were found to give physically reasonable values — refinements with anisotropic thermal parameters proved to be unstable. As the ambient structural study undertaken by Will *et al* (1987) shows that the thermal motion of both of the refinable boron atoms are almost isotropic and the positional parameters of the present high-pressure study agree with their values to within about 1.5σ, it appears that constraining the thermal parameters to be isotropic is not only appropriate but also does not bias the refinement significantly. The final cycles of the refinement of the 0.50 GPa data set gave a weighted residual (R_w) and goodness-of-fit of 0.079 and 1.63

respectively for 114 independent reflections and 8 refinable parameters.

With the refinement of the low-pressure reference data set completed, the pressure was increased to 4.00(5) GPa where the unit cell dimensions were determined using the four-position method of Finger and King (1979), and the same data collection and refinement procedures repeated. The final cycle of refinement gave an R_w and Gf of 0.073 and 1.24 for 114 reflections and 8 refinable parameters. The unit cell dimensions were also measured at 2.65(5) GPa to allow a more accurate determination of the bulk modulus than can be obtained with only two data points.

6.2.2 Neutron and X-ray Powder-Diffraction Studies of Boron Carbide B_4C

As relatively large quantities of chemically pure B_4C can be produced, in contrast to α-boron, a high-pressure structural study of B_4C is ideally suited to neutron-diffraction techniques. However, as the neutron absorption of naturally occurring boron is prohibitively high, due to the presence of 19% of the ^{10}B isotope ($\mu \approx 300 cm^{-1}$ for λ=1.08Å), the B_4C sample must be prepared from ^{11}B-enriched boron which has a much smaller absorption (^{11}B $\mu \approx 0 cm^{-1}$ for λ=1.08Å). Suitable powder samples, prepared from 98.5% ^{11}B enriched boron, were provided by Drs B. Morosin and T.L. Aselage of Sandia Laboratories, Albuquerque, New Mexico.

The high-pressure neutron powder-diffraction experiments were performed on the POLARIS diffractometer of the U.K. spallation source, ISIS, at the Rutherford Appleton Laboratory using time-of-flight techniques and the Paris-Edinburgh pressure cell. The Paris-Edinburgh cell, which employs a novel opposed-anvil design, has been described in detail in section 3.4.2 along with the collimation that has been developed to reduce the background and optimise the signal-to-noise ratio of the high-pressure powder patterns.

A sample, suitable for loading into the cell, was prepared from a mixture of B_4C and NaCl pressure-calibrant in the proportions 1:1 by volume and the material was pre-compressed to approximately 1 GPa prior to loading to produce a pellet

of the correct size to fit the pressure chamber formed by the gasket and anvils. The pellet was then placed in the cell and the tungsten-carbide anvils were closed by screwing the breech through the upper platen by hand. This ensured that both the sample and the composite Ti-Zr gasket (see section 3.4.2) were held firmly in place without pressurizing the sample. As it was assumed that NaCl, which has a relatively low shear strength compared to B_4C, would give adequately quasi-hydrostatic conditions a pressure transmitting fluid was not included. Before mounting the cell in the diffractometer sample tank, a 4mm diameter collimation piece was attached to the breech to ensure that the incident neutron beam would not illuminate the edges of the 6mm diameter gasket hole. As was previously described in section 3.4.2, collimation of the beam diffracted at 2θ=90° is provided by covering the faces of the anvils with a neutron absorbing Gd_2O_3-doped epoxy paint and by a slit mounted on the side of the cell to restrict the region viewed by the detectors to that immediately around the sample.

Data were collected at applied loads of 0, 40 and 70 tonnes, with the 90° bank of twenty 2 × 13 inch ^{3}He detectors, for data collection periods of 3 hours 45 minutes, 4 hours 15 minutes and 10 hours respectively. The longer data collection time at successively higher pressures was required to maintain a similar degree of counting statistics between the data sets as the anvils attenuated a progressively larger fraction of both the incident and diffracted beams. A powder pattern collected at an applied load higher than 70 tonnes showed pronounced pressure broadening of the diffraction peaks, thought to result from bridging between grains in the sample, and data collection was terminated at this point.

The powder patterns were normalized for the spectral function of the incident beam by the use of a vanadium standard powder pattern and were refined using the GSAS Rietveld program (Larson and Von Dreele (1990)) with the unit cell dimensions and atomic positional parameters of Morosin *et al* (1987) as starting values. Although the scale factors, background parameters and cell dimensions were found to refine stably along with a peak-width parameter to model the effects of pressure induced broadening, it was not possible to refine the atomic positional parameters freely and constraints had to be applied. As the principal aim of this study is to determine the relative compressibility of the twelve-atom icosahedra with respect to the crystal lattice, the positional parameters for both of the non-

symmetry related atoms in the icosahedron (two refinable positional parameters for each atom) were linked to allow the compression of the icosahedra to be expressed by one parameter. This was achieved by constraining the atoms to only shift in directions directly towards, or away from, the centre of the icosahedra (i.e. the origin of the unit cell) and by fixing the atoms to undergo the same magnitude of shift. In order to determine the effect of these constraints, the 4.0 GPa data set obtained from the single-crystal x-ray diffraction study of α-boron (see preceding section) was refined with similar constraints applied, using the atomic positional parameters derived from the 0.5 GPa data set as starting values. This refinement was then compared to the original refinement, where the atoms had been allowed to refine freely, by applying Hamilton's R-factor test (Hamilton (1974a)). The test revealed that the constraints changed the R-factor by less than the 75% confidence level and are therefore not statistically significant for the x-ray single-crystal data (Hamilton (1964)). Although it is not possible to perform a similar test on the neutron powder-diffraction data, it appears, nevertheless, that these constraints will not bias the refinement significantly. Isotropic thermal parameters were also refined for each atom at all pressures.

The values of the lattice parameter of NaCl, derived from each of the refinements, were used to obtain a pressure from the Decker equation-of-state which has an accuracy of 0.05 - 0.10 GPa in the range 0 - 10 GPa (Decker (1971)). The pressures corresponding to the applied loads of 40 and 70 tonnes were found to be 2.3 and 5.8 GPa respectively.

As the image plate has proved itself to be an extremely sensitive detector and, for example, has successfully recorded the very weak (2 0 0) reflection of the cubic phase of InSb under pressure (Nelmes *et al* (1992)), which arises from the difference in scattering between In and Sb (an equivalent of only two electrons), it was thought that the image plate would be suitable for collecting high-pressure x-ray powder diffraction patterns of B_4C, that were expected to be extremely weak. In view of this, a second high-pressure structural study of B_4C was planned, to compliment the neutron-diffraction experiment conducted at ISIS, using angle-dispersive techniques and the newly developed Edinburgh-Daresbury image-plate system.

The high-pressure x-ray powder-diffraction experiments were performed at station 9.1 at the SRS, Daresbury, which is located on the 5T wiggler magnet beamline. A water-cooled channel-cut Si (1 1 1) monochromator was used to select a wavelength of 0.4446(1)Å from the spectrum of the wiggler magnet and was calibrated by carrying out a conventional 2θ scan of a standard powder sample of Si and fitting to the measured peak positions. This wavelength was chosen so that the platinum pinhole could attenuate the $\frac{\lambda}{3}$ harmonic from the monochromator (see section 3.3.2).

A finely powdered sample of B_4C was provided by Drs B. Morosin and T.L. Aselage of Sandia Laboratories, Albuquerque, New Mexico (from a different batch than that used in the neutron powder-diffraction experiment), and loaded into a DXR-4 design of diamond-anvil pressure cell (section 2.3.1). The sample was enclosed in a tungsten gasket and, as the Daresbury ruby fluorescence system was found to be faulty, a small quantity of NaCl (approximately 25%) was added to the sample for pressure calibration. A mixture of methanol and ethanol, in the ratio of 4:1, was used as a pressure transmitting fluid. Initially, the cell was closed with a sufficient applied force to ensure that the gasket was firmly sealed and that the sample was held at only a relatively low pressure.

The pressure cell was then mounted on the image plate system and aligned with respect to the monochromated x-ray beam, using the procedures described in the first paragraph of section 3.3.4. (Note that the angular alignment procedures for the telescope and pressure cell had not been implemented on the beamline set up at the time this experiment was undertaken.) The dimensions of the monochromatic incident x-ray beam were reduced to a diameter of 75μm with a platinum pinhole and the sample to plate distance was set at approximately 250mm. After an exposure of approximately 90 minutes, the plate was read and the resulting image (shown in figure 6.5a) integrated with the Platypus suite of programs (Piltz *et al* (1992)). The powder pattern obtained from the integration showed several distinct B_4C diffraction peaks although, as can be seen from figure 6.5b, they were significantly weaker than those of the NaCl pressure calibrant. Having established that an acceptable B_4C powder pattern could be observed from a sample contained within the pressure cell, powder patterns were collected with the cell at two progressively higher applied loads. A further attempt to increase the pressure

resulted in pronounced pressure broadening of both the B_4C and NaCl peaks, due to the gasket failing, and data collection was terminated at this point.

The sample to plate distance was then calibrated by reloading the cell with only a NaCl powder sample and collecting a reference powder pattern. As no pressure fluid was used and care had been taken to ensure that a pressurizing force had not been applied to the anvils, the ambient pressure NaCl unit cell dimensions were used to express the Bragg peak positions on the integrated profiles in terms of 2θ and subsequently, from a knowledge of the pixel dimensions (88 μm), the distance from the reference sample to the plate was determined to be 256.09(1)mm

However, the calibration of the high-pressure powder patterns from pixels to 2θ, derived using this sample to plate distance, was found to give erroneous unit cell dimensions and, for example, the refined cell dimensions for the NaCl pressure calibrant for the initial low-pressure powder pattern was found to be 0.14% higher than its ambient pressure value — corresponding to a *negative* pressure of about 0.1 GPa from Decker's equation-of-state (Decker (1971)). In view of this, the sample to plate distance was re-calculated using the NaCl peaks of the low-pressure pattern as a reference, assuming that the low-pressure loading of the cell was close to ambient pressure. (This assumption appears to be justified as a comparison of the NaCl:B_4C unit cell volume ratio for the low-pressure x-ray data with those of the 0 GPa and 2.3 GPa neutron data indicates that the pressure cell was initially loaded to less than 0.13 GPa.) The sample to plate distance was now determined to be 255.84(1)mm.

Although it is unclear how the discrepancy of 0.25mm (250μm) arose, it may be partly due to a purely mechanical shift of the cell with respect to the image plate, or, perhaps, a change in the wavelength, between data collection and distance calibration. Certainly, as the monochromator was scanned (for another experiment running parallel to this) and the synchrotron was refilled between data collection and distance calibration, a change in the wavelength due to stepping errors in the monochromator scan or a mis-steering of the synchrotron beam, cannot be ruled out.

The integrated powder patterns were now re-calibrated, in terms of 2θ, using

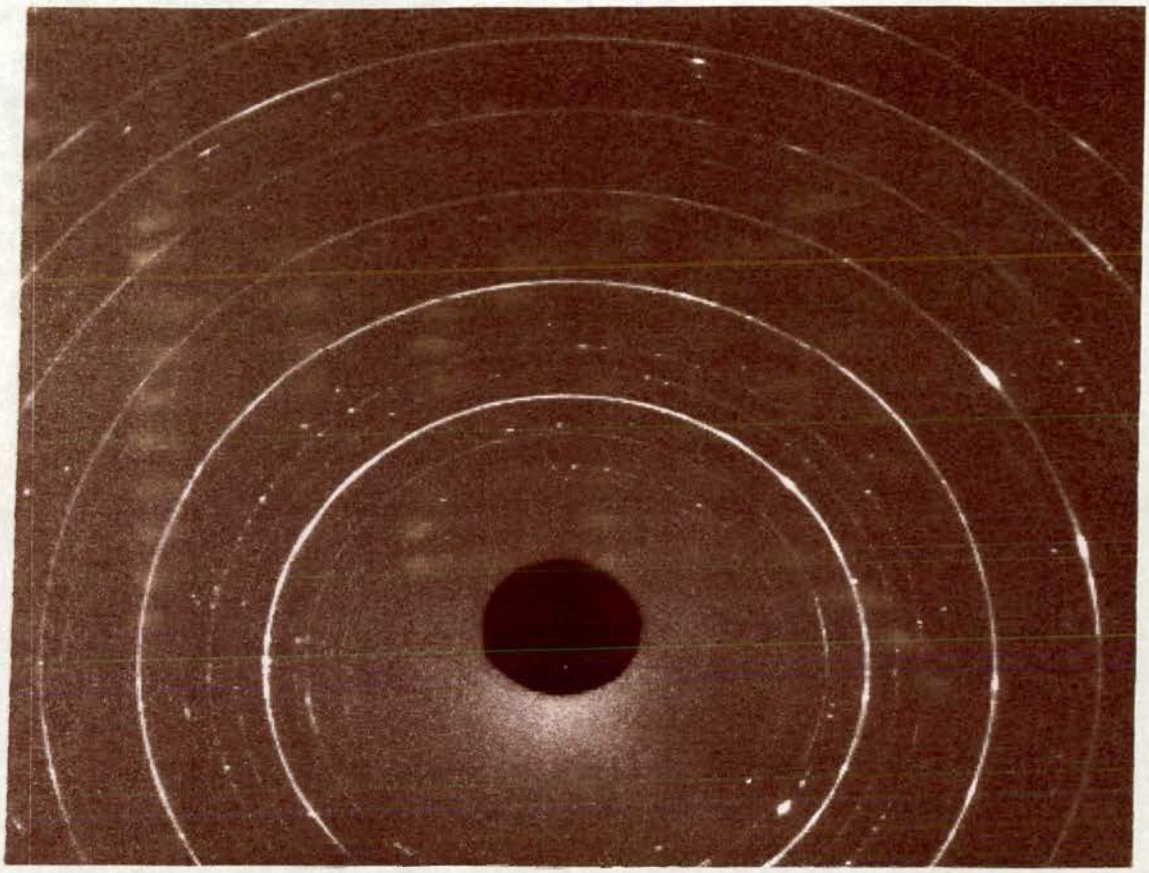

(a)

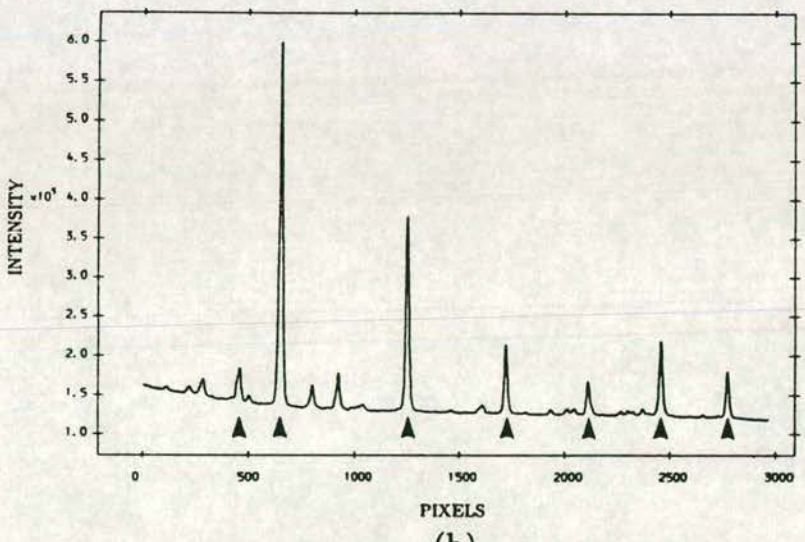

(b)

Figure 6.5: (a) — Part of the diffraction pattern obtained from the mixture of B_4C and NaCl. (b) — The fully integrated profile of the diffraction pattern shown in (a). The NaCl peaks are indicated by arrows.

the revised sample to plate distance, and were refined with the GSAS suite of programs. As with the neutron-diffraction data, the scale factors, background parameters, cell dimensions and peak shape parameters were all found to refine stably with the exception of the positional parameters which had to be constrained. The same constraints as those used in the neutron powder-diffraction refinements were applied. Isotropic thermal parameters were also refined for each atom at all pressures. The values of the NaCl lattice parameter, obtained from each of the refinements, were used to determine a pressure from the Decker equation-of-state (Decker (1971)). The pressures for consecutive applied loads were found to be 0, 2.5 and 3.7 GPa.

6.3 Results and Discussion

The unit cell dimensions, the refined atomic coordinates and the radius of the B_{12}-icosahedron (as defined by the average of the B(1) and B(2) distances from the origin of the unit cell) for the α-boron study are given in table 6.1 along with the ambient-pressure single-crystal x-ray diffraction results of Will *et al* (1987) for comparison. In order to allow the α-boron results to be compared directly with those of the neutron and x-ray powder-diffraction studies of B_4C, the unit cell dimensions and the atomic coordinates (which were refined in the rhombohedral setting) are also given in terms of the equivalent hexagonal unit cell. The unit cell dimensions and the constrained atomic coordinates, and radius, of the $B_{11}C$-icosahedron for the neutron and x-ray powder diffraction studies of B_4C are given in tables 6.2a and 6.2b respectively. The results of the ambient-pressure single-crystal x-ray diffraction study of B_4C, conducted by Morosin *et al* (1987), are also given in tables 6.2a and 6.2b for comparison.

The relative unit cell volumes ($\frac{V}{V_0}$) for both α-boron and B_4C are plotted as a function of pressure in figure 6.6. It is apparent, upon examination of figure 6.6, that the x-ray and neutron powder-diffraction techniques give an almost identical pressure dependence for the $\frac{V}{V_0}$ value of B_4C, and a linear fit through both sets of data yields a bulk modulus B=321.64(21) GPa. This is somewhat larger than the bulk modulus, B=247 GPa, that Gieske *et al* (1990) obtained for B_4C from

ultrasound measurements. A linear fit through the data points for α-boron gives a bulk modulus B=224(15) GPa. As no other experimentally determined value for the bulk modulus of α-boron has been published, this value can only be compared with the value of 246 GPa determined by Mailhiot *et al* (1990) from first-principles total-energy calculations. Allowing for the approximations in these calculations, the value of B for the present x-ray diffraction study is in reasonable agreement with that predicted by Mailhiot *et al* (1990).

From table 6.1, it is clear that the refined positional parameters for the α-boron B(1) and B(2) atoms exhibit almost no change under pressure, with the 0.5 GPa and 4.0 GPa values agreeing to within about 2σ (rhombohedral setting) and indicates that the structure undergoes an almost uniform compression. This is confirmed by examining the radius of the B_{12}-icosahedra (r_{icos}) which exhibits a 0.53±0.18% reduction between 0.5 and 4.0 GPa — comparable to the 0.54±0.01% and 0.50±0.07% compressions of the a- and c-axes of the hexagonal unit cell respectively. This is a surprising result since (as has already been stated in section 6.1) bonding theory and indirect experimental evidence have suggested that the icosahedra will be the most compressible parts of the structure due to the relatively weak three-centre intraicosahedral bonds. The intericosahedral three-centre bonds, which are the longest bonds in the structure, are also expected to be relatively weak. However, upon examination of table 6.3 (which gives all the non-symmetry related intericosahedral and intraicosahedral bond lengths in the α-boron structure) it is apparent that the intericosahedral three-centre bond (B(2)-B(2'))$_T$ exhibits a 0.45±0.15% reduction in length between 0.5 and 4.0 GPa and, given the magnitude of the uncertainties, this reduction is again no more than would be expected from a uniform compression of the structure.

As can be seen from tables 6.2a and 6.2b, the constrained refinements of the 0 GPa x-ray and neutron powder-diffraction data are in excellent agreement. However, it is apparent that at higher pressure the x-ray powder-diffraction results diverge from those of the neutron data and imply that the radius of the icosahedra (r_{icos}) increases with pressure. This is clearly not a physically sensible result

		AP	0.50 GPa	2.65 GPa	4.00 GPa
rhombohedral					
	a (Å)	5.063(7)	5.0680(8)	5.0505(7)	5.0421(10)
	α (°)	58.23(5)	58.043(8)	58.033(8)	58.027(12)
	V (Å^3)	88.0(4)	87.91(5)	86.98(4)	86.54(8)
B(1)	x	0.01008(2)	0.0102(4)		0.0094(4)
	z	-0.34650(3)	-0.3454(7)		-0.3445(7)
B(2)	x	0.22118(2)	0.2216(4)		0.2212(4)
	z	-0.36940(3)	-0.3699(6)		-0.3699(6)
hexagonal					
	a (Å)	4.927(3)	4.9174(9)	4.8896(8)	4.8910(11)
	c (Å)	12.564(7)	12.594(7)	12.552(6)	12.532(8)
	V (Å^3)	264.1(5)	263.74(24)	260.95(21)	259.61(29)
B(1)	x	0.11886(1)	0.1185(6)		0.1180(6)
	z	-0.10867(1)	-0.1083(5)		-0.1086(5)
B(2)	x	0.19689(1)	0.1972(5)		0.1970(5)
	z	0.02432(1)	0.0245(5)		0.0242(5)
	r_{icos} (Å)	1.691(3)	1.702(3)		1.692(3)

Table 6.1: The unit-cell dimensions, the unit-cell volume, the refined atomic fractional coordinates and the radius of the B_{12} icosahedra (r_{icos}) of α-boron as a function of pressure. The unit-cell dimensions, the unit-cell volume and the fractional coordinates are also given in terms of the equvalent hexagonal cell. The ambient-pressure (AP) results of Will *et al* (1987) are also given for comparison.

		AP	0 GPa	2.38 GPa	5.80 GPa
	a (Å)	5.6012(4)	5.5984(13)	5.583(3)	5.574(11)
	c (Å)	12.0734(13)	12.055(5)	12.036(13)	11.939(46)
	V (Å^3)	328.04(8)	327.21(14)	324.9(4)	321.3(1.2)
B(1)	x	-0.17030(3)	-0.1695(5)	-0.1690(6)	-0.1685(8)
	z	-0.02505(3)	-0.02494(8)	-0.02486(9)	-0.02478(12)
B(2)	x	-0.10741(3)	-0.1070(3)	-0.1067(3)	-0.1064(5)
	z	0.11391(3)	0.1134(3)	0.1131(4)	0.1128(5)
	r_{icos} (Å)	1.7025(5)	1.693(5)	1.685(6)	1.674(8)

		AP	0 GPa	2.50 GPa	3.70 GPa
	a (Å)	5.6012(4)	5.6088(24)	5.5911(20)	5.5858(22)
	c (Å)	12.0734(13)	12.081(5)	12.076(6)	12.060(8)
	V (Å^3)	328.04(8)	329.13(9)	326.93(14)	325.88(22)
B(1)	x	-0.17030(3)	-0.1697(12)	-0.1724(11)	-0.1760(27)
	z	-0.02505(3)	-0.02496(17)	-0.02536(16)	-0.0259(4)
B(2)	x	-0.10741(3)	-0.1071(6)	-0.1086(6)	-0.1106(16)
	z	0.11391(3)	0.1136(7)	0.1152(6)	0.1173(17)
	r_{icos} (Å)	1.7025(5)	1.700(11)	1.721(11)	1.752(28)

Table 6.2: The unit-cell dimensions, the unit-cell volume, the constrained atomic fractional coordinates and the radius (r_{icos}) of the $B_{11}C$ icosahedra of B_4C as a function of pressure, for (a) the neutron powder-diffraction study and (b) the x-ray powder diffraction study. The ambient-pressure (AP) results of Morosin *et al* (1987) are also given for comparison.

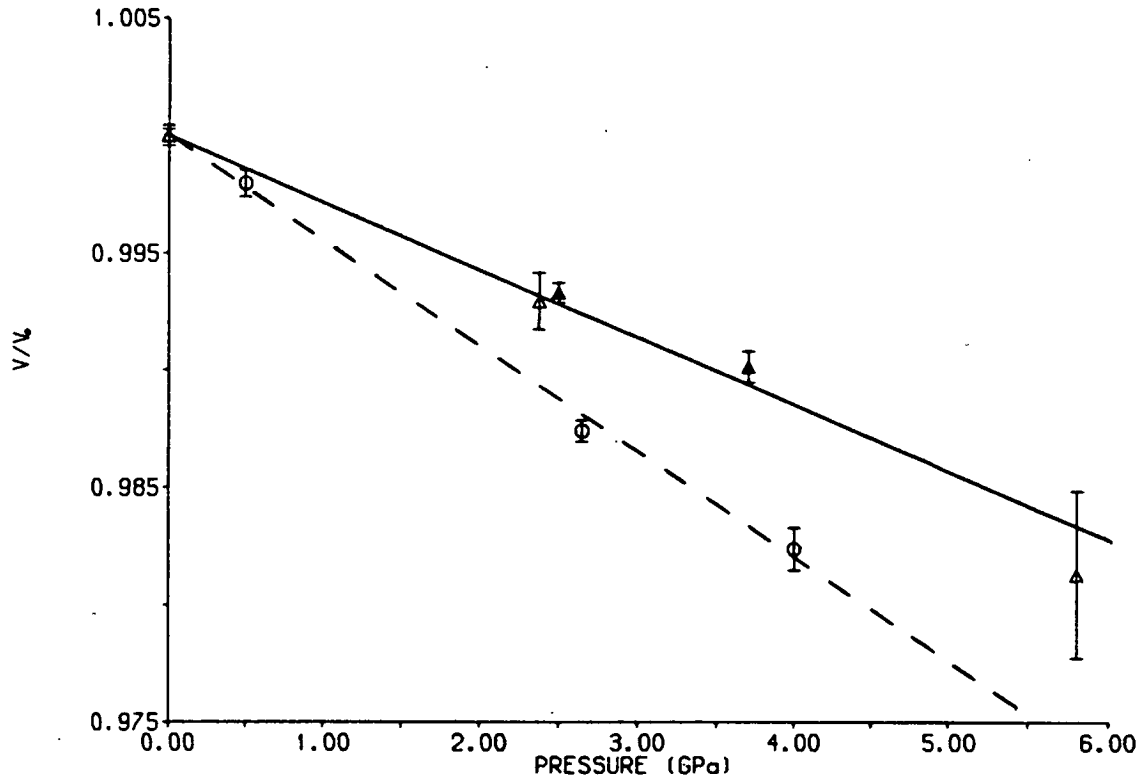

Figure 6.6: The relative unit-cell volumes (V/V_0) of α-boron and B_4C as a function of pressure. The points shown as ▲ and △ are for the x-ray and neutron powder-diffraction studies of B_4C respectively, and the points shown as ◯ are for the single-crystal x-ray diffraction studies of α-boron. The solid line represents a linear fit to the data for B_4C and the dashed line represents a linear fit to the data for α-boron.

	AP	0.50 GPa	4.00 GPa
Intericosahedral			
B(1)—B(1')	1.671(0)	1.682(7)	1.674(7)
B(2)—B(2')	2.014(0)	2.009(4)	2.000(3)
Intraicosahedral			
B(1)—B(1')	1.753(0)	1.749(4)	1.731(4)
B(1)—B(2)	1.800(0)	1.801(4)	1.793(4)
B(1)—B(2')	1.807(0)	1.806(3)	1.798(3)
B(2)—B(2')	1.784(0)	1.788(3)	1.776(3)

Table 6.3: The intericosahedral and intraicosahedral bondlengths (Å) of α-boron as a function of pressure. The ambient-pressure (AP) results of Will *et al* (1987) are also given for comparison.

and suggests, along with the increased esds for the 3.7 GPa refinement, that the x-ray data is of insufficient quality to follow the pressure dependence of the B_4C structure accurately. A close examination of the raw two-dimensional image plate data and the integrated powder pattern patterns reveals that, as well as generally being dominated by the NaCl diffraction peaks, the B_4C powder lines have numerous intense spots generated by relatively large sample crystallites. Although the Platypus integration software allows such spots to be averaged around the Debye-Scherrer rings and thereby improve the powder averaging, the large number of relatively intense diffraction spots in the B_4C powder pattern was sufficient to cause significant variations in the intensity of the integrated B_4C diffraction peaks. This effect, combined with the domination of the powder pattern by the NaCl pressure calibrant powder lines would inevitably lead to errors in the Reitveld refinement of the data.

On the other hand, the neutron-diffraction data appears to give physically rea-

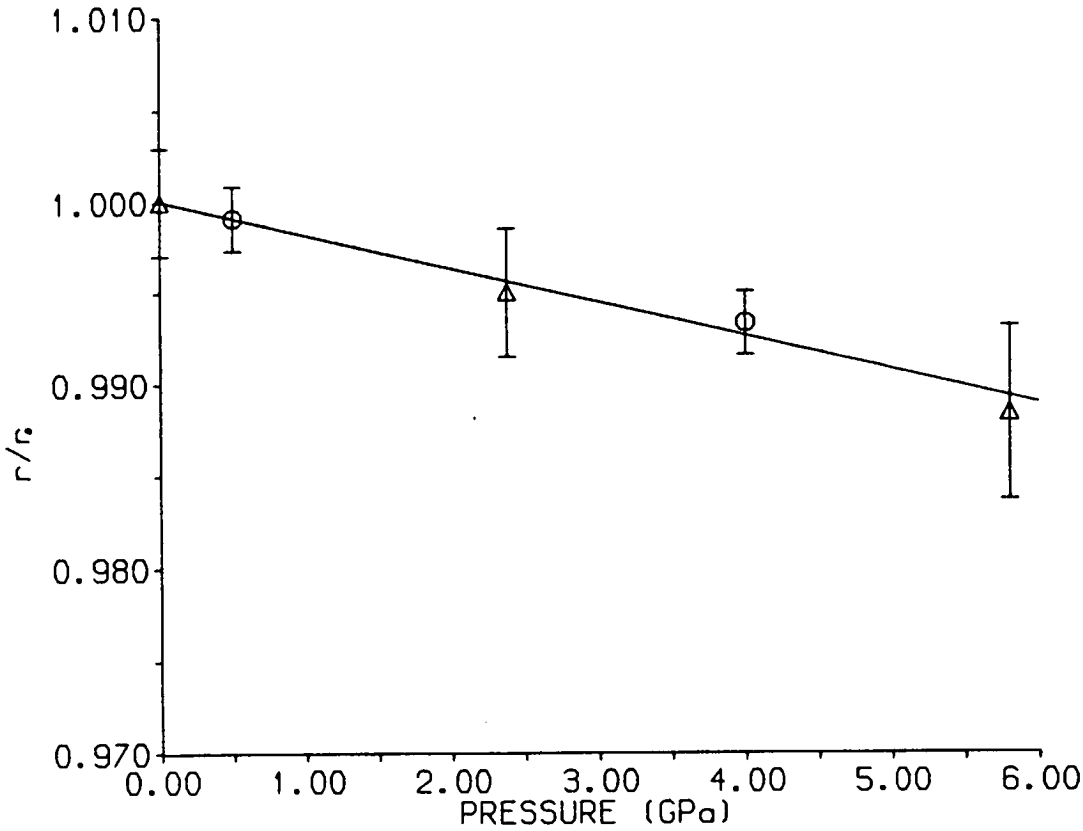

Figure 6.7: The relative radii (r/r_0) of the α-boron (○) and B_4C (△) icosahedra as a function of pressure. The line is a guide to the eye only.

sonable results with both the 2.4 and 5.8 GPa sets of constrained fractional coordinates agreeing to within 1.5σ with those of the 0 GPa data. As for the α-boron study, this implies that the icosahedra are compressing at a rate similar to that of the crystal lattice. However, upon close examination of table 6.2a it is evident that there is a trend in the fractional coordinates suggesting that the icosahedra may be compressing marginally faster than the crystal lattice. Indeed, as can be seen from figure 6.7, the trend in the fractional coordinates implies that, although the unit cell of B_4C is clearly less compressible than that of α-boron, within the precision of the refinements the radius of the $B_{11}C$ icosahedra decreases with pressure at the same rate as the B_{12} icosahedra of α-boron. This observation apparently contradicts the assumption that the $B_{11}C$ icosahedra are necessarily less compressible than the B_{12} icosahedra.

Finally, it is interesting to note that as the compressiblity of both the B_{12}-icosahedra and $B_{11}C$-icosahedra have not been shown to be significantly different, it appears that the pronounced decrease of the boron carbide bulk modulus below the 13% carbon concentration (observed by Gieski *et al* (1990)) can not be entirely explained by the substitution of the $B_{11}C$-icosahedra with B_{12}-icosahedra. It would, therefore, clearly be of interest to extend the present study and determine the pressure dependence of the boron carbide structure over a range of carbon concentrations so that it can be established whether or not icosahedral softening does indeed occur below the $B_{13}C_2$ stoichiometry.

6.4 Conclusions

The principal aim of the high-pressure crystal-structure studies presented in this chapter was to establish the relative compressibilities of the B_{12}-icosahedra and $B_{11}C$-icosahedra both with respect to one another and to the α-boron and B_4C unit cells. Although the neutron powder-diffraction refinements had to be constrained, this objective has been, on the whole, achieved and it appears, within the precision of the refined structural parameters, that the compressibilities of the B_{12} and $B_{11}C$ twelve-atom icosahedra do not differ significantly. Certainly, it has been found that the B_{12}-icosahedra are not sufficiently compressible to explain the pronounced

decrease in the bulk modulus of boron carbide below the 13% carbon concentration that was observed by Gieski *et al* (1990) from indirect measurements.

The problems encountered with the x-ray powder-diffraction refinements, described in the previous section, are principally due to the coarseness of the sample powder which did not allow a sufficient powder averaging to make the intensities of the B_4C diffraction peaks reliable. This is unfortunate, as the diffraction peaks, although relatively weak, are well defined and lie on an extremely flat background, which would otherwise make the B_4C powder pattern ideally suited to the Reitveld refinement method. Although no useful structural information could be obtained, the refinements did yield extremely precise cell dimensions which have relative errors considerably better than those obtained with energy-dispersive powder-diffraction techniques. For example the relative errors of the B_4C cell dimensions are a factor of 7 less than those obtained from an energy-dispersive powder-diffraction study of solid neon (Hemley *et al* (1989)) — an element which has a comparable x-ray scattering power to those of boron and carbon. However, to maintain the same level of accuracy great care has to be taken to ensure that systematic errors are not introduced from an incorrect sample to plate distance, as has been shown in section 6.2.2, or, perhaps, from other sources such as an incorrectly defined image centre or plate tilts during integration. As the ambient-pressure cell dimensions agree to within about 2σ, on average, with those of Morosin *et al* (1987), it is not expected that any residual error in the sample to plate distance will have a significant effect on the accuracy of the cell dimensions. Certainly, any residual errors in the unit cell dimensions on an absolute scale do not appear in the relative changes $\frac{V}{V_0}$ with pressure, since these lie on the same straight line, within error, as the $\frac{V}{V_0}$ values obtained from the neutron-diffraction study (as was previously shown in figure 6.6).

The problems encountered with the neutron powder-diffraction refinements, requiring the atomic positional parameters to be constrained, were principally caused by the relatively low signal-to-noise ratio of the B_4C powder patterns. However, an ambient-pressure powder pattern, collected from a sample contained within a vanadium can, was found to be suitable for an unconstrained Reitveld refinement and gave atomic positional parameters that agreed to within about 2σ, on average, with those of Morosin *et al* (1987). The gain in the signal-to-noise ratio, allowing

this free refinement of the structure, was determined to be a factor of two greater than the 0 tonne data collection for the sample contained within the pressure cell. As the residual 1.5% of ^{10}B contained within the B_4C accounts for almost all the sample absorption, an appreciable gain in the signal ought to be achieved by simply increasing the ^{11}B enrichment level. Detailed analysis of the absorption paths through the sample pellet indicates that a factor of two gain in the signal can be achieved with an ^{11}B enrichment level of about 99% and B_4C samples with this enrichment level can be prepared (Angel (1992)), although with considerable difficulty. Consequently, if the signal-to-noise ratio of the 'high-pressure' powder patterns of B_4C can be doubled, by increasing the ^{11}B enrichment level of the sample, it ought to be possible to follow the full structural changes of B_4C with neutron diffraction techniques using the Paris-Edinburgh cell. Nevertheless, the structural information derived from the present high-pressure neutron powder-diffraction study has proved to be extremely useful in determining the pressure dependence of the $B_{11}C$-icosahedra.

The single-crystal x-ray diffraction study of α-boron illustrates the high quality of data that can now be collected using a sealed tube laboratory x-ray source mounted on a standard four-circle diffractometer. Combining the use of a tungsten gasket, to eliminate a significant fraction of the background generated by the pressure cell, and the measurement of reflections at three points around the scattering vector, to identify and eliminate those sample reflections affected by simultaneous diamond reflections, it has been possible to successfully refine the crystal structure of a material whose atomic scattering power is comparable to that of the beryllium x-ray windows of the diamond anvil cell. It is also interesting to note that, as the typical sample dimensions for a high-pressure single-crystal x-ray diffraction study are of the order of $100 \times 100 \times 100\ \mu m^3$, the α-boron crystal employed in this study has a volume that is only 7% of that normally used —further reducing the effective scattering power of the sample. Recently, Hazen *et al* (1987) have used x-ray single-crystal techniques, on a standard laboratory diffractometer, to determine the crystal structure of solid H_2 at 5.4 GPa. As the crystal was found to assume the hexagonal-close-packed structure ($P6_3/mmc$, Z=2, V=26.55Å^3), the atomic coordinates are fixed by the crystal symmetry and only a single isotropic thermal parameter had to be refined. Therefore, as the elements He, Li and Be also adopt crystal structures that fix the atomic positions

by symmetry (Donahue (1982)), the present study of α-boron has successfully determined the full structural pressure dependence, including the refinement of the atomic positional parameters, of the most weakly scattering material that has yet been undertaken with high-pressure single-crystal x-ray diffraction techniques.

Chapter 7

Conclusions

The principal aim of this thesis was to examine the techniques by which crystal structures are determined at high pressure, whether using powders or single-crystals, x-ray or neutron radiation, and to apply the full range of the more recently developed state-of-the-art techniques to a number of interesting structural studies. To this end, a detailed review of high-pressure diffraction equipment and techniques has been presented, and the limits imposed on the collection of reliable diffraction data for the determination of accurate crystal structures at high pressure, prior to this thesis, have been described. An understanding of these limitations has allowed several major improvements to have been made using both x-ray and neutron-diffraction techniques on both powder and single-crystal samples.

For single-crystal x-ray diffraction, the very high absorption offered by tungsten gaskets for both MoKα and AgKα radiation has allowed extremely high quality data to be collected. The study of KTP illustrates how it is now possible to follow the structural changes of a crystal with pressure using AgKα radiation to a precision that is at least equivalent to that obtainable using MoKα radiation. Therefore, the use of tungsten gaskets significantly reduces many of the problems that have been associated with the use of AgKα radiation for high-pressure structural studies (Levien *et al* (1980)). The study of α-boron also illustrates that it is now possible, using a tungsten gasket to shield the detector from a significant fraction of the background generated by illuminated pressure cell components, to

collect reliable intensity data for the full structure determination of very weakly scattering materials with standard laboratory based equipment.

Simultaneous diffraction in the diamond anvils has been shown to reduce the intensity of a sample reflection by as much as 50% and, therefore, it is extremely important that those affected reflections are identified and eliminated from the data set so that the pressure dependence of a crystal structure can be determined accurately. For this reason, the data collection strategy developed by Loveday *et al* (1990), and reviewed in some detail in section 3.2.3, was adopted for the crystal-structure studies of KTP and α-boron.

For single-crystal neutron-diffraction studies, the combination of the Ahsbahs pressure cell and a position-sensitive detector has allowed the collection of intensity data that is not only extremely accurate but is also distributed over a relatively isotropic region of reciprocal space. As the position-sensitive detector is more sensitive to weak reflections than a single-detector (Lehmann *et al* (1989)) and also allows the accurate intensity integration of sample reflections in the proximity of contaminant scattering features from the pressure cell, its use was particularly important for the study of KDP at 2.9 GPa where the sample was an order of magnitude smaller in volume than that used by Tibballs *et al* (1982) (with a correspondingly lower scattering power) and the steel anvils of the pressure cell generated particularly intense powder lines (as was previously shown in figure 2.24). Although the precision on the refined atomic positional parameters is somewhat poorer than those of Tibballs *et al*, the study of KDP at 2.9 GPa, nevertheless, has precision significantly better than the corresponding single-crystal x-ray diffraction study of Endo *et al* (1989) and is the highest pressure single-crystal neutron-diffraction study undertaken to date.

The development of the Edinburgh-Daresbury Imaging Plate system uniquely provides the means of refining the atomic positional parameters, using the Rietveld method, from x-ray powder diffraction data collected from a sample contained at high-pressure within a diamond-anvil cell. Although the B_4C sample powder was insufficiently finely ground to allow an adequate powder averaging for a successful structural refinement, the study of B_4C, which was the first to attempt to determine the structural changes of a single-phase material with pressure using the

imaging plate system, does show that extremely precise, and accurate, equations of state can be determined if sufficient care is taken to eliminate systematic error. Certainly, as the diffraction peaks are well defined and lie on an extremely flat background, which would otherwise make the B_4C pattern ideally suited to the Rietveld refinement method, it appears that given a sample powder with sufficiently small crystallites (and the proposed cell-rocking mechanism described in section 3.3.4), to give an adequate powder averaging, it will be possible to refine the full crystal structures of weakly scattering (low Z) materials. Therefore, the combination of the image plate, with minimal background and careful collimation (to remove contaminant scattering), conical-aperture diamond anvil cells (to give full two-dimensional images) and a data analysis algorithm for integrating around the Debye-Scherrer rings (to improve powder averaging) clearly offers a great deal for high-pressure x-ray powder-diffraction.

The development of the Paris-Edinburgh pressure cell provides an unrivaled opportunity for studying crystal structures above 10 GPa with neutron powder-diffraction techniques and the Reitveld refinement method. However, the structural study of B_4C, and recently equation-of-state measurements of β-boron (Nelmes *et al* (1993)), does highlight the problem of maintaining hydrostatic conditions at such high pressures without a pressure transmitting fluid. It is, therefore, extremely important that a suitable pressure transmitting fluid, other than the prohibitively expensive deuterated alcohol mixtures, is found to enable the Paris-Edinburgh cell to be used to its full advantage.

Finally, although the newly developed techniques described in this thesis have allowed significant gains to be made for the determination of crystal structures at high pressure, it is, perhaps, worth speculating what other possible advances can be made in this field of research in the near future.

With the development of the new generation of brilliant synchrotron radiation sources, such as the ESRF in Grenoble, France, it appears that there are exciting prospects for high-pressure x-ray diffraction. The obvious advantages of the very intense radiation, the availability of high-photon flux at short wavelengths and the high inherent collimation of the synchrotron beam will offer significant gains in the signal-to-background ratio, allowing the precise measurement of extremely

weak reflections from weakly scattering (low Z) samples or from very small sample volumes. The decrease in sample volume offers the prospect of increasing the pressures that are currently obtainable, perhaps into the 1 TPa region.

In order to benefit from the high intensity provided by the new generation of synchrotrons and to improve the signal currently measurable with the synchrotron sources available at present, a new conical diffraction geometry is being developed for energy-dispersive powder-diffraction techniques (Hausermann (1992)). This new diffraction geometry, which uses a short conical diffracted-beam slit, not only ensures that the detector views the central region of the sample, thereby eliminating the detected parasitic scatter, but also increases the measured signal and effective powder averaging by allowing a larger solid angle of the diffracted radiation to be detected over conventional collimation techniques. The increased powder averaging may allow accurate intensity data to be collected with the energy-dispersive technique and, combined with some recent success at applying Rietveld refinement to energy-dispersive data (Neuling and Holzapfel (1992)), it may soon be possible to perform full structure determination (including the location of atoms not fixed by the crystal symmetry) with energy-dispersive x-ray powder-diffraction methods at high pressure.

The Edinburgh-Daresbury image plate system has already proved that the use of an image plate area detector is a very powerful technique for the study of polycrystalline samples at high pressure. As the image plate is certainly sensitive enough to discern the intensity of individual crystallites within a powder sample (as has been previously shown in figure 3.8 for the recrystallisation of InSb into a new phase at about 3.9 GPa), it may soon be possible to use the image plate as an area detector for monochromatic angle-dispersive studies of single-crystals at high pressure. The low divergence of the synchrotron beam compared to standard laboratory x-ray sources will allow a more pronounced separation of the reflections from the background with an accompanying improvement in the counting statistics, particularly for weak reflections. Comparative diffractometer studies of $AlPO_4$ at 2.90 GPa, conducted by Schulz and Sowa (1992), have already shown that a substantial gain in data quality can be achieved when synchrotron radiation is used rather than a laboratory x-ray source. It may also prove possible, with the use of so-called micro-crystals (approximately $10 \times 10 \times 10$ μm^3 in dimen-

sions), to take a single-crystal through a strongly first-order phase transition that would otherwise cause larger crystals to shatter, allowing single-crystal studies of high-pressure phases that would otherwise require powder-diffraction techniques.

Although high-pressure single-crystal neutron-diffraction studies have been performed at reactor based sources for a number of years, little or no structural work has been performed at high pressure with the Laue technique using spallation neutron sources. This is unfortunate as the considerable neutron flux at short wavelengths that such sources provide offers the prospect of very high resolution ($\sin\theta/\lambda > 2.0 \text{Å}^{-1}$) structural studies. The use of the Paris-Edinburgh cell, although its diffraction geometry is somewhat limited, would allow high-pressure structural studies to be made at pressures in excess of 10 GPa — a considerable advance on what has been achieved with monochromatic single-crystal neutron diffraction to date.

This then is an exciting time in the field of high-pressure crystallography. Modern laboratory, synchrotron and neutron sources, combined with advances in detector and pressure cell technology, are stimulating the rapid development of diffraction techniques to allow the collection of high-pressure data of sufficient quality to carry out full crystal-structure refinement.

References

Adams D.M. and Shaw A.C., J. Phys. D 15, 1609 (1982)

Adams D.M., Private Communication (1992)

Ahsbahs H., Rev. Sci. Inst. 55, 99 (1984a)

Ahsbahs H., Revue Phys. Appl. 19, 819 (1984b)

Alkire R.W., Vergamini P.J. and Larson A.C., Acta Cryst. C40, 1502 (1984)

Allan D.R., Loveday J.S., Nelmes R.J. and Thomas P.A., Ferroelectrics 124, 367 (1991)

Allan D.R., Loveday J.S., Nelmes R.J. and Thomas P.A., J. Phys.: Condens. Matter 4, 2747 (1992)

Allan D.R. and Nelmes R.J., J. Phys.: Condens. Matter 4, L395 (1992)

Angel R.J., American Mineralogist 73, 1114 (1988)

Angel R.M., Centronic Limited, Private Communication (1992)

Ardnt U.W. and Mathieson A. McL., editors. 'International Meeting on the Accurate Determination of X-ray Intensities and Structure Factors', Acta Cryst. A 25 (1969)

Bacon G.E., 'Neutron Diffraction' (Clarendon Press: Oxford (1975))

Bao Z.X., Schmidt H. and Howell F.L., J. Appl. Phys. 70, 6804 (1991)

Barnett J.D., Block S. and Piermarini G.J., Rev. Sci. Inst. 44, 1 (1973)

Bassett W.A., Takahashi T. and Stook P.W., Rev. Sci. Inst. 38, 37 (1967)

Bell P.M. and Mao H.K., Carnegie Inst. Yearb. 78, 665 (1979)

Bell P.M. and Mao H.K., Carnegie Inst. Yearb. 80, 404 (1981)

Besedin S.P., Makarenko I.N., Stishov S.M., Glazkov V.P., Goncharenko I.N., Idova A.V., Somenkov V.A. and Shilstein S., High Pressure Research 4, 447 (1990)

Besson J.M., Hamel G., Grima T., Nelmes R.J., Loveday J.S., Hull S. and Hausermann D., High Pressure Research 8, 625 (1992)

Bierlein J.D. and Vanherzeele H., J. Opt. Soc. Am. B 6, 622 (1989)

Blessing R.H., Cryst. Rev. 1, 3 (1987)

Blinc R., J. Phys. Chem. Solids 13, 204 (1960)

Bloch D., Paureau J., Voiron J., and Parisot G., Rev. Sci. Inst. 47, 296 (1976)

Bridgman P.W., 'The Physics of High Pressure' (Dover Publications: New York (1971))

Bruno M.S. and Dunn K.J., Rev. Sci. Instrum. 55, 940 (1984)

Bucher B., Karpinski J., Kaldis E. and Wachter P., Physica C 27, 143 (1990)

Bullett D.W., J. Phys. C 15, 415 (1982)

Cava R.J., Batlogg B., Rabe K.M., Reitman E.A., Galacher P.K. and Rupp L.W., Physica C 156, 523 (1988)

Chandran L., Krishna-Murthy H. R. and Ramakrishnan T.V., J. Phys.: Condens. Matter 4, 7067 (1992)

Coulson C.A., 'Valence' (Oxford University Press: London (1961))

Decker D.L., J. Appl. Phys. 42, 3239 (1971)

Denner W., d'Amour H., Schulz H. and Stoeger W., J. Appl. Cryst. 10, 177 (1971)

Denner W., Schulz H. and d'Amour H., J. Apll. Cryst. 11, 260 (1978)

Donahue J., 'The Structures of the Elements' (Krieger: Malabar, Florida (1974)) pp 48

Dunstan D.J. and Spain I.L., J. Phys E.: Sci. Instrum. 22, 913 (1989)

El Brahimi M. and Durand J., Rev. Chim. Miner. 23, 146 (1971)

Emin D., Physics Today 35, 34 (1982)

Emin D., Physics Today 40, 55 (1987)

Emin D., Phys. Rev. B 38, 6041 (1988)

Emin D., 'The Physics and Chemistry of Carbides; Nitrides and Borides' (Kluwer: Netherlands (1990)) pp 691

Endo S., Chino T., Tsuboi S., and Koto K., Nature 340, 452 (1989)

Finger L.W. and King H., American Mineralogist 63, 337 (1978)

Finger L.W. and Hazen R.M., Acta Cryst. B 47, 561 (1991)

Flack H., Acta Cryst. A 30, 569 (1974)

Forman R.A., Piermarini G.J., Barnett J.D. and Block S., Science 176, 284 (1972)

Fujii Y., Hase K., Ohishi Y., Fujihisa H., Hamaya N., Takemura K., Shimomura O., Kikegawa T., Amemiya Y. and Matsushita T., Phys. Rev. Lett. 63, 358 (1989)

Gieske J.H., Aselage T.L. and Emin D., American Institute of Physics Conference Proceedings, 'Boron-Rich Solids' (AIP: New York (1990)) pp 376

Gomez de Andrez D.,Helliwell M., Habash J., Dodson E.J., Helliwell J.R., Bailey P.D. and Gammonn R.E., Acta Cryst. B 45, 482 (1989)

Hamilton W.C., 'Statistics in Physical Science' (Ronald: New York (1964)

Hamilton W.C., International Tables for Crystallography Vol IV pp273 (Kynoch Press: Birmingham (1974a))

Hamilton W.C., International Tables for Crystallography Vol IV pp289 (Kynoch Press: Birmingham (1974b))

Hansen N.K., Protas J. and Marnier G., C. R. Acad. Sci. 307(II), 475 (1988)

Harrison W.T.A., Geir T.E., Stucky G.D. and Schultz A.J., J. Chem. Soc., Chem. Commun. 7, 540 (1990)

Hausermann D., High Pressure Research 8, 647 (1992)

Hazen R.M., American Mineralogist 61, 266 (1976)

Hazen R.M. and Finger L.W., Carnegie Inst. Washington Yearb. 76, 655 (1977)

Hazen R.M. and Finger L.W., American Mineralogist 74, 352 (1989)

Hazen R.M., Mao H.K., Finger L.W. and Hemley R.J., Phys. Rev. B 36, 3944 (1987)

Helliwell J.R., Habash J., Cruickshank D.W.J., Harding M.M., Greenhough T.J., Campbell J.W, Clifton I.J., Elder M., Machin P., Papiz M.Z. and Zurek S., J. Appl. Cryst. (1989) 22, 483 (1989)

Hemley R.J., Zha C.S., Jephcoat A.P., Mao H.K. and Finger L.W., Phys. Rev. B 39, 11820 (1989)

Hossack W.J., Private Communication (1992)

Huber G., Syassen K. and Holzapfel W.B., Phys. Rev. B 15 5123 (1977)

Ichikawa M., Chem Phys. Lett. 79, 583 (1981)

Ichikawa M., Acta Cryst. B 34, 2074 (1978)

Ichikawa M., Motida K. and Yamada N., Phys. Rev. B 36, 874 (1987)

Ida Y., Volfit (program), Institute for Solid State Physics, University of Tokyo (1985)

Jauch W., Schultz A.J. and Schneider J.R., J. Appl. Cryst. 21, 975 (1988)

Jayaraman A., Newton R.C., and McDonough, Phys. Rev. 159, 527 (1967)

Jayaraman A. Reviews of Modern Physics 55, 65 (1983)

Jephcoat A.P., Finger L.W. and Cox D.E., High Pressure Research 8, 667 (1992)

Jorgenson J.D., J. Appl. Phys. 49, 5473 (1978)

Jorgenson J.D., Private Communication (1991)

Kaldis E., Fischer P., Hewat A.W., Hewat E.A., Karpinski J. and Rusiecki S., Physica C 159, 668 (1989)

Katrusiak A. and Nelmes R.J., J. Appl. Cryst. 19, 73 (1986)

Keller R. and Holzapfel W.B., Rev. Sci. Inst. 48, 517 (1977)

Keopke J., Dietrich W., Glinnemann J. and Schulz H., Rev. Sci. Inst. 56, 2119 (1985)

Kikegawa T., High Pressure Research 8, 631 (1992)

King H.E. and Finger L.W., J. Appl. Cryst. 12, 374 (1979)

King H.E., 'High Pressure Crystallography with a CAD4' Instruction Manual, Enraf-Nonius, Delft (1981)

Kourouklis G.A., Jayaraman A. and Ballman A.A., Solid State Commun. 62, 379

(1987)

Kuhs W.F., Ahsbahs H., Londono D. and Finney J.L., Physica B 156 and 157, 684 (1989)

Larson A.C. and Von Dreele R.B., GSAS program, Los Alamos National Laboratory, Los Alamos (1990)

Le Page Y., J. Appl. Cryst. 21, 983 (1988)

Lee S.H., Luszczynski K., Norberg R.E. and Conradi M.S., Rev. Sci. Instrum. 58, 415 (1987)

Lehmann M.S., J. Appl. Cryst. 8, 165 (1975)

Lehmann M.S., Kuhs W.F., McIntyre G.J., Wilkinson C. and Allibon J.R., J. Appl. Cryst. 22, 562 (1989)

Lehmann M.S. and Larsen F.K., Acta Cryst. A 30, 580 (1974)

Le Sar R., Ekberg S.A., Jones L.H., Mills R.L., Schwalbe L.A. and Schiferl D., Solid State Commun. 32, 131 (1979)

Letoullec R., Pinceuaux J.P. and Loubeyre P., High Pressure Research 1, 77 (1988)

Levine B.F., Phys. Rev. B 10, 1655 (1974)

Levien L., Prewitt C.T. and Weidner D.J., American Mineralogist 65, 920 (1980)

Liebenberg D.H., Phys. Lett. 73, 74 (1979)

Lipson H. and Cochran W., 'The Determination of Crystal Structures' Vol III (Bell: London (1966))

Liu L. and Bassett W.A., 'Elements, Oxides, Silicates — High-Pressure Phases with Implications for the Earth's Interior' (Clarendon Press: Oxford (1986))

Loveday J.S., McMahon M.I. and Nelmes R.J., J. Appl. Cryst. 23, 392 (1990)

Loveday J.S., private communication (1993)

Macavei J. and Schulz H., Rev. Sci. Intsrum. 68, 2236 (1990)

Mailhiot C., Grant J.B. and McMahan A.K., Phys. Rev. B 42, 9033 (1990)

Makarova I.P., Muradyan L.A., Vinogradova I.S. and Siminov V.I., Ferroelectrics 107, 275 (1990)

Malinowski M., Lukaszewicz K and Asbrink S., J. Appl Cryst. 19, 7 (1986)

Malinowski M., J. Appl. Cryst. 20, 379 (1987)

Mao H.K. and Bell P.M., Carnegie Inst. Washington Yearb. 77, 904 (1978a)

Mao H.K. and Bell P.M., Science 200, 1145 (1978b)

Mao H.K., Bell P.M., Dunn K.J., Chrenko R.M. and DeVries R.C., Rev. Sci. Instrum. 50, 1002 (1979)

Mao H.K. and Bell P.M., Carnegie Inst. Washington Yearb. 79, 409 (1980)

Mao H.K. and Bell P.M., Rev. Sci. Inst. 52, 615 (1981)

Masse R. and Grenier J., Bull. Soc. Fr. Mineral. Crystallogr. 94, 437 (1971)

Matsushita E. and Matsubara T., Progress of Theoretical Physics 67, 1 (1982)

McKie D. and McKie C., 'Essentials of Crystallography' (Blackwell Scientific Publications: London (1986)) pp 328

McMahon M.I., Nelmes R.J., Kuhs W.F., Dorwarth R., Piltz R.O. and Tun Z., Nature 348, 317 (1990)

McMahon M.I., PhD thesis, The University of Edinburgh (1990)

McWhan D.B., Block D. and Parisot G., Rev. Sci. Inst. 45, 643 (1974)

McWhan D.B., J. Phys. C 8, L81 (1975)

Meade C. and Jeanloz R., Rev. Sci. Instrum. 61, 2571 (1990)

Merrill L. and Bassett W.A., Rev. Sci. Instrum. 45, 290 (1974)

Meyer G.M., Nelmes R.J. and Vettier C., J. Phys. C 13, 4035 (1980)

Mills R.L., Leibenberg D.H., Bronson J.C. and Schmidt L.C., Rev. Sci. Instrum 51, 891 (1980)

Morosin B. and Samara G.A., Ferroelectrics 3, 49 (1971)

Morosin B., Aselage T.L. and Feigelson R.S., Mat. Res. Soc. Symp. Proc. 97, 145 (1987)

Nelmes R.J., Ferroelectrics 71, 87 (1987)

Nelmes R.J., Tun Z. and Kuhs W.F., Ferroelectrics 71, 125 (1987)

Nelmes R.J., J. Phys. C 21, l881 (1988)

Nelmes R.J., Loveday J.S., Kaldis E. and Karpinski J., Physica C 172, 311 (1990)

Nelmes R.J., Loveday J.S., Besson J.M., Hamel G., Weill G. and Hull S., Rutherford Appleton ISIS Annual Report, Vol. II pp A52 (1991)

Nelmes R.J., McMahon M.I., Hatton P.D., Piltz R.O., Crain J., Cernik R.J. and Bushnell-Wye G., High Pressure Research 8, 677 (1992)

Nelmes R.J., Loveday J.S., Allan D.R., Besson J.M., Hamel G., Grima P. and Hull S. accepted for publication by Phys. Rev. B (1993)

Nelmes R.J, Loveday J.S., Wilson R.M., Besson J.M., Pruzon P., Gautier M., Hamel G.and Klotz S., in preparation (1993)

Neuling H.W. and Holzapfel W.B., High Pressure Research 8, 655 (1992)

Paureau J. and Vettier C., High Temperatures-High Pressures 7, 529 (1975)

Phillips M.L., Gier T.E., Eddy M.M., Kedder N.L., Stucky G.D. and Bierlein J.D., Solid State Ionics 32/33, 147 (1989)

Piermarini G.J. and Block S., Rev. Sci. Instrum. 46, 973 (1975)

Piermarini G.J., Block S. and Barnett J.D., J. Appl. Phys. 44, 5377 (1973)

Piltz R.O., McMahon M.I., Crain J., Hatton P.D., Nelmes R.J., Cernik R.J. and Bushnell-Wye G., Rev. Sci. Instrum. 63, 700 (1992)

Pisarev R.V, Farhi R., Moch P. and Voronkova V.I., J. Phys.: Condens. Matter 2, 7555 (1990)

Prince E. and Nicholson W.L., 'Structure and Statistics in Crystallography' (Adeline Press, New York (1985)) pp183

Rietveld H.M., J. Appl. Cryst. 2, 65 (1969)

Ruoff A.L., High Pressure Research 8, 639 (1992)

Samara G.A., Phys. Rev. Lett. 27, 103 (1971)

Samara G.A., Ferroelectrics 71, 161 (1987)

Samara G.A., Emin D. and Wood C., Phys. Rev. B 32, 2315 (1985)

Santoro A., Weir C.E., Block S. and Piermarini G.J., J. Appl. Cryst. 1, 101 (1968)

Sastry P.U.M., Solid State Commun. 78, 593 (1991)

Schiferl D., Rev. Sci. Instrum. 48, 24 (1977)

Schiferl D., Jamieson J.C. and Lenko J.E., Rev. Sci Instrum. 49, 359 (1978)

Schiferl D., Olinger B. and Livingston R., Rev. Sci. Instrum. 54, 1250 (1983)

Schulz H. and Sowa H., High Pressure Research 8, 661 (1992)

Seal M., High Temperatures-High Pressures 16, 573 (1984)

Seongbok L., Bylander D.M. and Kleinman L., Phys. Rev. B 42, 1316 (1990)

Serhane M., Dugautier C., Farhi R., Moch P. and Pisarev R.V., Ferroelectrics 124, 373 (1991)

Sharma S.K., Proc. SPIE — Int. Soc. Opt. Eng.155, 105 (1989)

Sherman W. and Stadtmuller B., 'Experimental Techniques in High Pressure Research' (Wiley: Chichester (1987))

Shimomura O., Takemura K., Fujii Y., Minomura S., Mori M., Noda Y. and Yamada Y., Phys. Rev. B 18, 715 (1978)

Shimomura O., Takemura K., Fujihisa H., Fujii Y., Kikegawa T., Amemiya Y. and Matsushita T., private communication, (1990)

Slobodyanik N.S., Nagornyi P.G., Skopenko V.V. and Lugovskaya E.S., Russ. J. Inorg. Chem. 32, 1023 (1987)

Spain I.L., Black D.R. and Menoni C.S., Rev. Sci. Instrum. 55, 1511 (1984)

Spain I.L. and Dunstan D.J., J. Phys. E: Sci. Instrum 22, 923 (1989)

Stucky G.D., Phillips M.L.F. and Gier T.E., Chem. Mater. 1, 492 (1989)

Takeuchi Y., J. Min. Soc. Jpn. 14, 258 (1986)

Thomas P.A., Glazer A.M. and Watts B.E., Acta Cryst. B 46, 333 (1990)

Thomas P.A. and Glazer A.M., J. Appl. Cryst. 24, 968 (1991)

Thomas P.A., Private Communication (1992)

Tibballs J.E., Nelmes R.J. and MacIntyre G.J., J. Phys. C 15, 37 (1982)

Tordjman I., Masse R. and Guitel J.C., Z. Kristallogr. 139, 103 (1974)

Toule L.C., Appl. Phys. Lett. 10, 317 (1967)

Tun Z., Nelmes R.J., Kuhs W.F. and Stansfield R.F.D., J. Phys. C 21, 245 (1988)

Van Vechten J.A., Phys. Rev. 182, 891 (1969)

Weir C.E., Block S. and Piermarini G., J. Res. Nat. Bur. Stand. C 69, 275 (1965)

Weir C.E., Piermarini G.J. and Block S., Rev. Sci. Instrum. 40, 1133 (1969)

Whitfield C.H., Brody E.M. and Bassett W.A., Rev. Sci. Inst. 47, 92 (1976)

Wilkinson C., Kahmis H.W., Stansfield R.F.D. and MacIntyre G.J., J. Appl. Cryst. 21, 471 (1988)

Will G., Keifer B., Morosin B. and Slack G.A., Mat. Res. Soc. Symp. Proc 97, 151 (1987)

Yu S.C., Liu C.Y. Spain I.L., and Skelton E.F., 'Solid State Physics under Pressure' editor. Minomura S. (Terra Scientific (1985))

Zucker U.H., Perenthaler E., Kuhs W.F., Buchmann R. and Schulz H., J. Appl. Cryst. 16, 358 (1983)

Zumsteg F.C., Bierlein J.D. and Gier T.E., J. Appl. Phys. 47, 4980 (1976)

Published Work

J. Phys.: Condens. Matter 4 (1992) 2747–2760. Printed in the UK

A high-pressure structural study of potassium titanyl phosphate (KTP) up to 5 GPa

D R Allan†, J S Loveday†, R J Nelmes† and P A Thomas‡

† Department of Physics, The University of Edinburgh, Mayfield Road, Edinburgh EH9 3JZ, UK

‡ Department of Physics, University of Warwick, Coventry CV4 7AL, UK

Received 4 July 1991, in final form 29 October 1991

Abstract. The crystal structure of $KTiOPO_4$ (KTP) has been determined as a function of pressure up to 5 GPa at room temperature, using x-ray diffraction techniques and a single-crystal sample. The principal changes with pressure are in the coordination environments of the potassium atoms and in the linking angles of the TiO_6–PO_4 structural framework. In general the distortions of the TiO_6 octahedra, which have been linked to the second harmonic generating properties of KTP, are retained although there are some small changes in the Ti–O bond lengths. The overall structural changes are consistent with a first-order character for the phase transition at 5.5 GPa.

1. Introduction

Potassium titanyl phosphate, $KTiOPO_4$ (KTP), exhibits highly non-linear optical properties and is finding an increasing number of applications in the field of optoelectronics. At room temperature the structure of KTP assumes the acentric $Pna2_1$ space group with lattice parameters $a = 12.819(3)$ Å, $b = 6.399(1)$ Å, $c = 10.584(2)$ Å, $V = 868.1$ Å^3 [1]. The principal structural origin of this non-linear optical behaviour has been considered to be the anomalously short Ti–O bonds in the highly distorted TiO_6 octahedra [2], which form characteristic chains in the [011] and [01$\bar{1}$] directions, linked by alternately long and short Ti–O bonds (e.g. the chain A, B, C, D, E in figure 1). Several structural analogues of KTP have been reported where K is substituted by (for example) Rb or Tl [3], P by As [4] and more recently where Ti is substituted by (for example) Sn [5] or Fe [6]. All of these have been extensively reviewed [7]. The KTP structure shows a pronounced pseudosymmetry derived from the centric $Pnan$ space group and recently the thallium analogue $TlTiOPO_4$ (TlTP) has been reported to undergo a transition into this $Pnan$ symmetry at 923 K [8]. In addition to this, a high-pressure Raman study of KTP, carried out by Kourouklis *et al* [9], provides evidence of a phase transition at 5.5 GPa to an, as yet, uncharacterized phase. This Raman study shows that there is an increase in the number of modes at the 5.5 GPa phase transition, which indicates a lowering of the symmetry or a multiplication of the unit cell. The mechanism of the transition is proposed to be polyhedral tilting in the TiO_6–PO_4 framework being driven by the softening low-frequency Raman mode near 56 cm^{-1}. This mode, which has been associated with the potassium atoms [10], has a small discontinuity at the phase transition, indicating that the transition is weakly

0953-8984/92/112747+14$04.50

first order. On release of pressure the original Raman spectrum appears with no microscopic change in the appearance of the sample. This indicates that although the transition is first order it is reversible. A high-pressure structural study of KTP was mentioned briefly towards the end of a review article by Stucky *et al* [7] although it has not been reported in more detail elsewhere. No structural results are given apart from a bond angle change of 6.1° at 1 GPa for an unspecified P–O–Ti linking bond. In the absence of any other information regarding the pressure dependence of KTP the present investigation was undertaken to establish the major structural changes occurring as the phase transition at 5.5 GPa is approached.

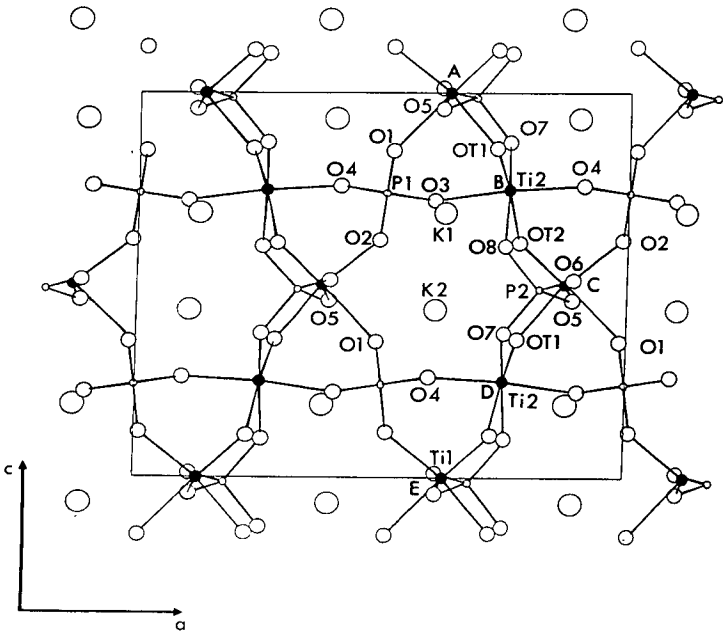

Figure 1. The structure of $KTiOPO_4$ viewed along the *b*-axis. The shaded circles represent the titanium atoms and the atoms labelled A, B, C, D, E are titanium atoms forming a chain linked by alternately long and short Ti–OT bonds.

2. The experiment and data analysis

A single crystal of flux-grown KTP was cut to the approximate dimensions of 100 μm × 100 μm × 100 μm and the resulting fragment was mounted and centred on a CAD4 four-circle diffractometer. The crystal quality was then checked and the crystallographic axes determined relative to the somewhat irregular crystal shape. A series of ψ scans was also performed to ensure that the crystal absorption had been adequately characterized. The data were to be collected using a Merrill–Bassett diamond-anvil pressure cell (DAC) which limits the region of accessible reflections to that lying close to the reciprocal lattice plane parallel to the diamond-anvil faces. In order to determine how the crystal should be mounted in the DAC, a series of trial refinements was performed on a previously collected three-dimensional ambient data set, taking the structural parameters of Thomas *et al* [1] as starting values. Regions of

inaccessible reflections were removed from the data to simulate the crystal mounted with either the a-, b- or c-axes perpendicular to the plane of the diamond-anvil face. The results of these refinements indicated that the lowest correlations between the positional parameters were observed for the a-axis setting. It was also found that the errors for the x-coordinates were not significantly higher than those for the y- and z-coordinates despite the a-axis being the direction of lowest resolution in the restricted data set. Therefore, it was decided to mount the crystal with its a-axis perpendicular to the diamond-anvil face.

The sample was secured to one diamond face, using petroleum jelly, with chips of ruby placed beside it for pressure calibration. The DAC was then assembled with a tungsten gasket confining the sample and a 4:1 methanol–ethanol fluid (dried with molecular sieve) used to transmit the pressure. Initially the cell was taken to a very low pressure of 0.2 GPa (measured to ± 0.05 GPa using the ruby fluorescence method) which is just adequate to ensure the cell is firmly sealed and the crystal mounting secure. The DAC was centred on the CAD4 and the sample carefully aligned using graphite-monochromated Ag Kα x-rays. This wavelength was chosen due to the superior resolution and lower absorption it offers over Mo Kα [11].

A low-pressure reference data set was then collected, measuring each reflection with the ω-scan method at the position of least attenuation by the pressure cell, according to the procedure of Finger and King [12]. The reflections were also measured at three positions over a narrow range around the scattering vector to detect and eliminate errors due to simultaneous diffraction by the diamond anvils [13]. Initially data were carefully collected in the region of $0° < \theta < 15°$ and, with a slightly increased scan speed, in the region of $15° < \theta < 30°$. At least two equivalents were present $(\pm h, -k, \pm l)$ in both shells. Reflections for which either the incident or reflected beam lay beyond 37° from the cylindrical symmetry axis of the cell were not collected, leaving a small safety margin on the limit (40°) imposed by the steel mounting of the beryllium discs [4]. All reflections affected by simultaneous diamond reflections were removed from the data set. After applying a correction for the absorption of both the pressure cell [12, 14] and the sample, the data were averaged over repeated measurements and used for an initial least-squares refinement of the structure, including an extinction correction, using the Prometheus crystallographic programs [15]. The structural parameters obtained by Thomas *et al* [1] were taken as starting values. It became apparent that since many of the reflections were relatively weak, particularly for the second shell, it was very important that the most structurally sensitive of these weak reflections were identified and their intensities measured more accurately. This was achieved with the 'leverage' procedure [16] as implemented by Hazen and Finger [17], which uses the derivatives calculated by the least-squares program to identify reflections most sensitive to the variable parameters of interest. The intensities of the 'leveraged' reflections were then remeasured with increased counting times, to improve their precision, and added to the data set. Structure factors were calculated for the remaining accessible reflections and for reflections whose intensities had not already been measured accurately. The strong and intermediate reflections predicted from these calculations were measured, as accurately as the 'leveraged' reflections, and added to the data set. All of the poorly determined reflections ($I < 3\sigma(I)$) present in the second shell were removed from the refinement. This had little effect on either the refined coordinates or on the magnitude of their errors. The resulting data set, which covers the whole range of accessible reflections (up to $\sin\theta/\lambda = 1.0$ Å^{-1}), was then used for a final least-squares

structural refinement. As for the initial refinement, all the reflections not rejected due to simultaneous diamond reflections were corrected for pressure-cell and sample absorption and averaged over identical reflections. In order to assign weights correctly to the reflections in the data set, averaging over the equivalent reflections and leveraged reflections only occurred after the final structural refinement. In the least-squares refinement each reflection was assigned a weight $w = 1/[\sigma^2(F_o) + f]$, where $\sigma(F_o)$ is the ESD for the observed structure factor and f is an estimate of the irreducible uncertainties in the measurement of intensities [18] (taken in this case to be 3% of the observed intensity of each reflection). Averaging over the equivalent reflections after the refinement allowed the internal consistency of the data to be determined.

The positional parameters for all of the atoms refined stably with no significant correlations between them. However, due to the rather limited data set, this was not found to be the case for the thermal parameters, and various constraints had to be applied. For all except the potassium atoms, only isotropic temperature factors were refined. This seems appropriate since the ambient structural study, carried out by Thomas *et al* [1], demonstrates that the potassiums are the only atoms exhibiting significantly anisotropic thermal motion: the other atoms, which form the TiO_6–PO_4 framework, have thermal motions which are almost isotropic. A further constraint was introduced by holding the anisotropic thermal parameters directed along a (the direction of lowest resolution in the data) to their ambient values. With all these constraints applied, the refinement converged and gave physically reasonable thermal parameters for the K, Ti and P atoms. However, the oxygen atoms were less well defined and additional constraints had to be applied to them. Since the oxygen atoms all have similar environments, their isotropic thermal parameters were all constrained to be the same, except for those involved in the short Ti–O bonds (labelled OT1 and OT2). The parameters for these two atoms were kept the same as each other, but allowed to differ from the other oxygens. In order to determine the effect of these further constraints, Hamilton's R-factor test [19] was applied between refinements where the oxygen thermal parameters were allowed to refine freely and where they were constrained. The test revealed that the constraints changed the R-factor by less than the 90% confidence limit and are therefore not statistically significant for the data [20]. The refined positional parameters were also found to agree to within 1.5σ or better, indicating that the constraints had not biased the refinement significantly. Physically reasonable values were then obtained for all the thermal parameters although the errors were fairly large. The anisotropic thermal parameters for the potassium atoms agreed with the values obtained by Thomas *et al* [1] to within 20% while the isotropic thermal parameters for the other atoms agreed with Trodjman *et al* [2] to within a factor of two. As a final check that the thermal-parameter constraints did not affect the positional parameters, a full data set, measured at ambient pressure, was refined with anisotropic thermal parameters for all the atoms. The results were compared with a second refinement where the above constraints had all been applied, and there were no significant differences between the positional parameters for the two refinements (all agreeing to within σ).

The purpose of the low-pressure reference data set was to determine to what extent (if at all) the restrictions imposed by the pressure cell bias the data, as well as establishing a reasonable data-collection strategy. Any bias in the data may result in some small offsets in the refined positional parameters from their ambient pressure values. The low-pressure reference data set therefore provides a secure starting point

from which any changes in the structure can be determined from data measured at higher pressures.

Data were collected for pressures of 2.2, 3.7 and 4.7 GPa following the strategy already outlined for the 0.2 GPa reference data and at each pressure, including 0.2 Gpa, (i) the unit-cell dimensions were determined accurately by the four-equivalent-settings procedure of King and Finger [21] which corrects for any sample miscentring, and (ii) the pressure was remeasured after the data collection to ensure it had remained constant. Again the data were corrected for pressure-cell and crystal absorption and averaged over identical reflections. As already explained, averaging over equivalent reflections was carried out after the final refinements and allowed the internal consistency of each data set to be determined.

3. Results and discussion

Table 1 presents the refined atomic coordinates, the measured unit-cell dimensions and unit-cell volume, the number of independent reflections, the number of refined parameters and the goodness-of-fit expressed as an R-factor. The results of the atmospheric-pressure study conducted by Thomas *et al* [1] are also given for comparison. All the R-factors for the high-pressure data are similar and the refined scale factors (not given) show only a small monotonic variation in the sequence in which the data were collected. The bond lengths of the K cages, Ti octahedra and P tetrahedra derived from these refinements are given in table 2.

The unit-cell volume is plotted as a function of pressure in figure 2. A Murnaghan fit to the values, using the Volfit program [22], yields a bulk modulus $B_0 = 58 \pm 8$ GPa with a curvature of $B' = 15 \pm 4$. The unit-cell volume decreases by 2.8(1)% at 2.2 GPa, comparable with that of the anorthite feldspar ($CaAl_2Si_2O_8$) which exhibits a decrease of 2.8(1)% at 2.5 GPa [23]. Anorthite has similar structural properties to those of KTP and will be described in more detail later.

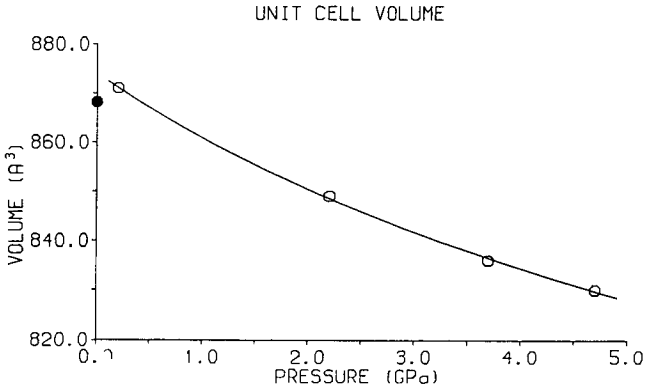

Figure 2. The unit-cell volume of $KTiOPO_4$ as a function of pressure. The atmospheric-pressure value, shown as ●, is calculated from the unit-cell dimensions of Thomas *et al* [1]. Note that errors are smaller than the symbols shown. The line is fitted to the high-pressure points using a Murnaghan function.

Table 1. Unit-cell dimensions (Å), unit-cell volume (Å^3) and refined atomic fractional coordinates of $KTiOPO_4$ as a function of pressure. The number of independent reflections (N_i), the number of refined parameters (N_r) and the weighted R factor (R_w) are also given. The R-factor for the refinements is defined as follows:

$$R_w = \left(\frac{\sum_N w(F_o - F_c)^2}{\sum_N wF_o^2}\right)^{1/2}$$

where N is the number of refined reflections and w is the weight assigned to each reflection. The estimated standard deviations (ESDs) for each of the values are given in parentheses. Note that the Prometheus refinement program requires that one atom be fixed along the polar axis. The Ti1 z coordinate was chosen to be fixed, and so no ESD is quoted for it. The atmospheric-pressure (AP) values were calculated from the refined atomic fractional coordinates of Thomas *et al* [1].

		Pressure (GPa)				
		AP [1]	0.2 GPa	2.2 GPa	3.7 GPa	4.7 GPa
	a (Å)	12.819(3)	12.832(7)	12.705(7)	12.639(7)	12.620(8)
	b (Å)	6.399(1)	6.412(3)	6.363(2)	6.331(2)	6.315(4)
	c (Å)	10.584(2)	10.586(4)	10.505(4)	10.447(4)	10.417(5)
	V (Å^3)	868.1(4)	871(1)	849(1)	836(1)	830(1)
K1	x	0.378 07(8)	0.3795(5)	0.3813(5)	0.3815(5)	0.3818(4)
	y	0.7806(1)	0.7799(5)	0.7796(5)	0.7807(5)	0.7819(5)
	z	0.6880(1)	0.6867(4)	0.6860(4)	0.6855(4)	0.6853(5)
K2	x	0.105 26(7)	0.1049(6)	0.1049(6)	0.1045(5)	0.1046(4)
	y	0.6990(1)	0.6989(5)	0.6946(5)	0.6921(4)	0.6911(5)
	z	0.9332(1)	0.9331(6)	0.9325(5)	0.9332(5)	0.9320(6)
Ti1	x	0.372 90(4)	0.3737(4)	0.3728(3)	0.3733(3)	0.3743(3)
	y	0.5001(1)	0.5013(5)	0.5004(4)	0.5013(4)	0.5006(4)
	z	−0.00040(8)	−0.0004	−0.0004	−0.0004	−0.0004
Ti2	x	0.246 58(6)	0.2450(6)	0.2450(5)	0.2467(5)	0.2461(4)
	y	0.2695(5)	0.2697(4)	0.2690(4)	0.2686(3)	0.2685(3)
	z	0.748 36(9)	0.7483(5)	0.7480(5)	0.7484(5)	0.7486(6)
P1	x	0.498 08(8)	0.4986(8)	0.4981(8)	0.4980(7)	0.4970(6)
	y	0.3363(1)	0.3360(4)	0.3338(4)	0.3318(4)	0.3318(4)
	z	0.7397(1)	0.7409(6)	0.7419(6)	0.7409(5)	0.7404(6)
P2	x	0.180 79(7)	0.1822(6)	0.1815(6)	0.1805(5)	0.1797(5)
	y	0.5020(1)	0.5000(9)	0.5003(7)	0.5029(8)	0.5024(6)
	z	0.4872(1)	0.4882(6)	0.4874(5)	0.4882(5)	0.4891(6)
O1	x	0.4859(2)	0.4852(14)	0.4873(12)	0.4868(13)	0.4890(12)
	y	0.4867(5)	0.4894(12)	0.4863(12)	0.4873(12)	0.4857(13)
	z	0.8497(2)	0.8478(9)	0.8522(8)	0.8500(9)	0.8481(11)
O2	x	0.5103(2)	0.5142(17)	0.5087(13)	0.5094(14)	0.5100(10)
	y	0.4657(5)	0.4616(12)	0.4604(12)	0.4583(13)	0.4600(13)
	z	0.6170(2)	0.6168(8)	0.6146(8)	0.6162(8)	0.6174(11)

Table 1. (Continued)

		Pressure (GPa)				
		AP [1]	0.2 GPa	2.2 GPa	3.7 GPa	4.7 GPa
O3	x	0.4004(2)	0.4009(12)	0.4023(12)	0.4009(12)	0.4004(9)
	y	0.1986(4)	0.2037(13)	0.1981(14)	0.1920(14)	0.1897(13)
	z	0.7208(2)	0.7192(10)	0.7234(9)	0.7226(10)	0.7272(13)
O4	x	0.5934(2)	0.5908(15)	0.5929(14)	0.5918(14)	0.5917(11)
	y	0.1930(4)	0.1888(13)	0.1851(13)	0.1836(13)	0.1840(14)
	z	0.7589(2)	0.7572(9)	0.7590(9)	0.7583(10)	0.7574(11)
OT1	x	0.2248(2)	0.2226(14)	0.2233(14)	0.2273(13)	0.2274(12)
	y	0.9653(4)	0.9694(16)	0.9714(15)	0.9737(14)	0.9703(15)
	z	0.3561(2)	0.3537(10)	0.3537(9)	0.3354(9)	0.3566(11)
OT2	x	0.2232(2)	0.2195(17)	0.2205(14)	0.2218(14)	0.2219(12)
	y	0.0413(5)	0.0423(18)	0.0388(17)	0.0428(15)	0.0407(15)
	z	0.6097(2)	0.6088(12)	0.6097(11)	0.6119(10)	0.6126(11)
O5	x	0.1126(2)	0.1118(14)	0.1089(14)	0.1126(11)	0.1094(10)
	y	0.3106(4)	0.3162(13)	0.3141(12)	0.3177(12)	0.3143(12)
	z	0.4585(2)	0.4560(10)	0.4545(9)	0.4574(10)	0.4594(15)
O6	x	0.1113(2)	0.1119(15)	0.1120(15)	0.1087(15)	0.1083(13)
	y	0.6918(4)	0.6938(13)	0.6904(12)	0.6961(12)	0.6937(13)
	z	0.5117(3)	0.5129(11)	0.5127(9)	0.5124(10)	0.5126(12)
O7	x	0.2525(2)	0.2506(17)	0.2551(17)	0.2575(15)	0.2560(13)
	y	0.5402(5)	0.5420(16)	0.5415(15)	0.5364(15)	0.5419(15)
	z	0.3718(2)	0.3713(10)	0.3720(9)	0.3734(10)	0.3747(11)
O8	x	0.2528(2)	0.2522(14)	0.2560(11)	0.2542(12)	0.2536(12)
	y	0.4619(5)	0.4598(16)	0.4598(14)	0.4602(15)	0.4602(16)
	z	0.6008(2)	0.6014(12)	0.6003(10)	0.6015(11)	0.6006(12)
	N_i	2158	490	491	496	417
	N_r	145	65	65	65	65
	R_w	0.024	0.044	0.042	0.047	0.051

From table 1 it is clear that the K2 atom exhibits a shift under pressure while the K1 atom remains relatively stationary. To illustrate this, their fractional coordinates are plotted as a function of pressure in figure 3. The potassium atoms occupy cavities, or cages, in the TiO_6–PO_4 framework and are loosely held in the structure. The movement of the K2 atom suggests that its cage exhibits a significant pressure dependence. This pressure dependence will manifest itself as a relative movement in the TiO_6–PO_4 framework and, upon examination of table 1, it is evident that the P1, P2 and O3 atoms undergo clear shifts. To illustrate the shifts, the fractional coordinate changes for the P1 and O3 atoms are also shown in figure 3 (note that P2 has a shift of similar magnitude to that of P1 and is not shown in the figure). The small but significant offset of the O3 y-coordinate at 0.2 GPa from the atmospheric-pressure value illustrates the need for the low-pressure reference data set in determining trends in the structure.

Table 2. The bond lengths (Å) of the K cages, Ti octahedra and P tetrahedra in $KTiOPO_4$ as a function of pressure. The atmospheric-pressure (AP) values were calculated from the refined atomic fractional coordinates of Thomas *et al* [1].

		Pressure (GPa)				
		AP [1]	0.2 GPa	2.2 GPa	3.7 GPa	4.7 GPa
$K(1)O_8$	K1–O1	2.894(4)	2.867(12)	2.889(11)	2.859(11)	2.865(12)
	K1–O2	2.738(4)	2.775(16)	2.703(13)	2.702(14)	2.693(12)
	K1–O3	2.712(3)	2.753(10)	2.705(10)	2.644(10)	2.622(10)
	K1–O5	2.872(3)	2.862(10)	2.832(9)	2.851(10)	2.864(15)
	K1–O7	3.057(3)	3.071(14)	3.099(15)	3.092(12)	3.100(13)
	K1–O8	2.755(4)	2.774(15)	2.736(11)	2.734(13)	2.743(13)
	K1–OT1	2.995(3)	2.967(12)	2.953(12)	2.969(11)	2.992(12)
	K1–OT2	2.722(4)	2.780(19)	2.745(16)	2.724(16)	2.705(13)
$K(2)O_9$	K2–O1	2.677(3)	2.677(12)	2.658(12)	2.663(15)	2.656(11)
	K2–O2	2.982(3)	2.991(14)	2.933(11)	2.927(12)	2.950(12)
	K2–O3	3.045(3)	3.029(11)	3.057(10)	3.024(11)	3.075(12)
	K2–O4	3.117(3)	3.112(9)	3.031(8)	3.003(9)	2.991(10)
	K2–O5	2.806(3)	2.793(19)	2.727(18)	2.757(16)	2.717(14)
	K2–O7	2.918(4)	2.951(15)	2.905(14)	2.861(14)	2.891(13)
	K2–O8	3.048(4)	3.055(16)	3.013(14)	3.027(14)	3.028(14)
	K2–OT1	2.765(4)	2.789(15)	2.733(15)	2.663(15)	2.656(15)
	K2–OT2	3.057(4)	3.089(22)	3.062(17)	3.033(17)	3.039(15)
$Ti(1)O_6$	Ti1–O1	2.150(3)	2.153(13)	2.126(12)	2.123(13)	2.144(14)
	Ti1–O2	1.958(3)	1.915(17)	1.946(14)	1.936(15)	1.923(13)
	Ti1–O5	2.042(3)	2.079(8)	2.065(8)	2.058(8)	2.035(9)
	Ti1–O6	1.987(3)	1.985(8)	1.986(8)	1.950(8)	1.956(9)
	Ti1–OT1	1.981(3)	1.988(14)	1.968(13)	1.978(13)	1.975(13)
	Ti1–OT2	1.716(3)	1.684(17)	1.675(13)	1.700(13)	1.710(13)
$Ti(2)O_6$	Ti2–O3	2.044(3)	2.067(15)	2.065(16)	2.026(15)	2.022(11)
	Ti2–O4	1.981(3)	1.999(16)	1.958(17)	1.983(17)	1.974(13)
	Ti2–O7	1.965(3)	1.957(11)	1.948(10)	1.967(10)	1.942(10)
	Ti2–O8	1.990(3)	1.978(11)	1.975(10)	1.958(10)	1.963(11)
	Ti2–OT1	1.733(3)	1.749(12)	1.748(10)	1.745(10)	1.732(11)
	Ti2–OT2	2.092(3)	2.101(12)	2.086(11)	2.043(11)	2.042(11)
$P(1)O_4$	P1–O1	1.519(3)	1.509(10)	1.517(9)	1.513(9)	1.489(12)
	P1–O2	1.548(3)	1.554(9)	1.567(9)	1.537(9)	1.525(12)
	P1–O3	1.544(3)	1.531(15)	1.505(15)	1.525(14)	1.520(12)
	P1–O4	1.541(3)	1.523(17)	1.542(18)	1.523(17)	1.527(13)
$P(2)O_4$	P2–O5	1.535(3)	1.523(15)	1.540(14)	1.488(13)	1.515(10)
	P2–O6	1.528(3)	1.557(14)	1.521(15)	1.544(15)	1.526(12)
	P2–O7	1.548(3)	1.541(15)	1.553(16)	1.559(14)	1.553(14)
	P2–O8	1.537(3)	1.520(13)	1.539(12)	1.530(13)	1.513(13)

In order to determine the relative compressibilities of the K cages, the PO_4 tetrahedra and the TiO_6 octahedra, their volumes were calculated for all four pressures by dividing each unit into constituent irregular tetrahedra. The PO_4 tetrahedra and TiO_6 octahedra require one and four such tetrahedra respectively, with an oxygen atom at each vertex. For the K cage sites the consituent tetrahedra were determined

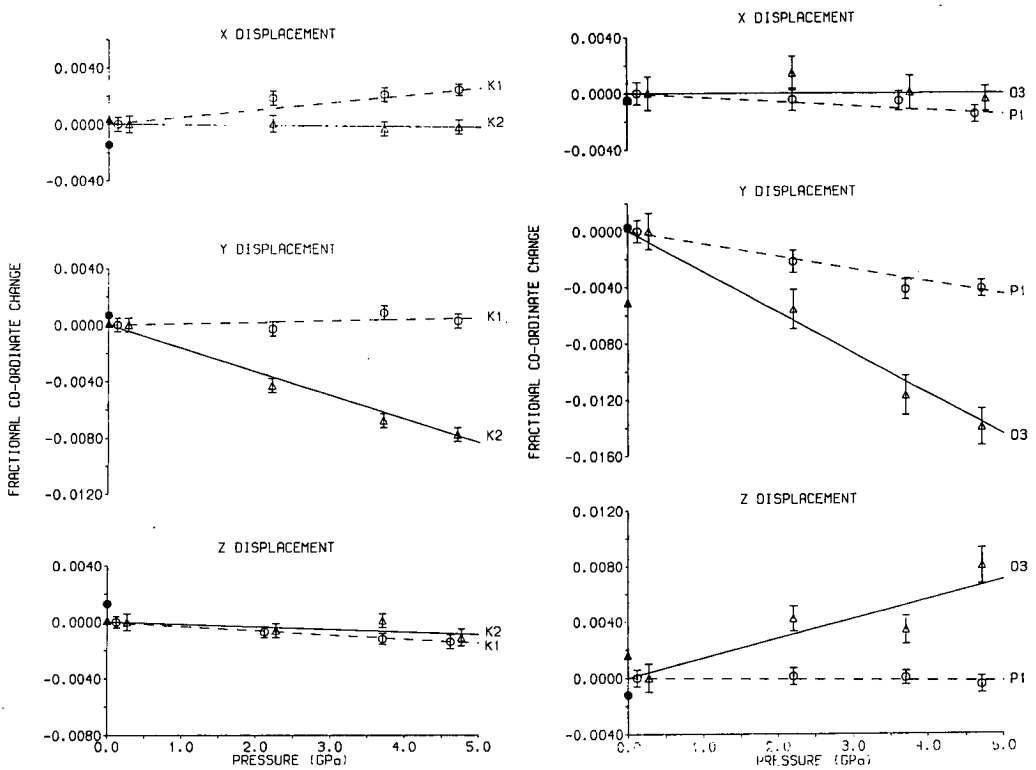

Figure 3. (*a*) Fractional coordinate changes for the K1 (○) and K2 (△) atoms, and (*b*) for the P1 (○) and O3 (△) atoms in $KTiOPO_4$ relative to the 0.2 GPa values. The atmospheric-pressure values, shown as ● and ▲, are from Thomas *et al* [1]. Note that some of the points have been translated slightly along the pressure axis to avoid overlap. The broken and full lines are a guide to the eye only.

by placing a K atom at one vertex and neighbouring oxygen atoms at the remaining three vertices. Describing the volume of the cage sites in this way requires twelve and fourteen such tetrahedra for the $K(1)O_8$ and $K(2)O_9$ cages respectively. The volume of each of the irregular tetrahedra can be readily calculated from the appropriate bond lengths and bond angles and then summed to yield the volume of each structural unit. As can be seen from table 3, all the units show a decrease in volume under pressure, although their relative volume changes are quite different: the K cages have a $5.7 \pm 1\%$ reduction in volume at 4.7 GPa, while the Ti octahedra and P tetrahedra have $2.8 \pm 2\%$ and $2.4 \pm 2\%$ reductions respectively. Therefore, it seems that the large potassium cage sites are readily compressible and absorb a significant fraction of the overall $4.7 \pm 0.2\%$ reduction in the unit-cell volume at 4.7 GPa. The average volume change of the K cage sites is plotted in figure 4 along with the change in the unit-cell volume. It is evident from figure 4 that the curvature of the pressure–volume relationship is significantly greater for the K cages than for the unit cell.

From figure 1, which presents the structure of KTP projected along the *b*-axis, it is evident that the environments for the K1 and K2 atoms are quite different. The $K(2)O_9$ cage forms a channel, parallel to the *b*-axis, which runs through the entire crystal structure and along which the K2 atom may be expected to move relatively

Table 3. The pressure dependence of the average M–O bond lengths (Å) in the TiO_6 octahedra, PO_4 tetrahedra and K cages of $KTiOPO_4$ and of the volumes (Å^3) of these structural units. The definition of the volumes is discussed in the text. The atmospheric-pressure (AP) values were calculated from the refined atomic fractional coordinates of Thomas *et al* [1].

	Pressure (GPa)				
	AP [1]	0.2 GPa	2.2 GPa	3.7 GPa	4.7 GPa
TiO_6 octahedra					
Average bond length (Å)	1.970(3)	1.971(13)	1.962(12)	1.956(12)	1.952(12)
Volume (Å^3)	10.08(5)	10.08(18)	9.94(17)	9.86(17)	9.80(16)
PO_4 tetrahedra					
Average bond length (Å)	1.537(3)	1.532(13)	1.534(13)	1.527(13)	1.521(12)
Volume (Å^3)	1.86(1)	1.84(5)	1.86(5)	1.83(5)	1.80(4)
K1 cage					
Average bond length (Å)	2.843(4)	2.856(14)	2.833(12)	2.822(12)	2.823(12)
Volume (Å^3)	26.15(6)	26.46(36)	25.72(33)	25.14(34)	25.00(31)
K2 cage					
Average bond length (Å)	2.934(3)	2.943(15)	2.902(13)	2.884(14)	2.889(13)
Volume (Å^3)	34.71(7)	35.12(45)	33.46(45)	32.91(45)	33.03(45)

freely; and it is seen in figure 3 that the only significant movement of the K2 atom with increasing pressure is along the *b*-axis (i.e. along the channel). On the other hand, the K1 atom is constrained from a similar motion by the confinement of the $P(1)O_4$–$Ti(2)O_6$ chain which restricts movement of the K1 atom along the *b*-axis (see figure 1). It is interesting to note that although the K1 cage forms a channel which runs parallel to the *a*-axis, the K1 atom does not show a significant movement along the *a*-axis with increasing pressure. The apparent difference in behaviour may be partly due to the greater restriction offered by the K1 cage environment, which has a volume 25% smaller than that of the K2 cage. There is also a significant difference in compressibility in the average K–O bond lengths which reduce by $1.2 \pm 0.3\%$ and $1.8 \pm 0.2\%$ for the K1 and K2 cages respectively.

As the $P(1)O_4$–$Ti(2)O_6$ chain deforms under pressure, the motion of the O3 atom, combined with that of the P1 atom, results in a reduction of the P1–O3–Ti2 bond angle by approximately 3° between 0.2 and 4.7 GPa (see table 4). This bond links the chain of alternate $P(1)O_4$ tetrahedra and $Ti(1)O_6$ octahedra which is directed along the *a*-axis (see figure 1). The most significant TiO_6–PO_4 linking angle change, however, is in the P2–O7–Ti2 bond which reduces by approximately 5° over the same pressure range (see table 4). (This is less than 20% of the angular change of 6.1° at 1 GPa reported by Stucky *et al* [7] for an unspecified P–O–Ti bond.) All the other P–O–Ti bonds have angular changes of approximately 2° or less, as do the Ti–OT–Ti bonds which link the titanium octahedra (the P1–O4–Ti2, P2–O6–Ti1 and Ti1–OT2–Ti2 linking bonds are given as examples in table 4).

The overall distortion of the $Ti(1)O_6$ and $Ti(2)O_6$ octahedra appears to be retained up to 4.7 GPa in as much as the general pattern of long and short Ti–O bond lengths remains the same (as can be seen from table 2) and the O–Ti–O bonds, within the octahedra, have angular changes of only 2° or less. The anomalously short Ti–OT

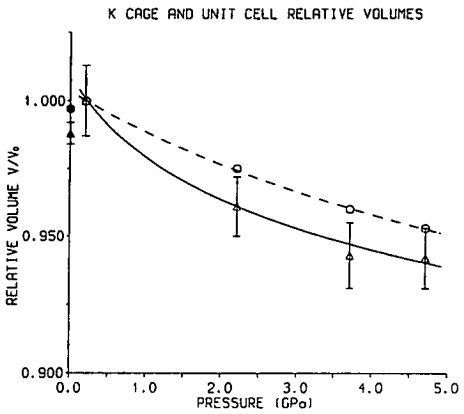

Figure 4. The relative volumes (V/V_o) of the unit-cell volume (○) and K cages (△) (the K1 and K2 cages averaged) in $KTiOPO_4$ as a function of pressure, referred to the value V_o at 0.2 GPa. The atmospheric-pressure values, shown as ● and ▲, are calculated from the unit-cell dimensions and the fractional coordinates of Thomas *et al* [1]. Note that where error bars are not shown, the errors are smaller than the circular symbols. The broken and full curves are from Murnaghan fits to the relative volumes of the unit cell and the K cages respectively.

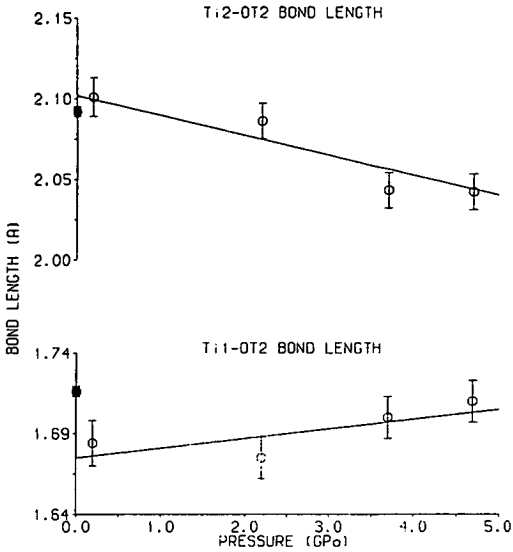

Figure 5. The Ti2–OT2 and Ti1–OT2 bond lengths in $KTiOPO_4$ as a function of pressure. The atmospheric-pressure values, shown as ●, are calculated from the fractional coordinates of Thomas *et al* [1]. The lines indicate the changes in the bonds and are a guide to the eye only.

bonds within the highly distorted TiO_6 octahedra have been considered to be linked to the non-linear optical properties of KTP and are consequently of great interest [2]. From table 2 it is evident that the Ti1–OT2 and Ti2–OT2 bond lengths both undergo systematic changes under pressure. The longer of the two, Ti2–OT2, clearly reduces in length while the shorter one, Ti1–OT2, appears to increase slightly, as shown in figure 5. (In the case of Ti1–OT2 there is a significant offset between the values obtained at ambient pressure and 0.2 GPa. The trend in this bond length is taken relative to the 0.2 GPa reference point.) These changes reduce the difference between the Ti1–OT2 and the Ti2–OT2 bond lengths by around 20%, but the Ti1–OT1 and Ti2–OT1 bonds appear to retain their bond length difference; it would now be of interest to find out whether there is any accompanying variation in the second-harmonic generating (SHG) properties as a function of pressure. From table 2, it is also evident that the relatively long Ti1–O5 and Ti2–O3 bonds undergo significant shortening under pressure (relative to the 0.2 GPa values). As indicated above, however, the shortening of these bonds does not significantly reduce the overall distortions of the TiO_6 octahedra.

The orientation of the Ti–O bonds, as well as the variation of their bond lengths, is also considered to be important for the non-linear optical properties of the KTP structure [1, 24, 25]. In the calculation of the non-linear tensor coefficients, the

Table 4. Selected P–O–Ti and Ti–OT–Ti bond angles (°) in $KTiOPO_4$ as a function of pressure. The atmospheric-pressure (AP) values were calculated from the refined atomic fractional coordinates of Thomas *et al* [1].

	Pressure (GPa)				
	AP [1]	0.2 GPa	2.2 GPa	3.7 GPa	4.7 GPa
P1–O3–Ti2	129.6(2)	131.0(7)	129.8(7)	128.2(7)	128.1(5)
P2–O7–Ti2	130.3(2)	132.9(9)	130.3(9)	126.6(9)	128.9(9)
P1–O4–Ti2	134.8(2)	132.9(7)	132.3(7)	131.9(7)	132.4(6)
P2–O6–Ti1	135.9(2)	136.6(9)	136.1(9)	134.8(9)	134.8(9)
Ti1–OT2–Ti2	133.4(2)	134.6(9)	133.6(8)	134.3(8)	133.5(7)

orientations of the bonds participate through products of their direction cosines, where the direction cosines are determined with respect to the crystallographic axes [25]. For the KTP structure the distortions of the TiO_6 octahedra give rise to an inherently asymmetric summation of the direction cosines along the polar axis of the crystal. Although the TiO_6 octahedra appear to be tilting with respect to the PO_4 tetrahedra, the magnitude of this re-orientation does not affect the summation of the direction cosines significantly.

As already outlined, the KTP structure assumes a pronounced pseudosymmetry derived from the centric $Pnan$ space group [1], and it is of interest to examine how the structure moves with respect to this space group as the phase transition at 5.5 GPa is approached. In order to do so the Missym computer program [1, 26] was utilized to compare the refined coordinates with the pseudosymmetry at all four pressures. The degree of pseudosymmetry was found to remain almost constant and, therefore, the structure neither appeared to be moving significantly towards or away from the prototypic $Pnan$ phase. It is also interesting to note that the Missym program did not indicate an approach towards any other pseudosymmetries at 4.7 GPa, suggesting that the structural transition is first-order in character.

The deformation of the TiO_6–PO_4 framework is not accompanied by a significant movement of the titanium atoms (table 1) although, as already indicated, there is a clear movement of the phosphorus atoms and a change in the P–O–Ti bond angles. Since the O–Ti–O angles show changes of 2° or less (to 4.7 GPa) the titanium octahedra remain fairly rigid in shape. Therefore the movement of the phosphorus atoms relative to the stationary titanium atoms, coupled with the angular changes in the P–O–Ti linking bond angles, suggest that the TiO_6 octahedra are tilting relative to the PO_4 tetrahedra.

The observed structural changes of KTP as it approaches its phase transition are similar in kind to those of the plagioclase feldspar anorthite $CaAl_2Si_2O_8$ which exhibits a first-order structural phase transition at 2.6 Gpa [23]. All of the feldspars have crystal structures consisting of a three-dimensional framework of corner-linked AlO_4 and SiO_4 tetrahedra. In the case of anorthite, cavities formed in the framework, which are analogous to the cage sites of KTP, contain Ca atoms. The mechanism for the transition, from the low-pressure $P\bar{1}$ structure to the $I\bar{1}$ high-pressure structure, is tilting of the essentially rigid tetrahedra of the framework. The resulting deformation of the framework from the ambient structure apparently reflects a need to accommodate both the applied pressure and the large Ca cations within the cavities of the framework. Initially the volumes of the cavities, as defined by the eight closest

oxygen positions, decrease under pressure in a manner similar to that of the cage sites in KTP. After the transition the volume of the cavities increases again as the framework tetrahedra suddenly tilt into new orientations. The tilting of the tetrahedra manifests itself as a change of the T–O–T (Al, Si–O–Al, Si) bond angles, which link neighbouring tetrahedra. The magnitudes of the T–O–T bond angle changes between atmospheric pressure and the phase transition are of the same order as those for the P–O–Ti linking bonds of KTP. After the transition in anorthite, however, there is a sudden angular change of the linking bonds with one such bond exhibiting an increase of 17°, where it had initially decreased by only 2° as the phase transition was approached. It is also interesting to note that the Ca atom environments, or rather the potential well within each cavity, show a marked change above the phase transition. In the low-pressure phase the potential within the cavities is wide and relatively flat while above the transition the potential becomes significantly sharper. Although the KTP cage sites are quite different from the anorthite cavities, the high-pressure Raman study and the present high-pressure structural study both indicate that a significant pressure dependence is present for the K atom environments as the phase transition is approached. The Raman study provides additional evidence that the potential well within the cage sites also becomes sharper after the transition, in as much as the initially softening 56 cm^{-1} mode becomes stiffer. However, it remains to be seen whether the cage sites increase their volume after the transition in a manner similar to that of anorthite.

The observed decrease of the K-cage site volumes under pressure intuitively suggests that the potential experienced by the K atoms will sharpen under pressure, thereby coupling the motion of the K atoms more closely to that of the cage oxygens. But in the absence of a detailed analysis of the phonon spectrum it is not possible to relate the observed structural changes of KTP with pressure to the softening 56 cm^{-1} A_1 mode. However, the tilting of the TiO_6 octahedra relative to the PO_4 tetrahedra does generally agree with the behaviour proposed by Kourouklis *et al* [9] as the phase transition is approached.

4. Conclusions

The principal changes of the KTP structure under pressure are in the region of the relatively compressible K cages. The PO_4 and TiO_6 units remain rigid in size and shape, and the compression of the cages appears to be accommodated by significant buckling of the framework structure, accompanied by a pronounced movement of the K2 atom. The observed angular changes in the P–O–Ti linking bonds suggest that the deformation of the structure around the the cage sites is principally achieved by tilting of the TiO_6 octahedra relative to the PO_4 tetrahedra.

The other structural changes up to 4.7 GPa are relatively small. In particular, the TiO_6 octahedra were found to retain their general distortion although there are some small changes in Ti–O distances, including a reduction in the difference between the Ti1–OT2 and Ti2–OT2 bond lengths. It is not known whether the SHG properties—thought to be associated with the distorted TiO_6 octahedra—remain unaltered with pressure and a study is being planned to determine this. The results of the analysis with the Missym program indicate that the changes in the structure are consistent with a first-order phase transition and it is not possible to predict the structure of the high-pressure phase. Therefore it is proposed to continue the study of the KTP structure through the phase transition.

Acknowledgments

We are grateful to Mr H Vass and Mr S Duffield for their technical assistance and to Dr P D Hatton, Dr R O Piltz and Dr R J Angel for many useful discussions. In particular, we thank Dr Angel for drawing our attention to the probable similarities between KTP and anorthite. This work is supported by a grant from the UK Science and Engineering Research Council.

References

[1] Thomas P A, Glazer A M and Watts B E 1990 *Acta Crystallogr.* B **46** 333–43
[2] Tordjman I, Masse R and Guitel J C 1974 *Z. Kristallogr., Bd.* **139** 103–15
[3] Masse R and Grenier J 1971 *Bull. Soc. Fr. Mineral. Crystallogr.* **94** 437–42
[4] El Brahimi M and Durand J 1986 *Rev. Chim. Miner.* **23** 146–53
[5] Slobodyanik N S, Nagornyi P G, Skopenko V V and Lugovskaya E S 1987 *Russ. J. Inorg. Chem.* **32** 1023–6
[6] Phillips M L, Gier T E, Eddy M M, Kedder N L, Stucky G D and Bierlien J D 1989 *Solid State Ionics* **32/33** 147–53
[7] Stucky G D, Phillips M L F and Gier T E 1989 *Chem. Mater.* **1** 492–509
[8] Harrison W T A, Gier T E, Stucky G D and Schultz A J 1990 *J. Chem. Soc., Chem. Commun.* **7** 540–2
[9] Kourouklis G A, Jayaraman A and Ballman A A 1987 *Solid State Commun.* **62** 379–82
[10] Pisarev R V, Farhi R, Moch P and Voronkova V I 1990 *J. Phys.: Condens. Matter* **2** 7555–68
[11] Nelmes R J, Loveday J S, Kaldis E and Karpinski J 1990 *Physica* C **172** 311–24
[12] Finger L W and King H E 1978 *Am. Min.* **63** 337
[13] Loveday J S, McMahon M I and Nelmes R J 1990 *J. Appl. Crystallogr.* **23** 392
[14] King H E and Finger L W 1981 *High Pressure Crystallography with a CAD4* Instruction manual (Delft: Enraf-Nonius)
[15] Zucker U H, Perenthaler E, Kuhs W F, Buchmann R and Schulz H 1983 *J. Appl. Crystallogr.* **16** 358
[16] Prince E and Nicholson W L 1985 *Structure and Statistics in Crystallography* ed A J C Wilson (New York: Adenine) pp 183–6
[17] Hazen R M and Finger L W 1989 *Am. Min.* **74** 352
[18] Lehmann M S 1975 *J. Appl. Crystallogr.* **8** 165
[19] *International Tables For X-ray Crystallography* vol 4 pp 288–92
[20] Hamilton W C 1964 *Statistics in Physical Science* (New York: Ronald)
[21] King H E and Finger L W 1979 *J. Appl. Crystallogr.* **12** 374
[22] Ida Y 1985 *Volfit* (program) Institute for Solid State Physics, University of Tokyo
[23] Angel R J 1988 *Am. Min.* **73** 1114–9
[24] Hansen N K, Protas J and Marnier G 1988 *C. R. Acad. Sci.* **307(II)** 475–9
[25] Sastry P U M 1991 *Solid State Commun.* **78** 593–7
[26] Le Page Y 1988 *J. Appl. Crystallogr.* **21** 983–4

Ferroelectrics, 1991, Vol. 124, pp. 367–372
Reprints available directly from the publisher
Photocopying permitted by license only

STRUCTURAL STUDIES OF POTASSIUM TITANYL PHOSPHATE (KTP) UNDER HIGH PRESSURE

[1]D.R.ALLAN,[1]J.S.LOVEDAY,[1]R.J.NELMES and [2]P.A.THOMAS
[1]Department of Physics,University of Edinburgh,Edinburgh,U.K.
[2]Department of Physics,University of Warwick,Coventry,U.K.

ABSTRACT The crystal structure of $KTiOPO_4$ (KTP) has been determined as a function of pressure towards its phase transition at 5.5 GPa. The principal changes with pressure are in the cage site environments of the potassium atoms and in the linking bond angles of the TiO_6-PO_4 framework. The distortions of the TiO_6 octahedra, which have been linked to the second harmonic generating properties of KTP, remain almost unchanged. An initial study of the structure in the high-pressure phase (at 6.2 GPa) suggests that the primitive orthorhombic cell is retained with a 5% reduction in the unit-cell volume at the transition.

INTRODUCTION

Potassium titanyl phosphate, $KTiOPO_4$ (KTP), has been of interest for a number of years due to its highly non-linear optical properties. KTP is a particularly efficient second harmonic generator of the 1.06 μm Nd-YAG laser light and is finding many applications in the field of optoelectronics. At room temperature the structure of KTP assumes the acentric $Pna2_1$ space group with lattice parameters[1] a=12.819(3) Å, b=6.399(1) Å, c=10.584(2) Å, V=868.1 Å^3. The principal structural origin of this non-linear optical behaviour has been proposed to be the anomalously short Ti-O bonds in the highly distorted TiO_6 octahedra, which form characteristic chains in the [0 1 1] and [0 -1 1] directions linked by alternately long and short Ti-O bonds[2]. Recently, a high-pressure Raman study of KTP, carried out by Kourouklis et al[3], provides evidence of an, as yet, undetermined phase transition at 5.5 GPa. This Raman study showed that at the phase transition there is an increase in the number of modes, accompanied by discontinuities in several of the modes. The behaviour of the modes, therefore, suggests a first-order transition into a high-pressure phase of lower symmetry. The purpose of this investigation is to establish the major structural changes occurring as the phase transition is approached and to determine the structure of the high-pressure phase. Full details of the structural changes towards the transition are presented in more detail in a forthcoming paper[4], while initial results of the structure determination of the high-pressure phase are presented here for the first time.

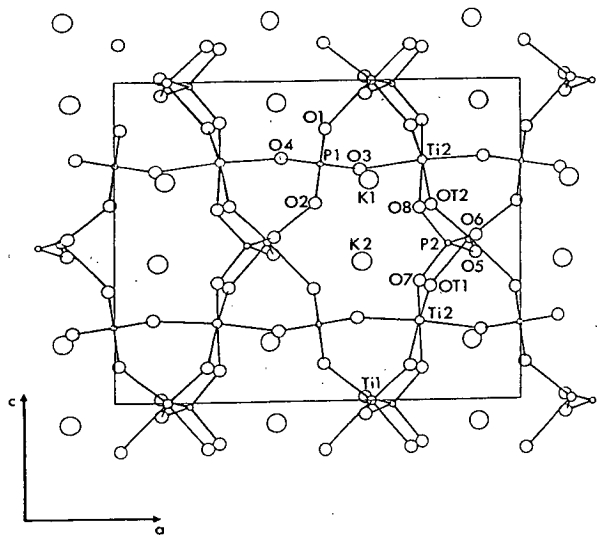

FIGURE 1 The structure of KTP viewed along the b-axis.

1. THE CRYSTAL STRUCTURE OF KTP AS A FUNCTION OF PRESSURE TOWARDS THE PHASE TRANSITION

Experiment

A suitably-sized single crystal fragment (approximate dimensions 0.1x0.1x0.1 mm) was mounted in a Merrill-Bassett type diamond-anvil cell, with a tungsten gasket used to confine the sample and the 4:1 methanol:ethanol pressure-transmitting fluid. Refinements of simulated data indicated that the lowest correlations and e.s.d's were given for the positional parameters with the b- and c-axes parallel to the diamond anvil faces. Therefore, this setting of the crystal was selected. The cell was mounted on an Enraf-Nonius CAD4 diffractometer, which was equipped with a graphite-monochromated AgKα xray source. This wavelength was chosen due to the superior resolution and lower absorption it offers over MoKα. Data were initially collected at the low pressure of 0.2 GPa, the pressure being determined from the frequency shift of the ruby fluorescence spectrum. The reflections were measured using the ω-scan method at the position of least attenuation of the pressure cell, following the procedure of Finger and King[5]. All reflections were measured at three positions over a narrow range around the scattering vector to detect reflections affected by simultaneous diffraction by the diamond anvils[6]. The affected reflections were removed from the data. After applying a correction for both the absorption of the pressure cell and the sample, the data were averaged over repeated measurements and used for a least-squares refinement of the structure, including an extinction correction, using the PROMETHEUS crystallographic programs.

The purpose of the low-pressure 0.2 GPa reference data set was to establish to what extent (if at all) the restrictions imposed by the pressure cell bias the refined structural parameters, as well as establishing a reasonable data-collection strategy. Any bias in the data may offset the refined positional parameters from their ambient pressure values. Therefore, the low-pressure reference data set establishes a starting point from which any changes in the structure can be determined for data measured at higher pressures.

Data were collected at pressures of 2.2, 3.7 and 4.7 GPa and at each pressure, including 0.2 GPa, the unit cell dimensions were determined accurately by the four-equivalent-settings procedure of King and Finger[7] which corrects for any sample mis-centering. The data collection and refinement procedures for the high-pressure data sets were the same as that for the 0.2 GPa reference data set.

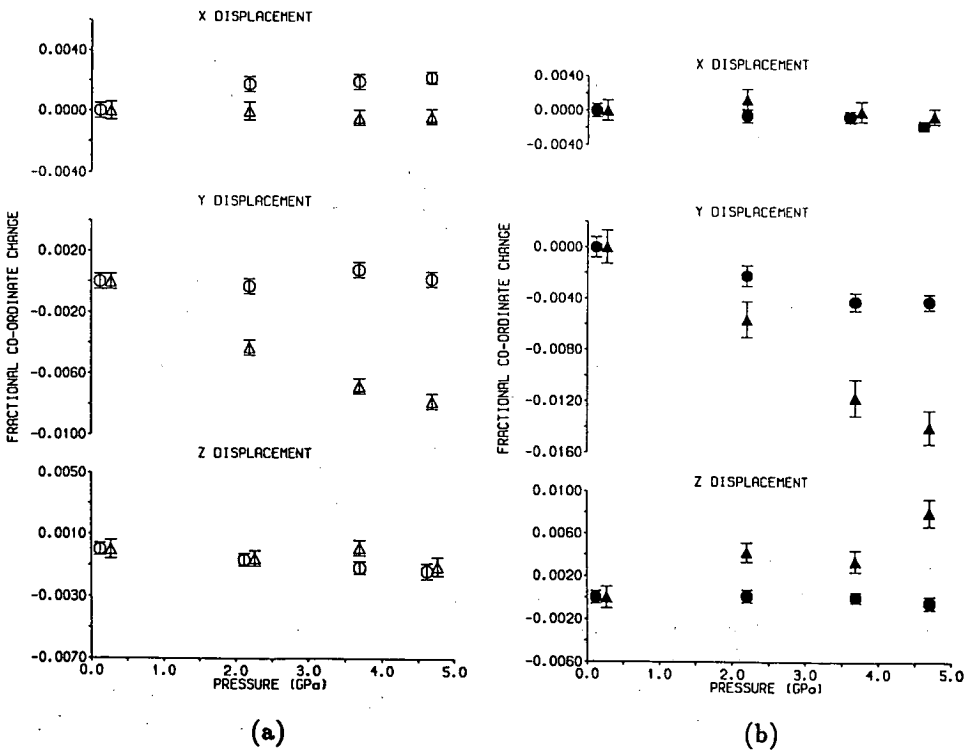

FIGURE 2 Fractional coordinate changes for (a) the K(1) (○) and K(2) (△) atoms, and (b) the P(1) (●) and O(3) (▲) atoms. Note that some of the points have been translated slightly along the pressure axis to avoid overlap

Results and Discussion

The principal changes of the KTP structure under pressure appear to be in the region of the relatively compressible K(1) and K(2) cages which absorb a significant fraction of the 4.7% reduction of the unit cell-volume. While the PO_4 and TiO_6 units remain fairly rigid in shape, the compression of the cages appears to be accommodated by significant deformation of the framework structure, accompanied by a pronounced movement of the K(2) atom. In contrast the K(1) atom remains relatively stationary (see Figure 2a). From Figure 1, which presents the structure of KTP, it is evident that the K(2) cage site forms a channel along the b-axis of the crystal. The K(2) atom, therefore, is relatively free to move in this direction. Conversely, the K(1) atom is constrained from a similar motion by the O(3) atom which is itself forced to undergo a relatively pronounced movement as the $P(1)O_4$-$Ti(2)O_6$ chain deforms under pressure (see Figure 2b). The deformation of the framework structure is also accompanied by strong movement of the P(1) and P(2) atoms. To illustrate the shifts, the fractional coordinate change of the P(1) atom is also shown in Figure 2b (note that P(2) has a shift of similar magnitude to that of P(1) and is not shown in the figure).The motion of the O(3) atom, combined with that of the P(1) atom, results in a reduction of the P(1)-O(3)-Ti(2) bond angle by approximately 3° in 4.7 GPa. However, the most significant TiO_6-PO_4 linking angle change is in the P(2)-O(7)-Ti(2) bond which reduces by approximately 6° over the pressure range. (But this is much less than the angular change of 6.1° at 1 GPa reported by Stucky et al [8] for an unspecified Ti-O-P bond). All the other Ti-O-P bonds have angular changes of 2° or less, as do the Ti-OT-Ti bonds which link the titanium octahedra.

The anomalously short Ti-OT bonds within the highly distorted TiO_6 octahedra have been proposed to be linked to the non-linear optical properties of KTP and are consequently of great interest. It is evident from Figure 3 that the Ti(1)-OT(2) and Ti(2)-OT(2) bond lengths both undergo systematic changes under pressure: the longer Ti(2)-OT(2) bond reduces in length while the shorter Ti(1)-OT(2) bond length appears to increase slightly. These changes reduce by around 20% the difference between the Ti(1)-OT(2) and Ti(2)-OT(2) bond lengths, while the Ti(1)-OT(1) and Ti(2)-OT(1) bonds appear to retain their bond length difference. It is not yet known whether there is any accompanying change in the pronounced second-harmonic generating properties of the crystal and a study to establish the SHG properties of KTP as a function of pressure is currently being planned. The overall distortion of the $Ti(1)O_6$ and $Ti(2)O_6$ octahedra appears to be retained up to 4.7 GPa in as much as the long to short distribution of the Ti-O bond lengths remains the same and the O-Ti-O bonds, within the octahedra, have angular changes of only 2° or less.

The deformation of the TiO_6-PO_4 framework is not accompanied by a significant movement of the titanium atoms, although, as already indicated, there is a clear movement of the phosphorus atoms and a change in the Ti-O-P bond angles. Since the O-Ti-O angles show changes of 2° or less the titanium octahedra remain fairly rigid in shape. Therefore, the movement of the phosphorus atoms relative to the stationary titanium atoms, combined with the angular changes in the Ti-O-P bond angles, suggest that the TiO_6 octahedra are tilting relative to the PO_4 tetrahedra.

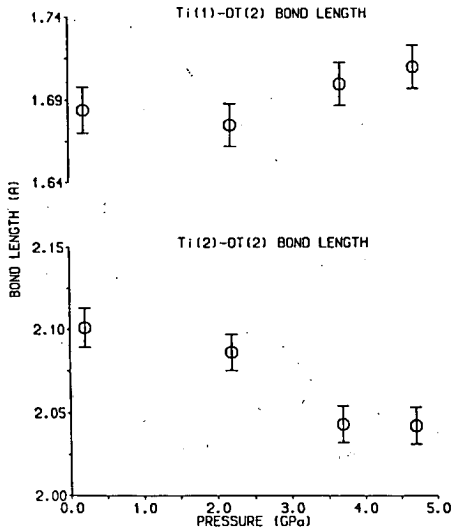

FIGURE 3 The Ti(1)-OT(2) and Ti(2)-OT(2) bond lengths as a function of pressure

2. THE UNIT CELL ABOVE THE PHASE TRANSITION

Experiment

In order to achieve the 5.5 GPa required to place KTP into its high-pressure phase, it was found necessary to use an alternative design of pressure cell. Although the Merrill-Bassett cell was capable of pressures just in excess of 6.0 GPa the pressure was found to be unstable and could not be sustained above the required 5.5 GPa. A cell of more robust construction, designed by D. Adams, was loaded with a freshly prepared sample of KTP. The crystal was cut to the dimensions of 0.1x0.1x0.05 mm^3 (from the same bulk sample of KTP used in the first part of the experiment) and the crystallographic axes determined relative to its regular box-like shape. The crystal was then mounted in the cell with its b- and c-axes parallel to the diamond-anvil faces. A tungsten gasket was used to enclose the sample and the ethanol-methanol pressure transmitting fluid. The cell was then taken to a pressure of 6.2 GPa and mounted on the CAD4. The sample was oriented using the same indexing scheme as that used for the low-pressure phase and the unit-cell dimensions were determined from the four-equivalent-settings procedure. A search was made along the [1 0 0] type,[1 1 0] type and [1 1 1] type directions for new reflections, and reflections within the (0 k l), (h 0 l) and (0 k l) layers were also measured to check space group absences.

Results and Discussion

No new reflections were found in the preliminary survey, and the unit cell appears to remain primitive, with the axes parallel to those of the low-pressure phase. The measured cell dimensions (table 1) indicate that the unit-cell undergoes a rather large 5% volume reduction at the phase transition with the a- and c-axes shortening

by 1% and 3% respectively. Initial studies of the reflection conditions indicate that the n-glide symmetry has been lost; however, the full symmetry of the cell has not been determined at this early stage of the study. A full structure determination of the new phase is now in progress.

TABLE 1 The unit cell dimensions and volume as a function of pressure

Pressure (GPa)	AP(ref[1])	0.2 GPa	2.2 GPa	3.7 GPa	4.7 GPa	6.2 Gpa
a(Å)	12.819(3)	12.832(7)	12.705(7)	12.639(7)	12.620(8)	12.477(9)
b(Å)	6.399(1)	6.412(3)	6.363(2)	6.331(2)	6.315(4)	6.322(3)
c(Å)	10.584(2)	10.586(4)	10.505(4)	10.447(4)	10.417(5)	10.058(4)
V(Å^3)	868.2(4)	871(1)	849(1)	836(1)	830(1)	793(1)

CONCLUSIONS

The structural changes up to 4.7 GPa are relatively small,with the overall distortions of the ambient-pressure KTP structure being maintained. In particular, the TiO_6 octahedra were found to retain their distortion although the difference between the Ti(1)-OT(2) and Ti(2)-OT(2) bond lengths was found to reduce. It is not yet known whether the second-harmonic generating properties associated with the distorted TiO_6 octahedra remain unaltered with pressure. The transition to the high-pressure phase appears to involve a large reduction (5%) in the unit-cell volume, implying substantial structural changes.

Acknowledgements

We are grateful to Mr H. Vass and Mr S. Duffield for their technical assistance and also Dr P.D. Hatton, Dr R.O. Piltz and Dr M.I. McMahon for many useful discussions. This work is supported by a grant from the Science and Engineering Research Council.

REFERENCES

1. P.A. Thomas, A.M. Glazer and B.E. Watts. Acta Cryst B46 333-343. (1990)
2. I. Tordjman, R. Masse and J.C. Guittel Z. Kristallogr. 139,103 (1974)
3. G.A. Kourouklis et al Sol. State. Comm. 62 379-382 (1987)
4. D.R. Allan, J.S. Loveday, R.J. Nelmes and P.A. Thomas submitted to J. Phys. Cond. Mat.
5. L.W. Finger and H.E. King Am. Min. 63 337 (1978)
6. J.S. Loveday, M.I. McMahon and R.J. Nelmes Appl. Crystallogr. 23 392 (1990)
7. H.E. King and L.W. Finger Am. Min. 12 374 (1979)
8. G.D. Stucky, M.L.F. Phillips and T.E. Gier. Chem. Mater. 1 492-509 (1989)

J. Phys.: Condens. Matter 4 (1992) L395–L398. Printed in the UK

LETTER TO THE EDITOR

The crystal structure of potassium titanyl phosphate (KTP) in its high-pressure phase

D R Allan and R J Nelmes

Department of Physics, The University of Edinburgh, Mayfield Road, Edinburgh EH9 3JZ, UK

Received 22 May 1992

Abstract. The structure of the high-pressure phase of KTP has been determined at 6.2 GPa using Patterson projections, Fourier difference maps and least-squares refinement. Although the phase transition is strongly first-order and involves a 4.2% reduction of the unit-cell volume, the $Pna2_1$ space-group symmetry of the low-pressure phase is retained. The main structural changes involve tilting of the PO_4 tetrahedra relative to the TiO_6 octahedra, while both units remain relatively unchanged in size and shape. In particular, the TiO_6 octahedra remain highly distorted and retain their anomalously short Ti–OT bonds. The potassium atoms are observed to undergo relatively large movements of about 0.5 Å along the polar *c*-axis.

Potassium titanyl phosphate (KTP) and its family of structural analogues form a unique class of non-linear optical materials. KTP is an extremely efficient second-harmonic generator (SHG) of Nd-YAG laser light [1] and is a particularly important material for many opto-electronic applications. The structure of KTP assumes the acentric $Pna2_1$ space group at atmospheric pressure ($a = 12.819(3)$ Å, $b = 6.399(1)$ Å, $c = 10.584(2)$ Å, $V = 868.1(4)$ Å^3 [2]) and is characterized by chains of TiO_6 octahedra linked by PO_4 tetrahedra. The TiO_6 octahedra are highly distorted and contain anomalously short Ti–O bonds. It is these anomalously short bonds that have been associated with the non-linear optical properties of the crystal [3]. The KTP structure exhibits a strong pseudosymmetry derived from the centric *Pnan* space group and it has been reported that the isomorphous thallium analogue $TlTiOPO_4$ (TlTP) undergoes a second-order transition into this *Pnan* symmetry at 923 K [4]. Recently, it has been demonstrated by Kourouklis *et al* [5] that KTP exhibits a structural phase transition at a pressure of 5.5 GPa. Their high-pressure Raman study shows that there is an increase in the number of detectable modes at 5.5 GPa, which was taken to indicate a lowering of the crystal symmetry into an antiferroelectric phase. In contrast, Serhane *et al* [6] have located a phase transition in TlTP at 6 GPa where the number of Raman modes *decreases* by about a factor of two. They postulate that TlTP adopts a centrosymmetric phase which is paraelectric and closely related to the high-temperature phase. It is of considerable interest to determine what relationship these high-pressure phases have to the high-temperature phase, and whether the high-pressure phases of KTP and TlTP have different structures. We have recently carried out a detailed investigation of the changes that occur as the high-pressure transition

0953-8984/92/290395+04$04.50

in KTP is approached [7]. We now report the successful determination of the structure of the high-pressure phase.

A single crystal of flux grown KTP was cut to the dimensions of $50\times100\times100\ \mu m^3$ and mounted in a Diacell diamond-anvil pressure cell so that the *b*- and *c*-axes were parallel to the diamond-anvil faces. From the previous study of the low-pressure phase [7], this orientation of the sample was found to give the lowest correlations and ESDs for the positional parameters during structural refinement of the restructed data. A tungsten gasket was used to enclose the sample and the ethanol–methanol pressure-transmitting fluid. The pressure cell was then taken to a pressure of 6.2 ± 0.1 GPa (measured using the ruby fluorescence method [8]) to place the sample crystal into the high-pressure phase. The cell was mounted on an Enraf–Nonius CAD4 diffractometer and oriented using the same indexing scheme as that used for the low-pressure phase [7], and a search was made along the [100], [110] and [111] directions for new reflections. No new reflections were found in the survey; the unit cell appears to remain primitive, with axes parallel to those of the low-pressure phase. (A series of precession photographs also showed no new reflections strong enough to be detected on film.) The unit-cell dimensions were then determined accurately by the four-equivalent-settings procedure of King and Finger [9] and found to be $a = 12.477(9)$ Å, $b = 6.322(3)$ Å and $c = 10.058(4)$ Å, giving a unit-cell volume $V = 793(1)$ Å^3. Comparing these values with an extrapolation to 6.2 GPa from our previous unit-cell measurements [7] indicates that there is a 4.2% volume reduction at the phase transition. The transition is, therefore, strongly first-order.

Intensity data were collected with the ω-scan method at the position of least attentuation of the pressure cell, according to the fixed-ϕ technique [10]. All accessible reflections in the hemisphere $\pm h, k, \pm l$ up to a maximum $\sin\theta/\lambda$ of 0.59 Å^{-1}, totalling 1056, were measured with graphite-monochromated MoK_α radiation. The systematic absences were consistent with either the $Pna2_1$ or *Pnam* space groups. Although observation of the $h0l$ layer of reflections was restricted by the pressure cell, a sufficient number of systematic absences could be recorded to establish that the *a*-glide was present. After applying a correction for the absorption of the sample the data were used to generate Patterson projections. Comparing the 6.2 GPa Patterson projections with those for the low-pressure data sets, the major structural changes were identified and an initial structural model developed in the $Pna2_1$ symmetry. (A satisfactory model could not be found in the *Pnam* space group since the atoms would have to undergo unrealistically large movements to conform to the mirror plane. These movements would require severe disruption of the TiO_6–PO_4 framework and the breaking of several bonds.) The model was then successfully refined using the Prometheus suite of crystallographic programs [11]. Fourier difference maps were generated at each stage of the refinement to check the quality of the fit. The atomic coordinates refined freely to a structure in which the TiO_6 octahedra and PO_4 tetrahedra have internal bond lengths and bond angles very similar to the low-pressure structure. Also, the fit to the data compared well with the fits obtained in refinements of equivalent data sets from the low-pressure phase.

If the true symmetry of KTP were lower than $Pna2_1$ as proposed by Kourouklis *et al* [5] from their high-pressure Raman study, the structure would have to be only slightly distorted from the one refined in the $Pna2_1$ space group, so the apparently absent reflections are in fact present but too weak to be observed. The only space groups allowing such a small distortion of the structure, and not introducing further reflection conditions, are monoclinic *Pn*, *Pa* and $P2_1$. Using the coordinates refined

with the $Pna2_1$ space group as starting values, refinements were performed in each of these space groups. However, the refinements did not give a significantly better fit to the data and the atomic positions differed by less than 0.1 Å from their $Pna2_1$ positions. It appears, then, that the $Pna2_1$ space group is retained after the phase transition, unless there is twinning not resolvable in this experiment.

The $Pna2_1$ refinement was completed by removing the systematically absent reflections from the data and averaging over symmetry-equivalent reflections, after their intensities had been corrected for extinction. The oxygen atoms were all refined with isotropic temperature factors while the potassium, titanium and phosphorus atoms were refined with anisotropic temperature factors (the anisotropic thermal parameters for the atomic motion directed along a, the direction of lowest resolution in the data, were constrained to their ambient values). Similar constraints were applied to the low-pressure refinements [7] and were shown not to bias the refinement of the positional parameters significantly. The final cycle of refinement resulted in a weighted R-factor, R_w, of 3.6% for 533 independent reflections and 88 refinable parameters. Table 1 presents the refined atomic coordinates and the structure is shown in figure 1.

Table 1. Atomic coordinates of $KTiOPO_4$ at 6.2 GPa. The estimated standard deviations (ESDs) are given in parentheses. Note that the Prometheus refinement program requires that one atom is fixed along the polar axis. The Ti1 z coordinate was chosen to be fixed to the same value used in the low-pressure study, and so no ESD is quoted for it.

	x	y	z		x	y	z
K1	0.3953(7)	0.7780(4)	0.6314(4)	O3	0.4373(21)	0.1848(11)	0.7130(9)
K2	0.1146(6)	0.7001(4)	0.8667(4)	O4	0.6246(19)	0.1795(12)	0.7590(9)
R1	0.3718(4)	0.4894(3)	−0.0004	OT1	0.1913(16)	0.9728(9)	0.3269(6)
T2	0.2800(5)	0.2572(3)	0.7240(3)	OT2	0.2510(17)	0.0398(9)	0.5783(7)
P1	0.5296(8)	0.3218(4)	0.7623(4)	O5	0.0998(15)	0.2982(11)	0.4702(7)
P2	0.1798(6)	0.4810(4)	0.4784(3)	O6	0.1218(15)	0.6777(12)	0.5285(8)
O1	0.5134(15)	0.4177(11)	0.8973(7)	O7	0.2300(16)	0.5126(9)	0.3390(7)
O2	0.5452(15)	0.5043(10)	0.6625(7)	O8	0.2754(15)	0.4380(9)	0.5672(6)

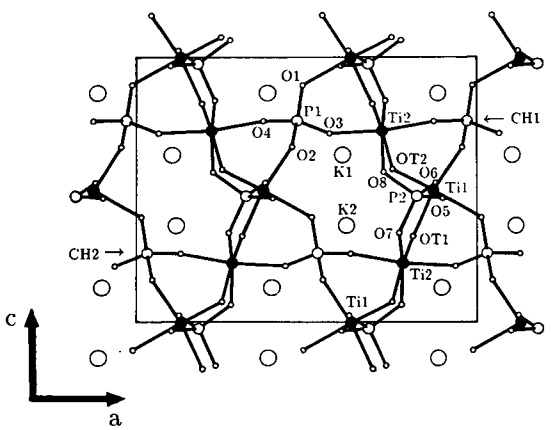

Figure 1. The high-pressure structure of $KTiOPO_4$ viewed along the b-axis. The shaded circles represent the titanium atoms and the TiO_6–PO_4 chains labelled CH1 and CH2 exhibit parallel/antiparallel translations along the a-axis, in the directions indicated by the arrows. This figure can be compared with figure 1 of Allan *et al* [7] to reveal the deformation of the potassium cage site environments and the pronounced movements of the potassium atoms along the c-axis.

The main structural changes involve the n-glide-related $Ti(2)O_6$–$P(1)O_4$ chains (labelled CH1 and CH2 in figure 1), which exhibit parallel/antiparallel translations along the a-axis. The cross-linking $Ti(1)O_6$–$P(2)O_4$ chains (which are directed along the b-axis) are rotated by the relative shifts of the $Ti(2)O_6$–$P(1)O_4$ chains. Within the chains there is pronounced tilting of the TiO_6 octahedra with respect to the PO_4 tetrahedra, with a considerably larger change in their relative orientation than is observed between ambient pressure and the phase transition [7]. The overall shape and distortions of the TiO_6 octahedra are almost unchanged by the phase transition and the distribution of the long, intermediate and short bonds is the same as in the low-pressure phase. In particular the anomalously short Ti–OT bonds are retained. However, some of the bond angles *within* the TiO_6 octahedra differ significantly from their values below the phase transition. This is in marked contrast with the bond-angles of the PO_4 tetrahedra which show almost no change. The potassium atoms undergo substantial movements along the polar c-axis, of the order of 0.5 Å with respect to the TiO_6–PO_4 framework. These movements are accompanied by large distortions of the coodination (or cage site) environments of the K atoms, which reduce in volume by about 10%.

Our conclusion that there is no symmetry change through the 5.5 GPa transition disagrees with interpretation that Kourouklis *et al* make of their high-pressure Raman data [5]. The apparent contradiction may be explained if the intensities of weak and previously unobserved Raman modes are augmented after the phase transition. This would give rise to an apparent increase of the number of modes without changing the crystal symmetry.

To summarize, we have solved the high-pressure structure of $KTiOPO_4$ and have demonstrated that the phase transition is first-order in character. Our results show that the $Pna2_1$ space group is retained and that there are substantial deformations of the TiO_6–PO_4 framework. The potassium atoms also exhibit relatively large movements along the polar c-axis. We are planning to investigate what effect the phase transition has on the SHG properties of the crystal and these results, along with a more detailed account of the structural changes, will be presented at a later date.

We thank Dr P A Thomas of the Physics Department at the University of Warwick for the KTP sample and her encouragement of this project. We also thank Dr A J Welch of the Chemistry Department at The University of Edinburgh for the use of his CAD4 diffractometer. This work is supported by a grant from the UK Science and Engineering Research Council.

References

[1] Bierlein J D and Vanherzeele H 1989 *J. Opt. Soc. Am.* B **6** 622–33
[2] Thomas P A, Glazer A M and Watts B E 1990 *Acta Crystallogr.* B **46** 333-43
[3] Tordjman I, Masse R and Guitel J C 1974 *Z. Kristallogr.* **139** 103–15
[4] Harrison W T A, Gier T E, Stucky G D and Schultz A J 1990 *J. Chem. Soc., Chem. Commun.* 7 540–2
[5] Kourouklis G A, Jayaraman A and Ballman A A 1987 *Solid State Commun.* **62** 379–82
[6] Serhane M, Dugautier C, Farhi R, Moch P and Pisarev R V 1991 *Ferroelectrics* **124** 373–8
[7] Allan D R, Loveday J S, Nelmes R J and Thomas P A 1992 *J. Phys.: Condens. Matter* **4** 2747–60
[8] Forman R A, Piermarini G J, Barnett J D and Block S 1972 *Science* **176** 284
[9] King H E and Finger L W 1979 *J. Appl. Crystallogr.* **12** 374
[10] Finger L W and King H E 1978 *Am. Miner.* **63** 337
[11] Zucker U H, Perenthaler E, Kuhs W F, Bachmann R and Schulz H 1983 *J. Appl. Cryustallogr.* **16** 358

Ferroelectrics, 1992, Vol. 128, pp. 93–98
Reprints available directly from the publisher
Photocopying permitted by license only

STRUCTURAL STUDIES OF COPPER-OXIDE SUPERCONDUCTORS [1]

J.S.LOVEDAY,R.J.NELMES,M.I.M^{c}MAHON,D.R.ALLAN

Department of Physics,University of Edinburgh,Edinburgh,U.K.

E.KALDIS,J.KARPINSKI

Eidgenössische Technische Hochschule,Zürich,Switzerland,CH-8093.

B.RAVEAU and V.CAIGNAERT.

Laboratoire Crismat,ISMRA,Caen, France

ABSTRACT The results of studies of the pressure dependence of the structures of $YBa_2Cu_4O_8$ and $La_{1.85}Sr_{0.15}CuO_4$ are presented. Comparison with the changes observed on oxidation of $YBa_2Cu_3O_{7-\delta}$ show that the large dT_c/dp in $YBa_2Cu_4O_8$ can be attributed to charge transfer. By contrast the the behaviour of $La_{1.85}Sr_{0.15}CuO_4$ shows no evidence of charge transfer.

INTRODUCTION

A striking feature of many of the copper-oxide superconductors is the large pressure-induced increases in the superconducting transition temperature (T_c). For example the transition temperature of $La_{1.85}Sr_{0.15}CuO_4$ increases by 3.3 $KGPa^{-1}$ from an ambient pressure value of 30K [1] , while that of $YBa_2Cu_4O_8$ increases initially at 5.5 $KGPa^{-1}$ from a value of 80K[2].

Clearly it is important to understand the mechanism of these large effects.To explore the relationship between T_c and the structure, we have carried out high-pressure structural studies of both $YBa_2Cu_4O_8$ and strontium-doped La_2CuO_4. The structures of these compounds are shown in figure 1. The common feature is the basal plane of corner-linked CuO_4 squares which are found in all the copper-oxide superconductors and are thought to be the superconducting part of the structure. In $YBa_2Cu_4O_8$ (hereafter 1-2-4) the basal-plane copper atoms have a five-fold oxygen co-ordination forming CuO_5 square pyramids. The apical oxygens are then linked to an adjacent layer of oppositely-directed pyramids by a double layer of O-Cu-O chains running along the b-axis. The structure of Sr doped La_2CuO_4 (hereafter Lasco) does not have these chains; the basal-plane copper atoms have a 6-fold oxygen

[1]Neutron diffraction data collected at INSTITUT LAUE-LANGEVIN, Grenoble , France

co-ordination and form layers of CuO_6 octahedra. Lasco has a phase transition from the tetragonal structure shown in figure 1, involving tilting of the CuO_6 octahedra about <110> to form an orthorhombic superstructure. At the optimal level of strontium doping for a maximum T_c (7.5 %) this transition occurs at T_d=140K.

To obtain structural changes large enough to determine reliable rates of change, it is necessary to collect data at pressures much above 1 GPa [5]; for Lasco it is desirable to collect data at low temperatures in the orthorhombic phase below T_d (i.e. in the phase that becomes superconducting). Unfortunately it is difficult to achieve these conditions simultaneously. High-pressure x-ray diffraction is not readily performed at low temperatures and neutron diffraction (with sufficient sample volume) is limited to 1 GPa. The best available option was to follow the pressure dependence at room temperature to above 3 GPa using x-ray techniques and then use neutron techniques to make a comparative study (to < 1GPa) at low temperature. This paper presents x-ray single-crystal studies of 1-2-4 and Lasco at ambient temperature, and neutron powder diffraction studies of Lasco at 55K.

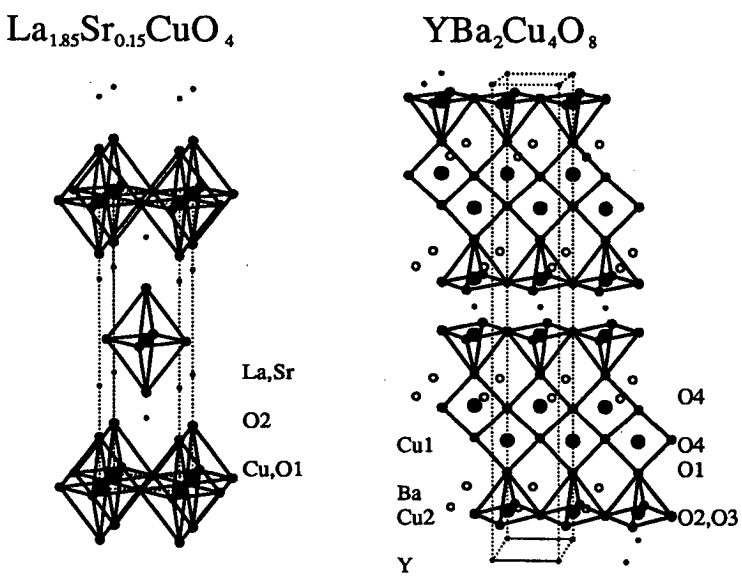

Figure 1: The structures of $La_{1.85}Sr_{0.15}CuO_4$ and $YBa_2Cu_4O_8$

X-RAY STUDIES

Single crystals of nominal composition $La_{1.85}Sr_{0.15}CuO_4$ were grown by a flux

method by the Crystal Growth Group,Clarendon Lab,Oxford. The sample of 1-2-4 was also grown from flux, using a high pressure oxygen technique[3] at ETH, Zurich.

In each study a piece of dimension .1x.1x.1 mm^3 was cut from the sample provided, and loaded into a Merrill-Bassett type diamond-anvil cell (DAC). Shadowing by the steel cell housing restricts the accessible reflections to those lying in or close to the reciprocal lattice plane parallel to the diamond faces[4] in both crystal structures all the x and y fractional co-ordinates are fixed by symmetry and so only the z co-ordinates have to be determined. The samples were mounted with their a and c axes in the plane of the diamond faces to allow access to the high l reflections and hence give the best precision on the structural parameters of interest.

The cell was assembled with a tungsten gasket and a 4:1 methanol:ethanol mixture ,dried with molecular sieve, as a pressure transmitting fluid. X-ray diffraction data were collected on an ENRAF-NONIUS 4-circle diffractometer with graphite-monochromated Ag K_α x-rays,following standard high-pressure procedures[5]. To establish a good data set all accessible reflections in the required layers (h0l in Lasco,h0l,h1l,h2l in 1-2-4) were measured out to $\sin\theta/\lambda = 1.2$ $Å^{-1}$. Data were collected from Lasco at pressures of 0.2,0.8,1.1,2.1 and 3.3 GPa and from 1-2-4 at pressures of 0.2,1.5,3.2,4.5 and 4.7 Gpa. After correction for absorption by both the pressure cell and the sample, and the removal of occluded reflections the data were used for a least-squares refinement of the structure , including an extinction correction, using the PROMETHEUS suite of programs[6].

NEUTRON POWDER DIFFRACTION STUDIES

A sample of $La_{1.85}Sr_{0.15}CuO_4$ synthesised at ISMRA, Caen, was loaded into a Paureau-Vettier type gas cell which has an effective sample volume of 4000 mm^3. The cell was mounted inside an ILL orange cryostat and pressure was applied using helium gas and measured using a digital strain gauge with a accuracy of 50 bar. Diffraction patterns were collected at 55K and pressures of 0.0001, 0.25 and 0.5 GPa on the D1A diffractometer at ILL using a calibrated wavelength of 1.909 Å. The data collection time was 12 hours for each pattern.

The structure was refined using the Rietveld method as implemented in the program PROFIL[7].Scattering from the pressure cells produces a small number of intense peaks which were excluded from the refinement. Otherwise the background was estimated visually. All positional parameters not fixed by symmetry were refined along with isotropic thermal parameters and instrumental zero and asymmetry parameters.

RESULTS AND CONCLUSIONS.

The pressure dependence of the principal features of the 1-2-4 structure are shown in figure 2. They are the shortening of the basal-plane copper to apical-oxygen bondlength (Cu2-O1), the reducing pucker of the barium apical oxygen layer (Ba-

O1) and the relatively small change in the chain-copper to apical-oxygen bondlength (Cu1-O1).

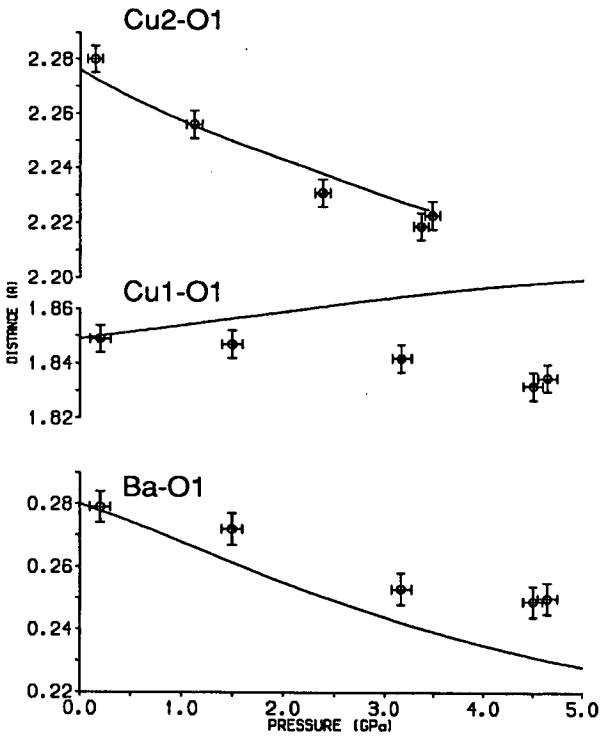

Figure 2: The pressure dependence of the bondlengths Cu2-O1(upper figure) ,Cu1-O1 (middle) and the Ba-O1 interlayer separation (bottom) in 1-2-4.The solid lines represent the changes of the corresponding bondlengths in 1-2-3 made using the procedure described in the text.

To understand the significance of these changes it is useful to compare them with the effect of oxidation on the structure of $YBa_2Cu_3O_{7-\delta}$ (1-2-3)[8]. 1-2-3 has a very similar structure to 1-2-4, the principal difference being that it has only one O-Cu-O chain instead of the two in 1-2-4. The oxygen atoms in this chain are not strongly bound and by controlling the preparation conditions δ may be varied from 1.0 to 0. As δ decreases from 0.5 to 0, T_c increases from 55k to 90K. The solid lines in figure 2 show the change in the corresponding distances in 1-2-3 under oxidation and are obtained by taking the average rate of change of the distance with T_c in 1-2-3 and using the known $T_c(P)$ for 1-2-4 to derive an equivalent pressure. The lines are thus estimates, subject to the various approximations, of the way Cu2-O1,Ba-O1 and Cu1-O1 should vary with pressure in 1-2-4 if the relationship between T_c and

the structure is the same as in 1-2-3.

It can be seen that there is a remarkable similarity, particularly in the case of Cu2-O1. This provides strong evidence that the charge transfer mechanism thought to be responsible for the increases in T_c in 1-2-3 is also responsible for the increase in T_c under pressure.

Figure 3 shows the behaviour of the length of the basal-plane copper to apical-oxygen bond in Lasco (Cu-O2) as a function of pressure. It can be seen that results obtained at 55k by neutron powder diffraction do not differ from those measured at ambient temperature by single-crystal x-ray measurements. Thus it is reasonable to expect that the behaviour of Cu-O2 near to T_c is very similar to that determined at ambient temperature.

The values of the bondlength determined from the x-ray data show a small decrease with pressure of 0.005 ÅGPa^{-1} due entirely to the compression of the c-axis. This is in contrast to the change in Cu2-O1 in 1-2-4 which decreases by 0.015 ÅGPa^{-1} over the same range. Only 1/3 of this is due to the compression of the c-axis.

It is possible to calculate the change in hole concentration from changes in bondlength using either bond valence sum or Madelung energy techniques and we are in the process of performing such calculations. Preliminary results indicate that charge transfer is reflected in a change in the fractional bondlength.- i.e. a change over and above the general compression of the unit cell. This leads us to conclude that the lack of change in z(O2) with pressure in Lasco suggests an absence of charge transfer.This means that some other mechanism is required to explain the pressure dependence of T_c in Lasco and that the charge transfer mechanism as currently developed for 1-2-3 and 1-2-4 does not offer a universal explanation of the variations of T_c with pressure.

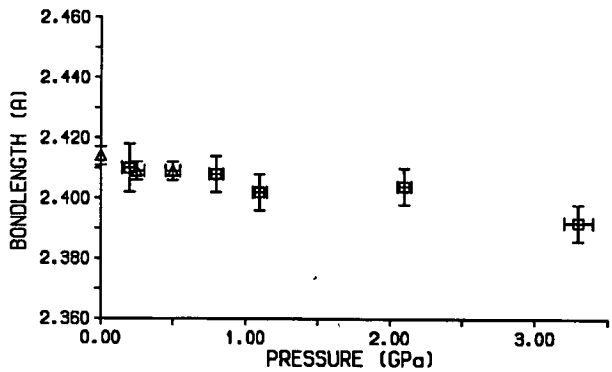

Figure 3: The pressure dependence of the bondlength Cu-O2 in $La_{1.85}Sr_{0.15}CuO_4$. The data shown as solid triangles are those measured in the gas cell at 55K and those shown as open squares are those measured at ambient temperature in the DAC.

ACKNOWLEDGEMENTS

We would like to thank Mrs B.M.Wanklyn (Oxford) for the single crystal of Lasco and Drs A.W.Hewat and C.Vettier (ILL) for their assistance with the neutron experiments. The work at Edinburgh is supported by the U.K Science and Engineering Research Council and that at Zurich by ETH and the Swiss National Science Foundation (program SUPRA$^+$)

REFERENCES

1.S.Yomo,C.Murayama,H.Takahasi,N.Mori,K.Kishio, K.Kitazawa and K.Fuekie, Jpn. J. Appl. Phys. 26 (1987) L602

2.B.Bucher,J.Karpinski,E.Kaldis and P.Wachter, Physica C 157 (1989) 478

3.J.Karpinski,E.Kaldis,E.Jilek,S.Rusiecki and B.Bucher, Nature 336 (1988) 660.

4.L.Merrill and W.A.Bassett, Rev.Sci.Instrum. 45(1974) 290

5.R.J.Nelmes, J.S.Loveday, E.Kaldis and J.Karpinski, Physica C 172 311 (1990)

6.U.H.Zucker,E.Perenthaler,W.F.Kuhs,R.Bachmann and H.Schulz, J.Appl.Cryst. 16(1983) 358.

7.J.K.Cockcroft, PROFIL program, ILL Grenoble (1989)

8.R.J.Cava,A.W.Hewat,E.A.Hewat,B.Batlogg,M.Marezio,K.M.Rabe, J.J.Krajewski, W.F.Peck,and L.W.Rupp, Physica C 165 (1990) 419.